



اَبُو رَسِيْدِيْنِ اَبِي بَكْرٍ اَلْمَدَنِيُّ

UNIVERSITI
TEKNOLOGI
MARA

Jmeche

Journal of mechanical engineering

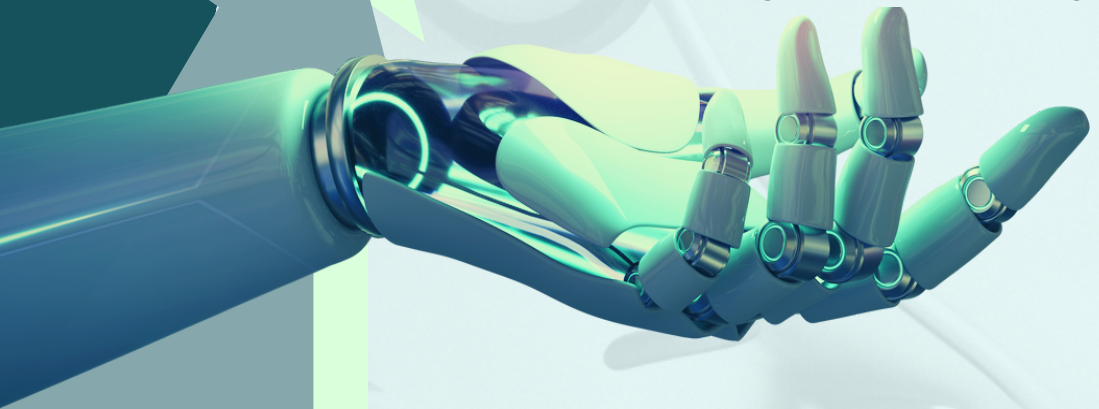
Regular Issue April 2023

Volume No.20(2)

ISSN : 1823 - 5514

e-ISSN : 2550 - 164x

jmeche.uitm.edu.my



JOURNAL OF MECHANICAL ENGINEERING

EDITOR-IN-CHIEF:

Professor Jamaluddin Mahmud – Universiti Teknologi MARA, Malaysia

EDITORIAL BOARD:

Professor Wahyu Kuntjoro – Universiti Teknologi MARA, Malaysia

Professor Hoffmann – Elektrische Meßtechnik, Prozeß- und Analysenmeßtechnik

Professor Martin Bednarz – Technische Hochschule Ingolstadt, Germany

Professor Naveed Ramzan -University of Engineering & Technology, Lahore Pakistan

Professor Abdelmagid Salem Hamouda – Qatar University, Qatar

Professor Abdul Rahman Omar – Universiti Teknologi MARA, Malaysia

Professor Bernd Schwarze – University of Applied Science, Osnabrueck, Germany

Professor Bodo Heimann – Leibniz University of Hannover Germany

Professor Darius Gnanaraj Solomon – Karunya University, India

Professor Essam E. Khalil – University of Cairo, Egypt

Professor Hazizan Md. Akil – Universiti Sains Malaysia, Malaysia

Professor Ichsan S. Putra – Bandung Institute of Technology, Indonesia

Professor Masahiro Ohka – Nagoya University, Japan

Professor Mirosław L. Wyszynski – University of Birmingham, UK

Professor Mohd. Zulkifly Abdullah – Universiti Sains Malaysia, Malaysia

Professor Muhammad Azmi Ayub – Universiti Teknologi MARA, Malaysia

Professor Roslan Abd. Rahman – Universiti Teknologi Malaysia, Malaysia

Professor Salmiah Kasolang – Universiti Teknologi MARA, Malaysia

Professor Shahrir Abdullah – Universiti Kebangsaan Malaysia

Professor Shahrum Abdullah – Universiti Kebangsaan Malaysia

Professor Wirachman Wisnoe – Universiti Teknologi MARA, Malaysia

Professor Xinkai Chen – Shibaura Institute of Technology, Japan

Professor Yongtae Do – Daegu University, Korea

Dr. Yongki Go Tiauw Hiong – Raytheon Company, USA

Dr. Mohd. Afian Omar – SIRIM Malaysia Advanced Materials Research Center

Dr. Valliyappan David Natarajan – Universiti Teknologi MARA, Malaysia

MANAGING EDITORS:

Dr. Mohd Hanif Mohd Ramli

Dr. Siti Mariam Abdul Rahman

SECTION EDITORS:

Assoc. Prof. Ir. Ts. Dr. Baljit Singh Bathal Singh

Ir. Ts. Dr. Kausalyah Venkatasen

Dr. Abdul Malek Abdul Wahab

Dr. Nurul Hayati Abdul Halim

ASSISTANT MANAGING EDITORS:

Dr. Freddawati Rasyiddy Wong

Dr. Izdihar Tharazi

Dr. Mohd Afzan Mohd Anuar

Dr. Mohd Nor Azmi Ab Patar

Dr. Muhd Faiz Mat @ Muhammad

Dr. Natasha Ahmad Nawawi

Mrs. Ahsana Aqilah Ahmad

Mr. Muhamad Fauzi Othman

Mrs. Nurul Syuhada Khusaini

Mrs. Rosnadiyah Bahsan

Copyright © 2022 by the College of Engineering, Universiti Teknologi, MARA, 40450 Shah Alam, Selangor, Malaysia.

All published articles in this journal are open accessed. This allows anybody to freely download, print, copy, distribute or read them, as well as to reused and quoted with proper credit to the original published version. By submitting an article to JMechE, the authors grant full right to the journal to publish the article online once it has been accepted. However, the authors held ownership of their article.

Journal of Mechanical Engineering (ISSN 1823-5514, e-ISSN 2550-164X) is published by Penerbit UiTM (UiTM Press), Universiti Teknologi MARA, 40450 Shah Alam, Selangor, Malaysia.

The views, opinions, and technical recommendations expressed herein are those of individual researchers and authors and do not necessarily reflect the views of the university.

JOURNAL OF MECHANICAL ENGINEERING

An International Journal

Vol 20 (2)	15 April 2023	ISSN 1823-5514	eISSN 2550-164X
------------	---------------	----------------	-----------------

1	Numerical Study of Contra-Rotating Vertical Axis Wind Turbine H-Rotor Darrieus Type <i>Aditya Ilham Setyawan Haryogo, Vivien S. Djanali*, and Bagus Nugroho</i> https://orcid.org/0000-0003-3964-1297	1
2	Seismic Behaviour of Beris Dam Under Six Earthquake Excitations by using Finite Element Method <i>Rozaina Ismail*, Nurul Nabilah Moktar, Nurul Damia Sukati, Ainnur Zulsyamilatil Huda Abd Halim, Dayang Nur Erliyani Fitri Erwan, Azmi Ibrahim, Norliyati Mohd Amin, Azlan Adnan, and Ade Faisal</i> https://orcid.org/0000-0003-1991-1122	21
3	Stress Shielding Prediction of Unicortical and Bicortical Screws: A Finite Element Analysis <i>Anis Amira Mat Zuki, Fauziah Mat, Khairul Salleh Basaruddin*, Ruslizam Daud, Masniezam Ahmad, and Fauzan Djamaluddin</i> https://orcid.org/0000-0002-9806-3565	37
4	Evaluation of Crosslinking Degree on the Integral Membrane by using Rice Husk Ash (RHA) <i>Nurul Atirah Fitriah Mohd Zainuddin, Norin Zamiah Kassim Shaari*, Nur Syazwanie Izzati Chik, and Fazlena Hamzah</i> https://orcid.org/0000-0001-5754-2183	57
5	Investigation on Surface Roughness and MRR in WEDM of Titanium Grade 7 (Ti-0.15Pd) Alloy using Statistical Techniques <i>H. R. Basavaraju, S. S. Manjunatha, and R. Suresh*</i> https://orcid.org/0000-0002-6956-9751	73
6	Effect of Rice-Husk as Replacement Cement on Mechanical Properties Concrete <i>Mohd Najmudin Helmi Abu Bakar, Sakhiah Abdul Kudus*, Nur Kamaliah Mustaffa, Adiza Jamadin, Hasan Ali Abbas, Rohana Hassan, and Nadia Kamaruddin</i>	91

	https://orcid.org/0000-0002-5215-0436	
7	Evaluation of Energy Production using Parabolic-Dish Solar Collector: A Case Study of Iraq <i>Samir Gh Yahya, Ahmed Shihab Al-Samari, and Itimad D J Azzawi*</i> https://orcid.org/0000-0002-9795-7903	105
8	Concrete with Coconut Fibre Treated with Sodium Hypochlorite – Compressive and Flexural Strength <i>Norisham Ibrahim*, and Muhammad Hafizhin Abdul Halim</i> https://orcid.org/0000-0002-5972-6637	125
9	Corrosion Resistance Enhancement for Low Carbon Steel by Gas Phase Coating <i>Sameer K. Fayyadh*, and Faras Q. Mohammed</i> https://orcid.org/0000-0002-9166-9601	139
10	Effects of Pre-Treated Crumb Rubber as Sand Partial Replacement on Compressive Strength of Engineered Cementitious Composites (ECC) <i>Atiqah Abdul Aziz*, Mohd Ikmal Fazlan Rozli@Rosli, Kay Dora Abd Ghani, Nor Asyiqin Jafri, and Noorliyana Zakaria</i> https://orcid.org/0000-0002-2053-809X	153
11	The Analysis of Dual Axis Solar Tracking System Controllers Based on Adaptive Neural Fuzzy Inference System (ANFIS) <i>M.S.I Zulkornain, S.Z. Mohammad Noor*, N.H. Abdul Rahman, and Suleiman Musa</i> https://orcid.org/0000-0002-3028-4978	167
12	Optimization of Uniaxial Tensile Stress-Strain Response of 3D Angle Interlock Woven Fabric Composite using Weft Density and Draw-In Plan Variables <i>Muhammad Nasrun Faris Mohd Zulkifli, Mohamad Faizul Yahya*, Suzaini Abdul Ghani, and Bilal Zahid</i> https://orcid.org/0000-0002-5012-1914	185
13	Evaluating and Predicting Overall Equipment Effectiveness for Deep Water Disposal Pump using ANN-GA Analysis Approach <i>Soud Al-Toubi*, Babakalli Alkali, David Harrison, and Sudhir C.V.</i> https://orcid.org/0000-0002-7087-0090	199

Numerical Study of Contra-Rotating Vertical Axis Wind Turbine H-Rotor Darrieus Type

Aditya Ilham Setyawan Haryogo

Postgraduate Study, Department of Mechanical Engineering,
Institut Teknologi Sepuluh Nopember, Sukolilo, Surabaya 60111,
INDONESIA

Vivien S. Djanali*

Department of Mechanical Engineering,
Institut Teknologi Sepuluh Nopember, Sukolilo, Surabaya 60111,
INDONESIA

*vivien_s@me.its.ac.id

Bagus Nugroho

Department of Mechanical Engineering,
The University of Melbourne, Parkville, Victoria, 3010, AUSTRALIA

ABSTRACT

The new Contra-rotating Darrieus turbine configuration has been invented to enhance the Vertical Axis Wind Turbine (VAWT) performance. This configuration increases the relative rotational speed of the generator, resulting in higher output power. It is well known that the increase can reach four times the output power. However, how the Darrieus turbine VAWT contra-rotating configuration influences its aerodynamic performance still needs to be discovered. This study investigates the aerodynamic performance of the contra-rotating configuration by comparing it to the single-rotating Darrieus turbine VAWT under the same conditions. The freestream speed is 5 m/s, with TSR varying from one to two intervals of 0.2. This research is being completed using Computational Fluid Dynamics (CFD) 3D cases with an Unsteady Reynold Average Navier-Stokes (URANS) equation as the turbulent model equation. The results of this study show that in terms of output power or Power coefficient (C_p), the contra-rotating has a greater value than the single-rotating configuration. However, in all TSR variations, contra-rotating outperforms single-rotating in terms of aerodynamic performance or moment coefficient (C_m). This is due to the fact that the aspect ratio of stage 1 contra-

rotating rotor is lower than the single-rotating rotor, resulting in more significant blade tip losses in contra-rotating. The flow was discovered through the gap between stages 1 and 2 contra-rotating, providing additional momentum. This phenomenon increases C_m at an azimuth angle of 200° - 255° .

Keywords: *Darrieus Turbine; Contra-Rotating; Numerical Simulation; Power Coefficient; Moment Coefficient*

Introduction

The development of renewable energy, especially the Vertical Axis Wind Turbine (VAWT), is increasing. due to the awareness of the current pollution levels from the use of fossil energy [1]. VAWT itself has several advantages when compared to Horizontal Axis Wind Turbine (HAWT), such as a simple design so that the costs required are not much, being able to work in urban areas or areas with low wind speeds and being able to work in all different wind directions [2]. However, people still use HAWT more than VAWT because HAWT produces better performance when compared to VAWT and has a better self-start. Many researchers were trying to improve the quality of VAWTs, such as [3]-[4], who import hybrid VAWTs to have good performance and self-start. Bausas and Danao [5] used an airfoil camber to improve the performance of the Darrieus turbine VAWT. Several studies [2], [6]–[8] examined the effect of solidity on tip speed ratio. Li et al. [9] examined the effect of aspect ratio on turbine performance. Zhu et al. [10] investigated the addition of a flap. Liu et al. [11] investigated the effect of the trailing edge movable flap on the VAWT performance of the Darrieus turbine. Several studies from [12]-[16] examined the effect of pitch angle on VAWT performance. Azizuddin et al. [17] studied VAWT with a novel blade design.

Didane et al. [18] conducted an experiment using a new rotor configuration, namely the contra-rotating VAWT, especially with the Darrieus turbine. This configuration has two rotors with the same airfoil type and dimensions rotating in opposite directions but having one axis of rotation. This configuration is inspired by contra-rotating HAWT where the configuration utilizes the residual wind speed from the main rotor by using an additional rotor located behind the main rotor so that the turbine's performance can be increased. The incoming wind speed in the contra-rotating either through the first stage or the second stage has the same magnitude, so the moment was greater than just the first stage. In contra-rotating, both the rotor and stator at the generator rotated in opposite directions, so it produced a higher relative rotation. This configuration used a semi-cylindrical pipe placed on the connector between the rotor and the shaft to assist in self-starting. This configuration did not require an electric motor as a helper in self-starting, so the tip speed ratio used can be less than one. That study stated the increasing

Coefficient Performance (C_p) with contra-rotating configuration up to 40% compared to the single-rotating. Contra-rotating VAWT produced a greater moment than single-rotating VAWT. Therefore, the contra-rotating effect on the Darrieus turbine performance can significantly increase the turbine performance. After following this study, there came researcher research this configuration, such as examining the concept of contra-rotating VAWT using a Savonius turbine conducted by Ahmudiarto et al. [19]. From this study, it was found that the performance obtained increased up to two times. Didane et al. [20] also conducted research on contra-rotating using a Savonius turbine. The three blades of Savonius were tested in a wind tunnel within an inlet velocity of 2 m/s up to 9 m/s. The best results were obtained at low wind speeds (2 m/s), with an average C_m increasing up to 42% and C_p 28% for contra-rotating configuration. Then the research was conducted by Didane et al. [21] to determine the effect of axial distance and aspect ratio. The study found that the best performance was obtained by using the smallest axial distance and the largest aspect ratio. Didane et al. [22] also studied using Savonius and Darrieus turbines in the contra-rotating VAWT configuration with low wind speed starting from 2 m/s to 9 m/s. it was found that contra-rotating increased the efficiency system by up to 42%. Particularly, the Darrieus turbine resulted in a higher efficiency along with the increasing wind speed. While in the savonius turbine, the efficiency was opposite with the Darrieus turbine.

Jung et al. [23] investigated contra-rotating HAWT with optimal variations in axial distance and diameter size of the auxiliary rotor. The best performance is discovered in the size and axial distance, which is at 12 of the main rotor diameters. Ko et al. [24] conducted a numerical study of contra-rotating using a Darrieus turbine. This study adopted the contra-rotating geometry from [18], with variations of thickness airfoil, camber airfoil, and also the axial distance between the first stage and the second stage. The tip speed ratio value was conditioned as same as in [18]. this study aimed at the effect of contra-rotating without semi-cylindrical pipes that connected the rotor's shaft with the performance. The results showed that the greatest thickness can produce better performance. In contrast, airfoils with the largest camber can produce the best performance. However, this study resulted in a very small C_p compared to the research conducted by Didane at the same tip speed ratio value.

Previous studies [18], [24] showed that contra-rotating Darrieus turbines were still limited to a low tip speed ratio which was below one while this tip speed ratio was not an ideal condition for Darrieus turbine working on [22]. Therefore, the aerodynamic performance characteristic of the configuration was yet to be explained. This study aims to determine the effect of the contra-rotating VAWT configuration on the Darrieus turbine with an ideal tip speed ratio for the Darrieus turbine working using Computational Fluid dynamics (CFD). This study uses the three-dimensional unsteady simulation case to obtain more accurate results and representation of the three-

dimensional flow structure across the contra-rotating turbine rotors. To the best of our knowledge, this is the first paper to analyze the flow structure around the contra-rotating turbine and compare it with the single-rotating one.

Method

Turbine configuration

This study used a single-rotating configuration to compare the performance with contra-rotating. This single-rotating configuration followed the turbine model from [28], Darrieus turbine with the H-rotor with a diameter rotor of 0.74 m, rotor height of 0.6 m, airfoil NACA 0015 with a chord length of 0.15 m as shown in Figures 1a and 1d. Meanwhile, the contra-rotating configuration consisted of two stages rotating in opposite directions i.e. the first stage rotated clockwise direction while the second stage rotated counterclockwise direction. This configuration has the same dimensions as single-rotating, only this configuration, was divided into two parts as shown in Figure 1d. based on research from [1], stated that the smallest axial distance gave the best performance. More details are shown in Table 1

Table 1: Details of the single-rotating and contra-rotating turbine

Parameter	Single - Rotating	Contra-Rotating
Diameter, D (m)	0.74	0.74
Radius, R (m)	0.37	0.37
Height, H (m)	0.6	0.3 x 2 stage
Number of Blades, N	3	3 x 2 stage
Chord Length, c (m)	0.15	0.15
Airfoil	NACA 0015	NACA 0015
Pitch Angle (β) ($^{\circ}$)	0	0
Aspect Ratio, H/D (-)	0.81	0.405 x 2 stage
Solidity Ratio, σ (-)	0.193	0.193
Re_D (-)	228914.14	228914.14

Numerical method

The three-dimensional simulation was carried out using the finite volume method with the Unsteady Reynold Averaged Navier Stokes (URANS) as the basic flow equation to be solved. The URANS equation has several variables such as time, velocity, pressure, and turbulent properties. The velocity, time, and turbulent properties were solved using a second-order discretization scheme to get good accuracy, while the pressure variable uses a SIMPLE pressure-velocity coupling scheme [26]. The turbulent model used was SST-kw because this turbulent model can capture the phenomenon of flow

separation in the adverse pressure gradient region to provide more accurate results [27].

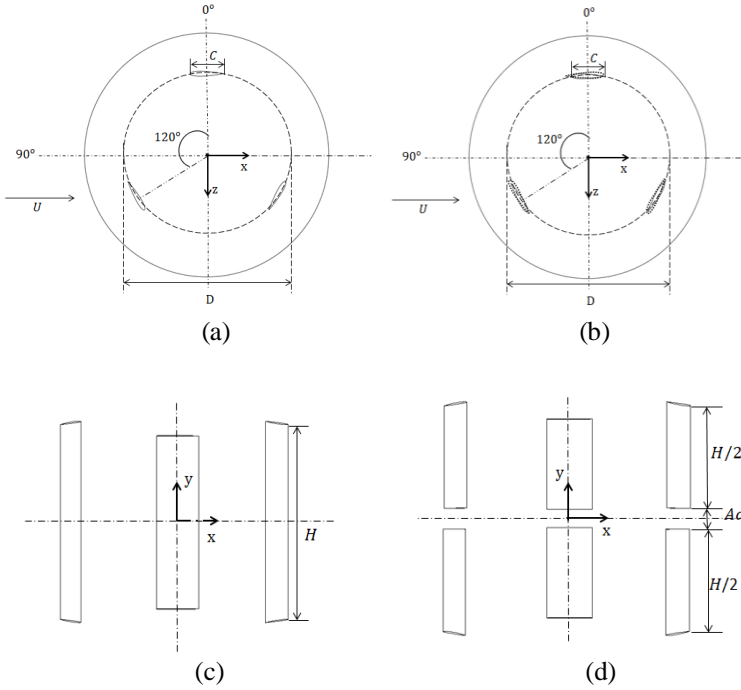


Figure 1: Geometry and dimensions of the contra-rotating Darrieus VAWT turbine; (a) top view single-rotating, (b) top view contra-rotating, (c) side view single-rotating, and (d) side view contra-rotating

The boundary condition used was the velocity inlet with a value of 5 m/s while the outlet used a pressure outlet with a value of 0 pascals. The side wall, the top wall, and the bottom wall used a slip condition wall, but the airfoil used a no-slip condition wall. The cell zone in the fixed zone was set to stationary while the rotating zone was set to rotary with the boundary between the fixed zone and the rotating zone set as an interface so that the two cell zones can communicate. The time step was set using the azimuth angle interval ($d\theta$) of 0.5° so the results obtained are accurate while the computation time is also not too long [26]. As many as 22 revolutions were conducted to obtain accurate and stable results [26]. Therefore, in this study, the simulation was divided into 2 steps. The first step of the simulation was carried out with 20 revolutions with a $d\theta$ of 10° . The discretization scheme especially for turbulent properties used first-order and the convergence criteria were set to 10^{-4} for all properties. This simulation aimed to obtain a stable calculation. After that, the simulation

was repeated with 2 revolutions at a $d\theta$ of 0.5° . The discretization schemes used all second order, and the convergence criteria were set 10^{-5} . This simulation aimed to get accurate results so that the simulations carried out in this study obtained stable and accurate results.

The domain calculation that was simulated consists of two different cell zones, namely the fixed zone and the rotating zone. There are two rotating zones each on the first stage and the second stage which allows for the rotor to rotate in opposite directions. The length of the calculation domain itself was $25D$ while the width was $10D$. The height was made of $6D$ as shown in Figure 2. The dimensions of the calculation domain were determined in such a way that the resulting blockage ratio was not more than 5% whereas the blockage ratio is a ratio between swept area turbine with a cross-sectional area of domain calculation [25].

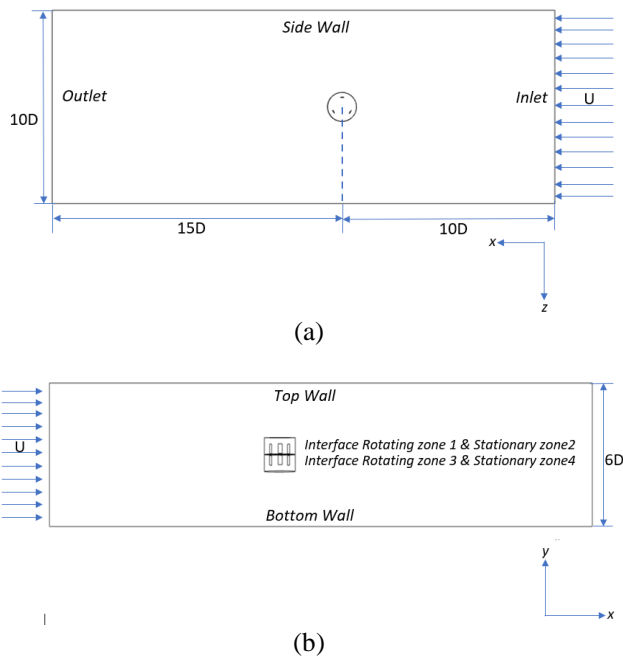


Figure 2: Domain calculation (a) top view, and (b) side view

The mesh that can be applied to the calculated domain can only use a mesh with a tetrahedral mesh. This was because the domain calculation that has been made has a slightly complicated form. The use of tetrahedral mesh was more flexible for complex domain calculations but has a drawback related to accuracy. In addition, using tetrahedral requires a longer process in the simulation than using a hexahedral mesh which will be a problem in this study

because this research relied heavily on high accuracy but with fast computation time. Therefore, it was necessary to make some auxiliary lines in the calculation domain to ensure that a hexahedral mesh dominates the mesh that can be applied to the calculation domain as in Figure 3. Thanks to the helplines provided for the domain calculation, the mesh can be used for the domain calculation using hexahedral. However, for the mesh around the rotating zone, it was very difficult to condition the hexahedral with a structured mesh because the geometry of the Darrieus turbine was quite complicated. Therefore, auxiliary lines were added around the airfoil so that the mesh around the airfoil can be hexahedral conditioned with a structured mesh. The first distance between the wall of the blade and the first cell was described as y^+ . Therefore y^+ was conditioned at $y^+ < 5$ so that the calculation reached the viscous sub-layer area to increase the accuracy.

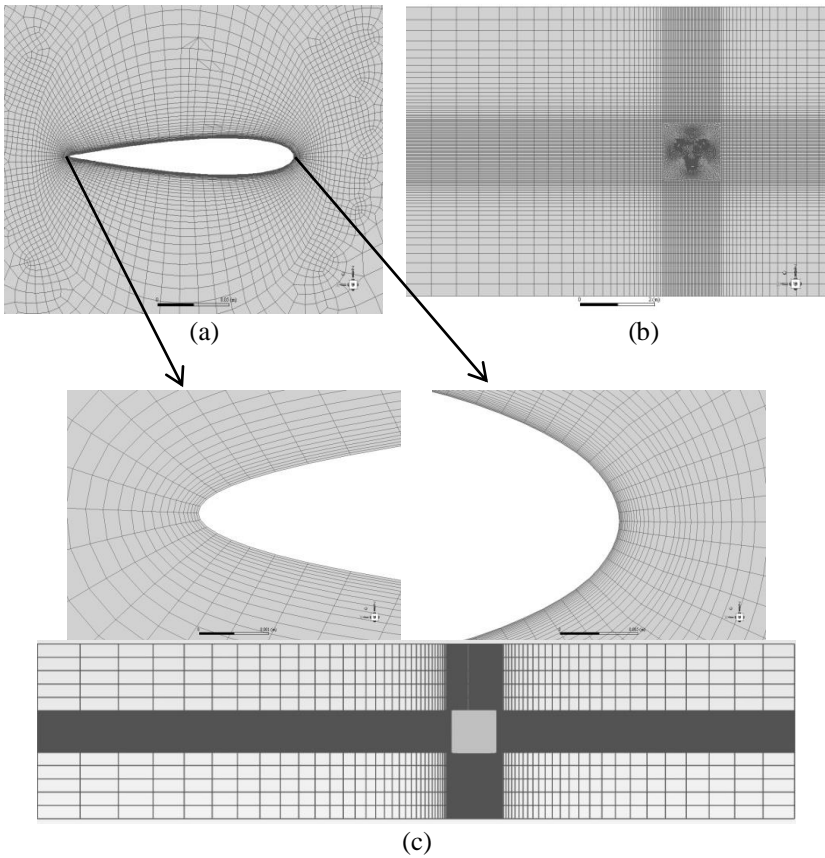


Figure 3: Overall mesh; (a) around the airfoil, (b) top view, and (c) side view

Grid independence test

One of the factors that affect the simulation process's accuracy is the number of cells used. Ideally, the more cells used, the more accurate the simulation results will be.

Table 2: GIT result

Number of cells	Coefficient moment	Maximum y+	Maximum skewness	Relative error coefficient moment
1067739	0.269627	2.042	0.77	-
1393864	0.267208	2.032	0.77	0.008972
1719989	0.264362	2.045	0.75	0.010651
2046114	0.2602057	2.038	0.7	0.0026
2372239	0.260884	2.02	0.7	0.0026

However, with many cells, the computation time will also be longer. Then it is necessary to use the optimal number of cells. Optimal means that by using as few cells as possible, the desired parameter results slightly different from higher cells. A test was carried out namely the Grid independence test (GIT). In this study, it was determined that there were five numbers of cells used, namely 1 million, 1.4 million, 1.7 million, 2 million, and 2.4 million. The parameter to be compared is the mean Coefficient Moment (C_M) for each number of cells produced. In the GIT process, It was used a constant wind speed of 5 m/s with a constant tip speed ratio of 1.4.

From the tests carried out, Table 2 shows that the number of cells of 2 million began to show a small difference in mean C_M . It was found that the number of cells 1 million, 1.4 million, and 1.7 million still produced fluctuations in mean C_M . Therefore, in this study, the number of mesh 2 million was taken as the optimum mesh with maximum y^+ at 2.038.

Governing Equations

Conservation mass and momentum equation

When using the CFD approach to solve problems, two basic equations of flow are used, namely the conservation of mass and momentum. Equation 1 refers to the mass conservation of the fluid flowing in the control volume, in which the dot product of nabla (∇) and the velocity vector (\vec{V}) are equal to 0. This implies that the fluid mass flow in the control volume must be constant.

$$\nabla \cdot \vec{V} = 0 \quad (1)$$

Equation 2 depicts the fluid momentum equation when working in volume control with the x coordinate. Due to the turbulent conditions, there are several additional variables ($\overline{u'^2}$, $\overline{u'v'}$, $\overline{u'w'}$) as Reynold Stresses that are resolved in this study. This is known as the Reynold Average Navier Stokes (RANS) equation.

$$\rho \left(\frac{\partial u}{\partial t} + u \frac{\partial u}{\partial x} + v \frac{\partial u}{\partial y} + w \frac{\partial u}{\partial z} \right) = \rho \cdot g - \frac{\partial p}{\partial x} + \mu \left(\frac{\partial^2 u}{\partial x^2} + \frac{\partial^2 u}{\partial y^2} + \frac{\partial^2 u}{\partial z^2} \right) + \frac{1}{\rho} \left[\frac{\partial(-\rho u'^2)}{\partial x^2} + \frac{\partial(-\rho uv')}{\partial y^2} + \frac{\partial(-\rho uw')}{\partial z} \right] \quad (2)$$

Model turbulent

The K- ω SST is one of several turbulence models that combine the K- ϵ and K- ω models. It is well known that the use of the K- ϵ model is less sensitive in areas far from the wall. However, it is extremely sensitive to the boundary layer in the adverse pressure gradient area near the wall. As a result, the K- ω SST employs the K- ϵ model in areas far from the wall and the K- ω model in areas close to the wall. Equation 3 depicts the transport equation for K- ω SST.

$$\frac{\partial(\rho\omega)}{\partial t} + \text{div}(\rho\omega U) = \text{div} \left[\left(\mu + \frac{\mu_1}{\sigma_{\omega,1}} \right) \text{grad}(\omega) \right] + \gamma_2 \left(2\rho S_{ij} \cdot S_{ij} - \frac{2}{3} \rho \omega \frac{\partial(U)}{\partial x_j} \delta_{ij} \right) - \beta_2 \rho \omega^2 + 2 \frac{\rho}{\sigma_{\omega,2} \omega} \frac{\partial k}{\partial x_k} \frac{\partial \omega}{\partial x_k} \quad (3)$$

Parameter analysis VAWT

Coefficient Power (C_p) is a dimensionless number that is used to measure or compare the output power of wind turbines. This C_p value is calculated by dividing the power on the rotor shaft by the freestream power. Where Equation 4 shows the mathematical expression for C_p . M is the moment of the rotor, relative velocity angular for the ω , and U for freestream velocity.

$$C_p = \frac{2 \cdot M \cdot \omega}{\rho D H U^3} \quad (4)$$

The coefficient Moment (C_M) is a dimensionless number that represents the ratio of the moment by the rotor to the moment that is available in the freestream. This number is used to compare or determine the working rotor's aerodynamic performance.

$$C_M = \frac{M}{\frac{1}{2} \rho A R U^2} \quad (5)$$

TSR is a dimensionless number that represents the ratio of the tangential speed at the rotor to the incoming freestream speed. This TSR is an important component in the discussion of wind turbines; besides being used in calculating turbine performance and turbine characteristics, this TSR value is used in the Darrieus turbine design [18].

$$TSR = \frac{\omega R}{U} \quad (6)$$

Results and Discussion

To determine the effect of the contra-rotating VAWT Darrieus turbine by comparing the performance of contra-rotating and the performance of single-rotating. The compared performance is the value of C_p and aerodynamic performance can be compared from the value of C_M . After the data is obtained from the simulation and calculated, C_p graphs are obtained for contra-rotating and single-rotating as shown in Figure 4.

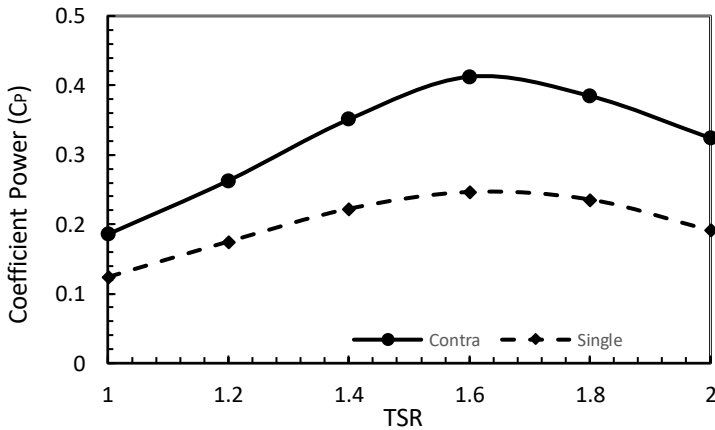


Figure 4: Graph of the change of C_p versus tip speed ratio

From Figure 4 it is known that both contra-rotating and single-rotating have the same peak C_p at TSR 1.6. This shows that although contra-rotating has a higher number of blades than single-rotating which indicates a larger solidity ratio, there should be a different trend of C_p changes to tip speed ratio according to research conducted by [11]. contra-rotating has a total of 6 blades while single-rotating only has 3 blades, it does not change the trend of C_p versus tip speed ratio because in contra-rotating, the addition of the number of blades is not placed on the same rotor so that the solidity remains constant.

The difference in C_p between contra-rotating and single-rotating can be seen clearly in each of the existing tip speed ratios (see Figure 4). The biggest difference lies in tip speed ratio 2 where the difference can reach 70%. This large difference in C_p is mostly due to the difference in angular velocity used, as previously explained that contra-rotating can increase the relative rotational speed.

In this study, the first and second stages have the same tip speed ratio, theoretically, the increase of C_p in contra-rotating can reach 4 times from single-rotating because the relative angular velocity increases up to 2 times [19]. However, the largest increase in C_p contra-rotating only reaches 70%. The loss about 30% of the total increase in C_p from contra-rotating was due to a loss in aerodynamic performance. Figure 5 shows that in terms of aerodynamic performance, single-rotating is superior to contra-rotating for all tip speed ratios.

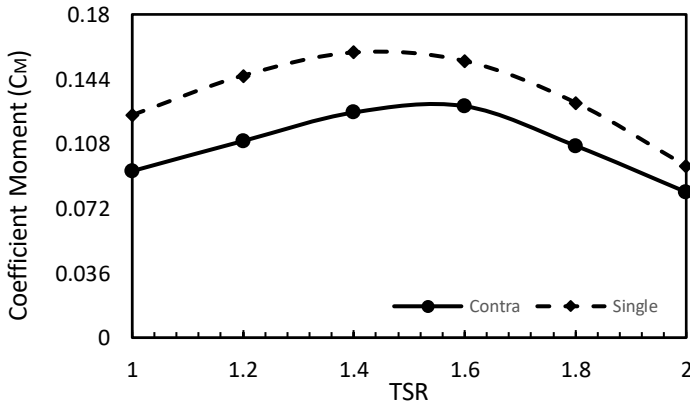


Figure 5: Graph of change in average C_M to tip speed ratio

The greatest reduction in C_M through contra-rotating versus single-rotating was found in tip speed ratio 1 and the smallest was in tip speed ratio 2, with 25% and 15% respectively. Figure 5 depicts the trend of change in C_M versus tip speed ratio, which is identical to the trend of change in C_p to tip speed ratio. Peak C_M differs slightly between single-rotating and contra-rotating, with single-rotating having a C_M of 0.158 at tip speed ratio 1.4 and contra-rotating having a C_M of 0.128 at tip speed ratio 1.6.

The cause of the significant difference in aerodynamic performance between contra-rotating and single-rotating in Figure 5 can be explained in the graph of the change in C_M on the azimuth angle of 1 blade as shown in Figure 6. As an example, the graph C_M as a function of the azimuth angle for one blade is taken at tip speed ratio 1.6 because this tip speed ratio has the largest

different value of C_M between the single-rotating and the contra-rotating. From Figure 6 it can be shown that there is a large difference in the value of C_M when the blade passes through an azimuth angle equal to 90° or at the peak C_M .

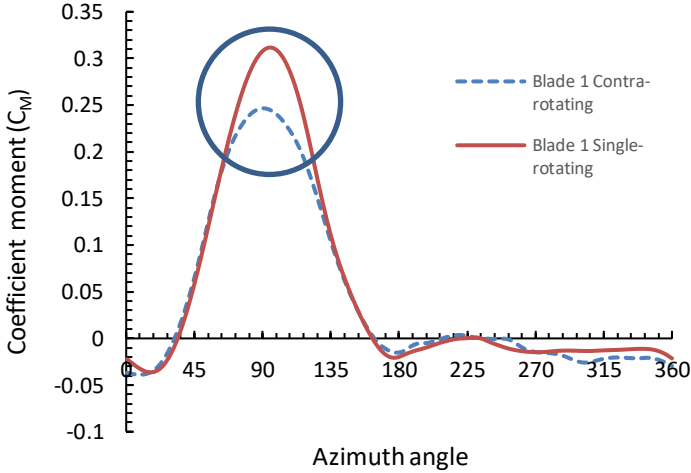


Figure 6: Graph of C_M change to azimuth angle at a tip speed ratio of 1.6

In single-rotating, it is found that the C_M at the azimuth angle of 90° is around 0.31 while in contra-rotating the C_M is 0.246. The difference between the two configurations with the relative ratio is 20%. The difference in the C_M value at the azimuth angle of 90° can occur because there are different aspect ratios for contra-rotating and single-rotating blades, which causes blade tip losses in contra-rotating blades to be greater than for single-rotating blades. Although this study uses the same dimensions between the height of the single-rotating rotor and the combined rotor 1 and 2 in contra-rotating, it does not make the two configurations have the same aspect ratio. This is because rotor 1 and rotor 2 have different rotation directions. When blade 1 on the contra-rotating is at an azimuth angle of 90° or is at the peak C_M , none of the blades on rotor 2 are in the same position as blade 1 on rotor 1.

Figures 7a and 7b for contra-rotating and single-rotating respectively show streamlined pulses at both ends of the blade, indicating a blade phenomenon of tip losses. On the pressure contour, this phenomenon is indicated by a change in the pressure distribution on the low-pressure side from the blade's tip to the center of the blade. The closer the blade tip, the more pressure on the low-pressure side will increase. This is due to the fact that the tip vortex from the high pressure side reduces flow on the low pressure side thus the pressure is increased. In contra-rotating (see Figure 7a), the effect of blade tip losses is strongly marked by an increase in pressure on the low-

pressure side which is almost to the center of the blade due to the small aspect ratio of the blade, while in single-rotating (see Figure 7b), The increase of pressure on the low-pressure side can only be seen around the blade's tip. The closer to the center of the blade, the less noticeable this increase of pressure is. This increase in pressure on the low-pressure side will reduce the difference between the pressure in the high-pressure area and the low-pressure side so that the lift force on the blade is reduced.

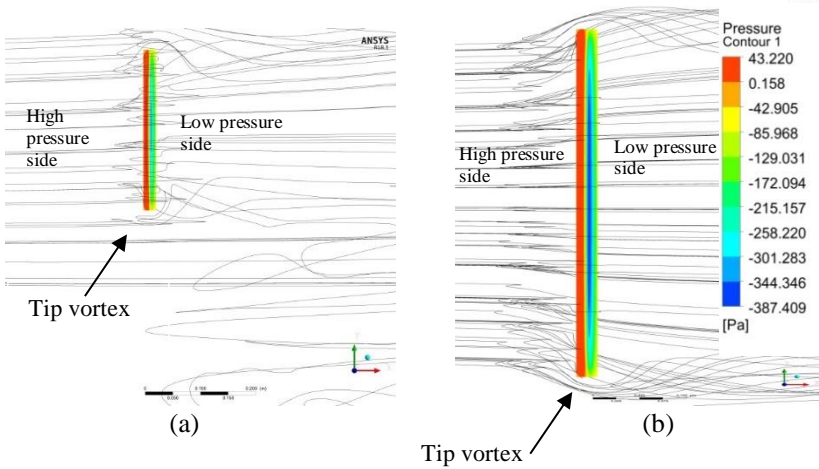


Figure 7: Streamline and contour blade pressure 1 azimuth angle 90° Z view; (a) contra-rotating, and (b) single-rotating

In addition to the effect of blade tip losses due to the difference in aspect ratio between contra-rotating and single-rotating, it is known that the effect of contra-rotating on the VAWT of the Darrieus turbine can be seen in Figure 8. In the graphic image, it is known that there is an increase in C_M in the azimuth angle around 200° - 255° for contra-rotating.

The increase in C_M in the azimuth angle 200° - 255° is due to the contra-rotating gap between rotor 1 and rotor 2 or what is commonly called the axial distance. In the single-rotating shown in Figure 9b, blade 1 with an azimuth angle position of 200° - 255° does not get an additional moment. This is because the flow velocity through blade 1 is the residual velocity from blade 3 with an azimuth angle of 0° - 180° . However, in contra-rotating, the freestream velocity through the axial distance formed from blade 3 and blade 4 which forms a straight line parallel to the axial axis does not experience a decrease in velocity due to energy conversion from rotor 1 or rotor 2, so that when the flow flows blade 1 whose position is in the azimuth angle of 200° - 255° gets an additional momentum as in Figure 9a and the addition of this momentum can be shown from the larger wake area in Figure 10. It can be seen that the effect of this

axial distance not only increases the momentum around blade 1 but also increases the angle of attack at the azimuth angle of 200°-255°.

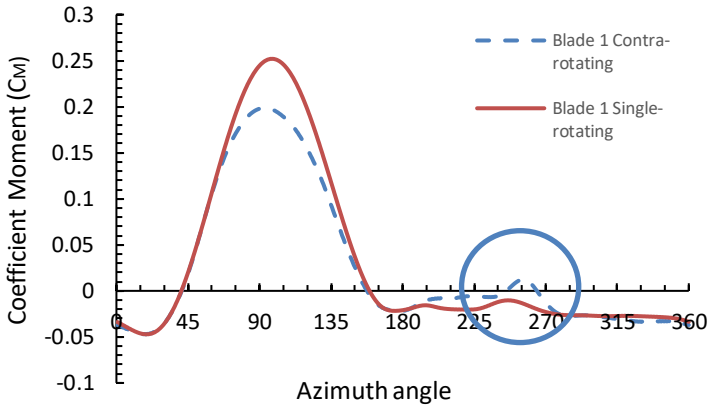


Figure 8: Graph of the change in C_M with respect to the azimuth angle at tip speed ratio 2

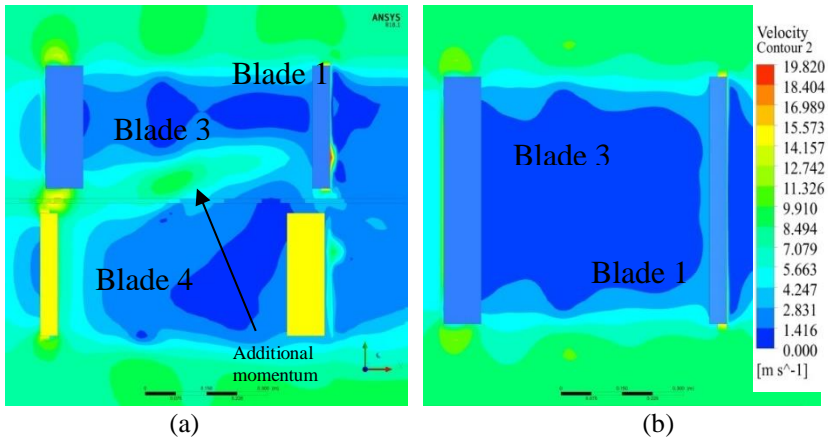


Figure 9: Absolute velocity contour $Z = 0.14$ m; (a) contra-rotating, and (b) single-rotating

The contra-rotating moment at the azimuth angle of 200°-255° is still far from the moment produced when blade position 1 is at the optimum azimuth angle or 35°-90°. However, both blade positions receive the same freestream velocity. This is because the moment on the blade is obtained by integrating the tangential force over the entire area of the blade multiplied by the rotor

radius, when the position of blade 1 is at an azimuth angle of 0° - 180° , the blade gains moment from the freestream velocity with the same value for the entire area of the blade. When the position of blade 1 is at an azimuth angle of 200° - 255° or in a position to obtain additional momentum from the axial distance, not all blade areas receive the additional momentum because some areas on blade 1 receive residual wind or wake from blade 3 (see Figure 9a). Even though the freestream velocity received on blade 1 is the same, the resulting moment generated by blade 1 when it is in position 200° - 255° is not as large as when it is in position 35° - 90° .

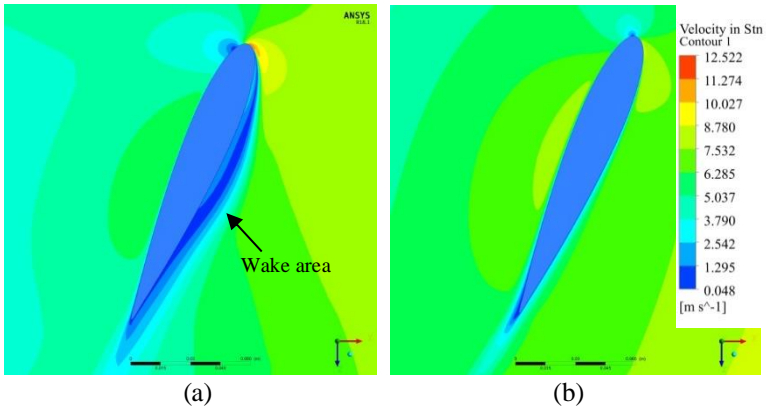


Figure 10: Relative velocity contour on blade 1 at azimuth angle 247° ; (a) contra-rotating, and (b) single-rotating

Conclusion

From this study can be concluded that the contra-rotating configuration on the VAWT Darrieus turbine can increase the C_p of the Darrieus turbine VAWT up to 70% through an increase in the relative rotation of the rotor so that the power generated is greater in all variations of tip speed ratio. However, when viewed through aerodynamic performance or C_M , the contra-rotating configuration of the Darrieus turbine VAWT reduces performance in all variations of tip speed ratio. This is because the blade tip losses in the contra-rotating configuration are greater than the single-rotating due to the different aspect ratios of the two configurations.

The effect of contra-rotating on the VAWT Darrieus turbine can also be seen from C_M when the blade is at an azimuth angle of 200° - 255° . There is an increase in C_M due to freestream flow flowing through the axial distance providing fresh air and is known to increase the velocity and the angle of attack of the blade. This axial distance effect is only beneficial for the contra-rotating

VAWT of the Darrieus turbine when the turbine operates at tip speed ratio of 1.6 to tip speed ratio of 2.

The Darrieus contra-rotating configuration is a new configuration that comes with the potential to generate more output power than the conventional Darrieus turbine. The Darrieus turbine VAWT contra-rotating will be better described as a result of this research, mainly its effect on aerodynamic performance. However, further research on the Darrieus contra-rotating VAWT turbine is needed to determine how the aerodynamic performance with axial distance variations and when the aspect ratio between stage 1 and the single-rotating rotor is made the same.

Contributions of Authors

The authors confirm the equal contribution in each part of this work. All authors reviewed and approved the final version of this work.

Funding

This work received no specific grant from any funding agency.

Conflict of Interests

All authors declare that they have no conflicts of interest

Acknowledgment

Special thanks to the staffs and members of fluid mechanic laboratory who always provide facilities that are needed in order to complete this work.

References

- [1] M. M. Aslam Bhutta, N. Hayat, A. U. Farooq, Z. Ali, S. R. Jamil, and Z. Hussain, "Vertical axis wind turbine - A review of various configurations and design techniques," *Renewable and Sustainable Energy Reviews*, vol. 16, no. 4, pp. 1926–1939, 2012, doi: 10.1016/j.rser.2011.12.004.
- [2] A. Subramanian *et al.*, "Effect of airfoil and solidity on performance of small scale vertical axis wind turbine using three dimensional CFD model," *Energy*, vol. 133, pp. 179–190, 2017, doi:

- 10.1016/j.energy.2017.05.118.
- [3] S. Chhin and V. S. Djanali, “Numerical Simulation on Hybrid Savonius Turbine with NACA-Airfoils as H-rotor Blades,” *Proceeding-2020 International Seminar on Intelligent Technology and Its Applications ISITIA 2020*, pp. 123–128, 2020, doi: 10.1109/ISITIA49792.2020.9163710.
- [4] M. H. Mohamed, “Impacts of solidity and hybrid system in small wind turbines performance,” *Energy*, vol. 57, pp. 495–504, 2013, doi: 10.1016/j.energy.2013.06.004.
- [5] M. D. Bausas and L. A. M. Danao, “The aerodynamics of a camber-bladed vertical axis wind turbine in unsteady wind,” *Energy*, vol. 93, pp. 1155–1164, 2015, doi: 10.1016/j.energy.2015.09.120.
- [6] Q. Li, T. Maeda, Y. Kamada, J. Murata, K. Furukawa, and M. Yamamoto, “Effect of number of blades on aerodynamic forces on a straight-bladed Vertical Axis Wind Turbine,” *Energy*, vol. 90, pp. 784–795, 2015, doi: 10.1016/j.energy.2015.07.115.
- [7] Q. Li *et al.*, “Effect of solidity on aerodynamic forces around straight-bladed vertical axis wind turbine by wind tunnel experiments (depending on number of blades),” *Renewable Energy*, vol. 96, pp. 928–939, 2016, doi: 10.1016/j.renene.2016.05.054.
- [8] M. A. Miller, S. Duvvuri, and M. Hultmark, “Solidity effects on the performance of vertical-axis wind turbines,” *Flow*, vol. 1, pp. 1–15, 2021, doi: 10.1017/flo.2021.9.
- [9] Q. Li *et al.*, “Effect of rotor aspect ratio and solidity on a straight-bladed vertical axis wind turbine in three-dimensional analysis by the panel method,” *Energy*, vol. 121, pp. 1–9, 2017, doi: 10.1016/j.energy.2016.12.112.
- [10] H. Zhu, W. Hao, C. Li, and Q. Ding, “Numerical study of effect of solidity on vertical axis wind turbine with Gurney flap,” *Journal of Wind Engineering and Industrial Aerodynamics*, vol. 186, no. December 2018, pp. 17–31, 2019, doi: 10.1016/j.jweia.2018.12.016.
- [11] Q. Liu, W. Miao, C. Li, W. Hao, H. Zhu, and Y. Deng, “Effects of trailing-edge movable flap on aerodynamic performance and noise characteristics of VAWT,” *Energy*, vol. 189, pp. 116271, 2019, doi: 10.1016/j.energy.2019.116271.
- [12] C. C. Chen and C. H. Kuo, “Effects of pitch angle and blade camber on flow characteristics and performance of small-size Darrieus VAWT,” *Journal Visualization*, vol. 16, no. 1, pp. 65–74, 2013, doi: 10.1007/s12650-012-0146-x.
- [13] A. Rezaeiha, I. Kalkman, and B. Blocken, “Effect of pitch angle on power performance and aerodynamics of a vertical axis wind turbine,” *Applied Energy*, vol. 197, pp. 132–150, 2017, doi: 10.1016/j.apenergy.2017.03.128.
- [14] M. Elkhoury, T. Kiwata, and E. Aoun, “Experimental and numerical

- investigation of a three-dimensional vertical-axis wind turbine with variable-pitch,” *Journal of Wind Engineering and Industrial Aerodynamics*, vol. 139, pp. 111–123, 2015, doi: 10.1016/j.jweia.2015.01.004.
- [15] G. Abdalrahman, W. Melek, and F. S. Lien, “Pitch angle control for a small-scale Darrieus vertical axis wind turbine with straight blades (H-Type VAWT),” *Renewable Energy*, vol. 114, pp. 1353–1362, 2017, doi: 10.1016/j.renene.2017.07.068.
- [16] Y. Guo, X. Li, L. Sun, Y. Gao, Z. Gao, and L. Chen, “Aerodynamic analysis of a step adjustment method for blade pitch of a VAWT,” *Journal of Wind Engineering and Industrial Aerodynamics*, vol. 188, no. February, pp. 90–101, 2019, doi: 10.1016/j.jweia.2019.02.023.
- [17] S. N. Ashwindran, A. A. Azizuddin, A. N. Oumer, and A. A. Razak, “An Introductory CFD Analysis Study of Novel Cavity Vane Driven Wind Turbine Blade Design,” *Journal of Mechanical Engineering*, vol. 17, no. 3, pp. 55–68, 2020.
- [18] D. H. Didane, N. Rosly, M. F. Zulkafli, and S. S. Shamsudin, “Performance evaluation of a novel vertical axis wind turbine with coaxial contra-rotating concept,” *Renewable Energy*, vol. 115, no. 2018, pp. 353–361, 2018, doi: 10.1016/j.renene.2017.08.070.
- [19] Y. Ahmudiarto, T. Admono, A. Salim, and M. Furqon, “Performance and productivity enhancements on vertical axis wind turbines with a novel multi-stages contra-rotating technique,” *International Conference on Sustainable Energy Engineering and Application ICSEEA 2018*, pp. 44–50, 2019, doi: 10.1109/ICSEEA.2018.8627119.
- [20] D. H. Didane, S. M. Maksud, M. F. Zulkafli, N. Rosly, S. S. Shamsudin, and A. Khalid, “Performance investigation of a small Savonius-Darrius counter-rotating vertical-axis wind turbine,” *International Journal Energy Research*, vol. 44, no. 12, pp. 9309–9316, 2020, doi: 10.1002/er.4874.
- [21] D. H. Didane, N. Rosly, M. F. Zulkafli, and S. S. Shamsudin, “Numerical investigation of a novel contra-rotating vertical axis wind turbine,” *Sustainable Energy Technologies and Assessments*, vol. 31, no. May 2018, pp. 43–53, 2019, doi: 10.1016/j.seta.2018.11.006.
- [22] D. H. Didane, D. Kudam, M. F. Zulkafli, S. Mohd, M. F. M. Batcha, and A. Khalid, “Development and Performance Investigation of a Unique Dual-rotor Savonius-type Counter-rotating Wind Turbine,” *International Journal Integrated Engineering*, vol. 13, no. 6, pp. 89–98, 2021, doi: 10.30880/ijie.2021.13.06.008.
- [23] S. N. Jung, T. S. No, and K. W. Ryu, “Aerodynamic performance prediction of a 30 kW counter-rotating wind turbine system,” *Renewable Energy*, vol. 30, no. 5, pp. 631–644, 2005, doi: 10.1016/j.renene.2004.07.005.
- [24] B. Ko, S. Liu, Z. Fang, Y. Ahmudiarto, B. Nugroho, and R. Chin, “Numerical simulation of two-stages contra-rotating vertical axis wind

- turbine,” *22nd Australasian Fluid Mechanics Conference AFMC2020*, no. December, pp. 3–6, 2020, doi: 10.14264/d1c920e.
- [25] A. Eltayesh *et al.*, “Effect of wind tunnel blockage on the performance of a horizontal axis wind turbine with different blade number,” *Energies*, vol. 12, no. 10, pp. 1–15, 2019, doi: 10.3390/en12101988.
- [26] A. Rezaeiha, H. Montazeri, and B. Blocken, “Towards accurate CFD simulations of vertical axis wind turbines at different tip speed ratios and solidities: Guidelines for azimuthal increment, domain size and convergence,” *Energy Conversion and Management*, vol. 156, no. September 2017, pp. 301–316, 2018, doi: 10.1016/j.enconman.2017.11.026.
- [27] F. Balduzzi, A. Bianchini, R. Maleci, G. Ferrara, and L. Ferrari, “Critical issues in the CFD simulation of Darrieus wind turbines,” *Renewable Energy*, vol. 85, pp. 419–435, 2016, doi: 10.1016/j.renene.2015.06.048.
- [28] Y. T. Lee and H. C. Lim, “Numerical study of the aerodynamic performance of a 500W Darrieus-type vertical-axis wind turbine,” *Renewable Energy*, vol. 83, pp. 407–415, 2015, doi: 10.1016/j.renene.2015.04.043.

Seismic Behaviour of Beris Dam Under Six Earthquake Excitations by using Finite Element Method

Rozaina Ismail*, Nurul Nabilah Moktar, Nurul Damia Sukati,
Ainnur Zulsyamilatil Huda Abd Halim, Dayang Nur Erliyani Fitri Erwan,
Azmi Ibrahim, Norliyati Mohd Amin
School of Civil Engineering, College of Engineering,
Universiti Teknologi MARA, 40450, Shah Alam Selangor, MALAYSIA
*dr.rozaina.ismail@gmail.com

Azlan Adnan
Faculty of Civil Engineering, Universiti Teknologi Malaysia,
81310 Johor Bahru, Johor, MALAYSIA

Ade Faisal
Program Studi Teknik Sipil, Universitas Muhammadiyah Sumatera Utara,
Medan 20238, INDONESIA

ABSTRACT

This paper focused on the behavior of the dam when exposed to seismic loading and ability of the dam to withstand the applied loads from various seismic events. The chosen concrete dam to be referred to in the two-dimensional analysis is Beris Dam located in Kedah, Malaysia. A nonlinear dynamic analysis is chosen to analyse the behavior of Beris Dam under selected ground motion. Analysis of the dam is performed using the finite element method by utilizing ABAQUS software. From the cracking analysis pattern, a crack appeared at the upstream face of the dam caused mainly by the excessive tensile stress. Based on the results, the displacement of the dam is increased with the increasing of ground motion data where the displacement occurred in the horizontal direction. The maximum stresses exerted by the dam structure do not exceed the allowable capacity of concrete dams. The stress behaviour of the dam was satisfactorily acceptable as the maximum normal stress and shear stress of the dam when numerous seismic loadings are applied do not exceed the allowable stress capacity which is 800 kN/m².

Keywords: *Seismic Behaviour; Finite Element Method; Crack Pattern; Stress*

Introduction

Dam is an engineered structure that was built for domestic and industrial water supply or for irrigation works. A multipurpose dam is often designed to provide water- control structures and for generating the hydroelectric power or to reduce the peak discharge of floodwater. However, the dams need to be designed with an ability to resist the natural disasters such as earthquakes and devastating floods as the dam failure would result in life losses and structural damages [1]. In order to acknowledge the geological characteristics of a selected area to establish a dam structure, a geological survey needs to be executed. The geological survey cost a huge amount of money as the earthquake issues need to be considered in designing the dam structure. The effect of an earthquake with Richter magnitude exceeding 6 M caused a destruction to dams. The Shih-Kang dam was seriously damaged due to the Chichi earthquake with 7.6 M that resulted in fractures and split of dam body from foundation bedrock [2]. The damages of Shih-Kang dam also resulted in heavy flooding in the D/S direction and disrupted the power and water resources to the location involved.

Earthquake effects towards concrete dams differ based on the dam types. The consequences of the earthquakes towards the dam can result in the damage and failures of dam structure. The dam's failure due to the earthquake effects would bring a disaster towards the surrounding area and humans. As a safety measurement, a dam structure should be evaluated on its ability to resist seismic waves. The essential parameter in designing and performance evaluation of the concrete dams is the safety level subjected to the seismic safety. Nonlinear dynamic analysis utilizes the combination of ground motion records with a detailed structural model. Therefore, this method is capable of producing results with relatively low uncertainty. In nonlinear dynamic analyses, the detailed structural model subjected to a ground-motion record produces estimates of component deformations for each degree of freedom in the model [3]. Hence, the study on the seismic assessment of Beris Dam under earthquake loading performed by using nonlinear dynamic analysis utilizing finite element method. Impact of earthquakes has been one of the major concerns of scientists and engineers for a long time. Enhancement on the material performance for the application due to seismic effect was conducted in previous studies [4]-[8]. Furthermore, many studies have been made to mitigate the seismic responses of dams [9]-[13], buildings [14]-[18] and bridges [19]-[20] due to seismic loads.

Crack patterns on concrete dams appear as the reaction of the dam structure towards seismic loading. The crack pattern is a parameter of performance of a dam subjected to the different ground motion with varying

intensity levels. Thus, the safety measure should be taken by studying the crack pattern to ensure the durability and sustainability of the dam. A safety need for a concrete dam regarding the dynamic loads should be taken into consideration during assessment of the stability of dam structure [21]. For instance, the ability of structure to withstand the applied lateral forces and moments and averting the unnecessary cracking of the concrete dam.

Under the earthquake effect, a concrete structure would undergo cracking and not be able to contain the structural loads [22]. Koyna Dam has encountered crack damage due to the Koyna earthquake that struck with a strength of 6.5 M in December 1967. The dam structure has an elongated shape with a constant cross section. The design of the dam can be determined under planar deformation conditions because the position of the load does not change in direction [2]. There are several factors that lead to the cracking of concrete dams which are the suitability of concrete materials, site selection of the dam, temperature control and maintenance of the dam and lastly, profile design of the dam [23]. These factors need to be considered carefully as the performance of dam structure would be affected when seismic excitations present. Shukai [24] and Santos [25] conducted an efficient numerical framework for the seismic analysis of concrete dams as well.

The relative horizontal and vertical displacements of different dams have been reported by many researchers. Crest displacement normally occurs at the neck and heel of the dam when the body structure is exposed to seismic loading. The maximum horizontal displacement of the dam crest happened due to the hydrostatic pressure [12]. In this study, the maximum crest displacement is investigated to determine the effect of the seismic loading on the dam structure.

Stress appears in the dam structure when seismic loading is applied to the body structure. Through dynamic analysis, the stress distributions in the body structure can be seen. The normal stress and shear stresses of a dam when seismic loading is applied need to be analysed to obtain the ability of dam structure to withstand the applied force. The maximum and minimum stresses are different for each mode of shape under time history data analysis [26]. The capability of a concrete dam to withstand the applied force can be determined by comparing the maximum normal and shear stresses with the allowable stress capacity of concrete [9], [11]-[13].

Research Background

The Beris Dam is chosen for this research to observe the behaviour of the dam under earthquake excitations by using finite element modelling using computer software. This research study begins with the collection of reading concerned with the dam's performance under earthquake effect followed by data collection of Beris, 2-dimensional modelling of Beris Dam using ABAQUS

software and discussion on the crack pattern and behaviour of dam under seismic loading subjected to the seismic safety and finally summary of the main conclusions from the findings of this research paper.

Beris Dam is established in Sik, Kedah, Malaysia. The purposes of Beris Dam are to manage the water flows along Muda River in order to increase the water for irrigation purposes such as paddy and crops, for water supply either for domestic or industrial consumption and others. The dam is a concrete-faced rockfill dam with a total height of 40 meters and can accommodate a gross storage capacity of 122.4 mm³ with effective storage of 144 mm³ [27]. Figure 1 shows the typical cross section of Beris Dam while the background and information of structure were tabulated in Table 1 and Table 2.

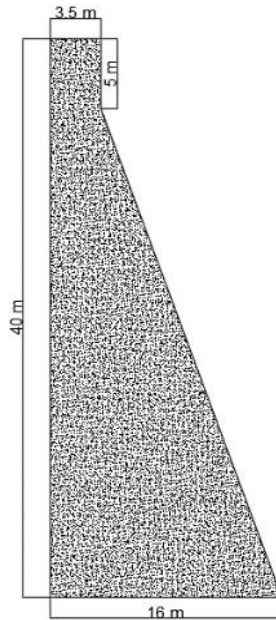


Figure 1: Typical cross section of Beris dam [27]

Table 1: Background of project [27]

Location	Year completed	Year of construction	Project cost
Sik, Kedah	2004	2000	Rm 360 million

Table 2: Information of structure [26]

Item	Description
Reservoir area	16.1 km ²
Crest length	155.0 m
Catchment area	116.0 km ²
Crest elevation	88.0 m
Capacity	122.4 mm ³
Material of structure	Concrete-faced Rockfill
Height	40.0 m
Spillway type	Overflow ogee with side channel chute and bucket

Modal analysis

The seismic behaviour of Beris Dam due to the seismic excitations is performed by using ABAQUS. The seismic excitation that has been used in the analysis is obtained from the Malaysian Meteorological Department's intensity data and Pacific Earthquake Engineering Research Center (PEER). Table 3 tabulates the list of earthquake events that have occurred at various locations and different recorded intensity data respectively that are essential for data analysis of the 2-dimensional dam model. There are five intensities of motion data based on peak ground acceleration (PGA) which are 0.05 g, 0.10 g, 0.15 g, 0.20 g, and 0.30 g, respectively.

Table 3: Selected earthquake data for analysis of 2D model

Earthquake	Location	Year	Magnitude (M)	Peak ground acceleration (g)	Step (s)
Aceh	Indonesia	2004	9.3	0.012	0.02
Ranau	Malaysia	2015	6.0	0.013	0.02
Chuetsu	Japan	2007	6.8	0.175	0.01
Northridge	USA	1994	6.69	0.194	0.01
Chichi	Taiwan	1999	6.2	0.361	0.01
Trinidad	USA	1983	5.7	0.568	0.01

The material properties of dams such as density, Poisson's ratio, Young's modulus is essential in modelling of dam structure by using finite element method. Some of the mechanical properties of Beris Dam are unknown, hence the data on mechanical properties referred to Koyna Dam's properties. Material behaviours in terms of concrete damaged plasticity are based on Koyna Dam data. Table 4 shows the material properties used in this analysis.

Table 4: Material properties of concrete

Properties of concrete			Value
General properties		Density	2700 kg/m ³
Mechanical properties	Elasticity	Young's modulus	31 GPa
		Poisson's ratio	0.15
	Plasticity	Dilation angle	36.31°

The dam analysis is carried out by applying several ground motion data on the dimensional model of Beris Dam where the self-weight of dam and hydrostatic pressure is also considered. The value of self-weight of dam or gravity load is 9.81 N/kg while hydrostatic pressure can be determined from Equation 1.

$$F_p = \rho gh \quad (1)$$

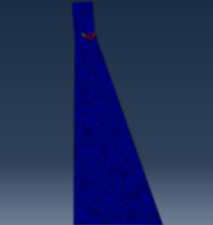
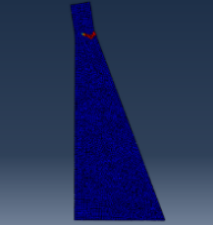
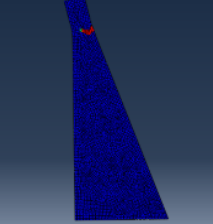
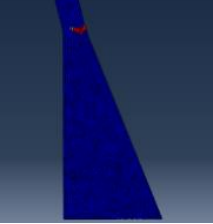
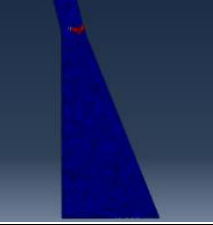
where, F_p = fluid pressure
 ρ = fluid density
 g = acceleration due to gravity
 h = fluid depth

Crack pattern analysis

Crack patterns on concrete dams appear as the reaction of the dam structure towards seismic loading. The crack pattern is a parameter of the performance of a dam subjected to the different ground motion with varying intensity levels. Thus, safety measure should be taken by studying the crack pattern to ensure the durability and sustainability of the dam. However, the cracking pattern depends on the peak ground acceleration (PGA) of the motion. Table 5 shows the cracking pattern of the dam structure underground motion data of the Chichi Earthquake with a minimum PGA of 0.05 g and maximum PGA of 0.30.

Crack patterns appeared at the upstream face of the dam. From Figure 2, the tensile stress distributed in the dam structure indicates that the crack pattern is caused mainly by excessive tensile stress. However, the crack pattern appeared at half of the neck and did not connect with the other side. The connection of the crack pattern indicating the failure of the dam was in good agreement with the results obtained by Azizan et al. [2] and Ghaedi et al. [28]. Crack patterns can be a parameter to observe the capability of a dam to withstand the seismic loading. Therefore, in this analysis, the dam structure has severe damage due to the applied ground motion, yet the damage of the dam is not extreme as the maximum crack pattern appeared is half of the upstream face. The dam is unsafe as the cracking on the dam body required to be repaired to avoid further damages occurred.

Table 5: The crack pattern of Beris dam under Chichi earthquake data

Earthquake intensity	Normal stress	
0.05 g		
0.10 g		
0.15 g		
0.20 g		
0.30 g		

Crest displacement analysis

Crest displacement occurs when seismic loading is applied to the dam structure. Maximum crest displacement is observed to determine the deformation and performance of the dam. Table 6 tabulates the maximum crest displacement of the dam under several sets of ground motion data. Based on the results, the displacement of the dam is increased with the increase of ground motion data. The increasing deformation of the dam should be taken into consideration when evaluating the safety of the dam. Figure 2 shows the maximum crest displacement of the dam where the displacement occurred in the horizontal direction. Ghaedi et al. [28], Hong et al. [29], and Chen et al. [30] reported that the displacements occurred in the same direction at the crest of the dam. The maximum crest displacement indicates the ability of the dam to resist the applied load based on its capacity. Therefore, the crest displacement would be increased if greater motion data is present. The maximum crest displacement is related to the crack pattern and stress distribution in assessing the safety of the dam under earthquake excitations.

Table 6: Maximum crest displacement of Beris dam under selected ground motion (unit in cm)

EQ Data	Aceh	Ranau	Chuetsu	Trinidad	North-ridge	Chichi
0.05g	0.000	0.000	1.38	0.05	0.11	8.95
0.10g	0.000	0.000	3.45	0.25	0.18	10.20
0.15g	0.001	0.001	5.59	0.42	0.28	15.43
0.20g	0.001	0.001	7.54	0.75	0.32	21.88
0.30g	0.002	0.002	9.035	0.88	0.44	21.88

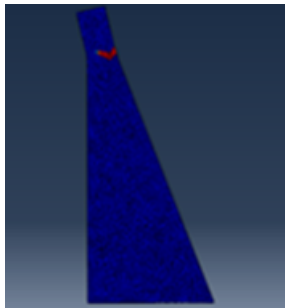


Figure 2: The maximum crack pattern of Beris dam (21.88 cm)

Stress analysis

The dynamic analysis shows the stress in the dam structures when subjected to the dynamic loading. Stress analysis is crucial to observe the performance of a dam where the ability of the dam to resist the applied forces. Normal stress and shear stress are the parameters observed in this analysis. The positive value of stress indicates that the structure is in a tension state. While the negative value of stress shows that the structure is in a compression state. Self-weight of the dam which is the gravity force and the hydrostatic pressure are the static forces that need to be considered in the shear force state. Figure 3 illustrates the stress distribution of normal stress and shear stress.

Based on Figure 3, the dam structure is in compression state when normal stress is exerted on the dam body while the structural body consists of the tension force more than compressive force when shear stress is presented. The maximum compressive force occurred due to the high hydrostatic force exerted on the dam structure. Tension force occurs in the body structure depending on the type of dam, the magnitude of earthquake loading and the distribution of the peak ground acceleration. The more tension force exerted in the dam structure is due to the rigidity of the dam structure depending on the height of the dam [12].

The tensile force is only presented near the neck of the dam. Critical force tends to happen near the crest of the dam due to the tendency of the body structure to resist the force exerted from the core and foundation [27]. This acceleration shows that the crest of the dam on the upstream side is the most critical zone if an earthquake occurs and is highly affected by both ground motion characteristics such as acceleration, duration, and frequency and characteristics of dams such as material properties [12]. Therefore, under the ground motion data with a maximum PGA of 0.3 g and minimum PGA of 0.05 g, the dam structure has more compressive force in the dam structure. The lower peak ground motion applied to the structure could help to reduce the forces exerted on the dam. In Malaysia, the dam structure would survive during an earthquake event as the magnitude of the earthquake that normally happens in surrounding Malaysia is quite lower than other countries.

The comparison of the maximum stresses exerted by the dam structure with the allowable capacity of the dam was done to determine whether the stresses obtained from the analysis are acceptable. Table 7 shows the comparison of the maximum stresses with the allowable stress capacity of the concrete dam among six different earthquake events.

Figure 3: Stress distribution of Beris dam

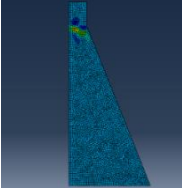
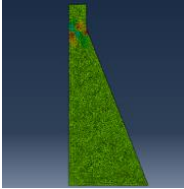
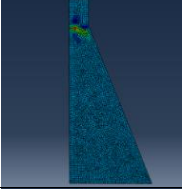
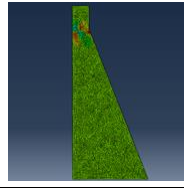
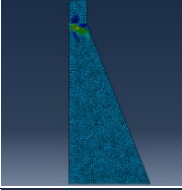
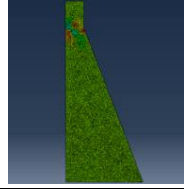
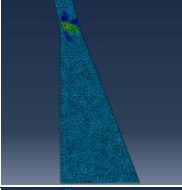
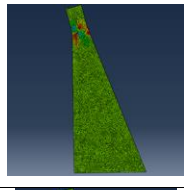
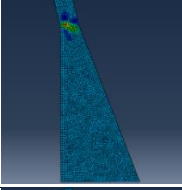
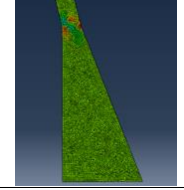
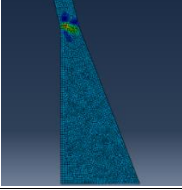
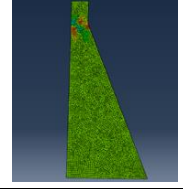
Earthquake data	Normal stress	Shear stress
Aceh		
Ranau		
Northridge		
Chichi		
Cheutsu		
Trinidad		

Table 7: Comparison of maximum stresses with allowable stress capacity

Earthquake data	Normal stress (kN/m ²)	Shear stress (kN/m ²)	Allowable capacity
Aceh	600.70	289.50	800
Ranau	603.20	290.2	800
Northridge	612.40	295.80	800
Chichi	614.50	294.70	800
Cheutsu	610.70	296.60	800
Trinidad	602.30	297.30	800

Based on the table above, the maximum stresses exerted by the dam structure do not exceed the allowable capacity of concrete dams. Therefore, the maximum normal stress and shear stress were considered acceptable. The performance of the dam also can be evaluated from the maximum stresses obtained from the analysis. As the value of stresses is acceptable, it can be said that the dam can withstand the load applied and exert maximum stresses lower than allowable capacity. The results obtained in this study agreed well with that reported by Ismail et al. [9].

Conclusion

The seismic behavior of the dam such as crack pattern, displacement, and stress is obtained from the finite element analysis to measure the capability of the dam to withstand the seismic loading applied. The method has been explained previously and the analysis is carried out by using ABAQUS software. The seismic behaviour of Beris Dam is analyzed under 6 selected ground motion data with a minimum PGA of 0.05 g and maximum PGA of 0.30 g. Based on the analysis, the crack patterns appeared mostly at the upstream face of the dam and resulted in damage to the dam body but not too extreme as the applied loads are inadequate to break or split the neck of the dam. The dam is considered unsafe as the cracking pattern shown is severe even though the applied loads are not enough to break the neck of the dam. The performance of the dam can be considered a satisfactory result due to the acceptable maximum crest displacement of the dam under seismic excitations which is 21.88 cm. The stress behaviour of the dam was also satisfactorily acceptable as the maximum normal stress and shear stress of the dam when numerous seismic loadings are applied do not exceed the allowable stress capacity which is 800 kN/m². The obtained results from this dynamic analysis indicated that ABAQUS software is able to analyze the seismic behaviour of a body structure under ground motion data. The maximum crest displacement was discussed by comparing the maximum crest displacement of the dam under different ground

motion data. The findings in this research paper are important as a safety measure to overcome the dam's failure due to the earthquake as the consequence of the failure of the dam to resist seismic loading is tsunami and surroundings damage.

Contributions of Authors

The authors confirm the equal contribution in each part of this work. All authors reviewed and approved the final version of this work.

Funding

This work received no specific grant from any funding agency.

Conflict of Interests

All authors declare that they have no conflicts of interest

Acknowledgment

The authors would like to acknowledge the facilities provided by Universiti Teknologi MARA (UiTM), Research Nexus UiTM (ReNeU), Institute of Quality and Knowledge Advancement (InQKA), and support from the School of Civil Engineering, College of Engineering, Universiti Teknologi MARA (UiTM). The author is grateful for the constructive comments and guidance of the Editor and anonymous reviewers.

References

- [1] Mahmoodi, K., Noorzad, A., Mahboubi, A., & Alembagheri, M., "Seismic performance assessment of a cemented material dam using incremental dynamic analysis", *Structures*, vol. 29, pp. 1187–1198, 2021.
- [2] Azizan, N. Z. N., Majid, T. A., Nazri, F. M., Maity, D., & Abdullah, J., "Incremental Dynamic Analysis of Koyna Dam under Repeated Ground Motions", *IOP Conference Series: Materials Science and Engineering*, vol. 318, no. 1, pp 1-12, 2018.

- [3] Manjhi, R. M., “Approaches for analysis of seismic behavior of structures: A review”, *International Research Journal of Engineering and Technology*, vol. 5, no. 9, pp. 1306-1313, 2018.
- [4] Ismail, R. Rajhan, N. H., Hamid, H. A., & Ibrahim, A., “Experimental data for effect of carbon black loading on tensile, hardness and rebound of magnetic iron filled natural rubber composites”, *Data in brief*, vol. 25, no. 104166, pp. 1-10, 2019.
- [5] R Ismail, A Ibrahim, M Rusop, A Adnan, “Dynamic mechanical properties of natural rubber vulcanizates with different carbon nanotubes-loaded”, *AIP Conference Proceedings*, vol. 2151, no. 1, pp. 1-7, 2019.
- [6] R Ismail, A Ibrahim, M Rusop, A Adnan, “Magnetic properties of carbon nanotubes-natural rubber composites”, *AIP Conference Proceedings*, vol. 2151, no. 1, pp. 8-14, 2019.
- [7] R. Ismail, A. Ibrahim, H. Hamid, M. Rusop, A. Adnan. “Experimental study on mechanical properties of elastomer containing carbon nanotubes”, *Journal of Engineering Science and Technology*, vol. 13, no. 3, pp. 565 – 664, 2018.
- [8] Rozaina Ismail, Azmi Ibrahim, Hamidah Mohd.Saman@Hj. Mohamed, Mohamad Rusop Mahmood, Azlan Adnan. “Experimental data for the magnetic properties of vulcanized natural rubber nanocomposites using vibrating sample magnetometer (VSM)”, *Data in brief*, vol. 46, no. 108872, pp. 1-13, 2023.
- [9] Ismail, R., Hussin, N.S.A., Ibrahim, A, Rusop. M., Adnan, A., “The Performance of Roller Compacted Concrete (RCC) Dam Under Seismic Load”, *Journal of Architecture and Civil Engineering*, vol 6, no. 6, pp. 13-23, 2021.
- [10] A Faisal, TA Majid, F Ahmad, F Tongkul, SM Sari. “Influence of large dam on seismic hazard in low seismic region of Ulu Padas Area, Northern Borneo”, *Natural hazards*, vo. 59, no. 1, pp. 237-269, 2011.
- [11] Ismail, R. and Ismail, M.I., “Dynamic Analysis of Concrete Faced Rockfill Dam Using Finite Element Method”, *Journal of Engineering and Applied Sciences*, vol. 12, no. 7, pp. 1772-1776, 2017.
- [12] Ismail, R. Kamsani, M.H. and Mohd Nadzri, N.I., “Seismic Analysis of Concrete Dam by Using Finite Element Method”, *MATEC Web Conference*, vol. 103, no. 02024, pp. 1-9, 2017.
- [13] Rozaina Ismail, A'in Fatin Najihah Akmat, Ade Faisal, Azmi Ibrahim, Azlan Adnan, Izzul Syazwan Ishak, “Behaviour of Earth Fill Dam under Earthquake Load Using Finite Element Method: A Case Study of Semenyih Dam”, *Journal of Sustainable Civil Engineering and Technology*, vol. 1, no. 2, pp. 63-77, 2022.
- [14] Ismail. R., Shamsudin. N., Arshad. M.F., Ibrahim. A., Rusop. M., Adnan. A., “2-Dimensional Finite Element Analysis of Reinforced Concrete Buildings Subjected to Seismic Load”, *Journal of Architecture and Civil Engineering*, vol. 6, no. 6, pp. 01-06, 2021.

- [15] R. Ismail, A. Ibrahim and A. Adnan, “Damage Assessment of Medium-Rise Reinforced Concrete Buildings in Peninsular Malaysia Subjected to Ranau Earthquake”, *International Journal of Civil Engineering and Technology*, vol. 103, no. 02024, pp. 881–888, 2018.
- [16] MZAM Zahid, TA Majid, A Faisal, “The Effect of Behaviour Factor on The Seismic Performance of Low-Rise and High-Rise RC Buildings”, *Journal of Engineering Science and Technology*, vol. 12, no. 1, pp. 31-41, 2017.
- [17] Ismail, R., and Zamahidi, N. F., “An evaluation of High-Rise Concrete Building Performance Under Low Intensity Earthquake Effects”, *InCIEC 2014*, vol.1, no. 1, pp. 79-86, 2015.
- [18] Ismail R., Ibrahim, A., and Razali, N., “Vulnerability study of public buildings subjected to earthquake event”, *MATEC Web Conference*, vol. 103, no. 02023, pp. 1-9, 2017.
- [19] Ismail, R., and Abdul Karim, M.R., “Concrete Bridge Pier Performance Under Earthquake Loading”, *Journal of Engineering and Applied Sciences*, vol. 12, no. 9, pp. 2254-2258, 2017.
- [20] Ismail, R., Ibrahim, A., Adnan, “Determination of Shear Wave Velocity Profile by Using Multi-Channel Analysis of Surface Wave (MASW)”, *Journal of Architecture and Civil Engineering*, vol. 7, no.2, pp. 01-06, 2022.
- [21] Tosun, H., “Earthquakes and Dams. Earthquake Engineering - From Engineering Seismology to Optimal Seismic Design of Engineering Structures”, *Intechopen*, vol.1, no.1, pp. 410, 2015.
- [22] Sun, D. & Qingwen Ren, Q., “Seismic Damage Analysis of Concrete Gravity Dam Based on Wavelet Transform”, *Shock and Vibration*, vol 2016, no. 6841836, pp. 1-8, 2016.
- [23] Lin, P., Wei, P., Wang, W. & Huang, H., “Cracking Risk and Overall Stability Analysis of Xulong High Arch Dam: A Case Study”, *Computational Methods for Fracture*, vol. 8, no. 12, pp. 1-18, 2018.
- [24] Shukai Ya, Sascha Eisenträger, Yanling Qu, Junqi Zhang, Thomas Kuen, Chongmin Song, “Seismic analysis of post-tensioned concrete gravity dams using scaled boundary finite elements implemented as ABAQUS UEL”, *Soil Dynamics and Earthquake Engineering*, vol. 164, no. 107620, pp. 1-25, 2023.
- [25] Das, S.K., Mandal, K.K. & Niyogi, A.G. “Finite element-based direct coupling approach for dynamic analysis of dam–reservoir system”, *Innovative Infrastructure Solution*, vol. 8, no. 44, pp. 1-22, 2023.
- [26] Ismail, R., Ibrahim, A., & Adnan, A., “Damage Assessment of High-Rise Reinforced Concrete Buildings in Peninsular Malaysia Subjected to Ranau Earthquake”, *IOP Conference Series: Materials Science and Engineering*, vol. 513, no. 1, pp. 0–7, 2019.

- [27] Department of Irrigation and Drainage, <https://www.water.gov.my/index.php/pages/view/1257>, last accessed 2022/6/23.
- [28] Ghaedi, K., Hejazi, F., Gordan, M., Javanmardi, A., Khatibi, H. & Joharchi, A., “Seismic Response Characteristics of RCC Dams Considering Fluid-Structure Interaction of Dam-Reservoir System”, *Computational Overview of Fluid Structure Interaction*, vol. 1, no. 97859, pp. 1-23, 2021.
- [29] Hong, Z., Na-li, W. & Gao, L., “Seismic response of concrete gravity dam reinforced with FRP sheets on dam surface”, *Water Science and Engineering*, vol. 6, no. 4, pp. 409-422, 2013.
- [30] Chen, D. H., Yang, Z. H., Wang, M., & Xie, J. H., “Seismic performance and failure modes of the Jin’anqiao concrete gravity dam based on incremental dynamic analysis”, *Engineering Failure Analysis*, vol. 100, pp. 227– 244, 2019.

Stress Shielding Prediction of Unicortical and Bicortical Screws: A Finite Element Analysis

Anis Amira Mat Zuki, Fauziah Mat, Khairul Salleh Basaruddin*,
Ruslizam Daud, Masniezam Ahmad
Faculty of Mechanical Engineering Technology, Universiti Malaysia Perlis,
Arau, Perlis, MALAYSIA
*khsalleh@unimap.edu.my

Fauzan Djamaluddin
Department of Mechanical Engineering, Faculty of Engineering,
Hasanuddin University, Gowa, INDONESIA

ABSTRACT

The stability in an implant fixation plays a vital role in ensuring proper formation and remodelling process of the fractured bone. Failure in implant fixation is commonly associated with short- and long-term instability of the bone-implant interface. The bone-implant interaction creates a complicated mechanical interplay that might influence the stress distribution and hence the biomechanical performance stability of the implant fixation. Furthermore, implant screw parameters namely thread size, geometrical design and material properties become additional factors that affect the bone-implant interaction. The purpose of this study was to investigate the effect of unicortical and bicortical screws' parameters on the screw-bone interaction mechanism. To evaluate the stress transfers between screw and bone, the stress parameters namely stress transfer parameters (STP) was employed. A two-dimensional (2D) finite element model of full threaded screw was simulated while varying the parameters of the screw: two types of material (stainless steel A316 and titanium alloy Ti-6Al-4V), screw length and screw pitch. It was found that the lower in elastic modulus results to the higher stress transfer between implant-bone interface. As the titanium have lower elastic modulus, it gave higher values of STP which help to transmit and distribute stress better compared to the stainless steel. While the effect of varying screw pitch between two types of screws shows that STPs values of fully threaded bicortical screws shows significant result for finer pitch size that may advancing bone remodelling process at the early stage.

Keywords: *Unicortical; Bicortical; Implant Fixation; Stress Transfer*

Introduction

Fracture fixation device such as internal fixation is one of the leading ways that surgeons used to treat the fractures of the femur bone. The purpose of the fixation implant is to restore the bones' structure and assist in the stabilization of the fractured bone in accordance with the types of fractures while bone regenerates. Failure of implant fixation usually occurs due to short-term and long-term instability of the bone-implant interface. Implant material properties [1]-[2] implant geometry [3]-[4] and configuration [5]-[7] external loading [8], and interfacial bonding [9] are among the factors that affect the stability of the implant-bone interface.

In order to enhance secondary bone healing and prevent bone resorption, a suitable fixation that generates the sufficient amount of strain in the newly formed bone tissue is vital to allow a controlled interfragmentary movements along the bone's axial direction [10]. However, when implant fixations were introduced into bone, the implant is stiffer than the surrounding bone which consequently undergoes changes in shape and stiffness. This affects the mechanical environment in the bone which is supposed to be an active participant of the fixation process. Proper bone formation and remodelling process would not occur without suitable implant type and placement technique used for improving mechanical stability, thus causing the implant placement to fail.

For an internal fixation screws system, there are two types of screws: (1) bicortical, and (2) unicortical. Bicortical screw is known as a screw-type that can penetrate both sides of cortical bone cross section. Meanwhile, unicortical can only penetrate through one side of cortical bone cross section. Screws can be considered as the gold standard for internal fracture fixation [11] as it is responsible for retaining the stability of the implant [12]. Bone-implant screw interface plays a significant role in providing fixation stability on the formation of bone. To transmit stress between the implant and the tissue around the bone, the screw parameters have a major influence in determining the primary implant stability. Screw material, core diameter, outer diameter, thread depth, pitch, length, and number of threads engage to the bone are important characteristics that could affect the construct strength.

The result from Ros et al. [13] shows that loosening rate of the Wagner Standard Cup was significantly related to a lack of bone coverage of the acetabular cup as result from a poor design that delay osseointegration since it is crucial to maximise the contact area between the implant and the bone as the mechanical stability of the acetabular component depends on proper implant positioning. Other than that, thread depth and width of the screw could also clinically influence implant insertion and surface area; however, thread

depth had a more significant impact on the effective stress distribution than thread width [3], [13]. The previous studies show that continuous stress transfer between bone-screw interaction can be enhanced by increasing the number of screw thread and thread diameter and reduce the core diameter [14]-[15]. Moreover, the thread depth and width also influenced the implant insertion and surface area where it has significant effect on the stress distribution [3]. The result from previous study related to implant dentistry shows that von Mises stresses are inversely proportional to thread depth which will result in maximizing the necessary area for osseointegration and providing good initial stability [16]. Contact surface area at the bone-screw interface also can be increased by increasing the pitch of the screw thus increasing the number of threads per inch. Increasing the pitch increase the number of threads engaged in bone thus increasing the amount of bone chips and debris engaged between the threads [17].

Santos et al. [18] highlight the importance of screw length by using bicortical and unicortical to determine the stability of the implant fixation with a different type of plate system in vitro study. According to the previous in-vitro study [5], the bicortical has greater stability where it can make a connection between plate and bone interface with the distal cortex of the bone. However, the bicortical are more invasive than unicortical screws because according to the Wu et al. [19], the unicortical fixation is a surgically less complex operation, can theoretically cause less damage to surrounding soft tissues and avoids the complications associated with incorrect screws size. While the result from an experiment demonstrated that the bicortical fixation resulted in higher pull-out strengths for 40 cadaveric human proximal phalanges than unicortical, but recommended unicortical fixation for diaphyseal fractures, as the pull-out strength of unicortical screws at the mid-diaphysis was significantly higher than bicortical screws [20]. Despite the wealth of literature available in the field, there still lack of study regarding transmission of stress and strain between an implanted screw and the surrounding bone as previous research only focused on in-vitro study.

Fully threaded screws commonly used as an internal fixation compared to partially threaded screws to produce optimal compression and absolute stability. Meanwhile, Downey et al. [15] compared performant of partially and fully threaded lag screw and suggest that fully threaded lag screw perform better than partially threaded lag screw in shear and superior in the initial stiffness and failure strength. Sayyed et al. [21] stated that fully threaded cancellous bone screw with higher numbers of threads may have better purchase in the porous metaphyseal bone of distal tibia and increase the pull-out strength thereby leading to better outcomes, thus become optimal internal fixation device for use in elder patients with complications. Compression experimental results showed that fully threaded screws demonstrated significant improvement in stability of fixation of a medial malleolar fracture compared to partially threaded isometric cancellous screws [22]. As such,

multiple published data have studied the strength, flexibility, and maximum insertion torque of partially threaded cancellous screws and dental implant. But the bone-screw interaction of fully threaded bicortical and unicortical in internal fixation application are not well defined. Therefore, it remains questionable whether the fully threaded unicortical or the bicortical is more practical for patients in terms of stability and fewer surgical complications.

Other than geometry, the material of the implant also plays a vital role in the stability of the bone-implant interaction. According to the Fouda et al. [17], an implant with carbon hydroxyapatite (C/HA) contribute to the greatest stress along with the fracture site and increase stress 16% than stainless steel implant. Defective material will not only result to early fatigue and breakage but contribute to the increased corrosion and increase tissue reaction. However, most of the implant from available manufacturing are made from stainless steel and titanium.

The stress distribution between bone-implant can be measured by mechanical stimuli that develops around it to stabilize the interaction between bone-implant and thus ensuing bone remodelling process. Various mechanical measures have been used to evaluate the bone remodelling process such as stress transfer parameters (STP) and strain energy density transfer parameter (SEDTP). One example of study used STP to determine the effect of different types of half pins on STP during osseointegration [23] while others used to evaluate the effect of thread profile on stress transfer in a magnesium fixation [11] and material [24]. While Chun-Li Lin [25] used SED to investigate the interactions for implant placement of dental implant. Therefore, by understanding the mechanic interaction between implant and bone of screws contact for improving its stability may promoting better osseointegration process.

These situations demonstrate that at the bone-implant interaction, it experienced stress shielding response where normal mechanical stress of bones reduced, resulting in bone loss in the region of implants [26]. Even though loosening of the screw has been well reported in the literature, there are still lacking regarding the bone-screw interaction involving the reduction of stress shielding and bone remodelling of fully threaded cortical screw as most of previous study focused on partial thread screw and dental implant. In vivo, a loss of compression between implanted screws and bone is unavoidable, especially with lag screws.

Implants should be constructed in such a way that the stress shielding effect is minimized. Without an appropriate implant design that increases primary reliability, the necessary bone development and remodelling mechanism will not be triggered, and implant placement may fail. Analysis of stress distribution can provide information on the consequences of implant characteristics. This is important for effective bone healing and avoids unnecessary secondary or revision surgery. Therefore, the aim of this study is to determine the effects of fully threaded cortical screw parameters such as

material, pitch size and screw length on stress transfer parameters in order to improve implant stability and thus promoting the better formation of a direct interface between bone and implant.

Methods

The risk of loosening can be reduced by optimizing screw geometric and material features in a way that produces and distributes stress equally between bone and around screw threads. In this study, the effect of screw parameter on stress transfer was simulated using a 2-D finite element model. An axisymmetric screw-bone model was generated using ANSYS APDL to observe stress transfer of the fully threaded cortical screw configurations for the varied parameter such as material, size of pitch and length of screws as shown in Table 1. Two materials have been used in this study which are stainless steel A316 and titanium Ti-6Al-4V ELI. The effect of pitch, the size of screws pitch was varied with 0.50, 1.00, 1.25, 1.50, 1.75, and 2 mm. The thread profile, major and minor diameter of the screw were kept constant. The screw length was varied from 6 mm to 27 mm to investigate the effect of length on stress transfer between the implant and the bone. The unicortical (U) screw refers to the shorter screw while the longest screw was set as a bicortical (B) screw as unicortical fixation only engaging the near cortical bone to hold the reduction. On the other hand, the bicortical fixation always engage with both the near and far cortical bones [19]. Rectangular shape of screw thread was used in this study as it shown to give a uniform surface stress distribution [26]-[27].

Table 1: Parameters of cortical screw

Material properties		Pitch size (mm)	Thread profile	Minor diameter (mm)	Major diameter (mm)	Screw length (mm)
Stainless Steel A316 [29]: E=190GPa V=0.31	Titanium Ti-6Al-4V ELI[28]: E=110GPa v=0.31	0.5-2	Rectangular	0.5	1.0	6.00- 27.00

The 2D model was constructed by 3 mm homogeneous cortical bone layers at upper and bottom of cancellous bone and 20 mm cancellous bone region as listed in Table 2. The model was considered as linear elastic and isotropic for simplification purposes to allow the model to focus on the influence of the screw parameter [11].

Table 2: Material properties of bone

Bone	Material properties	Thickness (mm)
Cortical	E=17 GPa, $\nu=0.33$	3 [12]
Cancellous	E=1G Pa, $\nu=0.35$ [30]	20 [12]

The placement and the design of screw were mimic the bicortical and unicortical screws as shown in Figure 1. The axisymmetric screw-bone displacement was constrained in x-axis direction but allowed in y-axis direction. Fixed boundary condition was applied to the one side of the model (right) and the bottom. The contact between screw and bone are assumed to be bounded to simulate a perfect contact between screw and bone [11]. It was also considered that the contact between cortical and cancellous bone was bounded. A vertical load of 80 N was subjected in the y-direction on the top surface of the screw’s head to simulate pull out process [14].

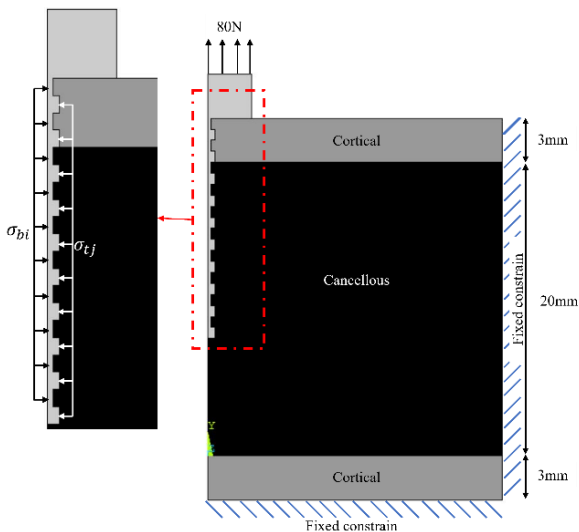


Figure 1: 2D of screw–bone interaction model

The convergence test was used to determine the optimum mesh size of the model for accurate calculation with reasonable computational time. Figure 2 shows the maximum equivalent stress obtained from the simulation at different number of elements. The result shows that the maximum of equivalent stress rapidly increases from 13426 to 84133 of element numbers until it steadily increases to 148783 of element numbers. From there, the increment of maximum equivalent stress of the element number from 84133 to

148783 was small compared to others number of elements. Thus, 84133 number of elements was used to simulate in screw-bone interaction models effective number for meshing due to small increment about 1% to the following element number. The number of element and element type were configured at 9678 and plane 183 solid elements with 8-node quadrilateral, respectively.

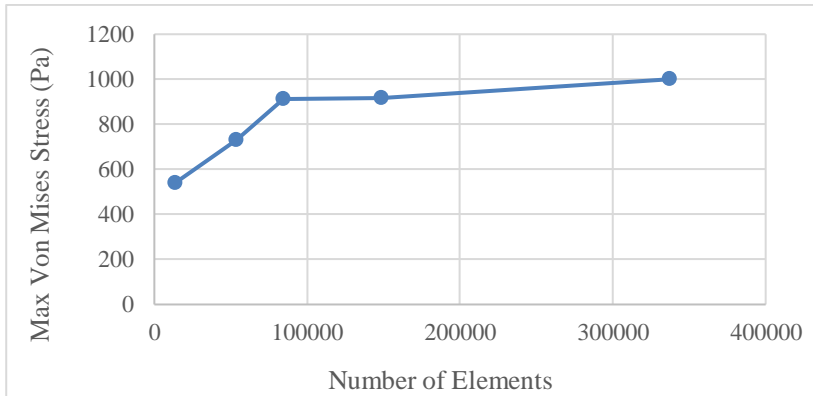


Figure 2: The convergence test between number of element and maximum equivalent stress with element meshing model

To characterize this stress transfer, stress transfer parameters (STP) was applied to evaluate the load transfer between the bone and the screw fixation. STP is defined as a ratio of von Mises stress transferred to bone, σ_b versus the stress in the adjacent screw thread, σ_t [30]. The STP of mechanical stimuli between screw and bone is computed after the simulation using following equations [31]:

$$STP = \sum_{i=j=N} \frac{\sigma_{bi}}{\sigma_{tj}} \quad (1)$$

where σ_{bi} is average von Mises stress (bone) and σ_{tj} is average von Mises (thread).

Table 3 summarizes the range of screw pitch and the length of the screw used in this study. Length of screw for different pitch have been grouped into 6-8, 9-11, 12-14, 15-17, 18-20, 21-23, 24-25, 26-27. The groups were selected to avoid incomplete or partial thread at the end of each screw. For example, in the group length of 6-8 mm, each screw has different length for different pitch namely 0.50, 1.00, 1.25, 1.50, 1.75, and 2.00 mm. For pitches 0.50, 1.00, 1.50, and 2.00 mm, the thread completes at 6 mm of length while at pitch 1.25 and

1.75, its complete at 6.25 mm and 7 mm, respectively. The length of screw from 6 mm to 23 mm is in cancellous zone, whilst 24 mm to 27 mm is in cortical zone.

Table 3: Screw’s length and pitch

Group of length (mm)	Pitch (mm)					
	0.50	1.00	1.25	1.50	1.75	2.00
6-8	6.00	6.00	6.25	6.00	7.00	6.00
9-11	9.00	9.00	10.00	9.00	10.50	10.00
12-14	12.00	12.00	12.50	12.00	12.25	12.00
15-17	15.00	15.00	15.00	15.00	15.75	16.00
18-20	18.00	18.00	18.75	18.00	19.25	18.00
21-23	21.00	21.00	21.25	21.00	21.00	22.00
24-25	24.00	24.00	25.00	24.00	24.50	24.00
26-27	26.00	26.00	26.25	27.00	26.25	26.00

Results and Discussions

Effect of cortical screw materials on STP

Figure 3 presents the results of STP value obtained for two types of screw material namely stainless steel A316 and titanium alloy Ti-6Al-4V. Pitch, core diameter and thread diameter were kept constant with 0.5 mm, 0.5 mm and 1 mm, respectively. Based on the results obtained for both of materials, the highest STPs values of titanium is 0.4852 gained by the 26-27 mm group of length. While, from the group of length 6-8mm to 24-25 mm, the graph shows fluctuated trend with maximum, minimum, and average value are 0.4483, 0.3255 and 0.3712, respectively.

The similar trend observed for stainless steel A316. For stainless steel A316, the most significant value of STP is 0.3369 at 26-27 mm group of length. STPs values fluctuated at the maximum of 0.3106 with the lowest of 0.2246 and 0.2611 of average. Compared to the stainless steel A316, titanium alloy shows higher values of STP. The minimum and maximum STP value for stainless steel of all pitch are 0.0516 and 0.4985, respectively. While the minimum and maximum STP value for titanium alloy are 0.07782 and 0.5537, respectively.

For the same group of length and pitch, it is found that the STP percentage differences resulted in an 6.4% to 85.4% increased between the SS A316 and the titanium. Among the groups observed, the largest different between the two types of material is the 12 mm group of length where the titanium has higher value of STP compared to the stainless steel. STP value of stainless steel 0.0887 while STP value of titanium is 0.1645 with percentage

different 85.4%. This indicates that titanium alloy Ti-6Al-4V gave better load transfer between the bone and the screw fixation compared to stainless steel A316 based on STP values. The similar observation is found in previous research where it compares effect of pins materials on average STPs, it found the percentage difference of the STP value is 0 to 23.5% between stainless steel and titanium alloy of half pin uniaxial external fixation [30].

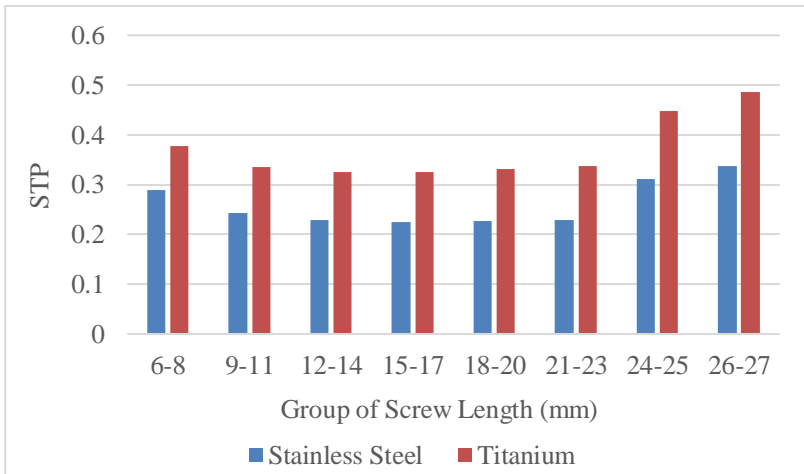


Figure 3: Effect of screw materials on the average STPs

The present study found that a screw material with a lower Young's modulus results in improved load transfer, as evidenced by the calculated stress-transfer parameter (STP) values. This finding is consistent with previous research on the bone-implant fixator stress-strain behaviour under three-point and four-point bending, which found that the STP of stainless steel was lower than that of titanium due to the fact that stainless steel has a higher elastic modulus than titanium for both bending loads at a constant pitch [32]. Another study on nails and canals also found that a titanium nail (with a modulus of 110 MPa) resulted in lower gap deformation and provided a higher contact force, resulting in a higher frictional force against the applied load, in comparison to a stainless steel nail (with a modulus of 200 MPa) [33]. Furthermore, previous research on cancellous screws has reported an average 20-35% increase in stress transfer upon reduction of the elastic modulus of the screw material from 105 GPa to 40 GPa [12], [29]. This suggests that a lower Young's modulus results in better STP values.

Effect of varying cortical screw pitch on STP

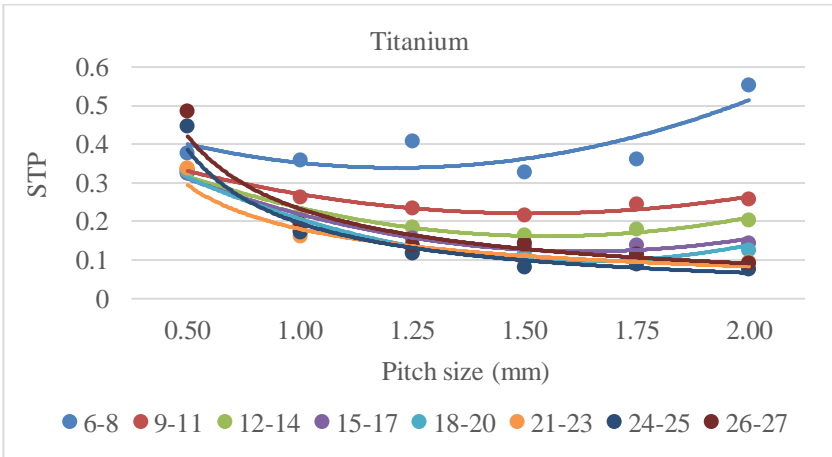
Figure 4 presents STPs values on two types of materials for different pitch. The results show similar trends of the STPs values for all pitch of the stainless steel A316 and titanium alloy. The STPs values of all group length show the same trends where the highest STP is at the finer pitch size before STPs values start to decrease as the size of pitch increased except for group length of 6-8 mm. The result shown similar pattern as that of Hosseinitabatabaei et al. [34], where simulated 4 years healing process to observe the effect of maximum stress parameter and STP by varying screw pitch from 1.5 mm to 2.5 mm and the results shows that by decreasing screw pitch size would improve the screw performance and reduce the effects of stress shielding. However, at the group length of 6-8 mm, the STPs values start to increase simultaneously as the size of pitch increased. Among of all the pitch, the highest STPs values is found at the shortest group of length of 6-8 mm for both of materials at the 2 mm of pitch size.

Considering the above, the stress transfer performance is optimized with the appropriate combination of screw pitch and material thus reducing the undesirable stress shielding effect of the implant to the surrounding bone. This is consistent with the previous findings which suggest that using a less stiff screw and reducing the pitch of the screw would improves the stress transfer from screw to bone, and consequently diminishes the risk of stress shielding [14], [25]. Study by Fatin et al. [29] also found that implant with high elastic modulus may cause severe stress concentration, which may weaken the bone and lead to the deterioration of the implant-bone interface.

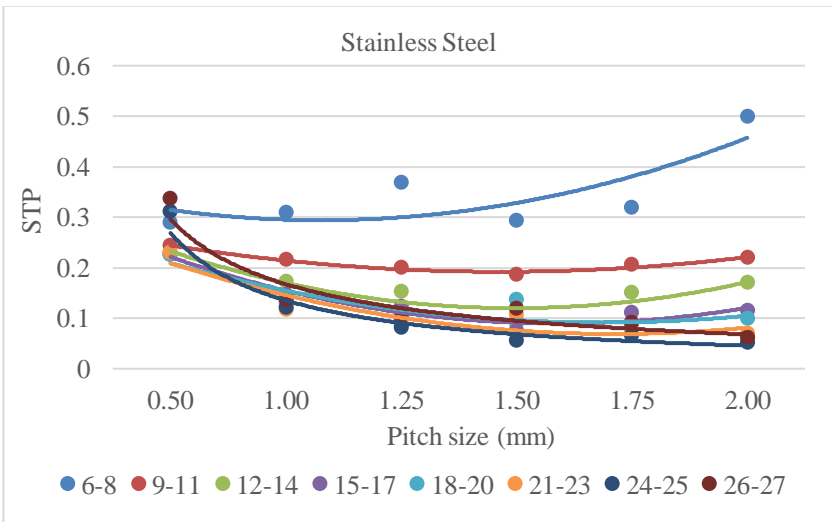
An orthopaedic screw implant is a crucial aspect of a patient's physical and psychological recovery, as well as their rehabilitation and rehabilitation regimen. The ability of an orthopaedic screw to transmit stress uniformly between the threads and the surrounding bone determines its biomechanical compatibility. As elastic modulus decreases, the stress parameters such as STP was increased. This indicates that decreasing elastic modulus help to transmit and distribute stress better than higher elastic modulus in implant-bone contact.

A study on material of dynamic hip screw during fall and gait loading found that smaller elastic modulus materials help to induce less stress on the implant and decrease stiffness of implant during loading [2]. Finite element analysis on dental implant also showed by using low modulus would result in lower flexural resistance [1]. Similarly results found on research using viscoelastic finite element modelling where it stated that reducing the elasticity of screw will reduce the amount of the stress shielding of the screws [35]. Furthermore, an vivo study on sheep from previous research on dental implant found that by using small size of screw pitch showed the greater surface area and better stress distribution thus may improve primary stability in cancellous bone [36]. Experimental study of screw on synthetic bone also demonstrated the screws pitch as one of the important parameters on holding power as finer

thread was reported gave greater purchase compared to coarse thread pitch [17].



(a)



(b)

Figure 4: STP on two types of material: (a) titanium, and (b) stainless steel, for different pitch size

Figure 5 shows the effect of screws length on the constant pitch size. The graph of all pitch shows same pattern where the STPs values start to

decrease from 6-8 mm of group length until 21-23 mm (unicortical screw region) before STPs values start to increase at the 24-25 mm until 26-27 mm of group length (bicortical screw region). This trend also shows that it is anticipated that with appropriate combination of screw pitch, screw length and material able to improve the performance of the stress.

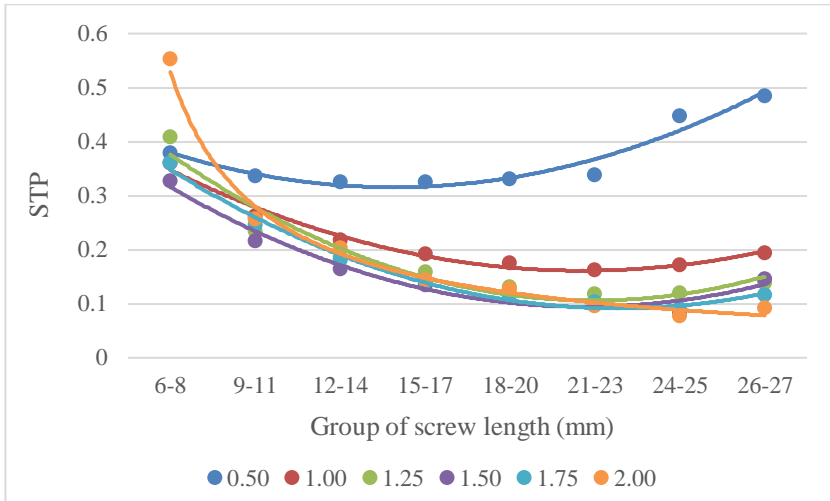


Figure 5: STPs on constant pitch and material for different length

The results in Figure 5 demonstrate that there is a significant difference in STP values for a pitch size of 0.5 mm when compared to other pitch sizes, particularly at higher screw lengths. This variation is attributed to the significant difference in the number of threads, as group lengths between 6 mm-8mm until 21-23 mm are classified as unicortical screws, while group lengths between 24-25 mm and 26-27 mm are classified as bicortical screws, as depicted in Figure 6. To avoid incomplete or partial threading at the end of each screw, the screw lengths for different pitches were grouped accordingly. This finding is in line with previous research, which suggests that decreasing the modulus of elasticity of screws, increasing the number of threads per screw, decreasing the pitch of screws, and decreasing the diameter of the screws shaft can all contribute to reducing stress shielding and loosening of the screws [35].

Ricci et al. [37] stated that bicortical lag screws offer better benefit regarding quality of bone at the end of the screw as compared to unicortical lag screws. Experimental results of bicortical and unicortical placement at proximal tibia fractures shows that bicortical screw present a mechanically superior construct than unicortical screw placemen as it significantly outperformed unicortical screw placement in stiffness and maximum load [38].

The mean load to failure of unicortical fixation also was lower compared to bicortical plate fixation in transverse metacarpal fracture models subjected to cyclic loading [39]. Others study also shows that specimens fixed with bicortical locked plating gave increased in stiffness during torsional loading when compared to unicortical locked fixation [40].

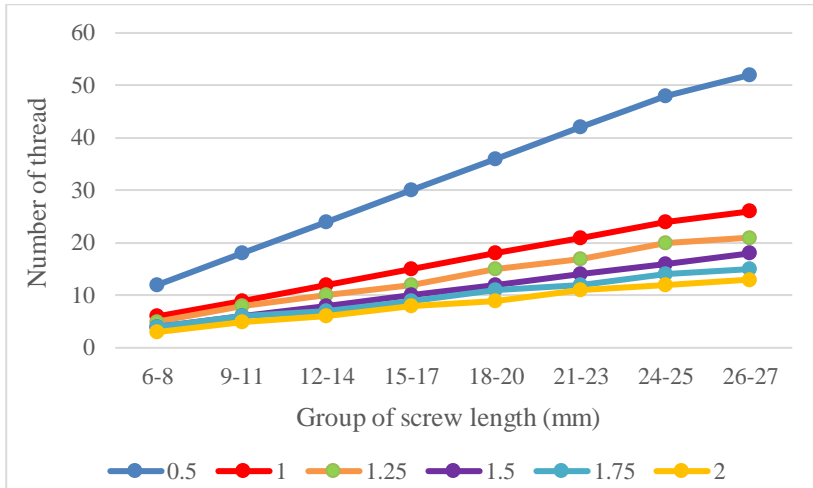


Figure 6: Number of threads on constant pitch and material for different length

However, the experimental study on synthetic bone shows that the stability of temporary screws length depends on the bone thickness where 2 or 1 mm of cortical thickness coupled to cancellous bone was deemed sufficient enough to achieve mechanical stability [41]. Another study presents the comparison between unicortical and unicortical plate and screw fixation of metacarpal fractures. It showed that unicortical can act as standard method of fixing metacarpal fractures due to the reason it requires less technically demanding and quicker producer [19]. Unicortical fixations also demonstrated higher stability against bending loads of the forearm, and potentially decreased refracture risk following plate removal [40].

Stress and strain distribution

Referring to Figure 7, it shows the von Mises distribution in unicortical (6-8 mm) and bicortical (26-27 mm) fully threaded screw profiles for both materials. The figure shows that the maximum amount of stress occurs in the head for the 6-8 mm length group with 793.14 (titanium) and 865.76 (stainless steel). Moreover, large stresses are noticed in screws where the thread is placed next to the combined sections of cortical and cancellous bone. This is because

the screw's head being secured to the cortical surface, which compresses the bone between the head and the first thread [29]. Also, as seen in the figure, the cortical region has higher stress than the cancellous region.

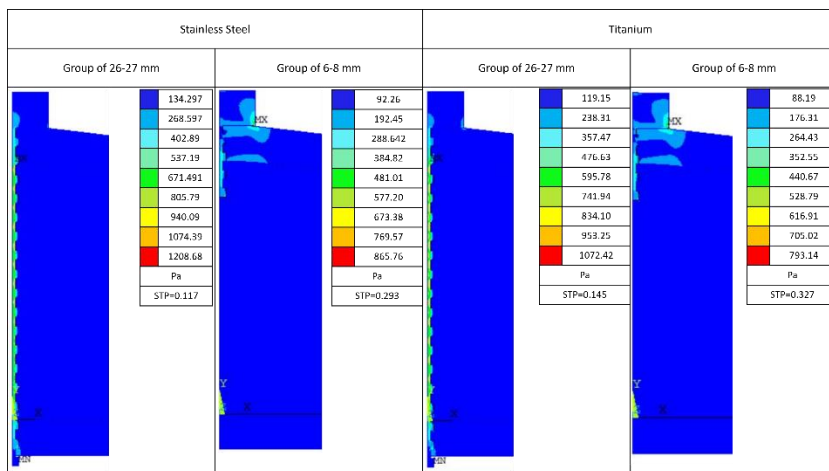


Figure 7: von Mises stress distribution on varied screw length with different material

While, at group of length 26-27 mm, the maximum stress happened at the screw region with 1072.42 (titanium) and 1208.68 (stainless steel) while at the surrounding of the bone, the highest stress values are 119.15 (titanium) and 134.297 (stainless steel). It also shows that the highest concentration stress occurs in the screw thread region, adjacent to the joined portions of cortical and cancellous bone. The stress from the head of screw start to significantly increases and well distributed until at the thread in cancellous region before it reduces in stress value in the thread at the far cortical region. However, the stress value in the bone is lower in comparison with those of the screw for both type of screw.

Titanium screws Ti-6Al-4V ELI has a maximum von Mises stress of 1072.42 Pa while maximum von Mises of stainless-steel screws A316 is 1208.68 Pa at 26-27 mm group length where titanium screw approximately 12.71% lower than stainless steel. Because the elastic young's modulus of the titanium screw (110 GA) is substantially smaller than that of the stainless-steel screw (190 GPa). The titanium screw Ti-6Al-4V ELI model results in a lower von Mises stress, which is advantageous since greater mechanical stimuli conveyed to bone will possibly bring about much less pressure shielding as STP values shows in Figure 3.

Furthermore, it showed that the screw in group of 26-27 mm had the largest contact area with the bone and at the same time the maximum von Mises

stress occurred in the surrounding bone for both materials. This means that the longest screw length transfers the most amount of stress to the surrounding bone through the bone-screw interface as shown in Figure 7. These findings are in line with those found in the literature, where critical stress seems to yield at the thread location [11] and material with elastic modulus of 45 GPa produce lower stress compared to 193 GPa of elastic modulus [30].

The limitation still existed in this finite element simulation which can be improved in future studies. Specific situations are considered such as material properties of bone, bone thickness, and contact condition that may not exactly reflect the real situations. The material properties in this study were assumed as linear elastic, homogeneous and isotropic. Another assumption was the contact between bones and screws were perfectly bonded. Furthermore, the outcomes of this study were based only on the 2D cross-section of the model. These simplification purposes to allow the model to focus on the impact of the screw parameters.

Conclusion

The bone-implant screw contact is critical in providing fixation stability during bone growth. The screw parameter is important in transmitting stress between the implant and the tissue around the bone. In the application of internal fixation, the interaction of fully threaded bicortical and unicortical is not clearly defined. Therefore, in this study the results demonstrated low in elastic modulus of fully threaded bicortical and unicortical will provide better stress transfer and distribution to the bone. As in this study, titanium alloy Ti-6Al-4V provide improved biomechanics compared to stainless steel A316 as it has lower elastic modulus. The effect of varying screw pitch and screw materials between two types of screws shows that bicortical gave better performance at pitch of 0.5 mm, followed by 1.00 mm and 1.25 mm. This mean bicortical screws produce significant and strong stress transfer when using finer pitch size. For unicortical (9-11 mm until 21-23 mm of group length), the most optimum values of stress parameters were at pitch of 0.5 mm and followed by 1.00 mm however unicortical screw with 6-8 mm of group length shows contrast result where the optimum stress transfer happened at pitch of 2 mm, followed by 1.25 mm. The results of this study may provide better understanding of the impact of fully threaded cortical screws parameters such as material, pitch size and screw length on the formation of a direct interface between bone and implant. By gaining a greater insight into these factors, it may be possible to improve implant stability during the early stages of healing, thereby promoting optimal healing outcomes.

Contributions of Authors

It is confirmed that all authors were fully involved in the study and preparation of the article and that the material within has not been and will not be submitted for publication elsewhere. We have read and concur with the content in the article.

Funding

This work was supported by the “Fundamental Research Grant Scheme (FRGS)” [FRGS/1/2018/TK03/UNIMAP/02/22] from Ministry of Higher Education (MOHE) of Malaysia

Conflict of Interests

Fauziah Mat has received a research grant from “Ministry of Higher Education (MOHE) of Malaysia”. The authors confirm that there is no conflict of interest regarding the publication of this manuscript.

Acknowledgement

The authors would like to be obliged to Universiti Malaysia Perlis and Ministry of Higher Education (MOHE) of Malaysia for providing laboratory facilities and financial assistance under FRGS/1/2018/TK03/UNIMAP/02/22.

References

- [1] A. Korsel, “3D Finite Element Stress Analysis Of Different Abutment Materials in Screw, Implant and Cortical Bone,” *Egyptian Dental Journal*, vol. 66, no. 1, pp. 415–421, 2020.
- [2] N. S. Taheri, A. S. Blicblau, and M. Singh, “Comparative study of two materials for dynamic hip screw during fall and gait loading: Titanium alloy and stainless steel,” *Journal of Orthopaedic Science.*, vol. 16, no. 6, pp. 805–813, 2011.
- [3] H. S. Ryu, C. Namgung, J. H. Lee, and Y. J. Lim, “The influence of thread geometry on implant osseointegration under immediate loading: A literature review,” *Journal of Advance Prosthodontics*, vol. 6, no. 6, pp. 547–554, 2014.
- [4] Q. Wu, Y. Zhang, S. Wang, R. Liu, and G. Liu, “Different Lengths of

- Percutaneous Transverse Iliosacral Screw in Geometric Osseous Fixation Pathway : A Finite - Element Analysis,” *Indian Journal of Orthopaedics*, no. 0123456789, 2022.
- [5] G. J. G. Quintero, “Biomechanical Evaluation Of Hybrid, Bicortical And Unicortical, Screw Configurations For Internal Bone Plate Fixation Of Long Bone Fracture: An In-Vitro Study Of Porcine Femur Bone Models,” Thesis, 2017.
- [6] M. Zhu *et al.*, “Initial stability and stress distribution of ankle arthroscopic arthrodesis with three kinds of 2-screw configuration fixation: A finite element analysis,” *Journal of Orthopaedic Surgery and Research*, vol. 13, no. 1, pp. 1–7, 2018.
- [7] B. Zhang, J. Liu, Y. Zhu, and W. Zhang, “A new configuration of cannulated screw fixation in the treatment of vertical femoral neck fractures,” *International Orthopaedics*, vol. 42, no. 8, pp. 1949–1955, 2018.
- [8] L. E. Butignon, M. de A. Basilio, R. de P. Pereira, and J. N. A. Filho, “Influence of Three Types of Abutments on Preload Values Before and After Cyclic Loading with Structural Analysis by Scanning Electron Microscopy,” *International Journal of Oral & Maxillofacial Implants*, vol. 28, no. 3, pp. e161–e170, 2013.
- [9] S. Xie, K. Manda, and P. Pankaj, “Effect of loading frequency on deformations at the bone–implant interface,” *Proceedings of the Institution of Mechanical Engineers, Part H: Journal of Engineering in Medicine*, vol. 233, no. 12, pp. 1219–1225, 2019.
- [10] H. K. Uthhoff, P. Poitras, and D. S. Backman, “Internal plate fixation of fractures: Short history and recent developments,” *Journal of Orthopaedic Science*, vol. 11, no. 2, pp. 118–126, 2006.
- [11] E. Tetteh and M. B. A. McCullough, “Impact of screw thread shape on stress transfer in bone: a finite element study,” *Computer Methods in Biomechanics*, vol. 23, no. 9, pp. 518–523, 2020.
- [12] K. Haase and G. Rouhi, “Prediction of stress shielding around an orthopedic screw: Using stress and strain energy density as mechanical stimuli,” *Computer in Biology and Medical*, vol. 43, no. 11, p. 1748, 2013.
- [13] V. Ros *et al.*, “High short-term loosening rates with the wagner standard cup,” *Journal of Arthroplasty*, vol. 29, no. 1, pp. 172–175, 2014.
- [14] G. Rouhi, M. Tahani, B. Haghighi, and W. Herzog, “Prediction of stress shielding around orthopedic screws: Time-dependent bone remodeling analysis using finite element approach,” *Journal of Medical and Biological Engineering*, vol. 35, no. 4, pp. 545–554, 2015.
- [15] M. W. Downey, V. Kosmopoulos, and B. B. Carpenter, “Fully Threaded Versus Partially Threaded Screws: Determining Shear in Cancellous Bone Fixation,” *The Journal of Foot and Ankle Surgery*, vol. 54, no. 6, pp. 1021–1024, 2015.
- [16] E. Reinaldo, S. Bonifacius, and A. Adenan, “Influence of short implant

- thread pitch and depth to primary stability on D4 bone density: A laboratory study,” *Journal of International Oral Health*, vol. 13, no. 5, p. 456, Sep. 2021.
- [17] T. A. Decoster, D. B. Heetderks, D. J. Downey, J. S. Ferries, and W. Jones, “Optimizing bone screw pullout force,” *Journal of Orthopaedic Trauma*, vol. 4, no. 2, pp. 169–174, 1990.
- [18] R. R. Santos et al., “Biomechanical analysis of locking reconstruction plate using mono-or bicortical screws,” *Material Research*, vol. 19, no. 3, pp. 588–593, 2016.
- [19] F. Wu et al., “Stability of Unicortical versus Bicortical Metacarpal Fracture Internal Fixation Trial (SUBMIT): Study protocol for a randomized controlled trial,” *Trials*, vol. 17, no. 1, pp. 1–7, 2016.
- [20] M. Khalid, K. Theivendran, M. Cheema, V. Rajaratnam, and S. C. Deshmukh, “Biomechanical comparison of pull-out force of unicortical versus bicortical screws in proximal phalanges of the hand: A human cadaveric study,” *Clinical Biomechanics*, vol. 23, no. 9, pp. 1136–1140, Nov. 2008.
- [21] S. H. Sayyed-Hosseini, F. Bagheri, M. H. Ebrahimzadeh, A. Moradi, and S. Golshan, “Comparison of partially threaded and fully threaded 4mm cancellous screws in fixation of medial malleolar fractures,” *The Archive Bone and Joint Surgery*, vol. 8, no. 6, pp. 710–715, 2020.
- [22] L. Parker, N. Garlick, I. McCarthy, S. Grechenig, W. Grechenig, and P. Smitham, “Screw fixation of medial malleolar fractures: A cadaveric biomechanical study challenging the current AO philosophy,” *The Bone and Joints Journal*, vol. 95 B, no. 12, pp. 1662–1666, 2013.
- [23] N. F. I. Ibrahim, R. Daud, M. K. Ali Hassan, N. A. M. Zain, and A. F. Azizan, “The effect of different types of half pins on stress transfer parameter during osseointegration,” *Material Today Proceedings*, vol. 16, pp. 2179–2186, 2019.
- [24] M. H. Khan, R. Daud, M. K. Ali Hassan, A. F. Azizan, B. Izzawati, and N. N. Mansor, “The effect of cannulated screw material on stress transfer parameter in orthotropic femur bone with Pauwels type-III fracture,” *Material Today Proceedings*, vol. 16, pp. 2135–2143, 2019.
- [25] C. L. Lin, Y. H. Lin, and S. H. Chang, “Multi-factorial analysis of variables influencing the bone loss of an implant placed in the maxilla: Prediction using FEA and SED bone remodeling algorithm,” *Journal of Biomechanics*, vol. 43, no. 4, pp. 644–651, 2010.
- [26] S. Kebdani, S. Zahaf, B. Mansouri, and B. Aour, “Numerical study of the effect of rigid and dynamic posterior attachment systems on stress reduction in cortical and spongy bones of the lumbar segments L4-L5,” *Nano Biomedical Engineering*, vol. 9, no. 3, pp. 249–274, 2017.
- [27] A. Dhanopia and M. Bhargava, “Finite Element Analysis of Human Fractured Femur Bone Implantation with PMMA Thermoplastic Prosthetic Plate,” *Procedia Engineering*, vol. 173, pp. 1658–1665, 2017.

- [28] H. Mehboob and S. H. Chang, "Application of composites to orthopedic prostheses for effective bone healing: A review," *Composite Structures*, vol. 118, no. 1, pp. 328–341, 2014.
- [29] A. Gefen, "Computational simulations of stress shielding and bone resorption around existing and computer-designed orthopaedic screws," *Medical and Biological Engineering and Computing*, vol. 40, pp. 311–322, 2002.
- [30] N. F. I. Ibrahim, R. Daud, M. K. A. Hassan, N. A. M. Zain, and Y. Bajuri, "Half pins stress shielding interaction behavior at implant-bone interface," *International Journal of Integrated Engineering*, vol. 10, no. 5, pp. 204–208, 2018.
- [31] J. P. Paul and A. Gefen, "Optimizing the biomechanical compatibility of orthopedic screws for bone fracture fixation (multiple letters)," *Medical engineering & physics*, vol. 25, no. 5, pp. 435–436, 2003.
- [32] B. Izzawati, R. Daud, M. Afendi, M. S. A. Majid, N. A. M. Zain, and Y. Bajuri, "Prediction of Stress Shielding Around Implant Screws Induced by Three-Point and Four-Point Bending," *International Medical Device and Technology Conference*, vol. 15, no. 4, p. 50, 2017.
- [33] P. Y. Lee, Y. N. Chen, J. J. Hu, and C. H. Chang, "Comparison of mechanical stability of elastic titanium, nickel-titanium, and stainless steel nails used in the fixation of diaphyseal long bone fractures," *Materials (Basel)*, vol. 11, no. 11, pp. 1-11, 2018.
- [34] S. Hosseinitabatabaei, N. Ashjaee, and M. Tahani, "Introduction of Maximum Stress Parameter for the Evaluation of Stress Shielding Around Orthopedic Screws in the Presence of Bone Remodeling Process," *Journal of Medical and Biological Engineering*, vol. 37, no. 5, pp. 703–716, 2017.
- [35] M. Torabi, S. Khorrammehr, M. Nikkhoo, and M. Rostami, "The role of orthopedic screws threads properties on the success of femoral fracture fixation," *Proceedings of the Institution of Mechanical Engineers, Part C: Journal of Mechanical Engineering Science*, vol.236, no. 17, pp. 095440622210947, 2022.
- [36] E. Orsini, G. Giavaresi, and S. Salgarello, "Osseointegration Process : An In Vivo Comparison Study," *International Journal of Oral & Maxillofacial Implants*, vol. 27, no. 2, pp. 383–392, 2012.
- [37] W. M. Ricci, P. Tornetta, and J. Borrelli, "Lag screw fixation of medial malleolar fractures: A biomechanical, radiographic, and clinical comparison of unicortical partially threaded lag screws and bicortical fully threaded lag screws," *Journal of Orthopaedic Trauma*, vol. 26, no. 10, pp. 602–606, 2012.
- [38] P. J. Dougherty, D. G. Kim, S. Meisterling, C. Wybo, and Y. Yeni, "Biomechanical comparison of bicortical versus unicortical screw placement of proximal tibia locking plates: A cadaveric model," *Journal of Orthopaedic Trauma*, vol. 22, no. 6, pp. 399–403, 2008.
- [39] R. Afshar, T. S. Fong, M. H. Latifi, S. R. Kanthan, and T. Kamarul, "A

biomechanical study comparing plate fixation using unicortical and bicortical screws in transverse metacarpal fracture models subjected to cyclic loading,” *Journal of Hand Surgery (European Volume)*, vol. 37, no. 5, pp. 396–401, 2012.

- [40] T. J. Pater, S. I. Grindel, G. J. Schmeling, and M. Wang, “Stability of unicortical locked fixation versus bicortical non-locked fixation for forearm fractures,” *Bone Research*, vol. 2, no. March, pp. 1-5, 2014.
- [41] D. J. Fernandes, C. N. Elias, and A. C. O. Ruellas, “Influence of screw length and bone thickness on the stability of temporary implants,” *Materials (Basel)*, vol. 8, no. 9, pp. 6558–6569, 2015.

Evaluation of Crosslinking Degree on the Integral Membrane by using Rice Husk Ash (RHA)

Nurul Atirah Fitriah Mohd Zainuddin, Norin Zamiah Kassim Shaari*,
Nur Syazwanie Izzati Chik

Membrane Technology Research Group, School of Chemical Engineering,
College of Engineering, Universiti Teknologi MARA, Shah Alam, MALAYSIA
*norinzamiah@uitm.edu.my

Fazlena Hamzah

Biocatalysis and Biobased Material Technology,
School of Chemical Engineering, College of Engineering,
Universiti Teknologi MARA, Shah Alam, MALAYSIA

ABSTRACT

Rice husk ash (RHA) is a waste product from the harvesting and processing of rice that contains a high quantity of silica, approximately 95% after combustion. Membrane technology is being developed to remove impurities like heavy metals and dyes as the natural environment deteriorates and water supplies become scarce. Many researchers and developers are now adopting this type of technology. However, it has various drawbacks such as being costly and easily being fouled during the separation process. Therefore, matrix modification of the membrane should be carried out to mitigate these problems. The incorporation of fillers from biomass materials is one of the ways. This research aims to demonstrate the significant effect of incorporating the extracted silica from rice husk ash (RHA) in a polymer-based membrane from a blend of Polyvinyl alcohol/chitosan/polysulfone on the membrane characteristics and antifouling properties. The membranes were prepared by using a phase inversion technique by the incorporation of silica from rice husk ash (RHA) at various concentrations such as 5 wt.%, 7.5 wt.%, and 10 wt.% with a fixed amount of the polymer blends. The results showed that the integral membrane M4 with 10wt.% silica has the best hydrophilicity properties and possesses excellent antifouling properties, which were portrayed through the greater value of pure water flux (PWF) of 20.38 L/m².h and the highest flux recovery ratio of 76.32%. This study has proven the potential utilization of rice

husk ash to enhance the membrane properties for industrial wastewater treatment.

Keywords: *Rice Husk Ash (RHA); Polymer-based Membrane; Phase Inversion Technique; Antifouling; Silica*

Introduction

Water pollution is a critical issue that needs to be tackled because there is a large generation of wastewater effluent which can lead to environmental pollution. According to the United Nations World Water Development Report published in 2018, about 6 billion people throughout the world will encounter clean water scarcity by 2050, where the demand for clean water is growing at a rate of 1% annually [1]. Heavy metals, hydrocarbons, dyes, nitrogenous chemicals, pharmaceutical residues, detergents, and phosphorus are the most prevalent chemical contaminants in wastewater. These contaminants result in difficulty in treating wastewater since the contaminants are easily adsorbed to the suspended particles in water, then settled in the riverbed, and pose harm to the ecology. As a result, modern treatment for wastewater such as membrane separation technology (MST) consisting of polymeric membranes and ceramic membranes is being used to solve this problem.

The membrane is a selective barrier that is employed in the separation process to separate the presence of various phases by allowing some components to flow through while others are retained. When a membrane contains its driving force, which is a gradient of pressure, chemical, or electrical potential across the membrane, the separation process will occur. Membrane technology has been revived as a promising technology for removing impurities from effluent discharged from wastewater industries because it does not require phase change or chemical addition, making it a viable alternative to traditional wastewater treatment techniques such as distillation, precipitation, coagulation, and flocculation [2]. In wastewater treatment, the membrane is used to remove the pollutants such as suspended solids or dissolved solids to clean the water before being discharged into groundwater [3]. Membrane technology is also utilized in many types of industries such as gas separation, food processing, and protein purification.

As a biomass material, rice husk ash (RHA) is widely used as a filler in a polymeric membrane, where the formulated membranes are subsequently used in wastewater treatment [4]. Based on the findings from Alias et al. [5], the extracted silica from rice husk was used for fouling mitigation in the membranes since the amorphous structure from RHA creates strong hydrophilicity and improved the separation performance in terms of pure water flux, rejection of humic acid, and fouling mitigation for applications in liquid separation and water treatment respectively. Rice husk (RH) is a waste from

agriculture that is abundantly generated year by year, especially in the countries that produce rice as their staple food. As reported in World Atlas, rice is a staple food all over the world and Asia countries are the largest consumers of rice [6]. Rice husk contains approximately 20 wt.% of ash generated when it is burnt at a certain temperature. The silica dioxide in the ash offers a function to improve the wettability of the polymeric membranes to enhance the antifouling properties [4]. This study aims to extract the silica from rice husk ash by using a modified acid leaching process, and it was subsequently incorporated into the membrane formulation through a sol-gel reaction. The properties of the formulated membrane were evaluated in terms of functional group, thermal stability, and surface morphology, and the performance of the membrane was tested through pure water flux (PWF) and antifouling analysis. The effort to utilize rice husk ash (RHA) in the membrane fabrication will be able to reduce the amount of rice husk ash (RHA) generated as waste from the incinerator because the higher airborne concentration of rice husk ash (RHA) can cause a problem to the human respiratory system.

Methodology

Material

In the silica extraction method, the rice husk ash (RHA), 37% purity of hydrochloric acid (HCl), and 1N sodium hydroxide (NaOH) were used. The RHA was obtained from BT Science Sdn. Bhd., Selangor Malaysia. HCl and NaOH were purchased from R&M Chemicals, Subang, Malaysia. Polyvinyl alcohol (PVA) 87-89% hydrolyzed with a molecular weight average of 85000-124000, dimethyl sulfoxide (DMSO), and chitosan were purchased from Sigma-Aldrich (M) Sdn. Bhd., Merck Sdn. Bhd. and Aman Semesta Enterprise Sdn. Bhd., respectively. Polysulfone beads with 22000 molecular weights were purchased from Sigma-Aldrich (M) Sdn. Bhd. N-Methyl-Pyrrolidone (NMP) and polyethylene glycol (PEG 400) were purchased from Merck Sdn. Bhd.

Extraction of silica from rice husk ash (RHA)

The 50 g of rice husk ash (RHA) was mixed with 250 g of deionized water and 8 g of 37% purity of hydrochloric acid (HCl). This mixture was heated at 90 °C and stirred at the speed of 650 rpm for 1 hour. Then, this mixture was left at room temperature before being filtered using a Smith filter paper to obtain a cleaned RHA. This cleaned RHA residue then was treated with 250 g of 1 N NaOH for the acid-leaching process by heating the solution to 80 °C while stirring at 600 rpm for 1 hour. After that, the solution was filtered by using a Smith filter paper to extract sodium silicate.

Preparation of 2wt% of acetic acid

To prepare 2 wt.% of the acetic acid aqueous solution, 2 g of glacial acetic acid was added into 98 g of distilled water and the mixture was stirred at 150 rpm for 1 hour [7].

Preparation of polymer blend solution

To prepare the polymer blend PVA/chitosan, both solutions were prepared separately. 10 g of polyvinyl alcohol (PVA) was added into 90 g of dimethyl sulfoxide (DMSO) followed by heating at 90 °C while stirring at 400 rpm for 4 hours until the solution become homogeneous. Then, 0.02 g of chitosan was dissolved into 99.98 g of 2 wt% aqueous acetic acid solution followed by stirring at 400 rpm and heating at a temperature of 90 °C for 4 hours [8].

Preparation of polysulfone solution

To prepare 13 wt.% of polysulfone solution, 13 g of polysulfone beads pellets were dissolved in the 82 g of N-Methyl-Pyrrolidone (NMP). Next, 5 g of polyethylene glycol (PEG) was added to the mixture before it was stirred at a speed of 400 rpm with heating at 60 °C for 6 hours. Then, this solution was left at room temperature.

Preparation of hybrid solution with rice husk ash (RHA)

The hybrid solution was prepared by mixing 50 g of the prepared polyvinyl alcohol (PVA) with 50 g of chitosan solution, followed by the addition of 5 wt.% of the extracted sodium silicate and 2 g of hydrochloric acid. The mixture was heated at 60 °C for 7 hours with continuous stirring at 400 rpm. The solution was cooled at room temperature before the membrane making process. The above procedure was repeated with the 7.5 wt.%, 10 wt.% sodium silicate, and without sodium silicate respectively.

Preparation of membrane

In the last stage, the membrane was prepared by adding 1 g of hybrid solution to 50 g of polysulfone solution. Then, this mixture was stirred at 80 °C at 750 rpm until the solution turned into a homogeneous mixture. After that, the solution was left at room temperature for 1 hour before proceeding to the casting process. In the casting process, the thickness of Baker's film applicator was adjusted to 100 µm. The produced film was left at room temperature for 30-40 seconds before it was immersed in a large amount of water for a coagulation process. This membrane was left in the water for 24 hours. Then, it was dried at room temperature for 2 days before the characterization process was conducted. Table 1 depicts the formulations used in this study.

Table 1: Formulation of integral membrane

Membrane	Composition (g)			
	PVA	CS	RHA	HCl
M1	50	50	-	2
M2	50	50	5	2
M3	50	50	7.5	2
M4	50	50	10	2

Membrane characterization

The formulated membranes were characterized in terms of the functional group by using FTIR, and surface morphology by using FESEM.

Fourier Transform Infrared Spectroscopy (FTIR)

Fourier-Transform Infrared Spectroscopy (FTIR) is an analytical technique used to identify the organic, polymeric, and inorganic materials in a membrane film by determining the presence of the peak of wavenumber in the graph of transmittance versus wavenumber. In this study, the observation was done with the wave number that ranges from 4000-400 cm^{-1} . The equipment used was PerkinElmer/TGA/SDTA851 [9].

Field Emission Scanning Electron Microscopy (FESEM)

Field Emission Scanning Electron Microscopy (FESEM) is an analysis technique to identify the structure of the membrane. The samples were coated with the platinum coating to obtain the perceived images and to avoid the charging effect. Then, the images were taken by magnifying them at 10 k until 20 k, and the voltage was accelerated at 5 k. The configuration of samples was obtained by using electron dispersive spectroscopy (EDS) attached to the machine. The model used was Jsm-7600f Joel [10].

Performance test

The performances of the formulated membranes were evaluated in terms of pure water flux and antifouling analysis.

Pure Water Flux (PWF)

For pure water flux analysis, a membrane filtration rig with a dead-end mode was used. The membrane was cut into a circular shape with a surface area of 19 cm^2 before placing it onto the porous disk of the stainless-steel filtration cell. Then, 300 mL of deionized water was filled inside the cell as the feed solution before applying a nitrogen gas at 6 bars of pressure for the filtration process. The flux was recorded at 15-minute interval time for 1 hour of duration and the water flux value was measured by using Equation 1.

$$J_w = \frac{Q}{A\Delta T} \quad (1)$$

where, J_w is the pure water flux ($L.m^2.h$), Q is the volume of permeate (L), A is the area of the membrane (m^2), and Δt is the sampling time (h).

Antifouling analysis

The antifouling analysis was performed to determine the antifouling resistance of the membrane and it was carried out through 3 stages at 10 bars of pressure [11]. Humic acid was used as the foulant model. In the first stage, the deionized water was used as the feed solution and the flux was recorded after 30 minutes (J_{w1}). In the second stage, the humic acid solution that consists of 0.2 g of humic acid (HA) in 1 L of 1000 ppm sodium hydroxide (NaOH) was then used as the feed solution, where the permeation was conducted for 120 minutes. Every 20 minutes, the permeate volume was recorded, and the final flux was recorded as J_{HA} . In the third stage, the membrane was backwashed to remove the adsorbed foulant for 30 minutes by immersing it in the deionized water with a stirring speed of 150 rpm. Then, the first step was repeated and the final flux was recorded as J_{w2} . Lastly, the flux recovery ratio (FRR), reversible fouling ratio (RFR), irreversible fouling ratio (IFR), and relative flux decay (RFD) were calculated using the equations below [12]:

$$FRR = \frac{J_{w2}}{J_{w1}} \times 100 \quad (2)$$

$$RFR = \frac{J_{w2} - J_{HA}}{J_{w1}} \times 100 \quad (3)$$

$$IFR = \frac{J_{w1} - J_{w2}}{J_{w1}} \times 100 \quad (4)$$

$$RFD = \frac{J_{w1} - J_{HA}}{J_{w1}} \times 100 \quad (5)$$

Result and Discussion

Membrane characterization

Fourier Transform Infrared Spectroscopy (FTIR)

Figure 1 demonstrates the Fourier Transform Infrared Spectroscopy (FTIR) for all formulated membranes. Based on the figure, the similar peaks existing in

the spectra are illustrating the fingerprint region that composes of polysulfone, polyvinyl alcohol, and chitosan for membrane M1 with an additional peak that corresponds to rice husk ash components for M2, M3, and M4 ranging from 600 cm^{-1} to 1500 cm^{-1} . For the membranes incorporated with sodium silicate from RHA, the crosslinking process resulted in two peaks emergence at 1015 cm^{-1} and 1105 cm^{-1} that was corresponding to the absorption bands from organic siloxane (Si- O- Si) and (Si- O- C) respectively, where these peaks are very intense for the M4 membrane due to the highest crosslinking process involved [5], [13]. For M1, the peak at 1105 cm^{-1} is attributed to the presence of C-O-C from the blended polymer [6]. Membrane M1 also shows the strongest bonds of C=O at 2700 cm^{-1} to 2800 cm^{-1} reflecting that the acetaldehyde group was not completely transformed and it indicates no crosslinking process occurs for pure membrane [14].

The existence of the stretching hydroxyl (O-H) symmetric group appears at 3369 cm^{-1} and 3560 cm^{-1} respectively for all membranes, where strong intensity represents great hydrophilicity of the membrane surface and the anticipated increase in the water permeation performance of the membrane [15]. These bands were attributed to the vibration of hydroxyl groups that bonded to the chitosan, polyvinyl alcohol, and carbon of silica, respectively. For membranes M2 to M4, the stretching vibrations of a secondary amine (N-H) from sodium silicate overlapped with the adsorption band of a hydroxyl group (O-H) at the wavenumber of 3422 cm^{-1} . As a result of crosslinking reaction, the intensity of the peak shows a decreasing trend due to the interaction of silica from sodium silicate with amide and hydroxyl groups of the blended organic polymers [16]. The enhanced integral stability of the membranes was expected to happen as a result of the rapid crosslinking reaction especially on membrane M4 [17].

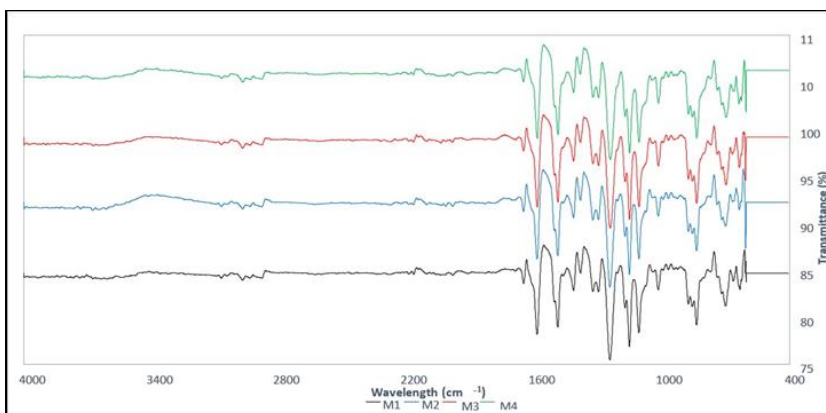
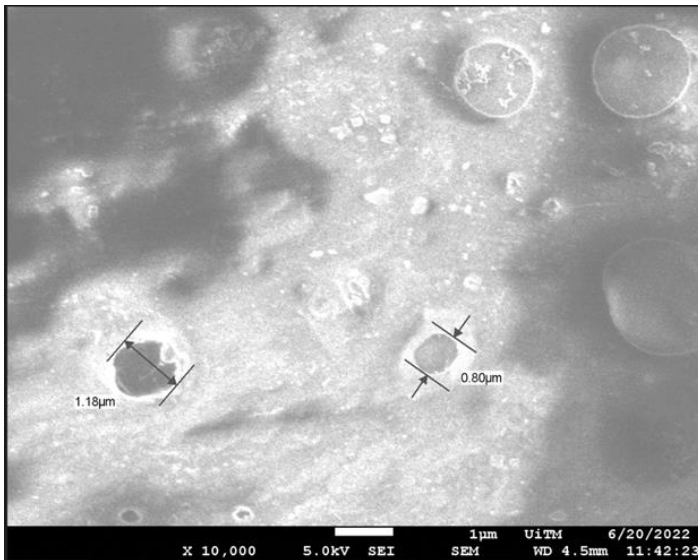


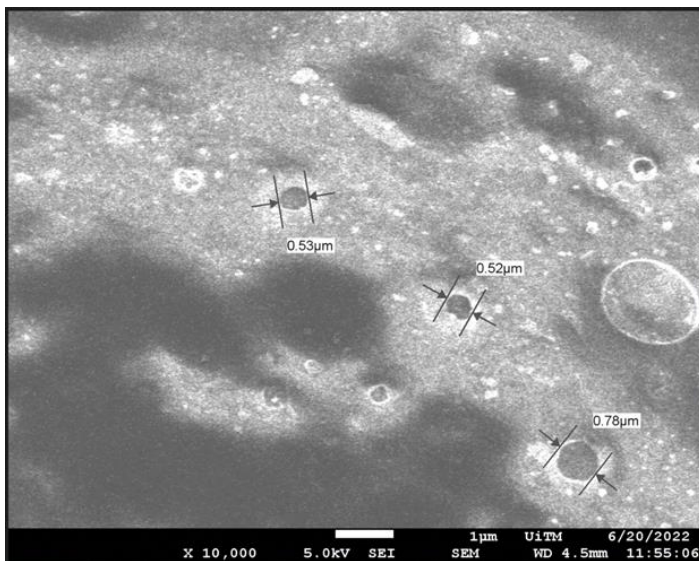
Figure 1: FTIR spectra for membranes

Field Emission Scanning Electron Microscopy (FESEM)

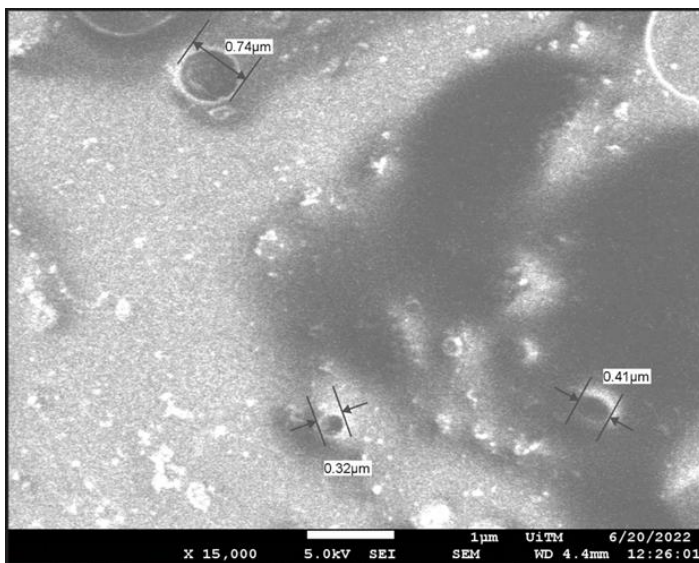
Figure 2 shows the images of the surface morphology of each membrane from FESEM analysis. Based on the images, the pore size of each membrane was extracted and presented in Table 2. As can be seen from the table, the mean pore size of the membrane decreases with the increasing amount of silica incorporated in the membrane. The cross-linking process between the -OH group of the blended polymers with the silica resulted in a dense structure of the membrane with the increment of small finger-like pores on the membrane surfaces. The dense structure provides a significant adsorption area for greater rejection of ions particularly for heavy metal ion rejection as a potential application of the formulated membrane [18]. Furthermore, it can be observed that many microvoids are present in Figures 2b until 2d due to the increased silica content incorporated in the membrane, where it is highly preferable for rejection properties [14]. Besides tightening the surface of the membrane, the addition of silica from RHA has been reported to create high hydrophilicity properties of the membrane [18].



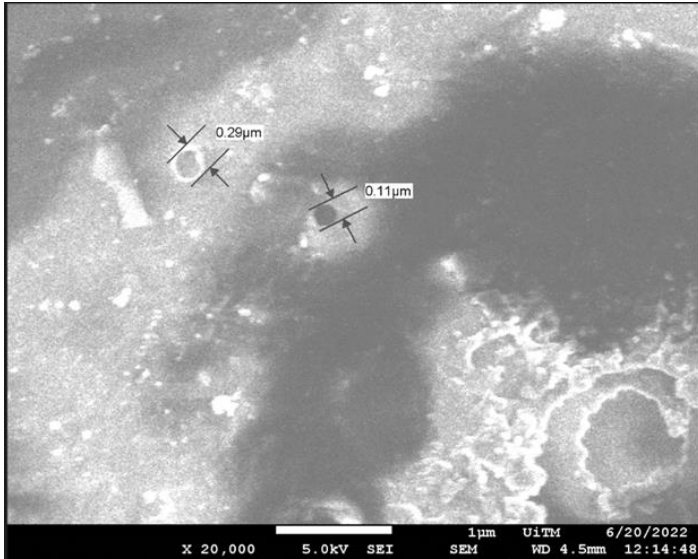
(a)



(b)



(c)



(d)

Figure 2: FESEM images for (a) M1, (b) M2, (c) M3, and (d) M4

Table 2: Formulation of integral membrane

Membrane	Mean pore size
M1	0.99
M2	0.61
M3	0.49
M4	0.20

Performance test

Pure water flux

Figure 3 illustrates the performances of each membrane in pure water flux (PWF) analysis. Based on the figure, the value of permeation flux for M1, M2, and M3 shows a higher flux for the first 30 minutes as compared to M4. However, the fluxes for these three membranes (M1, M2, and M3) declined significantly after 30 minutes while M4 shows a constant flux value throughout the one-hour filtration period. Membrane M4 portrays good surface hydrophilicity that contributes to the antifouling characteristic as less concentration polarization was observed from the plot.

Furthermore, M4 incorporated with the highest concentration of sodium silicate has greater water permeation compared to membrane M1 because the silica itself possesses strong hydrophilicity properties [14]. This hydrophilicity

also corresponds to the amounts of microvoids exhibited on the membrane surface as observed by FESEM because more microvoids will allow greater amounts of water molecules to pass through the membrane.

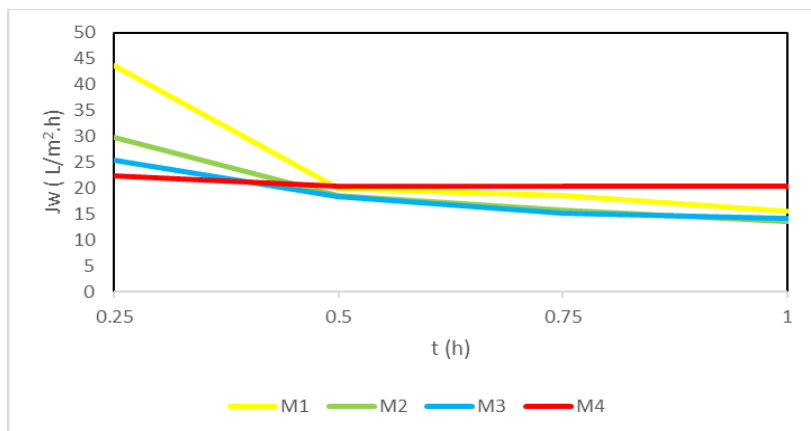


Figure 3: Permeation of pure water for all membrane

Antifouling analysis

Based on Table 3, although all the recorded fluxes for M1 were the highest, it has the lowest FRR and RFR, and the highest RFD and IFR, which show poor antifouling behaviour of the membrane. On the other hand, the flux recovery ratio (FRR) for membranes incorporated with sodium silicate showed higher values with M4 marked as the highest. The flux recovery rate is a vital parameter in the evaluation of antifouling properties because a higher flux recovery rate suggests a better antifouling performance and better hydrophilicity of the membrane, where the preferable value is ranging between 40% to 90 % [19]. It was proven from the obtained result that the membrane with the highest amount of silica shows stronger hydrophilicity properties in the membrane resulting in the highest antifouling ability. The relative flux decay (RFD) shows a declining trend with the increasing amount of incorporated silica inside the membrane. The membrane M4 has the lowest value of RFD which is 66.84%, which further indicates the presence of a hydration layer on the membrane's surface. As for IFR (irreversible flux ratio), it measures the degree of the particles attached to the membrane that causes clogging, which cannot be subsequently removed by the physical cleaning of the membrane unlike the RFR (reversible fouling ratio). As can be observed from the table, the value of RFR decreased with the incorporation of sodium silicate from 5 wt.% to 10 wt.%, indicating a better resistance of the membranes against the fouling exerted by the humic acid. There was a trend shown from the result that when the FRR increases with the incorporation of

sodium silicate, IFR showed a declining trend which indicates the clogging of foulant inside the porous structure of the membrane can be removed easily, particularly for M4. Furthermore, the coarse structure of membranes due to the incorporation of silica also facilitates the removal of the foulant from the membrane by enhancing the internal hydraulic flow across the membrane [20]. Based on the smaller pore size displayed by M4 as shown through FESEM analysis, it will provide a larger area for water permeation through the membrane [21], and most importantly membrane M4 has the best antifouling properties.

Table 3: Antifouling properties of membranes from various formulations

Membrane code	J_{W1}	J_{HA}	J_{W2}	FRR (%)	RFD (%)	RFR (%)	IFR (%)
M1	49	11.4	27	55.10	76.73	31.84	44.90
M2	35	7.5	25	71.43	78.57	50	28.57
M3	23	7.4	17.1	74.35	67.83	42.17	25.65
M4	19	6.3	14.5	76.32	66.84	43.16	23.68

Conclusion

It is apparent from this research that an extraction process of sodium silicate from rice husk ash was successfully conducted. The incorporation of sodium silicate has resulted in the enhanced hydrophilicity and antifouling behaviour of the membranes where membrane M4 with 10 wt.% silica displayed the best performance. These findings have demonstrated the value addition to rice husk as the biomass material and the formulated membranes have the potential to be used for wastewater treatment.

Contributions of Authors

The authors confirm the equal contribution in each part of this work. All authors reviewed and approved the final version of this work.

Funding

This work was supported by the “Geran Penyelidikan Khas” [600-RMC/GPK 5/3 (119/2020), Newly Formulated Positively Charged Thin Film Composite Membrane with Rice Husk Ash As The Cross Linker For Lithium Ions Separation From Lithium-Rich Concentrated Solution, 2020].

Conflict of Interests

All authors declare that they have no conflicts of interest

Acknowledgment

The authors would like to express gratitude to the College of Engineering and Faculty of Applied Sciences, UiTM Shah Alam for providing the laboratories and equipment necessary to conduct this research and carry out the analysis. Thanks to the College of Engineering for the publication sponsorship.

References

- [1] A. Boretti and L. Rosa, "Reassessing the projections of the world water development report," *npj Clean Water*, vol. 2, no. 1, pp. 15, 2019, <https://doi.org/10.1038/s41545-019-0039-9>
- [2] A. Zirehpour, A. Rahimpour, P. M. Vikash, and O. Nazarenko, "Chapter 4: Membranes for wastewater treatment," *Nanostructured Polymer Membranes*, vol. 2, pp. 159-207, 2016, <https://doi.org/10.1002/9781118831823.ch4>
- [3] G. Jianwen, "Membrane separation technology for wastewater treatment and its study progress and development trend," in *Proceedings of the 2016 4th International Conference on Mechanical Materials and Manufacturing Engineering*, Atlantis Press, 2016, <https://doi.org/10.2991/mmme-16.2016.202>
- [4] K. Abuhasel, M. Kchaou, M. Alquraish, Y. Munusamy, and Y. T. Jeng, "Oily wastewater treatment: Overview of conventional and modern methods, challenges, and future opportunities," *Water*, vol. 13, no. 7, pp. 2-35, 2021, <https://doi.org/10.3390/w13070980>
- [5] S. S. Alias, Z. Harun, N. Manoh, and M. R. Jamalludin, "Effects of temperature on rice husk silica ash additive for fouling mitigation by polysulfone-rhs ash mixed-matrix composite membranes," *Polymer Bulletin*, vol. 77, no. 8, pp. 4043-4075, 2020, <https://doi.org/10.1007/s00289-019-02950-5>
- [6] B. E. Sawe, "Top 10 Rice Consuming Countries," *WorldAtlas*, July 27, 2022. [Online]. Available: WorldAtlas, <https://www.worldatlas.com>. [Accessed July 27, 2022].
- [7] A. Aivars and K. Pavel, "Research in some medical plant drying process," in *15th International Scientific Conference Engineering for Rural Development*, 2016, <https://www.tf.llu.lv/conference/proceedings2016/Papers/N227.pdf>

- [8] U. Kalapathy, A. Proctor, and J. Shultz, "A simple method for production of pure silica from rice hull ash," *Bioresource Technology*, vol. 73, no. 3, pp. 257-262, 2000, [https://doi.org/10.1016/S0960-8524\(99\)00127-3](https://doi.org/10.1016/S0960-8524(99)00127-3)
- [9] I. Ounifi, Y. Guesmi, C. Ursino, S. Santoro, S. Mahfoudhi, A. Figoli, E. Ferjanie, and A. Hafiane, "Antifouling membranes based on cellulose acetate (CA) blended with poly(acrylic acid) for heavy metal remediation," *Applied Sciences*, vol. 11, no. 10, pp. 4354, 2021, <https://doi.org/10.3390/app11104354>
- [10] Z. Nur Saadah, M. Zaleha, M. Mohammad Sukri, B. Nur Azam, and Z. Abdullah Zulfairis, "The ability of crystalline and amorphous silica from rice husk ash to perform quality hardness for ceramic water filtration membrane," *International Journal of Integrated Engineering*, vol. 11, no. 5, pp. 229-235, 2019, <https://doi.org/10.30880/ijie.2019.11.05.029>
- [11] H. Etemadi, R. Yegani, M. Seyfollahi, and M. Rabiee, "Synthesis, characterization, and anti-fouling properties of cellulose acetate/polyethylene glycol-grafted nanodiamond nanocomposite membranes for humic acid removal from contaminated water," *Iranian Polymer Journal*, vol. 27, no. 6, pp. 381-393, 2018, <https://doi.org/10.1007/s13726-018-0616-7>
- [12] K. S. Norin Zamiah, R. Lydia Hannah, and B. Muhammad Faiz, "Synthesis and evaluation of polysulfone/chitosan/polyvinyl alcohol integral composite membranes for the removal of mercury ion," *EVERGREEN Joint Journal of Novel Carbon Resource Sciences & Green Asia Strategy*, vol. 8, no. 2, pp. 484-491, 2021, <http://doi.org/10.5109/4480733>
- [13] X. Yang, P. Roonasi, and A. Holmgren, "A study of sodium silicate in aqueous solution and sorbed by synthetic magnetite using in situ ATR-FTIR spectroscopy," *Journal of colloid and interface science*, vol. 328, no. 1, pp. 41-47, 2008, <http://doi.org/10.1016/j.jcis.2008.08.061>
- [14] Y. Huang, J. Fu, X. Huang, and X. Tang, "Characterization of poly(vinyl alcohol) membranes cross-linked by aldehyde-substituting cyclotriphosphazene," *Journal of Macromolecular Science Part B*, vol. 48, no. 5, pp. 941-954, 2009, <http://doi.org/10.1080/00222340903029066>
- [15] B. D. N. Asep, O. Rosi, and R. Risti, "How to read and interpret FTIR spectroscopy of organic material," *Indonesian Journal of Science & Technology*, vol. 4, no. 1, pp. 97-118, 2019, <http://doi.org/10.17509/ijost.v4i1.15806>
- [16] R. Nurshahida, M. S. Mohd Nazri, F. H. A. Muhammad Ikmal, A. Nor Asikin, and M. R. Norhana, "Chitosan/silica composite membrane: Performance on water permeability and rejection of lead(II) ion from aqueous solution," *Malaysian Journal of Fundamental and Applied Sciences*, vol. 10, no. 3, pp. 314-317, 2020, <http://doi.org/10.11113/mjfas.v16n3.1489>

- [17] L. Zhang, "Infrared spectroscopic study of cross-linked polyamines for CO₂ separation," in *The University of Akron*, 2013.
- [18] M. Jamalludin, Z. Harun, S. Hubadillah, H. Basri, A. Ismail, M. H. Othman, M. Shohur, and M. Yunus, "Antifouling polysulfone membranes blended with green SiO₂ from rice husk ash (RHA) for humic acid separation," *Chemical Engineering Research and Design*, vol. 114, no., pp. 268-279, 2016, <http://doi.org/10.1016/j.cherd.2016.08.023>
- [19] J. Yin, "Fabrication of a modified polyethersulfone membrane with anti-fouling and self-cleaning properties from SiO₂-g-PHEMA NPs for application in oil/water separation," *Polymers*, vol. 14, no. 11, pp. 2169, 2022, <https://doi.org/10.3390/polym14112169>
- [20] S. Saberi, A. A. Shamsabadi, M. Shahrooz, M. Sadeghi, and M. Soroush, "Improving the transport and antifouling properties of poly(vinyl chloride) hollow-fiber ultrafiltration membranes by incorporating silica nanoparticles," *ACS Omega*, vol. 3, no. 12, pp. 17439-17446, 2018, <https://doi.org/10.1021/acsomega.8b02211>
- [21] S. A. Naziri Mehrabani, B. Keskin, S. Arefi-Oskoui, I. Koyuncu, V. Vatanpour, Y. Orooji, and A. Khataee, "Ti₂AlN MAX phase as a modifier of cellulose acetate membrane for improving antifouling and permeability properties," *Carbohydrate Polymers*, vol. 298, pp. 120114, 2022, <https://doi.org/10.1016/j.carbpol.2022.120114>

Investigation on Surface Roughness and MRR in WEDM of Titanium Grade 7 (Ti-0.15Pd) Alloy using Statistical Techniques

H. R. Basavaraju, S. S. Manjunatha

Department of Mechanical Engineering, Government Engineering College,
Haveri-581110, Karnataka, INDIA

R. Suresh *

Department of Mechanical and Manufacturing Engineering,
M.S. Ramaiah University of Applied Sciences,
Bangalore- 560058, Karnataka, INDIA
*sureshchiru09@gmail.com

ABSTRACT

Wire Electric Discharge Machining (WEDM) of Titanium grade alloys with coated electrodes has several advantages over the traditional machining process such as increased productivity, reduction of processing cost, and improved material properties. The main objective is to create a relationship between WEDM parameters such as Pulse-on (T_{ON}), Pulse-off (T_{OFF}), and Indicated Power (IP) with surface roughness (R_a) and Material Removal Rate (MRR). In the present work, the performance of zinc-coated brass electrodes for WEDM of Titanium Grade-7 alloy was assessed and optimized with statistical technique. ANOVA analysis is used to analysis of the MRR and R_a and validated with regression. The ANOVA analysis results indicated that T_{ON} is the highest statistically significant and followed by T_{OFF} and IP on MRR and surface roughness. The optimum combination of higher IP(6 A) and T_{ON} time(60 μ s) and lower T_{OFF} time (12 μ s) is lucrative for a higher MRR of 8.5682 mm³/min and lower surface roughness of 1.66 μ m. The SEM images showed homogeneous solidification, columnar grain structure, recast layer surface, and minor surface crack density were noticed at higher cutting conditions. The predicted model and confirmation test results were close to each other with minimum error (<5%), so the model is adequate.

Keywords: Wire EDM; Titanium Grade 7 Alloy; T_{ON} ; T_{OFF} ; IP; MRR; Surface Integrity; Surface Roughness

Introduction

Titanium (Ti) based alloys are having excellent physical and mechanical properties including strength-to-weight ratio, corrosion, and wear resistance. These alloys are the best material choice for many applications like space crafts, aerospace, automotive, nuclear, sports, chemical plant, and medical applications. However, these alloys are challenging to cutting by regular conventional machining process due to high thermal resistance accelerates to tool wear, and induces residual stress and oxidation on the machined surface. Certain advanced machining methods like laser cutting and electric discharge machining are suitable in cutting high-strength alloys. During the machining of advanced alloy materials, surface integrity is one of the significant parameters for assessing the surface integrity of finished components. Besides, surface, and subsurface alterations, micro/macro cracks, machining burns (heat affect zone), surface cavities, material side flow, residual stress, fatigue strength and stress corrosion factors are serious issues due to safety aspect and also sustainability concerns [1]-[4].

Various researchers have employed the WEDM process to study the machinability characteristics of Ti alloys under different cutting conditions and optimized the process parameters through mathematical models [5]-[8]. Ramamurthy et al. [6] illustrated that surface roughness decreased with increased pulse-on-time duration and discharge/peak current during WEDM of Ti alloy. Prakash et al. [7] deliberated the impact of WEDM factors and Ti-Nb electrode material on surface modification during Ti alloy processing. The authors detected that the machined surface roughness has considerably reduced by a trim cut strategy during WEDM of titanium alloy. Devarasiddappa et al. [8] examined the effect of pulse-off time, pulse-on time, peak current, and wire speed on WEDM of titanium alloy with reusable wire electrode using modified teaching learning-based optimization method. The authors noticed reduced surface roughness values at settings of higher peak current and lower T_{ON} time. Debnath and Patowari [9] recommended a mathematical model and test analysis to find the impact of machining parameters on surface and sub-surface characteristics of Ti alloys based micro-fins fabrication using the WEDM process. They revealed that the pulse time, current intensity, and duty cycle shows substantial outcome on surface superiority.

Pramanik et al. [10] evaluated the dimensional accuracy of WEDM-processed Ti alloy parts. They showed that the lower peak current and higher pulse-on-time aid to improve machined surface quality. Also, proposed that the choice of machining parameters are precise in the cutting of Ti alloys. Gohil [11] examined the EDM of Ti-6Al-4V alloy with various cutting

parameters using mathematical models. They observed that the recast layer formed was prejudiced by higher pulse duration, discharge current, and spark energy. The authors demonstrated that the peak current and pulse-on time considerably influences surface roughness and MRR. Torres et al. [12] measured the surface and sub-surface modifications in WEDM of hard-to-machine alloys with zinc and brass wire electrodes. The obtained results demonstrated the significant influence of wire feed and single pulse discharge energy on machined surface quality.

Tonday et al. [13] analysed the machining parameters effect on MRR and surface integrity during WEDM of Ti-based alloy with copper electrode. The authors observed that the discharge current is the most vital parameter on machined surface characteristics and MRR. Thus, to enhance machinability characteristics and productivity of the EDM process, continuous pulsation and higher peak current are very important [14]-[16]. However, better-machined surface integrity characteristic is much essential for preventive maintenance and better product performance. The surface topography of components encompasses surface and sub-surface alterations, microhardness, residual stress distribution, and recast layer. Compared to the bulk material, recast layer have a dramatic drop in surface hardness. It is due to considerable thermal degradation of the machined components [17]-[20].

Gupth et al. [21] studied the effect of wire feed speed, wire tension, and servo voltage on surface roughness and cutting speed in the machining of pure and heat-treated Ti-6Al-4V alloy using Response Surface Methodology (RSM). The analysis results indicate the wire tension and servo voltage were the highest impact on surface roughness of and cutting speed of 1.75 mm/min during machining of annealed Ti-6Al-4V alloy when compared to other heat-treated Ti-6Al-4V alloy. Thangaraj et al. [22] optimized the WEDM process parameters on surface quality during the machining of titanium alloy using Taguchi–Grey analysis-based (TGRA) method. The analysis results show the best input parameters combination in attaining optimal surface measures such as discharge current (15 A), gap voltage (70 V), and duty factor (0.6) when the WEDM process of titanium. The authors also suggested that the selection of wire electrodes and dielectric fluid are most influential on the surface quality in the machining of titanium, due to its importance in creating the spark energy. Similar results can be found elsewhere [23]-[26].

The above literature review reveals that the work carried out on the effect of WEDM process parameters on MRR and Surface roughness in machining Ti grade 7 alloy is minimum using zinc-coated brass wire electrodes. The study reported herein is continuing effort to examine cutting parameters effect on productivity enhancement and quality of surface during WEDM of titanium-based alloy using statistical techniques. The current work aims to study the influence of process parameters on surface roughness and MRR during titanium grade 7 alloy with Zn-coated brass wire electrode machining of using the design of experiments technique (L_{27} orthogonal array).

The surface and sub-surface discrepancies occur with WEDM of titanium grade 7 alloy using scanning electron microscopy (SEM) analysis.

Experimentation

Material and methodology

Titanium (Ti) grade 7 alloy is the material of research interest in recent years due to its extensive use in a chemical plant, marine, medical and aerospace, desalination, brine concentration/evaporation equipment, and pulp/paper bleaching/washing equipment, hydrometallurgical extraction applications. The composition of the grade 7 alloy and its mechanical properties are illustrated in Tables 1 and 2, respectively. The high yield strength and tensile strength of Titanium grade 7 make it a more suitable material for applications where strength is critical. The elongation property allows it to withstand stress and deformation without fracturing, suitable for high-temperature applications. Titanium grade 7 alloy size of 20x20x100 mm³ was used as workpiece material, which was pre-machined by CNC Wire-EDM using an appropriate sequence of cuts including roughing and finishing cut. The tests were carried out using the 'CONCORD CNC WEDM', Model: DK-7732VC, which controlled input process parameters to be selected from a restricted level of potential values. The wire EDM machining process was carried out with a diameter of 0.25 mm zinc (Zn) coated brass wire electrode for WEDM processing of Titanium grade 7 alloy. Zinc liquefies at a lower temperature than brass and absorbs heat as it boils away. As a result, less heat enters the wire to retain its strength. Coated wire typically enhances material removal by 10 to 15 percent. Coated wire usually comes in three grades, hard, semi-hard, and soft. Hard wires are used for machining when high tensile strength is required. Soft brass wires are typically used while cutting tapers [20]. The properties of brass wire with Zn-coated electrode are in Table 3.

Test trials were accompanied by different levels of the peak current (IP), pulse-off time (T_{OFF}), and pulse-on time (T_{ON}) during WEDM processing of Ti grade 7 alloy. Some parameters of wire EDM such as wire tension, wire speed, and servo control voltage were maintained as default machine settings. Some studies have been done on surface roughness (*Ra*) and material removal rate (MRR) in WEDM using brass wire-coated zinc as electrode. Owing to its fast-cooling rate and low viscosity, WEDM uses deionized water as an alternative to hydrocarbon oil as the dielectric fluid. The WEDM setup and employed samples are presented in Figure 1.

Table 1: Chemical composition (weight %) of Ti grade 7 alloy

Fe	O	C	N	H	Pd	Ti
0.30	0.25	0.08	0.03	0.015	0.15	Bal.

Table 2: Mechanical properties of Ti grade 7 alloy

Tensile strength, ultimate (MPa)	Yield strength (MPa)	Modulus of elasticity (GPa)	Elongation (%) at break	Shear modulus (GPa)	Rockwell hardness (HRB)
344	375	105	20	45	75

Table 3: Electrode material properties

Wire material	Zn-coated brass wire
Tensile strength	900 N/mm ²
Wire grade	A1 Hard
Wire diameter	0.25 mm



Figure 1: Working setup of WEDM machining process and machined samples

Experimental design

In this work, three process parameters T_{OFF} time, T_{ON} time, and IP were considered for wire EDM machining. The process parameters and their levels are illustrated in Table 4. They were chosen considering material properties and suggestions taken from EDM machine experts. The MRR is reliant on the

various input parameters which affects the productivity of any process. The experimental plan was employed as per Taguchi’s experimental design (L₂₇ Orthogonal Array) using Minitab-17 software. It aids to capture experimental response data in a systematic manner. The L₂₇ orthogonal array and responses like surface roughness and MRR are tabulated in Table 5. The shape machined by WEDM was 20x20x5 mm³ in thickness. The tests were carried out for each trial 2 times and the average response reading was considered for analysis. The machined surface roughness was determined using a roughness tester (‘Model: SJ201; Make: Mitutoyo’) and surface morphology analysis was carried out with SEM images. The MRR is measured using the relation in Equation 1.

$$MRR = \frac{\text{Volume of material removed}}{\text{Machining time}} \quad (1)$$

Table 4: Parameters and their levels considered in the study

Sl. No.	Description	Level 1	Level 2	Level 3
1	T _{ON} (μs)	20	40	60
2	T _{OFF} (μs)	10	14	18
3	IP (A)	2	4	6

Results and Discussion

The MRR and surface roughness (*Ra*) are major parameters that affect the quality and throughput of any production industry. MRR represents the total workpiece material volume removed within a unit working time. It indicates the machinability efficiency of the production machine. Correspondingly, surface roughness also has significant effects on the performance of WEDM machined parts. In general, the surface quality is measured as the average surface roughness (*Ra*) of machined parts [2], [27]-[28]. In addition, machinability characteristics are influenced by the type of electrode, work contact, dielectric fluid supply, accuracy, friction, and deformation.

In the present study, titanium grade 7 alloy was machined by WEDM at different machining conditions, and statistical analysis was supported and correlated with the assistance of a regression model. In the second half, enumerate the integrity of the machined surface such as process parameters that define the surface morphology and modifications on the machined components were discussed with SEM images.

Table 5: Orthogonal array (L_{27}) and obtained results

Sl. no.	T_{ON} (μs)	T_{OFF} (μs)	IP (A)	MRR (mm^3/min)	Surface roughness (Ra), μm
1	20	12	2	7.1221	2.146
2	20	12	4	7.9026	2.281
3	20	12	6	8.7630	2.493
4	20	16	2	7.0346	2.964
5	20	16	4	7.3682	2.130
6	20	16	6	7.4214	2.655
7	20	20	2	6.9842	2.872
8	20	20	4	7.1256	2.894
9	20	20	6	7.5682	2.869
10	40	12	2	7.4568	1.623
11	40	12	4	8.3850	1.884
12	40	12	6	8.8346	1.967
13	40	16	2	6.9824	2.142
14	40	16	4	6.9024	2.467
15	40	16	6	7.5248	2.566
16	40	20	2	6.9246	2.737
17	40	20	4	7.5728	2.904
18	40	20	6	8.1282	2.957
19	60	12	2	8.1456	1.912
20	60	12	4	8.5682	1.667
21	60	12	6	8.9412	1.846
22	60	16	2	8.1236	1.765
23	60	16	4	8.5248	2.162
24	60	16	6	9.3846	2.257
25	60	20	2	9.1264	1.396
26	60	20	4	9.3346	1.862
27	60	20	6	9.9624	2.134

Statistical analysis

The obtained results were evaluated through analysis of variance of MRR and Ra as illustrated in Tables 6 and 7, respectively. The analysis of variance (ANOVA) demonstrates that existing statistical models are viable for the prediction of surface roughness and MRR at a 95% confidence level. The experimental results were examined for the identification of influencing parameters on MRR and surface roughness with a confidence level of 95%. The attained results are established by using main effects plots for mean and

normal probability plots. Interaction terms of cutting parameters were included in the assessment [14], [20].

Table 6: ANOVA of MRR

Parameters	DOF	SS	MS	F	Test F	% of contribution
Pulse-on (μs)	2	16.386	8.194	120.75	8.66a	58.81
Pulse-off (μs)	2	3.627	1.815	26.73	8.66a	12.64
Peak current (A)	2	5.183	2.593	38.20	8.66a	18.23
Pulse-on * Pulse-off	4	1.444	0.362	5.32	3.85b	4.26
Pulse-on * peak current	4	0.409	0.103	1.52	--	0.00
Pulse-off * peak current	4	0.051	0.014	0.19	--	0.00
Residual error	8	0.543	0.067			6.06
Total	26	27.65				100.00

* SS = Sum of squares; DOF = degree of freedom; MS= Mean Square; Test F=Fisher's Value; a 99% Confidence; b 95% Confidence; %C = percentage of contribution

Table 7: ANOVA of surface roughness

Parameters	DOF	SS	MS	F	Test F	% of contribution
Pulse-on (μs)	2	2.598	1.304	306.530	8.66a	33.20
Pulse-off (μs)	2	2.843	1.419	333.520	8.66a	36.11
Peak current	2	0.150	0.073	17.140	8.65a	6.75
Pulse-on * Pulse-off	4	2.141	0.534	125.610	8.66a	22.09
Pulse-on * Peak current	4	0.063	0.016	3.850	3.85b	0.00
Pulse-off * Peak current	4	0.004	0.001	0.210	--	0.00
Residual error	8	0.033	0.004			1.85
Total	26	7.834				100

* SS = Sum of squares; DOF = degree of freedom; MS= Mean Square; Test F=Fisher's Value; a 99% Confidence; b 95% Confidence; %C = percentage of contribution

The ANOVA analysis of MRR for WEDM of Ti grade 7 alloy is presented in Table 6. It revealed that the effects of T_{OFF} time, T_{ON} time, and peak current are the highest statistical significance. The interaction effect between $T_{\text{ON}}*T_{\text{OFF}}$ is partially significant, while other interaction effects of

parameters are insignificant. The obtained results indicated the significance of T_{ON} on MRR during WEDM process of Ti grade 7 alloy is greater (58.81%) followed by IP (18.23%) and T_{OFF} (12.64 %) (Table 6). Whereas, ANOVA of surface roughness has shown that effects of peak current, pulse-on, and the interaction effect between T_{OFF} * T_{ON} are statistically significant and are shown in Table 7. The T_{OFF} is the highest (36.11%) significance on surface roughness trailed by T_{ON} (33.20 %), T_{OFF} * T_{ON} (22.09%), and IP (6.75%). Besides, the impact of T_{ON} *IP and T_{OFF} *IP was found insignificant.

Figures 2 and 3 correspondingly illustrate main effects plots for the mean for MRR and Ra . It indicates that MRR was found to enhance with increased levels of T_{ON} , while Ra was found to diminish. Whereas the upsurge of T_{OFF} has caused the decrease of MRR initially, a further increase of T_{OFF} from level 2 to level 3 has led to greater value of MRR value (Figure 2). However, surface roughness and MRR were increased with increased peak current values. The reason is that significant energy is supplied when the IP with sufficient T_{ON} time was increased to maximum. Thereby, it influences on the cutting speed. Consequently, increase in large discharge energy in turn improves drastically MRR. It indicates that the MRR was found to be greater in the combination of the upper level of IP and T_{ON} . Based on the above discussion, it can be revealed that the maximum MRR can be obtained using positive polarity of electrode. It suggests that positive polarity of the electrode and dielectric fluid are favored for the machining of titanium grade 7 alloy using WEDM process. Similar experimental results were found by other researchers [10], [12]-[13].

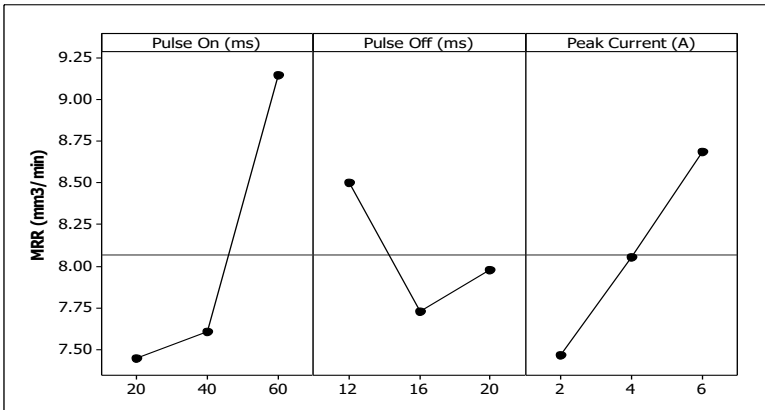


Figure 2: Main effects plot illustrating effect of individual process parameters on MRR

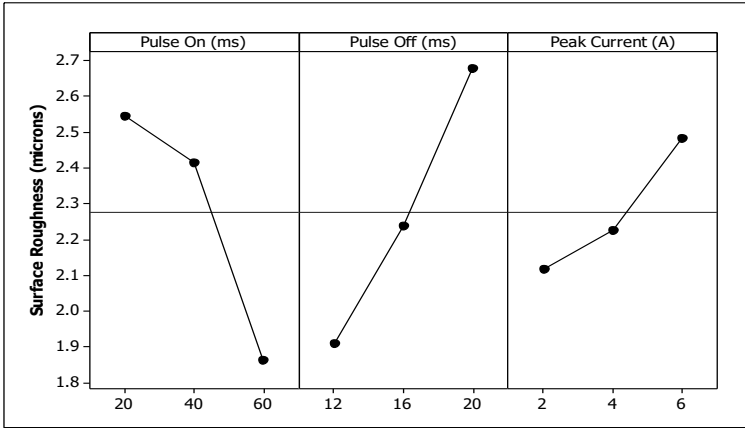


Figure 3: Main effects plot illustrating the effect of individual process parameters on surface roughness

The regression models represent an established correlation between WEDM parameters with responses like MRR and R_a . Consequently, obtained regression models of MRR and R_a are presented as Equations 2 and 3, respectively. The R -Sq and R -Sq(Adj.) values of developed models are greater than 89%, also the difference between R -Sq and R -Sq(pred.) is within 20%. Therefore, it can be inferred that established models are feasible and adequate to predict responses within the studied range of parameters.

$$MRR (mm^3/min) = 18.76 - 0.466 * Pulse-On - 0.998 * Pulse-Off + 0.5356 * Peak Current + 0.00812 * Pulse-On * Pulse-On + 0.03155 * Pulse-Off * Pulse-Off + 0.00482 * Pulse-On * Pulse-Off \quad (2)$$

R-sq(adj)- 91.75%; R-sq-93.60% and R-sq(pred)- 88.05%

$$R_a (\mu m) = -3.222 + 0.1363 * Pulse-On + 0.4549 * Pulse-Off + 0.0889 * Peak Current - 0.001378 * Pulse-On * Pulse-On - 0.00619 * Pulse-Off * Pulse-Off - 0.00717 * Pulse-On * Pulse-Off \quad (3)$$

R-sq(adj.):89.70%; R-sq:92.40% and R-sq(pred.):84.15%

The normal probability plots and Anderson–Darling test of residuals versus predicted response for MRR and R_a is shown as Figure 4 and Figure 5, respectively. The test values of responses (MRR and R_a) are normally distributed on the 45° line. It explains that the P-value is higher than the alpha (α) with a significance level of 0.05 and the null hypothesis cannot be rejected. Hence, data recorded from the established setup is rationally good agreement

with adequate range. Also, it confirms that the employed statistical method is adequate as shown in Figure 4 and Figure 5. Further, it is a typical model to predict WEDM process parameters for Ti grade 7 alloy.

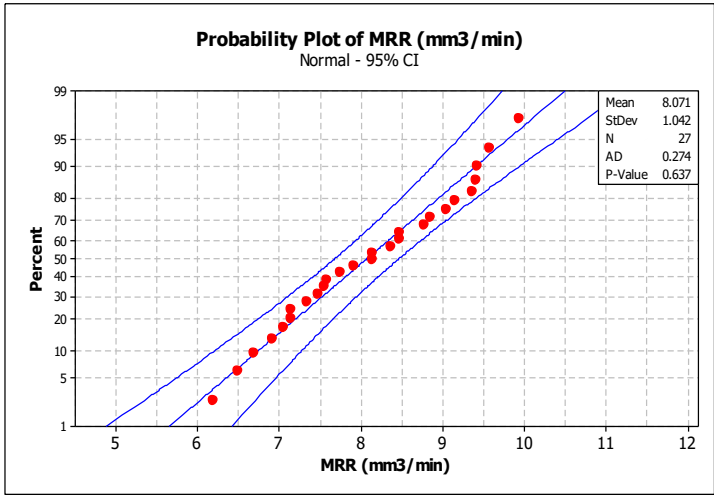


Figure 4: Probability plot for MRR

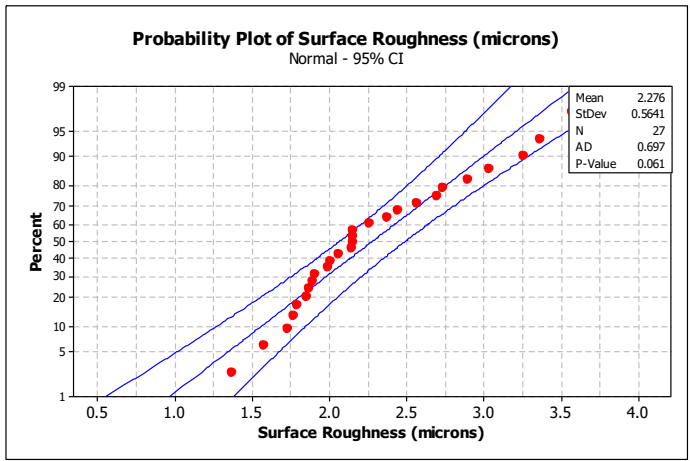


Figure 5: Probability plot for surface roughness

Confirmation test results

For validation purposes, new experimental trials were conducted with Ti grade 7 alloy during the WEDM process. The new WEDM parameters used for confirmation tests are shown in Table 8. Table 9 shows the experimental results attained where a comparison was done between the expected values from the developed regression models (Equation 2 and Equation 3) with new experimental trials. From the comparison analysis of Table 9, it is observed that the intended error for MRR (maximum of 2.204% and minimum of 1.68%) and surface roughness (maximum of 5.965% and a minimum of 4.142%). Therefore, MRR and surface roughness with the WEDM parameters with rational degrees of estimate.

Table 8: Experimental trials for comparison tests

Trials no.	New trials	T _{ON} (μs)	T _{OFF} (μs)	IP (A)
1	A	30	12	3
2	B	50	16	5

Table 9: Experimental results compared with regression model results

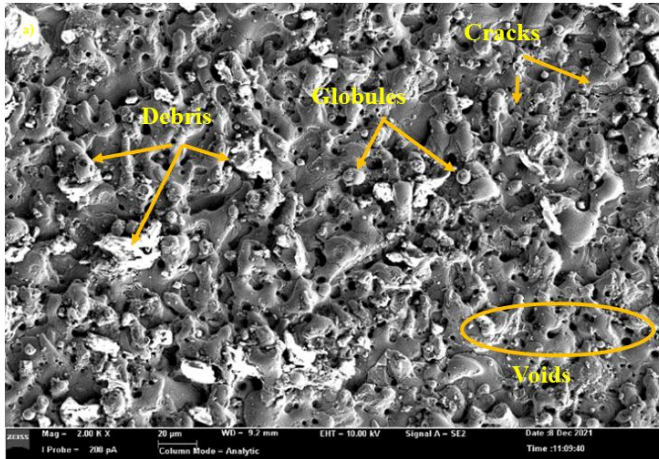
Sl. No.	Trials	Model results	Experimental results	% of error
1. MRR (mm ³ /min)				
	A	7.6972	7.5680	1.680
	B	8.928	9.1248	2.204
2. Surface roughness (Ra), μm				
	A	2.548	2.70	5.965
	B	1.69	1.76	4.142

Surface integrity assessment

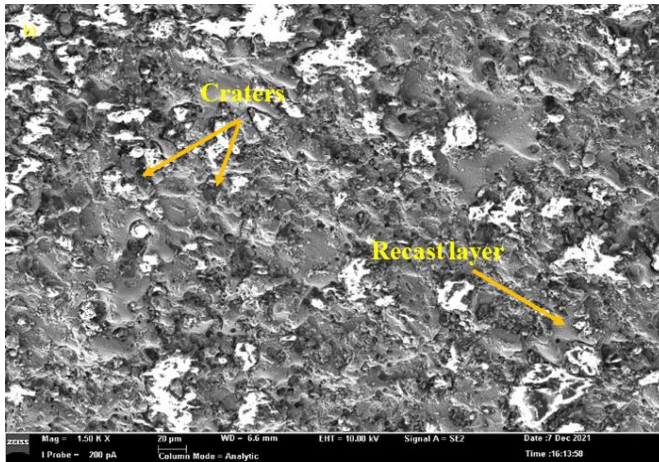
Surface quality is an important machining aspect, which signifies the performance and reliability of the products. In such cases, surface integrity is essential and is exaggerated by the machining process with surface and subsurface degradation. The surface integrity includes surface topography, recast layer formation, and stresses distributions on the machined components. Especially, the wire EDM process is inevitable for improved surface quality and greater throughput in industrial sectors.

Figure 6 demonstrates SEM images of WEDMed surface of Ti grade 7 alloy at various considered WEDM parameters. The description of SEM images indicates experimental results obtained for minimum *Ra* and maximum MRR attained machining conditions. The optimized parametric results and SEM image demonstrated in Figure 6a reveals the surface alterations at a pulse-off time of 12 μs, pulse-on time of 40 μs, and peak current of 6 amps. It is noticed that topography of surface defects like globules, micron-size cracks,

and voids as well as recast layers on machined surfaces. It depicts the machined surface produced at high IP and low T_{ON} time settings succeeding in maximum MRR. It may be because residual gases are produced and tend to get entrapped on the metal surface [21]-[22]. While these entrapped gases try to escape, they, initiate defects like bubbles, micro voids, and micro cracks.



(a)



(b)

Figure 6: SEM images show the machined surface of titanium grade 7 alloy at (a) $T_{on} = 40 \mu s$, $T_{off} = 12 \mu s$ and peak current = 6 A, and (b) $T_{on} = 60 \mu s$, $T_{off} = 12 \mu s$ and peak current = 2 amps

Similarly, SEM micrographs demonstrated in Figure 6b show a smooth surface free from craters, voids, and cracks at T_{OFF} time of 12 μ s, T_{ON} time of 60 μ s, and peak current of 2 amps. However, a limited amount of debris, globules, and minor cracks of recasted metal could be comprehended. It describes that the surface roughness is commensurate to high T_{ON} time with low IP. As peak current increases, increased energy discharged creates a large amount of molten materials. It further transforms into globules resulting in better surface finish. Also, the presence of slight cracks is apparent owing to impinging higher energy sparks over machined surface. Similar experimental results were found by other researchers [8], [18]-[19].

The cross-sectional SEM microstructure reveals the amount of recast layer corresponding to WEDM parameters depicted in Figure 7. Besides, recast layer thickness in case of T_{ON} time of 40 μ s, T_{OFF} time of 12 μ s, and IP of 6 A is shown in Figure 7a. In addition, MRR has increased with increased pulse-on, while Ra has decreased. As the T_{ON} time increased to 60 μ s, the T_{OFF} time of 12 μ s and IP of 2 A is depicted in Figure 7b. The surface roughness decreased with increased pulse-on time. However, the recast layer thickness decreased as a result of reduced peak current. It shows that a lower peak current causes less molten material and re-solidification. At the same time, it depicts the lower MRR. It can be concluded that higher T_{ON} time, lower T_{OFF} time, and IP are recommended for WED machining of Ti grade 7 alloy.

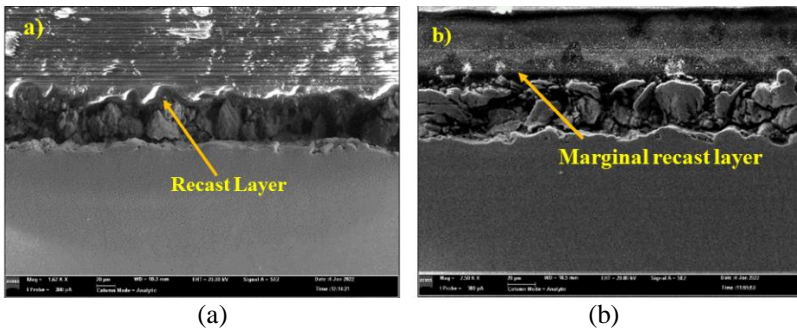


Figure 7: Cross section SEM surface of WEDM machined surface of titanium grade 7 alloy at (a) $T_{on} = 40 \mu$ s, $T_{off} = 12 \mu$ s and peak current = 6 A, and (b) $T_{on} = 60 \mu$ s, $T_{off} = 12 \mu$ s and peak current = 2 amps

Conclusions

The current experimental study was made to assess the WEDM parameters on surface roughness and MRR during Ti grade 7 alloy machining. The following

conclusions were drawn from the experimentation and successive statistical analysis.

- The experimental results indicate the MRR is strongly influenced by pulse-on time (T_{ON}) and peak current (IP). It owes maximum discharge energy at greater levels of T_{ON} and IP.
- The pulse-off (T_{OFF}) time is highly significant (58.81%) on MRR followed by IP (18.23%) and T_{ON} time (12.64 %)
- The T_{OFF} time is highly significant (36.11%) on surface roughness trailed by T_{ON} time (33.20 %), $T_{OFF} * T_{ON}$ (22.09%), and IP (6.75%).
- The material removal rate decreases as the T_{OFF} time increases due to reduced spark discharges in a certain duration.
- Surface quality significantly worsens with the increase in peak current due to high discharge energy affecting the surface quality and creating more cracks, globules, microvoids, and craters on the machined surface.
- Surface defects reduce with lower peak current (IP) and higher T_{ON} time. It is due to low discharge energy producing fine microstructure surfaces.
- Cross-sectioned SEM images indicate the minimum recast layer thickness at higher T_{ON} time with lower T_{OFF} time.
- Cross-sectioned SEM images indicate the minimum recast layer thickness at higher T_{ON} time with lower T_{OFF} time.
- The predicted model results and confirmation test results were close to each other with minimum error (< 5%), so the model is adequate.

Contributions of Authors

The authors confirm the equal contribution in each part of this work. All the authors together reviewed and approved the final version of this work.

Funding

This work received no specific grant from any funding agency.

Conflict of Interests

All authors declare that they have no conflicts of interest.

Acknowledgment

The authors are grateful to M.S. Ramaiah University of Applied Sciences, Bangalore, India for providing assistance to carry out our experiments in their facility.

References

- [1] A.Pramanik, “Problems and Solutions in Machining of Titanium Alloys”, *International Journal of Advanced Manufacturing Technology*, vol. 70, no. 5–8, pp. 919–928, 2014, doi: 10.1007/s00170-013-5326-x.
- [2] M. D. Moses, M. P. Jahan, “Micro-EDM Machinability of Difficult-To-Cut Ti-6Al-4V against Soft Brass”, *International Journal of Advanced Manufacturing Technology*, vol. 81, no. 5, pp. 1345–1361, 2015, doi: 10.1007/s00170-015-7306-9.
- [3] A.R. Khan, M.M Rahman, K. Kadirgama, “An experimental investigation on surface finish in die-sinking EDM of Ti-5Al-2.5Sn”, *International Journal of Advanced Manufacturing Technology*, vol. 77, pp. 1727–1740, 2015.
- [4] K. Mouralova, J. Kovar, L. Klakurkova, P. Blazik, M. Kalivoda, P. Kousal, “Analysis of Surface and Subsurface Layers after WEDM for Ti-6Al-4V with Heat Treatment”, *Measurement*, vol.116, pp. 556–564, 2018, doi: 10.1016/j.measurement.2017.11.053.
- [5] M.S. Kishore Kumar, B. Gurudatt, Reddappa H.N, R. Suresh, “Parametric Optimization of Cutting Parameters for Micro-Machining of Titanium Grade-12 Alloy Using Statistical Techniques”, *International Journal of Lightweight Materials and Manufacture*, vol. 5, no. 1, pp. 74-83, 2022, <http://doi.org/10.1016/j.ijlmm.2021.10.003>
- [6] A. Ramamurthy, R. Sivaramakrishnan, T. Muthuramalingam, S. Venugopal, “Performance Analysis of Wire Electrodes on Machining Ti-6Al-4V Alloy using Electrical Discharge Machining Process”, *Machining Science and Technology*, vol. 19. no. 4, pp. 577–592, 2015, doi:10.1080/10910344.2015.1085314.
- [7] C. Prakash, S. Singh, C. I. Pruncu, V. Mishra, G. Królczyk, D. Y. Pimenov, Pramanik, A., “Surface Modification of Ti-6Al-4V Alloy by Electrical Discharge Coating Process Using Partially Sintered Ti-Nb Electrode,” *Materials*, vol. 12, no. 7, pp. 1006-12, 2019. DOI: 10.3390/ma12091564.
- [8] D. Devarasiddappa, M. Chandrasekaran, Arunachalam, R. “Experimental Investigation and Parametric Optimization for Minimizing Surface Roughness during WEDM of Ti6Al4V Alloy Using Modified TLBO Algorithm”, *Journal of the Brazilian Society of Mechanical Sciences and*

- Engineering*, vol. 42, no. 3, pp.128–145, 2020, doi: 10.1007/s40430-020-2224-7.
- [9] T. Debnath, P. K. Patowari, “Fabrication of an Array of Micro-Fins Using Wire-EDM and Its Parametric Analysis”, *Material Manufacturing Processes*, vol. 34, no. 5, pp. 580–589, 2019, doi: 10.1080/10426914.2019.1566959
- [10] A. Pramanik, M.N. Islam, A.K. Basak, Y. Dong, G. Littlefair, C.Prakash, “Optimizing dimensional accuracy of titanium alloy features produced by wire electrical discharge machining”, *Material Manufacturing Processes*, vol. 34, pp.1083–1090, 2019.
- [11] Y. M., Puri, V. Gohil, “Experimental study of material removal rate in electrical discharge turning of titanium alloy (Ti-6Al-4V)”, *IOP Conference Series: Material Science Engineering*, vol. 187, pp. 1–6, 2017, <https://doi.org/10.1088/1757-899X/187/1/012036>
- [12] A. Torres, I. Puertas, C.J. Luis, “Modelling of surface finish, electrode wear and material removal rate in electrical discharge machining of hard-to-machine alloys”, *Precision Engineering*, vol. 40, pp. 33–45, 2015, doi: 10.1016/j.precisioneng.2014.10.001
- [13] H.R. Tonday, A.M. Tigga, “Analysis of effects of cutting parameters of wire electrical discharge machining on material removal rate and surface integrity”, *In: IOP conference series: materials science and engineering*, vol. 115, no. 012013, pp 1–7, 2016, <https://doi.org/10.1088/1757-899X/115/1/012013>
- [14] S. Suresh Kumar, F. Erdemir, TemelVarol, S. Thirumalai Kumaran, M. Uthayakumar, AykutCanakci, “Investigation of WEDM process parameters of Al-SiC-B4C composites using response surface methodology”, *International Journal of Lightweight Materials and Manufacture*, vol. 3, no. 2, pp. 127-135, 2019, <https://doi.org/10.1016/j.ijlmm.2019.09.003>
- [15] S. Ramesh, L. Karunamoorthy and K. Palanikumar, “Surface Roughness Analysis in Machining of Titanium Alloy”, *Materials and Manufacturing Processes*, vol. 23, pp. 174-181, 2008.
- [16] S. Kumar, M. A. Khan, B., Muralidharan, “Processing of Titanium-Based Human Implant Material Using Wire EDM”, *Materials and Manufacturing Processes*, vol. 34, no. 6, pp. 695–700, 2019, doi: 10.1080/10426914.2019.1566609.
- [17] A.R. Khan, M.M. Rahman, K. Kadirgama, “An experimental investigation on surface finish in die-sinking EDM of Ti-5Al-2.5Sn”, *International Journal of Advanced Manufacturing Technology*, vol. 77, pp. 1727–1740, 2015.
- [18] Mouralova, K.; Kovar, J.; Karpisek, Z.; Kousa, P. “Optimization Machining of Titanium Alloy Ti-6Al-4V by WEDM with Emphasis on the Quality of the Machined Surface”, *Journal of Manufacturing Technology*, vol. 16, pp. 1326–1331, 2016.

- [19] S. Kumar, A. Batish, R. Singh, T.P. Singh, “Machining performance of cryogenically treated Ti–5Al–2.5Sn titanium alloy in electric discharge machining: a comparative study”, *Proceedings of the Institution of Mechanical Engineers, Part C: Journal of Mechanical Engineering Science*, vol. 231, no. 11, pp. 2017–2024, 2017.
- [20] M. Manjaiah, S. Narendranath, J.Akbari, “Optimization of Wire Electro Discharge Machining Parameters to Achieve Better MRR and Surface Finish”, *Procedia Materials Science*, vol. 5, pp. 2635–2644, 2014.
- [21] N.K. Gupta, N. Somani, C. Prakash, R. Singh, A.S. Walia, S., Singh, C.I. Pruncu, “Revealing the WEDM Process Parameters for the Machining of Pure and Heat-Treated Titanium (Ti-6Al-4V) Alloy”, *Materials (Basel)*, vol. 14, no. 9, pp. 2292–2298, 2021, doi: 10.3390/ma14092292.
- [22] M. Thangaraj, R. Annamalai, K. Moiduddin, M. Alkindi, S.Ramalingam, and O. Alghamdi, “Enhancing the surface quality of micro titanium alloy specimen in WEDM process by adopting TGRA-based optimization”, *Materials*, vol. 13, no. 6, pp. 1440–1448, 2020.
- [23] MD. U. Iqbala, J. Santhakumar, and Suyash, Dixit, “Multi-objective optimization of WEDM process parameters on titanium grade 9 using ANN and grey relational analysis”, *AIP Conference Proceedings*, vol. 2460, pp. 030008, 2022, <https://doi.org/10.1063/5.0095657>
- [24] A. V. S. Ram Prasad, Koona Ramji, MurahariKolli, and G. Vamsi Krishna, “Multi-Response Optimization of Machining Process Parameters for Wire Electrical Discharge Machining of Lead-Induced Ti-6Al-4V Alloy Using AHP–TOPSIS Method”, *Journal of Advanced Manufacturing Systems*, vol. 18, no. 02, pp. 213–236, 2019, <https://doi.org/10.1142/S0219686719500112>
- [25] K.Fuse, A.Dalsaniya, D. Modi, J. Vora, D.Y. Pimenov, K. Giasin, P. Prajapati, R. Chaudhari, S.Wojciechowski, “Integration of Fuzzy AHP and Fuzzy TOPSIS Methods for Wire Electric Discharge Machining of Titanium (Ti6Al4V) Alloy Using RSM”, *Materials*, vol. 14, pp. 7408, 2021, <https://doi.org/10.3390/ma14237408>
- [26] S. Bose, T.Nandi, “A novel optimization algorithm on surface roughness of WEDM on titanium hybrid composite”, *Sādhanā*, vol. 45, pp. 236–241, 2020, <https://doi.org/10.1007/s12046-020-01472-5>
- [27] A. Mandal, A. R. Dixit, S. Chattopadhyaya, A. Paramanik, S. Hloch, G.Królczyk, “Improvement of Surface Integrity of Nimonic C 263 Super Alloy Produced by WEDM through Various Post-Processing Techniques”, *International Journal of Advanced Manufacturing Technology*, vol. 93, no. 1–4, pp. 433–443, 2017, doi: 10.1007/s00170-017-9993-x.
- [28] P. K. Saini, M.Verma, “Experimental Investigation of wire-EDM Process Parameters on MRR of Ti-6al-4v Alloy”, *International Journal of Innovative Technology and Exploring Engineering*, vol. 4, no. 5, pp. 16–20, 2014.

Effect of Rice-Husk as Replacement Cement on Mechanical Properties Concrete

Mohd Najmudin Helmi Abu Bakar, Sakhiah Abdul Kudus*,
Nur Kamaliah Mustaffa, Adiza Jamadin
School of Civil Engineering, College of Engineering,
Universiti Teknologi MARA, 40450 Shah Alam, Selangor, MALAYSIA
*sakhiah@uitm.edu.my

Hasan Ali Abbas
Department of Building and Construction Techniques Engineering,
Madenat Alelem University College, 10006, Baghdad, IRAQ

Rohana Hassan
Institute for Infrastructure Engineering and Sustainable Management
(IIESM), Universiti Teknologi MARA, MALAYSIA

Nadia Kamaruddin
Faculty of Architecture, Planning and Surveying,
Universiti Teknologi MARA, 40450 Shah Alam, Selangor, MALAYSIA

ABSTRACT

The cost of producing concrete has increased, and its effects on the natural environment have become apparent. The ideal solution is to use agro-waste material instead of cement in concrete. This research aims to determine how well RHA works as a cement substitute. At increments of 5%, 10%, and 15%, rice husk was applied in substitute of cement. Compressive and flexural tests were performed on a 100 mm x 100 mm x 100 mm cube and 100 mm x 100 mm x 500 mm prisms with varying percentages of RHA substitution. Findings show that the highest control sample has a compressive strength of 49.83 MPa while the compressive strength began to drop at 5% RHA substitution. The compressive strength decreased as the percentage of RHA used increased from 10% to 15%. The flexural strength data shows that the 10% RHA has a maximum of 4.90 MPa. The lowest value is 3.85 MPa, and it is only seen from 5% of RHA. Thus, it can be inferred that an RHA replacement level of 5% in cement yields a tremendous increase in compressive strength.

Keywords: *Rice Husk Ash; Mechanical Properties; Compressive Strength; Flexural Strength; Green Concrete*

Introduction

Cement, fine and coarse aggregate, and water are the most expensive of the concrete's standard components. This has led to a recent hike in the cost of concrete, a necessary used construction material. As the building industry expanded in Malaysia, so did the demand for cement, which in turn fueled the growth of infrastructure development in the country.

Due to its functions as a binder, cement is the primary component used in the production of concrete. Cement manufacturing is consequently resource-intensive, costly, and environmentally damaging [1]. Worth to mention that Ordinary Portland Cement (OPC) is the most common kind used in the major construction sector. Unfortunately, the main primary constituent of cement is limestone which is a non-renewable resource. Hence, cement production is highly-priced, uses a lot of energy, and depletes natural resources [2]. It is a great concern to the environment as long-running, extensive mining will eventually cause depleted sources of limestones. In addition, the cement is made up of components such as silica, alumina, and magnesia as well as iron oxide. Besides, the negative impact of this kind of cement is also degradative to the environment due to the high emission of carbon dioxide. It was estimated that around 7% of the world's carbon dioxide output emanates from the cement industry [3].

Auspiciously, developments in concrete technology are making it possible to lessen carbon dioxide emissions caused by the production of cement and to substitute industry and agricultural waste for concrete in construction projects. Since a few decades, cement-replacement materials like fly ash and powdered granulated blastfurnace slag have been routinely used to reduce the amount of cement used [4]. Pursuant to previous studies, rice husk can be burned to create rice husk ash (RHA). The physical and chemical composition of RHA is following the standards for mineral admixtures for it to perform as the substitute [5]. Based on earlier research, evidence suggests that the mechanical properties of concrete can be enhanced by adding RHA in the right proportions. Regarding the manufacture of concrete, because of its high content of silica, RHA is regarded as a highly reactive pozzolanic material [6]. Therefore, rice husk is one of the potential answers to the problem of mitigating the depletion of limestone.

The production of harvestable goods in agriculture results in the generation of a significant volume of waste. Straws, bagasse, and husks are the three most common types of biomass products that come from plants or crops. Burning agricultural waste in the open field is a typical method of disposal for farmers. Ashes have the potential to spread into neighbouring areas, which can

lead to environmental and landfill problems. On the other hand, the practise of dumping rice husks in landfills can occupy a substantial amount of space and is a major contributor to environmental damage [2].

Ash from burning rice hulls for energy production is a common agricultural byproduct known as rice husk ash (RHA) [7]. Another way to produce RHA is to employ boilers, where the paddy can be directly burned or gasified to produce the fuel [8]. Both methods have the potential to extract RHA from paddy. When compared to other agricultural wastes that can be used in the building sector, rice husk has shown the best performance as a supplemental cementitious material (SCM) due to the high silica content of the ash [9].

Production of a rice paddy in Malaysia increased from 3 million tonnes in 2015 to 4.6 million tonnes in 2018 and 6.1 million tonnes in 2020 [10]. Agricultural waste may be easily obtained due to global production on a huge scale, making it a cost-effective alternative to more conventional building materials. The waste can be used in place of traditional materials because it is abundantly produced all over the world and hence easy to acquire. The rice husk, which originates from the outermost layer of paddy grain, however, will be dumped or burned, which will add to existing disposal problems and environmental worries [11]. Therefore, using rice husk in replacement of concrete might be one step toward finding a solution that addresses the issue. This aids the country by reducing waste disposal costs and protecting the environment.

One of the distinguishing features of this material is its high concentration of amorphous silica, which, when combined with portlandite in cement, can lead to the creation of a pozzolanic phase. In addition, RHA could be utilised to enhance the bond between different concrete mixtures by filling in the spaces between the cement particles [12]. By infiltrating voids between cement grains, RHA is capable to strengthen bonds in various concrete combinations [13]. The overall performance characteristics of the cementitious product are enhanced through the use of this pozzolanic method at later ages. On the other hand, RHA is used to replace cement partially, a considerable reduction will be made to the amount of CO₂ annually discharged into the environment [14]. Another approach for cutting costs on cement and lime is making use of RHA to cut down on the overall quantity of binders that are needed for a variety of construction projects. RHA-blended concrete has been reported to have lower air permeability and chloride penetration, lower alkalisilica expansion, and higher sulphate and acid resistance, among other qualities [14].

Moreover, when compared to the other types of ashes that were tested, the RHA concrete had the highest normalised compressive strength. The prior research indicates that a replacement level of 10-20% RHA in concrete is optimal [15]. However, RHA concrete was found to have normalised compressive strengths that were nearly 1.2 times higher than those of the

control concrete. This is because elevating the proportion of amorphous silica in the RHA formula significantly improved both pozzolanic performance and concrete properties.

In the study, rice husk waste at 5, 10, or 15% were used to supplant portland concrete for compressive and flexural consistency. The objective of this research is to provide information on the utilization of RHA as a supplementary cementing material for producing green concrete. Additionally, to the effects of the percentage of RHA as cement replacement and water-cementitious materials ratio on the mechanical properties investigated, the properties of the RHA concrete were also compared with those of the control portland cement concrete and the concrete containing silica fume. The outcome of this study benefit in the field of green concrete.

Experimental Work

Concrete mix design commonly uses form of dimensions or ratios such as 1:2:4, respectively representing the proportions of cement, fine aggregates, and coarse aggregates. The ratio is either determined by weight or volume. Although in terms of its simplicity of expression, this concrete mix design system has an advantage. However, it will cause a disruption when describing the effect of the mixing measurement on the concrete features. This is related to the importance in defining the amount of cement needed to cast a given concrete size. Thus, using the typical mix concrete layout sheet to measure the concrete mixing percentage is the most ideal way to specify mixing parameters for each individual material engaged in concrete mixing in terms of volume. Moreover, by measuring specifically the mixing percentages required for concrete mixing, the waste of materials typically occurring will be minimized.

Material preparation

Cement

For this experiment, four different series of RHA replacement concrete were constructed: a control series, and RHA replacements of 5%, 10%, and 15%. The cement that was used throughout this experiment was acquired from Tasek Cement, which fulfills the requirements outlined in MS EN 197-1:2007 [16]. These tests were conducted with a 42.5-strength class of Ordinary Portland Cement (OPC). The Tasek Cement is obtained from concrete laboratory, UiTM Shah Alam.

Rice husk ash

Rice husk ash is generated by burning rice husk in a regulated manner. Having a high SiO₂ concentration after being properly burned, it can be applied as an additive in concrete. During the hydration process, calcium hydroxide crystals form in concrete, and the amorphous silica in RHA reacts favourably with

these crystals. The C-S-H gel that is created as a by-product of the concrete hydration can be implemented to fill the porous structure. This is possible since the gel's viscosity is lower than that of water. Rice husk ash is operated as an alternative to cement in concrete.

The rice husk is obtained from a local source of rice paddy. Then, the rice husk is dried and placed in the furnace until it changes into ash. The ash are collected from the furnace and grounded until achieving a specific size is needed.

Aggregate

Suitable selection of optimum coarse aggregate size is essential in concrete mix design as it affects concrete strength. In addition, the coarse aggregate should be cleaned and free of chemicals that can lead to concrete degradation. Crushed stones are typically coarse aggregates used for concrete mixing. The material that can be sieved through a 4.75 mm screen contains fine aggregates. Quarry coarse aggregates with a nominal size of 10 mm were selected for this study. Coarse aggregates is obtained from Kajang rock quarry and fine aggregate obtained from concrete laboratory, UiTM Shah Alam.

Superplasticizers

A chemical addition from the MasterGlenium Sky 8333 group was incorporated into the concrete mixing process to decrease the water-cement ratio, enhance the concrete's formability, and strengthen its strength. MasterGlenium Sky 8333 obtained from online purchase bmd.asia.

Design mix

There were four different RHA mixture ratios created. The concrete mixtures used in the casting process include a control mixture and variations with 5, 10, and 15% RHA, respectively. Table 1 outlines the relative amounts of RHA and materials incorporated into the concrete mix. Upon continuing to the casting process, the fresh concrete is then tested to assess its workability using the slump test. In addition, the vibrating table is being used to vibrate the mould to ensure that the concrete is evenly compacted while minimizing the air void produced in the concrete.

Hence, OPC was utilised with a constant water-cement ratio of 0.54. This study consisted of 36 total samples, consisting of 36 different prism sizes (100 mm x 100 mm x 500 mm) and 36 different cube specimens (100 mm x 100 mm x 100 mm). For further works, the tests comprised both a compressive and a flexural measure of the strength. The slump test was carried out to provide data supporting the applicability of fresh concrete. Curing times in water ranged from 7 days to 14 days to 28 days for each specimen.

Table 1: Different percentages of rice husk ash with the material

Mixture	Cement (kg/m ³)	RHA (kg/m ³)	Fine aggregate (kg/m ³)	Coarse aggregate (kg/m ³)	Water (kg/m ³)	SP (1% of cement weight) (ml)
Control	16.13	0.00	33.05	40.38	8.72	168.00
5% RHA	15.33	0.81	31.47	38.45	8.31	147.00
10% RHA	14.52	1.61	31.47	38.45	8.31	147.00
15% RHA	13.71	2.42	31.47	38.45	8.31	136.50

Experimental apparatus and procedure

Compressive test on the specimen

A component or structure's compressive strength is its capacity to resist cracking or surface deformation under stress. The concrete shrinks under compression and expands under strain. Additionally, compressive strength testing relies heavily on load rate. The observed strength increases with increasing loading rates. Slow loading rates have been suggested to initiate more subcritical cracking or to bring about the emergence of creep that modifies the amount of strain at a given load. Insight regarding concrete characteristics can be gained through this assessment. By conducting this check, it will be possible to ascertain whether or not the concreting activities have been performed correctly. This evaluation was carried out following the standards laid out in BS EN 12390-3:2019 [17].

Cube test uses 100 x 100 x 100 mm mould relying on the aggregate size used. The concrete is poured into the mould in three separate levels; after each addition, the table vibrates to compact the concrete. Cement pastes were applied to the top of the cubes and spread evenly to create a flat, level surface. After twenty-four hours, the cubes were taken from the moulds, and the curing tank was loaded to begin the curing process. The cubes are evaluated with a compression machine after 7, 14, and 28 days of curing, and thus were tested at the proper angles to the casted position. The load was imposed incrementally from this point on until the cube broke. When calculating the compressive strength of concrete, the failure load from the test must be divided by the cube's surface area. Figure 1 depicted the process of compressive test.

Flexural test on the specimen

Flexural strength, which can also be referred to as modulus of rupture, is the ability of a concrete to resist deformation as a result of bending. This test method covers the determination of the flexural strength of concrete by the use of a simple prism with four-point loading. The maximum flexural loads were determined using the UTM-1000 at the Concrete Laboratory, UiTM Shah Alam, Selangor. Remove the prism from the curing processes for 7,14 and 28

days from water tank and test while they are still wet. For this test, will be tested using 3 specimens each. Based on the peak load, the peak flexural stress within the prism is calculated. The significance of using 3 specimens for each period is to obtain the average flexural strength values. The standard that has been use can fullfill the requirement Figure 2.



Figure 1: The specimen after compressive test

Two-point loads, 100 mm apart, are applied to the third points along the span of a simply supported concrete prism. In accordance with BS EN 12390-5, the load is steadily raised at a rate of 0.5 mm/min until flexural failure occurs. Prism size of 100 mm x 100 mm x 500 mm was used in this study. Figure 3 depicted the process of Flexural strength test.

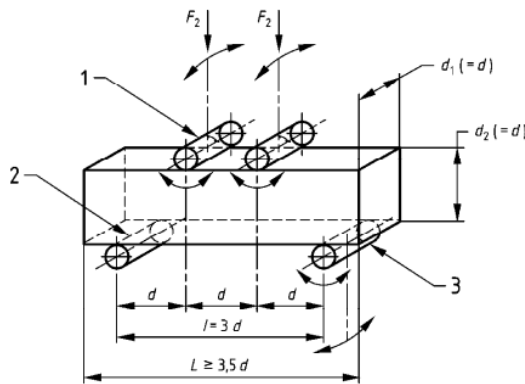


Figure 2: Arrangement of loading of test specimen (BS EN 12390-5) [18]

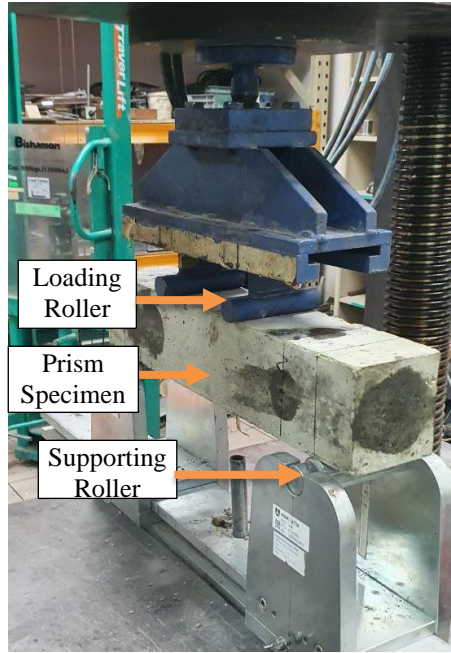


Figure 3: The specimen before flexural test

Results and Analysis

Figure 4 displays the changes in compressive strength that took place 7, 14, and 28 days after the RHA was replaced. During 7 days all RHA mixed concrete compressive strength is very low compared to control concrete. This might be due to the silica and the reduction of calcium hydroxide in the concrete mix not being able to enhance the concrete strength. These results indicate that the higher rate hydration process for normal mixed concrete compared to the concrete that contained pozzolanic material RHA starts at a later age and becomes significant when a considerable amount of $\text{Ca}(\text{OH})_2$ is produced as a hydration product of cement. RHA reacts with cement hydration product $\text{Ca}(\text{OH})_2$ to produce a secondary C-S-H gel. It happens because of the effect of the pozzolanic reaction which usually manifests at a later stage [19]-[20]. At 28 days, the strength of the control concrete reaches 49.82 MPa. After 28 days, the strength was 35.15 MPa when RHA was used for 5% replenishment. It was discovered that the optimal value of RHA significantly lowers the strength of concrete.

The result shows that the compressive strength of RHA concrete reduced as the percentage of RHA replacement increased and the concrete did not significantly influence the later age strengths. Results by [21] are in line with the present study, indicating that large amounts of RHA have an adverse effect and reduced the strength of concrete. This might be due to the lower calcium hydroxide content that has been reduced with the replacement of RHA in the mixes. Nevertheless, the strength of concrete with the replacement of cement by up to 15% RHA manage to attain the target strength of 30 MPa.

Meanwhile research [22] found that there is reduction in compressive strength at earlier ages with the increasing RHA content in concrete. In addition, superplasticizer (SP) improves the compressive strength of concrete with 5% and 10% cement replacement by RHA. SP is used to develop concrete with high early strength. It shows that the effect of SP can help to increase the compressive strength of the concrete. Thus, the increase in SP dosage parallel with the increment of RHA content contributed to the development strength in concrete. Hence the overall result of the compressive strength of concrete shows the different values from one another as the different dosages of SP are used as well RHA content.

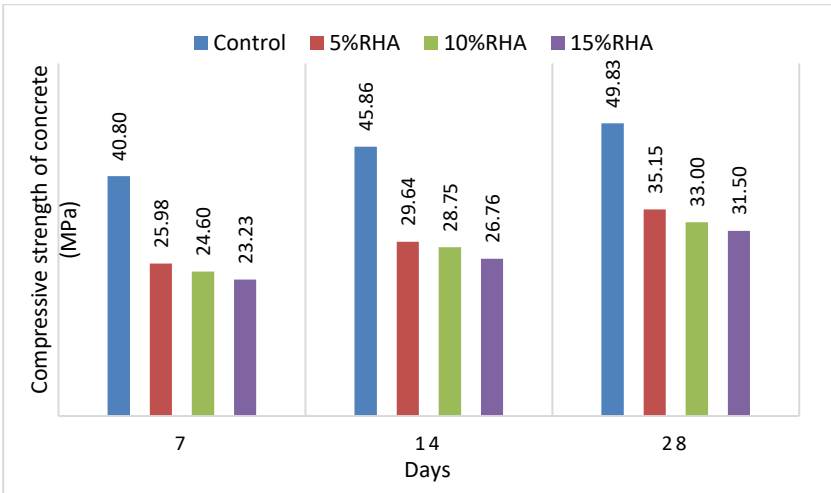


Figure 4: Compressive strength of concrete at 7, 14 and 28 days

Figure 5 displays the flexural strength at the age of 7, 14 and 28 days for different mix proportions. Flexural strength at 7 days of curing due to pozzolanic and filler effects of 5%, 10% and 15% RHA concrete is less significant than the hydration effect of control concrete. However, at 28 days of curing 10%, 15% RHA gained additional flexural strength than control

concrete due to pozzolanic reaction. Meanwhile, the lowest flexural strength was for 5% RHA concrete with a value of 3.85 MPa less significant at later ages when compared to the hydration effect of control concrete

When 10% RHA is used as a replacement for the OPC, the concrete gains a maximum strength of 4.90 MPa. In comparison to the standard concrete specimen, the value represents a 6% increase in strength. The 10% RHA has the highest strength because due to the higher specific area of the RHA which accelerated the pozzolanic reaction of reactive SiO_2 in RHA with CaOH to produce more C-S-H gel. Decrease portlandite content of the matrix can lead to the improvement of the pore structure of the concrete matrix, which is due to the high pozzolanic and compatibility of RHA with cement. RHA made concrete pore structure finer, and hence, reduced the volume of large pores and also showed a reduction in the total porosity in the concrete. RHA also acts as filler causing the foamed concrete to become denser while retaining its unique low density. The gel produced then fills up all possible voids in the sample and it will increase the flexural strength of the sample.

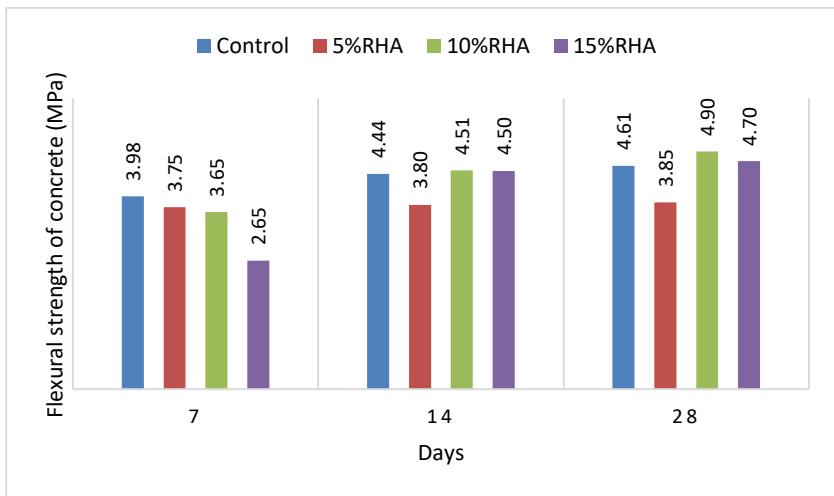


Figure 5: Flexural strength of concrete at 7, 14 and 28 days

When the amount of RHA in concrete increases by more than 10% relative to its replacement with cement, the strength of the concrete decreases. This reveals that the RHA's behaviour has been altered due to the presence of excessive silica in the bonding and material. Based on the overall result of flexural strength test of the concrete, the result shows an increase. The concrete that contains higher percentage of RHA, increased gradually compared to the percentage of control concrete. However, all the result of flexural strength of the replacement concrete has a higher value compare to control sample. It

proven that RHA can be use to replace cement and help the concrete to improve the strength.

Previous research [23] stated that the flexural strength of concrete specimens containing ordinary RHA is comparable to that of control mix specimens, while concrete containing RHA has much higher strength. Partial replacement with RHA improves flexural properties and durability by creating strong bonding that allows concrete to distribute loading during bending deflection. A study by [24] showed that optimal flexural strength can be achieved with 10% replacement of RHA. However, the same study also found that using 15% replacement of RHA resulted in a gradual decrease in flexural strength.

The pozzolanic products produced by RHA help to improve the bonding between cement mortar and aggregate. As the percentage of RHA replacement increases, there is a gradual increase in the flexural strength of rice husk ash concrete up to nearly 10% replacement, after which it decreases.

Conclusions

The following are some of the significant conclusions that can be drawn from this study:

- The results of a test to determine the material's compressive strength have been collected and appropriately tabulated. Research indicates that a concrete mixture containing 5% RHA adds the most to the average compressive stress, at 35.15 MPa.
- The concrete's compressive strength exceeded that of mixes made without RHA. This implies that the RHA qualities do not assist in enhancing the blended cement concrete's compressive strength.
- The compressive strength of concrete was significantly impacted by the RHA used. The compressive strength of concrete drops from 5% to 10% and 15% after RHA replacement. After 28 days, 5% RHA concrete reportedly has a 23% lower compressive strength than control concrete.
- While compared to the strength of control concrete after 28 days, the flexural strength of 10% RHA concrete exhibited a 6% increase in its strength.
- The percentage of RHA that should be added that yields the best result in this investigation is 5%. The findings of the compressive strength test show that on day 28, the RHA addition of 5% yields the highest strength. In contrast, adding 10% or 15% RHA is not recommended due to subpar results in terms of strength. Thus, it is more appropriate to incorporate 5% RHA into concrete mixes.
- This study will benefit mostly the material researcher that agricultural waste can be used as replacement cement in concrete. The researcher

can get information on using RHA as replacement cement and superplasticizer in concrete mixing that can be used in their research. Researchers can know about agricultural waste, which is RHA has many advantages in the construction industry. Researchers can use this study as a baseline and reference to other researchers.

Contributions of Authors

The authors confirm the equal contribution in each part of this work. All authors reviewed and approved the final version of this work.

Funding

This work was supported by the Grant Lestari Universiti Teknologi MARA 600-RMC/MYRA 5/3/LESTARI(053/2020).

Conflict of Interests

All authors declare that they have no conflicts of interest.

Acknowledgement

The authors wish to acknowledge the College of Engineering, Universiti Teknologi MARA and Universiti Teknologi MARA for supporting this research via research grant 600-RMC/MYRA 5/3/LESTARI (053/2020).

References

- [1] R. Khan, A. Jabbar, I. Ahmad, W. Khan, A. N. Khan, and J. Mirza, "Reduction in environmental problems using rice-husk ash in concrete", *Construction and Building Materials*, vol. 30, pp. 360–365, 2012, <https://doi.10.1016/j.conbuildmat.2011.11.028>
- [2] H. M. Owaid, R. B. Hamid, and M. R. Taha, "A review of sustainable supplementary cementitious materials as an alternative to all-portland cement mortar and concrete", *Australian Journal of Basic and Applied Sciences*, vol. 6, no. 9, pp. 287–303, 2012.
- [3] B. S. Thomas, "Green concrete partially comprised of rice husk ash as a supplementary cementitious material – A comprehensive review",

- Renewable and Sustainable Energy Reviews*, vol. 82, pp. 3913–3923, 2018, <https://doi.org/10.1016/j.rser.2017.10.081>
- [4] L. S. Wee, O. C. Lian, and M. R. M. Zain, “Mechanical properties of engineered cementitious composites using local ingredients”, *Journal of Mechanical Engineering*, vol. 16, no. 2, pp. 145–157, 2019. <https://doi.org/10.24191/jmeche.v16i2.15332>
- [5] C. Fapohunda, B. Akinbile, and A. Shittu, “Structure and properties of mortar and concrete with rice husk ash as partial replacement of ordinary Portland cement – A review”, *International Journal of Sustainable Built Environment*, vol. 6, no. 2, pp. 675–692, 2017. <https://doi.org/10.1016/j.ijbsbe.2017.07.004>
- [6] M. Jamil, A. B. M. A. Kaish, S. N. Raman, and M. F. M. Zain, “Pozzolanic contribution of rice husk ash in cementitious system”, *Construction and Building Materials*, vol. 47, pp. 588–593, 2013. <https://doi.org/10.1016/j.conbuildmat.2013.05.088>
- [7] M. Amran, R. Fediuk, G. Murali, N. Vatin, M. Karelina, T. Ozbakkaloglu, R.S. Krishna, A.K. Sahoo, S.K. Das, J. Mishra, “Rice husk ash-based concrete composites: A critical review of their properties and applications”, *Crystals*, vol. 11, no. 2, pp. 1–33, 2021. <https://doi.org/10.3390/cryst11020168>
- [8] L. Prasittisopin and D. Trejo, “Effects of Mixing Time and Revolution Count on Characteristics of Blended Cement Containing Rice Husk Ash”, *Journal of Materials in Civil Engineering*, vol. 30, no. 1, pp. 04017262, 2018, [https://doi.org/10.1061/\(asce\)mt.1943-5533.0002133](https://doi.org/10.1061/(asce)mt.1943-5533.0002133)
- [9] M. Harihanandh and K. Rajashekhar, “Study on durability of concrete by using rice husk as partial replacement of cement”, *Materials Today: Proceedings*, vol. 52, pp. 1794–1799, 2022, <https://doi.org/10.1016/j.matpr.2021.11.448>
- [10] S. C. Paul, P. B. K. Mbewe, S. Y. Kong and B. Šavija, “Agricultural solid waste as source of supplementary cementitious materials in developing countries”, *Materials*, vol. 12, no. 7, pp. 1–20, 2019, <https://doi.org/10.3390/ma12071112>
- [11] M. Hanif Khan, H. Zhu, M. Ali Sikandar, B. Zamin, M. Ahmad and M. Muayad Sabri, “Effects of Various Mineral Admixtures and Fibrillated Polypropylene Fibers on the Properties of Engineered Cementitious Composite (ECC) Based Mortars”, *Based Mortars. Materials (Basel)*, vol. 15, no. 8, pp. 1–21, 2022, <https://doi.org/10.3390/ma15082880>
- [12] V. Charitha, V. S. Athira, V. Jittin, A. Bahurudeen and P. Nanthagopalan, “Use of different agro-waste ashes in concrete for effective upcycling of locally available resources”, *Construction and Building Materials*, vol. 285, pp. 122851, 2021, <https://doi.org/10.1016/j.conbuildmat.2021.122851>
- [13] K. Rajashekhar Reddy, M. Harihanandh and K. Murali, “Strength performance of high-grade concrete using rice husk ash (RHA) as cement

- replacement material”, *Materials Today: Proceedings*, vol. 46, pp. 8822–8825, 2021, <https://doi.10.1016/j.matpr.2021.04.332>
- [14] A. Gholizadeh-Vayghan, S. Nasiri and P. Ghassemi, “Optimization of the Strength Activity of Rice Husk Ash in Cementitious Mixtures”, *Journal of Materials in Civil Engineering*, vol. 33, no. 8, pp. 1–9, 2021, [https://doi.10.1061/\(asce\)mt.1943-5533.0003838](https://doi.10.1061/(asce)mt.1943-5533.0003838)
- [15] I. Khan, T. Xu, M.S.H. Khan, A. Castel and R.I. Gilbert, “Effect of Various Supplementary Cementitious Materials on Early-Age Concrete Cracking”, *American Society of Civil Engineers*, vol. 32, no. 4, pp. 1–9, 2020, [https://doi.10.1061/\(ASCE\)MT.1943-5533.0003120](https://doi.10.1061/(ASCE)MT.1943-5533.0003120)
- [16] MS EN 197-1:2014 “Cement - Part 1: Composition, specifications and conformity criteria for common cements”, *Malaysian Standard*, pp 1-6.
- [17] BS EN 12390-3:2019 “Part 3: Compressive strength of test specimens”, *British Standard*, pp 1-18.
- [18] BS EN 12390-5:2009 “Testing hardened concrete Flexural strength of test specimens”, *British Standard*, pp 1-14.
- [19] H. Chao-Lung, B. Le Anh-Tuan and C. Chun-Tsun, Effect of rice husk ash on the strength and durability characteristics of concrete, *Construction and Building Materials*, vol. 25, no. 9, pp. 3768–3772, 2011, <https://doi.10.1016/j.conbuildmat.2011.04.009>
- [20] S. A. Kudus, N. K. Mustaffa and S. Shahidan, “Influence of Palm Oil Fuel Ash on Mechanical Properties of Ultra-High-Performance Concrete”, *International Journal of Sustainable Construction Engineering and Technology*, vol 13, no. 4, pp. 44-53, 2022. , <https://doi.org/10.30880/ijscet.2022.13.04.005>
- [21] C. L Hwang and O. S. Wu, “Properties of cement paste containing rice husk ash”, *American Concrete Institute, ACI Special Publication*, vol. 114, pp. 733–762, 1989.
- [22] V. Ramasamy, “Compressive strength and durability properties of Rice Husk Ash concrete”, *KSCE Journal of Civil Engineering*, vol 16, no. 1, pp. 93–102, 2012, <https://doi.org/10.1007/s12205-012-0779-2>
- [23] K. Kartini., H.B. Mahmud, and M.S. Hamidah. "Strength properties of Grade 30 rice husk ash concrete", *31st conference on our world in concrete & structures*, pp. 16-17, 2006.
- [24] N.K Krishna, S. Sandeep, and K.M. Mini. "Study on concrete with partial replacement of cement by rice husk ash", *IOP conference series: materials science and engineering*, vol. 149, no. 1, pp. 012109, 2016, <https://doi.org/10.1088/1757-899X/149/1/012109>

Evaluation of Energy Production using Parabolic-Dish Solar Collector: A Case Study of Iraq

Samir Gh Yayah, Ahmed Shihab Al-Samari and Itimad D J Azzawi*

Department of Mechanical Engineering, College of Engineering,
University of Diyala, IRAQ

*itimaddawood_eng@uodiyala.edu.iq

ABSTRACT

The parabolic dish reflector solar collector is one of the significant and most efficient steam-producing solar concentrating systems in thermoelectric power plants and, furthermore, it's considered to be environmentally friendly (renewable energy). Iraq has vast land for installing solar collectors to generate steam and use for thermal power plants. However, no such application/power plant has yet been built. Therefore, the proposed study investigates opportunities for using PDR solar collectors, including all advantages and challenges. To implement and estimate the productivity and efficiency of the PDR in (Diyala City / Iraq), a PDR solar collector with a total area of 0.708 m² (including the glass pieces used as a reflective surface) was designed and fabricated. These glass pieces have been utilized to increase the reflection of solar rays by 80% when compared to a traditional case/setup. Two different systems (open and closed) were considered to investigate the performance of thermal power. The results show that the absorption temperature was increased from 34.6 to 95 °C. On the other hand, the coefficient of heat loss by convection increases by about (795.5 W). In addition, it was pointed out that the coefficient of total heat loss over time was increased by about 25 to 41% (closed and open systems). Furthermore, the experimental findings clearly demonstrate the usefulness of PDR solar heaters in Iraq. Hence, its confidently believed that this research will be useful in the future for this type of thermal power plant.

Keywords: Environmentally Friendly; Parabolic Dish Reflector

Nomenclature

Latin characters

a parabola depth, m

h	diameter of the opening of the parabola, m
F	focus point, m
f	focal distance, cm
r_r	mean radius, m
r	outer reactor shell radius, m
d_{go}	outer dish diameter, m
$a/2$	radial displacement of focal point away from central axis, m
Gap	inner dish truncation diameter, m
A_r	solar reactor aperture area, m^2
A_a	dish aperture area, m^2
Q_s	incident radiant power, solar radiative power, W
Q_u	\dot{Q}_{reactor} , solar radiative power incident at calorimeter aperture, W
I_b	solar constant, assumed to be constant =1353 W/m ²
d_{ao}	inner diameter of the dish receiver, m

Greek characters

\emptyset	tracking offset,
\emptyset_r	rim angle,
r_r	mean radius, m
r	outer reactor shell radius, m
σ_1	oversizing angle for secondary dish,
σ_s	oversizing angle for secondary dish,
2σ	angle between optical axis before and after reflection at secondary reflector

Introduction

The current estimated world consumption is 100 million barrels of oil per day, and recent studies indicated that this number may rise to reach about 123 million barrels per day by 2025 [1]. Based on this immoderate global demand for energy, since the industrial revolution, the excessive consumption/burning of these fossil fuels (oil, gas, coal) can cause many disasters in terms of global warming and the greenhouse effect [2]. This might lead to an unbalance of the environment and the depletion of the world's fossil fuel reserves.

Hence, the utilization of solar power (renewable energy) can preserve the wealth of future generations to come within the framework of the concept – of sustainable development. This evolution must be achieved in a way that guarantees the needs related to the development and those of the environment of present and future generations [2]. Iraq can be considered one of the developing countries in terms of building renewable power plants and merging with the global trend that seeks to reduce the consumption of fossil fuels via wind and solar power by the end of 2024 [3]. It should be pointed out that solar

energy has priority in comparison with other sources to meet energy demands for human needs. In addition, it has an outstanding contribution to other energy activities due to its being environmentally friendly and it can be converted to other types of energy such as electrical, mechanical, and thermal energy. Recently, energy researchers witnessed the rapid expansion of applications in most world regions, including Arab countries, focusing on increasing and developing low efficiency. Figure 1 shows the extent of using renewable energy in the middle east, including Iraq.

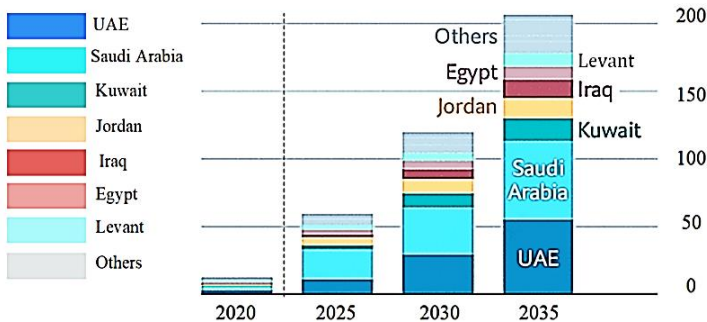


Figure 1: Middle East projects solar capacity (GW) [4]

In terms of solar energy, Iraq can be considered one of the blessed countries because of the advantage of getting sunlight almost during the whole year. There are two basic options when dealing with solar energy [5]. The first one is photovoltaic, and the second is solar thermal energy systems. The efficiency of photovoltaic systems is between (10-20%), while the solar thermal system has a noticeably higher efficiency to reach about 30% [1]. The present study attempts to take advantage of the intensity of solar thermal radiation by collecting it to be applied to the storage system of heating fluids. Solar energy can be harvested and concentrated in thermal form using a solar collector. The collected thermal energy can be transferred using working fluid in thermal applications such as heating space and domestic water heating [4]. Concentrating solar power plant (CSP) technology has the advantages of low cost, efficacy, and acceptability. It can be used in small applications (producing a few kilowatts, for instance, parabolic saucer (DP) Stirling system). It can also be centralized (producing a few megawatts, for example, parabolic cylindrical (PTC), solar towers (CRS), and Linear Fresnel Reflector (LFR) [6]. The solar activities available for investment in Iraq depend on many factors such as:

- The intensity of solar radiation: Iraq has the second level of solar radiation exposure (see Figure 2), the average daily solar radiation map in the world/Iraq, as shown in Figure 2. There are many potential areas for establishing large solar institutions on a large scale. In Iraq, the

annual average of solar energy per day ranges between (4.5-5.4 kW/m²) [5-7].

- Exposure to solar energy: the period of exposure in Iraq to solar energy is available for an extended period, as shown below. The familiarity with solar potential in Iraq is indispensable in developing solar power plant technology [8].

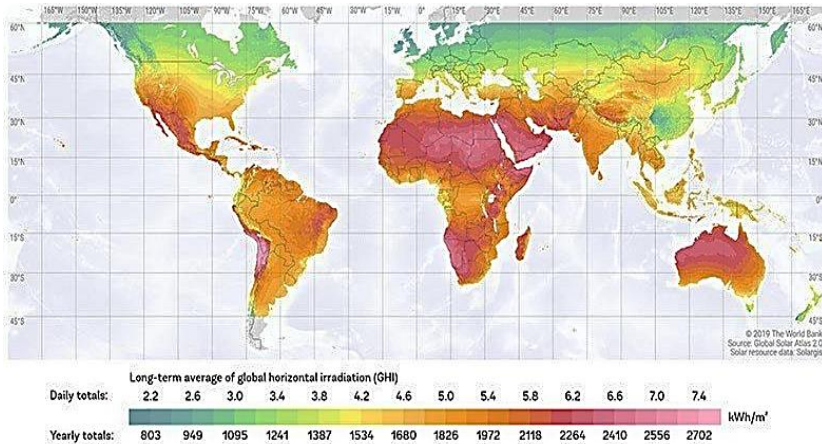


Figure 2: Areas of exposure to solar energy in the world [4]

Several researchers have employed concentrated solar dishes in many various applications for the purpose of energy generation. Studies by Iraqi researchers in this field have varied. For example, Hafez et al. [9] have fabricated a parabolic dish capable of generating steam to run a Stirling engine system to produce 10 kW from a 990 W/m² solar radiance. Al-Defiaie have successfully desalinated the water through the operation of solar Stirling engine (heat rejection process) [10]. In a similar approach, Alahmer et al. [9]-[10] have made an advantage of a CPC (compound parabolic collector) to operate a solar-adsorption refrigeration system. In terms of solar energy, a considerable number of studies have provided useful discussions concerning concentrated solar systems, such as [10]-[11]:

- Solar dishes are combined with others to create hybrid systems.
- Solar dishes (concentrators) were combined with the use of gasification and micro gas-turbines (during the processes) [12]-[13].

This study is a complement to a series of studies conducted in Iraq, and it is the first of its kind in Diyala, which has suitable atmospheric factors for solar radiation up to 1700 kilowatts per square meter, making it a promising technology in power generation with an average efficiency of 40% and a

The concentration ratio might be utilized to define the concentrated energy of the light for a defined collector. Dividing the area of the aperture of collector (A_a) by the surface area of receiver (A_r) is defined as geometric concentration ratio (CRg) (directly calculated, see Equation 1 [19], [21]:

$$CRg = A_a / A_r \quad (1)$$

Equations 2 and 3 would be used to calculate (h) (the distance between the vertex and aperture) after both aperture diameter (d) and focal length (f) being [10]-[11]:

$$h = a^2 / 16f \quad (2)$$

$$\frac{f}{a} = \frac{1}{4 \tan\left(\frac{\psi_{rim}}{2}\right)} \quad (3)$$

In the same manner, the rim angle (ψ_{rim}) can be expressed as follows:

$$\tan \psi_{rim} = 1 / [(a/8h) - (2h/a)] \quad (4)$$

The exergy analysis of solar collectors is parametrically dependent on the thermal analysis, it should be noted. As a result, thermal analysis needs to be done first [22]. The ratio of the supplied (useful) to the incident energy, which can be computed using the equation below [22], may be used to define the thermal efficiency of the collector.

$$\zeta_c = \frac{Q_u}{Q_s} \quad (5)$$

The dish concentrator has an aperture area A_a equal to 0.708 m² and receives solar radiation at the rate of about 1488.3 W from the sun by using split type Lux Meter. Multiplying the area of the aperture of collector (A_a) by the (I_b) (incident solar radiation - per unit of concentration area gives (Q_s : net transferred solar heat). This would be affected by the dish concentrator orientation, conditions of meteorological, geographical position on the earth, and finally the time during the day. For the current analysis, two conditions were imposed, which are steady state system and constant incident solar radiation (I_b) (see Equation 6) [22].

$$Q_s = I_b A_a \quad (6)$$

The beneficial heat energy (received from the solar collector) would be completely absorbed by the heat transfer fluid (equalized) when a steady-state

conditions being imposed. This could be determined by the radiant solar energy (received by the receiver) after subtracting either indirect or direct heat lost by the receiver into the surrounding (as shown in Equation 7) [22].

$$Q_u = Q_r - Q_l \quad (7)$$

This beneficial heat gain can also be defined based on the temperature differences of the fluid (see Equation 8) [22].

$$Q_u = \dot{m} C_p (T_{out} - T_{in}) \quad (8)$$

Equation 9 represents the Hottel–Whillier equation for the actual heat gain Q_u of a concentrating solar collector system [22]:

$$Q_u = F_R A_a \left[S - \frac{A_r}{A_a} U_L (T_{in} - T_a) \right] \quad (9)$$

The solar radiation absorbed by the absorbing tube (s); it is calculated from the following relationship [22]:

$$s = I_b (\rho_a \tau \alpha_r \gamma) \quad (10)$$

The heat removal factor (FR) is defined as follows [22]:

$$F_R = \frac{\dot{m} c_p}{A_r U_L} \left[1 - e^{-\left(\frac{A_r U_L \dot{F}}{\dot{m} c_p} \right)} \right] \quad (10)$$

Based on Equations 9 and 10, the actual heat gain might be given as follows [22].

$$Q_u = \frac{\dot{m} c_p A_a}{A_r U_L} \left(S - \frac{A_r}{A_a} U_L (T_{in} - T_a) \right) \left[1 - e^{-\left(\frac{A_r U_L \dot{F}}{\dot{m} c_p} \right)} \right] \quad (11)$$

where S is the absorbed flux ($I_b \times$ optical efficiency ζ_o), and T_a represents the temperature of the ambient. The factor of heat removal relates to the temperature gradients within the receiver and permits for inlet fluid temperatures in the energy balance as shown in Equation 1. The temperature at the inlet is often identified which make it more convenient when dealing with the analyzing of a solar energy system [22].

$$A_r = \frac{\pi}{4} d^2 \quad (12)$$

The diameter of the cavity of the receiver (modified, for minimum heat loss) can be given as a function of its aperture [19], [22] (see Figure 4).

$$D = \sqrt{3}d \quad (13)$$

where D = Aperture diameter, and d = Cavity diameter.

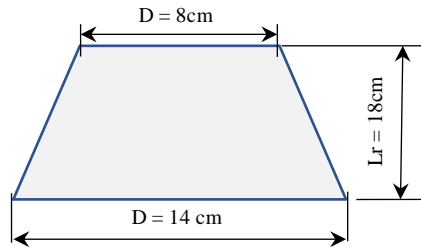


Figure 4: Schematic of cavity model-receiver

Equation 14 might be used to define the maximum angle about the aperture's diameter [23]:

$$\emptyset = 2\arctg(d/4f) \quad (14)$$

The parabolic dish is the edge radius (rr) or maximum distance value existing between the focal point and the paraboloid extreme (see Equation 15):

$$rr = \frac{2f}{(1+\cos\emptyset)} \quad (15)$$

The total heat transfer coefficient (U_L) can be calculated from the following equation [24]:

$$U_L = h_w + h_{\text{rad,r-sky}} \quad (16)$$

h_w is defined as the coefficient of heat transfer by convection due to wind, which can be found in Equation 17, while $h_{\text{rad,r-sky}}$ is denoted by the coefficient of heat transfer by radiation from the absorbing tube to the outer periphery and is calculated by using Equation 18 [25].

$$h_w = 5.7 + 3.8V \quad (17)$$

$$h_{\text{rad,r-sky}} = \varepsilon_r \cdot \sigma (T_r + T_{\text{sky}}) (T_r^2 + T_{\text{sky}}^2) \quad (18)$$

So, the sky temperature (T_{sky}) and the (T_r) temperature of the intake tube is calculated by the following equations as follows [26]:

$$T_{\text{sky}} = 0.055T_a^{1.5} \quad (19)$$

$$T_r = T_{m,f} + \frac{\dot{m}c_{p,r}(T_{in}-T_a)}{h_{c,i} \cdot A_{r,i}} \quad (20)$$

Specifically designed heat exchangers called solar energy collectors convert solar radiation energy into the internal energy of the transport medium. The solar collector is the most important part of any solar system. Incoming solar energy is absorbed by this device, which then transforms it into heat that should be delivered to a moving fluid (often air, water, or oil) through the collector. The solar energy must be transported from the circulating fluid to the space conditioning or hot water equipment to a thermal energy storage tank where it may be used later at night or on overcast days. Table 1 provides the intended dish's measurements.

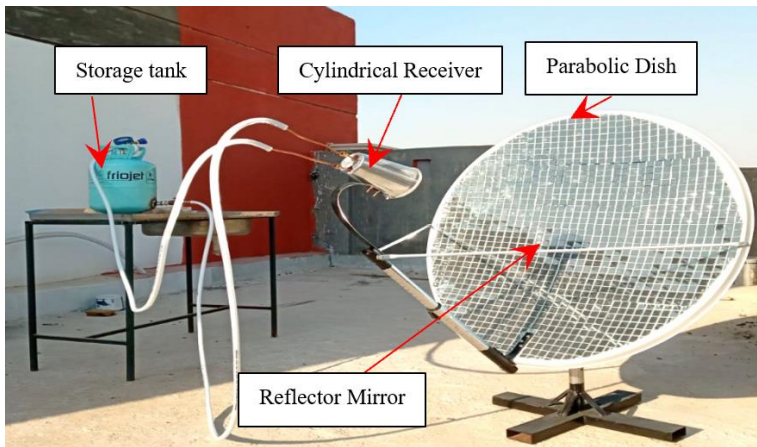
Table 1: Dimensions of the solar collector parabolic dish

Symbols	Value	Description
a	0.95 m	Diameter of the opening of the parabola
h	0.095 m	Parabola depth
A_a	0.708 m ²	The effective area of the reflector
f	0.76 m	Focal distance
ψ_{rim}	46°	Rim angle
f/d	0.56	Reflectivity of mirrors
m	0.001 - 0.0067 kg/s	Mass flow rate
\emptyset	34.7°	Rim angle degree
rr	0.834 m	Mean radius
C_p water & 15 °C	4.187 kJ/kg K	Specific heat at constant pressure.
A_r	0.5024 m ²	Receiver area
I_b	1353 W/m ²	Incident solar adiation
Qs	1488.3 W	Solar radiative power incident at solar dish aperture
S	1082.4 W/m ²	Direct normal beam irradiance.
Qu	795.5 W	Useful energy gain
ζ_c	53.4%	System efficiency

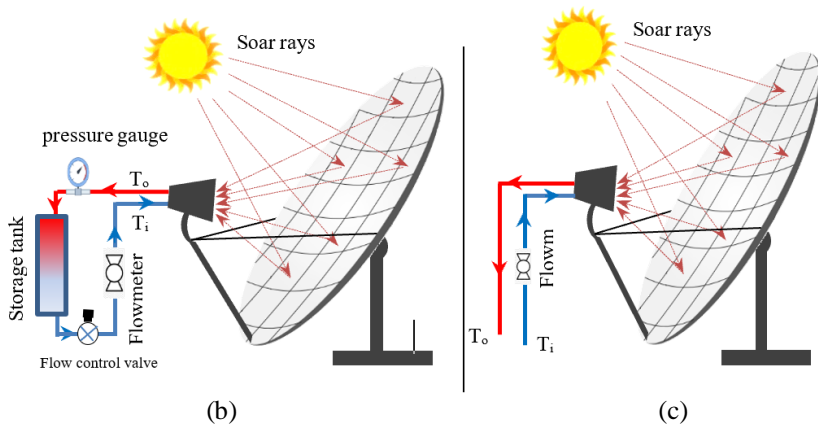
Experimental Setup and System Description

Parabolic dish

In the experimental setup, a parabolic/concave dish (made of aluminum and covered by pieces of glasses) was utilized. The method of a given focus and directrix has been employed in constructing the parabolic dish. The reflector plain mirror was cut into small rectangular pieces and fixed with adhesive with a reflectivity of 95%. The system was designed and built based on previous experiences and data (see Figure 5).



(a)



(b)

(c)

Figure 5: (a) Photographic view of the apparatus that located in the city of Diyala/Iraq, (b) schematic for the closed, and (c) open systems

Concentrator

The concentrator consisted of the following parts:

- **Metal Structure:** In order to reduce the cost of the fabrication and setup of the rig, an aluminum dish was utilized. It was designed with (1.20 m × 0.95 m). The oval/parabolic dish was mounted on a stand using bolts and nuts, while its free to move in both horizontal and vertical directions (see Figure 6). It should be pointed out that it was difficult to find a simple method for predicting the surrounding conditions. Most of the studies focus on the convection and radiation losses approximated by a simple equation at low operating temperatures. However, the convection losses are also relatively low to high temperatures. In addition, it was noted that the magnitude and the direction of the wind can significantly affect the number of heat losses. This heat loss becomes higher if the wind is parallel to the plane of the aperture and lower when facing it.
- **Cylindrical Receiver:** The cylindrical receiver was chosen for the current investigation because it has a small area towards the aperture window, which reduces reflection losses. Consequently, the design of this sort of receiver increases the likelihood that the internally reflected photons will be absorbed. Copper coil windings in an aluminum conical chamber make up the receiver. The components of the equipment were produced locally to reduce costs. The cylindrical chamber had an opening diameter of 170 mm and a depth of 180 mm. The coil had a 5 m length and produced ten smaller diameter windings. The tube's diameter was 12.5 mm. The constructed construction of the cylindrical receiver is shown in Figure 3. In the next part, the receiver's design will be discussed. The cylindrical receiver's aperture diameter was selected based on the focal diameter of the dish. Two thermocouples (Type-K) were used for measuring the inlet and the outlet temperatures of the heat transfer fluid (HTF) [27].



Figure 6: The structure of the solar system

- Connecting tubes: Two rubber tubes (for the inlet and outlet, as water begins to flow from the tank to the boiler) were used to handle the relatively internal high pressure as water turning into steam due to heating.
- Storage Tank: A 10-liter gas bottle was used for storage. It was modified to suit the work by adding two holes with fittings, one at the bottom for the liquid to exit and the other at the top where the liquid returns from the boiler in the form of steam and then adding a flow control valve for this process to control the water level outside the flow rate.

All the used thermocouples, gauges and flow meters are calibrated and the uncertainty of each was about ± 2 , 5 and 7 %, respectively.

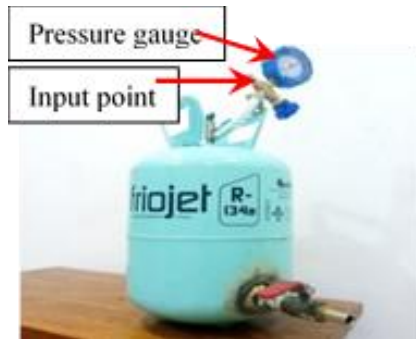


Figure 7: The used storage tank for the solar system

Results and Discussions

After fabricating all the necessary parts, the rig was assembled, and the center dish was directed towards the sunlight. The storage tank was filled with tap water and connected to the cylindrical receiver via the rubber pipes. Meanwhile, the solar radiation focused onto the boiler for about 10 minutes and the temperature was raised to reach almost 210 °C (with no water). The next step was to allow the water to flow between the receiver and storage tank. Both the inlet and outlet temperatures of the water were repeatedly recorded to calculate the heat transfer from the receiver to the hot tank. In the case of the open system of the current investigation, the amount of mass flow rate changes from 0.001 kg/sec (lowest value) up to 0.0067 kg/sec, whereas it was fixed to 0.0067 kg/sec during the experiments of the closed system.

To accurately analyze the system's overall performance, each experiment was repeated five times a day during four days. In general, the data indicated that the incident solar radiation increases with time and reaches its

maximum at mid-afternoon and then decreases until sunset. This would be due to a change in the optical path of radiation through the atmosphere during the day which leading to a change in the amount of incoming solar radiation (mainly through the absorption and diffusion process). Consequently, the change in the intensity of solar radiation over-time causes a change in the temperature values, as shown in Tables 2 and 3.

Table 2: Experimental results for the PDC using the closed system

Time (hr.)	T _w °C	T _{in} °C	T _{out} °C	S.R (Lux)	S.R (w/m ²)	Useful energy (w)
08:00	32	17	35	121000	139.101	585
09:00	33.2	32	43	125000	143.7	640
10:00	35.1	39	51	130000	149.448	700
11:00	39.9	45	73	136000	156.345	750
12:00	44.1	66	85	141000	162.093	815
13:00	44.8	78.3	89.1	143000	164.392	980
14:00	45.4	82	91.2	141000	162.093	800
15:00	45.8	85	91.7	135000	155.196	675
16:00	46.1	86.2	92.5	132000	151.747	520

Table 3: Experimental results for the PDC using open system

Time (hr.)	T _w °C	T _{in} °C	T _{out} °C	S.R (Lux)	S.R (W/m ²)	Useful energy (W)
08:00	42	21	35	139000	159.794	490
09:00	42	24	39	139000	159.794	585
10:00	42.5	29	45	139000	159.794	610
11:00	43	32	51	139000	159.794	710
12:00	43	35	56	140000	160.944	755
13:00	43.5	36	64	140000	160.944	725
14:00	44	37.5	71	141000	162.093	620
15:00	45	40.5	77.5	143000	164.392	430
16:00	47	44	82	145000	166.692	380

The solar concentrated parabolic dish collector was designed for heating water in a storage tank for basic household needs. The equipment was tested on sunny days to see if it could provide the necessary heat. During two single days (in the middle of June and July 2021), the relationship between solar radiation and time in the city of Diyala/Iraq was established (see Figure 8). Iraq is considered as one of the most appropriate regions for solar applications

(at the middle of the solar radiation zone) due to its geographical location. Figure 8 depicts the distribution of solar radiation in Diyala/Iraq based on the local time. It can be observed that the solar radiation increases from dawn until mid-afternoon in both June and July and then begins to drop until sunset.

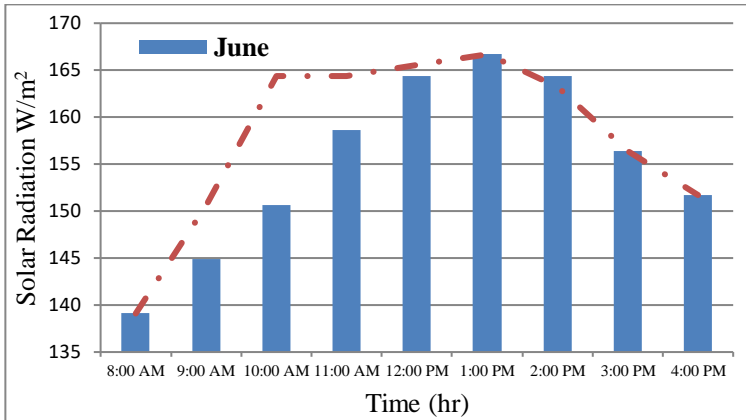


Figure 8: The relation between solar radiation and time in the city of Diyala/Iraq

Figure 9 shows the increase of the temperature during the time for the inlet and outlet temperatures of the water. It also shows the temperature of ambient and solar radiation during the day-time. The present results were recorded for a closed cycle between the storage tank and the boiler. It can be seen that both the inlet/outlet temperatures were increased with time until the sunset. Furthermore, it was noted that the outlet temperature was starting to be substantially higher than the input temperature between 10:00 and 01:00 PM, which might be attributable to an increase in solar radiation at this time of day. After that the difference between the two temperatures (T_{in} and T_{out}) becomes almost stable (maintaining same difference).

Figure 10 shows the increase of the temperature during the time for the inlet and outlet temperatures of the water and the temperature of ambient and solar radiation. These results were recorded for the open system. It can be noticed that the outlet temperature of the water is significantly higher when compared to the inlet temperature due to the effect of the open cycle.

Figure 11 represents the amount of energy generated as increases with increasing temperature and the amount of solar radiation falling on a unit area. In addition, it increases by increasing the amount of mass flow of the fluid to a certain extent and decreasing the concentration ratio to a certain extent.

Based on the current results, it can be pointed out that the percentage of improvement depends on the theoretical efficiency, which in turn depends on the percentage of concentration. The higher the concentration ratio, the higher the efficiency. However, practically, the efficiency was inversely proportional to the concentration ratio. This is due to the increase of the diameter of the supporting tube (lower concentration ratio) which led to the greater time of heat exchange between the absorbent tube and the fluid.

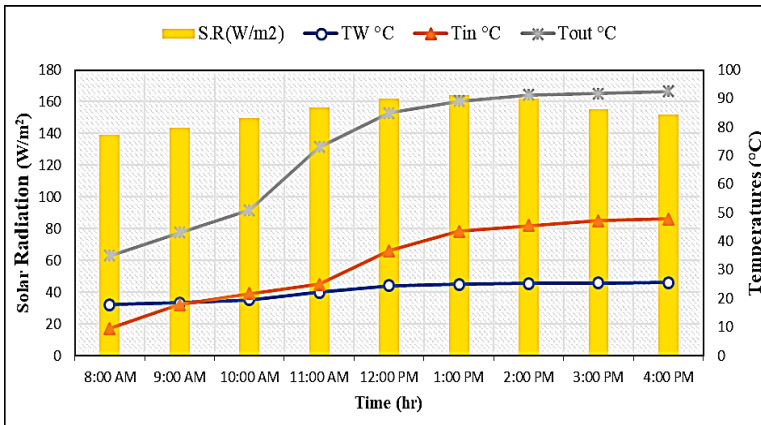


Figure 9: Relation between temperatures, solar radiation, and time (closed system)

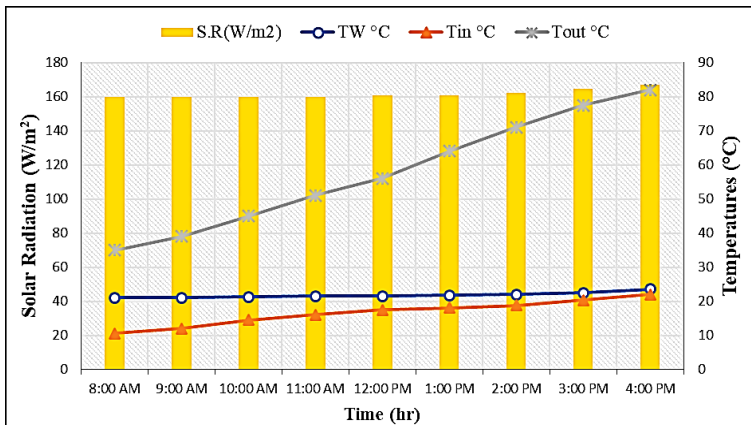


Figure 10: Relation between temperatures, solar radiation and time (open system)

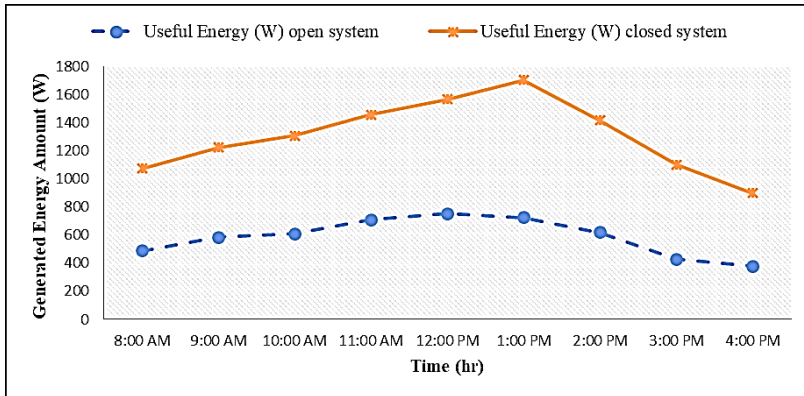


Figure 11: The amount of change in the energy produced by the solar collector with time, for open and closed systems

Conclusions

In this work, the heat losses coefficient with time has been studied for the parabolic-dish solar collector. It was concluded that the stored heat increases as solar radiation increases. The results were mainly obtained from two types of systems (open and closed). The closed system results showed that the maximum temperatures of the inlet and outlet water were 74.2 °C and 90 °C, respectively (differences of 16 °C). On the other hand, the open system showed a temperature difference of 38 °C ($T_{in} = 44$ °C and $T_{out} = 82$ °C, for the same time, i.e., at midnight). This is because the closed system uses circulating hot water and has a limited surface area (1 m²), whereas the open system has reverse effect owing to water flow speed. This would explain the difference between temperatures in the (open and closed) systems. It was found that the coefficient of total heat loss over time was increased by about 25 to 41% (closed and open systems). This is due to the increase in the amount of water (increase in the Reynolds number) flowing through the collector for the open system, which helps to extract more heat from the solar collector. Based on the present shown results and efficiency, it can be said that the current design of the apparatus is decent enough for use in our daily lives. The current experiment provides good insight into the relationship between solar energy and its harnessing to generate thermal energy and the conclusion is as follows:

- It can help reduce the consumption of electrical energy, especially in the current situation in Iraq.
- The used energy for operating the systems is widely available (free).
- Low cost of the construction of the system with a very long lifespan.

- Maintenance-free (except for the cleaning process from dust from time to time).

For future work, it would be recommended to do the following steps. Firstly, the parabolic-dish concentrated-collector can be modified concerning focal length and dish diameter. Secondly, an automatic tracking system can be integrated for tracking the sun's direction. In addition, material opportunities were also considered while designing the dish with reflectivity and thermal conductivity. Thus, the parabolic dish solar collector system may be implemented in the future for air conditioning systems and other industrial heating applications.

Contributions of Authors

The authors confirm the equal contribution in each part of this work. All authors reviewed and approved the final version of this work.

Funding

This work received no specific grant from any funding agency.

Conflict of Interests

All authors declare that they have no conflicts of interest.

Acknowledgment

The construction of all materials used in the current research is supported by University of Diyala (Mechanical Engineering Department).

References

- [1] Z. A. Baloch, Q. Tan, H. W. Kamran, M. A. Nawaz, G. Albashar, and J. Hameed, "A multi-perspective assessment approach of renewable energy production: policy perspective analysis," *Environment, Development and Sustainability*, vol. 24, no. 2, pp. 2164–2192, 2021, <https://doi.org/10.1007/s10668-021-01524-8>.

- [2] M. A. Ismael, S. Gh. Yahya, and I. D. J. Azzawi, "Experimental Investigation of Performance of Conventional Vapor Compression Refrigeration Cycle Using Geothermal Cooling in Extreme Hot Weather Conditions," *International Journal of Heat and Technology*, vol. 40, no. 2, pp. 449–456, 2022, <https://doi.org/10.18280/ijht.400212>.
- [3] O. S. Mahmood, A. M. A. Karim, S. Gh. Yahya, and I. D. J. Azzawi, "Miniaturized Traveling-Wave Thermoacoustic Refrigerator Driven by Loudspeaker: Numerical Design," *International Journal of Air-Conditioning and Refrigeration*, vol. 28, no. 04, pp. 2050035, 2020, doi: <https://doi.org/10.1142/s2010132520500352>.
- [4] A. Bejan, G Tsatsaronis, and M. J. Moran, Thermal design and optimization. New York: Wiley, 1996.
- [5] M. H. Khoshgoftar Manesh, M. Hajizadeh Aghdam, H. Vazini Modabber, A. Ghasemi, and M. Khajeh Talkhonchek, "Techno-economic, environmental and energy analysis and optimization of integrated solar parabolic trough collector and multi effect distillation systems with a combined cycle power plant," *Energy*, vol. 240, pp. 122499, 2022, <https://doi.org/10.1016/j.energy.2021.122499>.
- [6] C. Zamfirescu and I. Dincer, "How much exergy one can obtain from incident solar radiation," *Journal of Applied Physics*, vol. 105, no. 4, pp. 044911, 2009, <https://doi.org/10.1063/1.3081637>.
- [7] A. Bejan, Solutions manual for advanced engineering thermodynamics. New York: Wiley, 1988.
- [8] J. R. Howell, M Pinar Mengüç, and R. Siegel, Thermal radiation heat transfer. Boca Raton: Crc Press, 2016.
- [9] Z. A. H. Obaid, I. D. J. Azzawi, and K. Azeez, "The experimental study of energy features for solar air heaters with different turbulator configurations," *Heat Transfer*, vol. 52, no. 2, pp. 1380–1394, 2022, <https://doi.org/10.1002/htj.22745>.
- [10] S. A. Kalogirou, "Solar thermal collectors and applications," *Progress in Energy and Combustion Science*, vol. 30, no. 3, pp. 231–295, 2004, <https://doi.org/10.1016/j.pecs.2004.02.001>.
- [11] S. Farahat, F. Sarhaddi, and H. Ajam, "Exergetic optimization of flat plate solar collectors," *Renewable Energy*, vol. 34, no. 4, pp. 1169–1174, 2009, <https://doi.org/10.1016/j.renene.2008.06.014>.
- [12] W. Ajbar, A. Parrales, A. Huicochea, and J. A. Hernández, "Different ways to improve parabolic trough solar collectors' performance over the last four decades and their applications: A comprehensive review," *Renewable and Sustainable Energy Reviews*, vol. 156, no. 2, pp. 111947, Mar. 2022, <https://doi.org/10.1016/j.rser.2021.111947>.
- [13] Q. Liu, Y. Wang, Z. Gao, J. Sui, H. Jin, and H. Li, "Experimental investigation on a parabolic trough solar collector for thermal power

- generation,” *Science in China Series E: Technological Sciences*, vol. 53, no. 1, pp. 52–56, 2010, <https://doi.org/10.1007/s11431-010-0021-8>.
- [14] A. S. Kopalakrishnaswami and S. K. Natarajan, “Comparative study of modified conical cavity receiver with other receivers for solar paraboloidal dish collector system,” *Environmental Science and Pollution Research*, vol. 29, no. 5, pp. 7548–7558, 2021, <https://doi.org/10.1007/s11356-021-16127-z>.
- [15] S.-Y. Wu, L. Xiao, Y. Cao, and Y.-R. Li, “A parabolic dish/AMTEC solar thermal power system and its performance evaluation,” *Applied Energy*, vol. 87, no. 2, pp. 452–462, 2010, <https://doi.org/10.1016/j.apenergy.2009.08.041>.
- [16] W. G. Le Roux, “Maximum net power output from an integrated design of a small-scale open and direct solar thermal Brayton cycle.” PhD diss., University of Pretoria, 2011.
- [17] M. M. Aboelmaaref et al., “Hybrid solar desalination systems driven by parabolic trough and parabolic dish CSP technologies: Technology categorization, thermodynamic performance and economical assessment,” *Energy Conversion and Management*, vol. 220, no. 23, pp. 113103, 2020, <https://doi.org/10.1016/j.enconman.2020.113103>.
- [18] A. Suzuki, “General theory of exergy-balance analysis and application to solar collectors,” *Energy*, vol. 13, no. 2, pp. 153–160, 1988, [https://doi.org/10.1016/0360-5442\(88\)90040-0](https://doi.org/10.1016/0360-5442(88)90040-0).
- [19] W. G. Roux, T. Bello-Ochende, and J. P. Meyer, “Thermodynamic optimisation of the integrated design of a small-scale solar thermal Brayton cycle,” *International Journal of Energy Research*, vol. 36, no. 11, pp. 1088–1104, 2011, <https://doi.org/10.1002/er.1859>.
- [20] M. K. Gupta and S. C. Kaushik, “Exergetic performance evaluation and parametric studies of solar air heater,” *Energy*, vol. 33, no. 11, pp. 1691–1702, 2008, <https://doi.org/10.1016/j.energy.2008.05.010>.
- [21] A. El Ouederni, M. Salah, F. Askri, M. Nasrallah, and F. Aloui, “Experimental study of a parabolic solar concentrator,” *Revue des Energies Renouvelables*, vol. 12, no. 11, pp. 395–404, 2009, Accessed: June. 06, 2022. [Online]. Available: https://www.cder.dz/download/Art12-3_6.pdf
- [22] J. A. Duffie, W. A. Beckman, and W. M. Worek, “Solar Engineering of Thermal Processes, 2nd ed.,” *Journal of Solar Energy Engineering*, vol. 116, no. 1, pp. 67–68, 1994, <https://doi.org/10.1115/1.2930068>.
- [23] K. V. N. Rao, Srinivasa, B. J. M. Rao. "Low cost solar cooling system." *International Journal of Engineering and Innovative Technology (IJEIT)*, vol. 3, no. 4, pp. 58-61, 2013.
- [24] S. Gh. Yahya, Itimad D. J. Azzawi, M. K. Abbas, and A. A. Al-Rubaiy. "Characteristics of acoustic drivers for efficient coupling to thermoacoustic machines." *IMECS 2019*, pp. 469-474, Accessed: June.

- 06, 2022. [Online]. Available:
https://www.iaeng.org/publication/IMECS2019/IMECS2019_pp469-474.pdf
- [25] A. M. Dubey, “Modified vapour absorption refrigeration cycles,” *International Journal of Ambient Energy*, vol. 43, no. 1, pp. 2194–2200, 2020, <https://doi.org/10.1080/01430750.2020.1720807>.
- [26] E. M. Salilih, Y. T. Birhane, and N. H. Abu-Hamdch, “Performance prediction of a solar refrigeration system under various operating pressure of evaporator and condenser,” *Solar Energy*, vol. 209, no. 1, pp. 485–492, 2020, <https://doi.org/10.1016/j.solener.2020.09.033>.
- [27] B. Modi, A. Mudgal, B. D. Raja, and V. Patel, “Low grade thermal energy driven-small scale absorption refrigeration system (SSARS): Design, fabrication and cost estimation,” *Sustainable Energy Technologies and Assessments*, vol. 50, no. 2, pp. 101787, 2022, <https://doi.org/10.1016/j.seta.2021.101787>

Concrete with Coconut Fibre Treated with Sodium Hypochlorite – Compressive and Flexural Strength

Norisham Ibrahim*

School of Civil Engineering, College of Engineering,
Universiti Teknologi MARA, 40450, Shah Alam, Selangor, MALAYSIA
*noris024@uitm.edu.my

Muhammad Hafizhin Abdul Halim

Civil Engineer, PROLINTAS, Menara PNB, Jalan Tun Razak,
50400, Kuala Lumpur, MALAYSIA

ABSTRACT

Concrete needs to be reinforced to improve its engineering qualities. Coconut fibres were employed for this study since they are widely accessible and come in big numbers. The study compares the qualities of plain concrete and concrete reinforced with coconut fibre based on a laboratory experiment. Better management of these waste fibres will result from using coconut fibres. Two types of coconut fibre treatment were employed – treatment with tap water and treatment with sodium hypochlorite. It is found in this study that adding 1% of coconut fibre does not increase the concrete strength after 7 and 14 days of curing. However, it was discovered that using 1% coconut fibres treated using tap water increased the compressive and flexural strength of the concrete after 28 days of curing by roughly 4% and 3%, respectively. Compressive and flexural strength development agrees very well with each other. Hence, it is concluded that 1% was the ideal fibre concentration (by weight of cement) to obtain a better 28th day of compressive and flexural strength, although not for 7 and 14 days. However, concrete with the highest strengths demonstrated a very low slump value, only 20 mm. A smaller or bigger slump value showed smaller concrete strengths.

Keywords: Concrete; Coconut Fibre; Treatment; Compressive Strength

Introduction

Concrete is an essential material in the construction industry. The performance of concrete is evaluated on mechanical properties, which include compressive strength, tensile strength, and flexural strength. However, the use of cement in the current concrete has produced many environmental issues. Sustainable development can be attained by using coconut fibre reinforced concrete (CFRC) in the construction industry by declining CO₂ emissions and saving natural sources [1]. Therefore, much research has been carried out to replace cement with other materials. One of the most potential materials to replace cement is coir fibre.

Coconut fibre, also known as coir fibre, is a natural fibre that falls under fruit and comes from plants. Raja et al. [2] mentioned that CFRC is advantageous for commercial applications since it is lighter in weight, has a lower density, costs less money, and has less solidity than regular concrete. According to Ali et al. [3], coconut fibres have the highest toughness among natural fibres. The inclusion of coconut fibres effectively increased the splitting tensile strength and compressive strength of CFRC exposed to room temperature regimes for 7 and 28 days [4]. Findings in these studies [3]-[4] show that coconut fibre can be used as reinforcement in low-cost concrete structures.

Besides fibre length and content, the properties of CFRC can increase or decrease depending on fibre treatment [1]. For example, moisture in the coconut fibre contributes to the concrete's water volume if the fibre is not dried before mixing. In addition, the coconut fibre's density may affect the concrete's density. Therefore, the type of treatment used for the coconut fibre plays a vital role in determining the strength of the CFRC. According to Bhowmick et al. [5], the main drawback of natural fibres' use in composites lies in their hydrophilic nature, which can be improved by surface modification or matrix adjustments. Furthermore, selecting the correct content of coconut fibre in the mix design is very important because too much coconut fibre may decrease concrete performance [1]-[5].

Hence all properties such as mechanical, physical, method of fibre treatment and mix design must be considered in the study of the CFRC. Therefore, this study investigates the effect of treated coconut fibres on concrete density, compressive strength, and flexural strength. Thus, laboratory experiments were conducted to obtain the following:

1. The density of regular concrete and CFRC
2. The workability of regular concrete and CFRC
3. The compressive strength of regular concrete and CFRC
4. The flexural strength of regular concrete and CFRC

Treatment of Coir Fibres

A cementitious microstructure of high-performance concrete may give higher mechanical qualities with coir by improving its roughness through alkali treatment of the coir and protecting it with latex and pozzolana [6]. Brígida [7] reported three types of chemical treatment for coconut fibre; treatment with H_2O_2 , treatment with NaOCl, and treatment with NaOCl and NaOH. However, green coconut fibres were washed with distilled water before being treated and dried at 60 °C for 24 hours. For treatment with H_2O_2 , 2 g of coconut fibres were submitted to oxidation using 40 mL of a H_2O_2 solution in basic medium (0.05 g NaOH and 18 mL of H_2O_2 30%, v/v, for 100 mL of solution) at 85 °C for 2 hours. Meanwhile, for treatment with NaOCl, 5 g of fibres were soaked in 100 mL of 0.4% NaOCl (v/v, in glacial acetic acid) for about 2 hours at 85 °C. For treatment with NaOCl and NaOH, 5 g of fibres were soaked in 100 mL of NaOCl 4–6% (v/v): H_2O (1:1) for 2 hours at 30 °C. Finally, the fibres were washed with water and soaked in 100 mL of 10% NaOH for one hour at 30 °C to complete the treatment. After being treated, fibres were thoroughly rinsed with distilled water and dried under a vacuum for two hours.

Sodium Hydroxide (NaOH) was also used by Naveen [8]. This paper described how the coir fibres were processed before using them as replacement material. First, the coir fibres were immersed in a 5% Sodium Hydroxide (NaOH) solution for 24 hours to remove the unwanted layer of coconut coir fibres. The fibres were then washed abundantly with water to remove the NaOH before drying them in a furnace at 70 °C to 80 °C for 24 hours. Afterwards, the coir fibres were soaked in 5% silane and 95% methanol solution for 4 hours and dried at 70 °C for 24 hours. After the drying process finished, the coconut fibres were inserted into the cutting machine to cut into smaller pieces which lengths of less than 10 mm and this form is called whickers.

Other than concrete, coconut fibre was also tested as ropes. In this study [9], coconut fibre ropes were soaked in tap water for four hours to remove coir dust and dried in the open air afterwards. Ali and Chouh [9] conducted two types of treatment on the soaked ropes: treatment with boiling water and washing and treatment with chemicals. The soaked ropes were put in boiling water for two hours for treatment with boiling water. They were then washed with tap water until the colour of the water became clear. The ropes were finally dried in the same manner as soaked ropes. For chemical treatment, the soaked ropes were dipped in 0.25% Sodium Alginate ($NaC_6H_7O_6$) solution prepared with distilled water for 30 minutes. Next, these ropes were removed from the solution and soaked in 1% calcium chloride ($CaCl_2$) solution for 90 minutes. The ropes were finally dried.

Design Mix and Properties of CFRC

Ali [10] presents several researchers' results on the physical and mechanical properties of coconut fibres. Concerning this paper, the density of coconut fibre differs from 145 to 1370 kg/m³, while tensile strength varies from 15 to 500 MPa. The highest tensile strength presented in this paper comes from coconut fibre, with a density of 1150 kg/m³. The percentage of moisture present on a weight basis at the standard atmospheric condition for this coconut fibre is 11.4%. Ali [10] also reviewed the effect of fibre content, the impact of fibre pre-treatment and the development of fibre volume-fraction on the mechanical properties of mortar or concrete.

On the effect of fibre content, Ali [10] cited Slate [11] which used two types of design mix using cement sand ratio by weight. The first design mix was 1:2.75 with a water cement ratio of 0.54 and the second design mix was 1:4 with a water-cement ratio of 0.82. The fibre content was 0.08, 0.16 and 0.32% by total cement, sand, and water weight. Ali [10] found that the strengths of fibre-reinforced mortar increased for all designs with fibre contents. However, a drop in mortar strength was also noted when the fibre percentage rose.

On the effect of fibre pre-treatment, Ali [10] cited Li et al. [12], which studied untreated and alkalinized coconut fibres with two different lengths, 20 and 40 mm, in cementitious composites as reinforcement materials. This study used a design mix with cement: sand: water: superplasticizer ratio of 1: 3: 0.43: 0.01 by weight. The mortar with treated fibre has better flexural strength, higher energy absorbing ability and ductility and is lighter than the conventional mortar. In addition, a low amount of chemical agent and coconut fibres added to the cementitious matrix produced positive results.

On the effect of fibre volume, Ali [10] cited Baruah and Talukdar [13], which utilized a mixed design of cement: sand: aggregates as 1:1.67: 3.64 with a water cement ratio of 0.535 for ordinary concrete. Cement weighed 350 kg, fine aggregates weighed 568.40 kg, coarse aggregates weighed 1239.40 kg, and water weighed 182 kg per cubic meter of concrete mix. The maximum size of aggregates is 20 mm. For CFRC, Baruah and Talukdar [13] added 4 cm long by 0.4 mm wide coir fibres with volume fractions of 0.5, 1, 1.5, and 2%. They [13] found that the highest increment in all types of tested strength was obtained from a mixed design with 2% fibres. The compressive strength, splitting tensile strength, modulus of rupture and shear strength were increased up to 13.7, 22.9, 28.0 and 32.7%, respectively, compared to plain concrete. The strength of CFRC with other volume fractions also increased but in a smaller percentage. Meanwhile, Ali et al. [6] concluded in their review that most studies suggested that maximum gain in compressive strength of normal strength concrete is achieved at 0.5-1.5% incorporation of coir by the weight of cement.

Nadgouda [14] from Mumbai used local coconut fibre in his study of CFRC. The study used 3%, 5%, and 7% (by the weight of cement) of coconut fibre in the concrete mix. The nominal mix design was 1:1.5:3. Nadgouda [14] used cubes for compressive strength, beams for flexural strength and cylinders for tensile strength tests. Tests were conducted on 3, 7 and 28 days. Nadgouda [14] found that an increase in the fibre content decreases all the strength (compressive, flexural, and tensile) on the 28th day. Interestingly, the strength of the concrete specimen on day 7 dropped to a smaller value than that of the concrete specimen on day 3. This condition is valid for all the strengths for CFRC containing 7% fibre.

Raja et al. [2] present the properties of coir fibre as follows. The density, tensile strength, Young's modulus and failure strain of coir fibre is 1.2 g/cm³, 150-180 MPa, 4-6 GPa and 20-40%, respectively. According to them, factors affecting the mechanical performance of natural fibre composite include fibre selection, matrix selection, interface strength, fibre dispersion, fibre orientation, manufacturing method, and porosity. Furthermore, chemical treatment can further improve the physical and mechanical properties of coir fibre. Meanwhile, surface modification of coir fibre can reduce moisture adsorption. Hence, it is essential to consider all these factors before using coir fibre as a replacement material.

Bamigboye et al. [15] investigated cement replacement with coconut fibre. The replacement percentages were 0.25, 0.5, 0.75 and 1% by weight of cement in a design mix of 1:3:4. Types of fibre treatment were untreated, soaked in water, and soaked in 1% NaOH. The fibres were washed in water three times and oven dried at 110 °C. Concrete cubes were moulded and cured for 7, 14, 24 and 28 days. These concrete cubes were subjected to 250 °C and 150 °C for two hours. The compressive strength of the concrete increased when using 0.25 and 0.5% of cement replacement but reduced for more than 0.5% replacement. Concrete with 0.5% cement replacement and treated with water exhibited the highest 28th days compressive strength, 28.71 N/mm², 3.88% more significant than the control specimens. Hence, Bamigboye et al. [15] concluded that coconut fibres are an excellent material for improving the strength of concrete, even after it was exposed to a certain degree of elevated temperature. However, research by Avubothu [4] found that compressive strength and split tensile strength of CFRC only increased very little when subjected to 200 °C.

Syed [16] conducted a study to obtain a good compressive strength of CFRC, in which he concluded that the ideal water-cement ratio is 0.40 while the optimal fibre content ratio is 0.6% and 1.2%. In the same year, Hettiarachchi [17] used a mix design ratio by unit weight per metre cube (kg/m³) of 1:0.55:1.72:3.2 for cement:water:sand:gravel, respectively to study CFRC. The coir fraction was 0.5, 1.0, 1.5 and 2.5%. The fibres used were washed with potable water three times to remove impurities, naturally dried for 24 hours, and immersed in a 5% NaOH solution for 30 minutes. After

immersing the fibres in alkaline solutions, they were washed with water several times to allow the absorbed alkali to leach from the fibres and dried again naturally for over 24 hours before mixing with concrete. This study used two types of fibre coatings: epoxy paint and varnish coating.

Hettiarachchi and Thamarajah [17] found that an increase in coir fibre content reduced the workability of the coir-concrete mix. CFRC specimens with alkali-treated coir fibres and fibres coated with epoxy and varnish exhibited an apparent increase in workability. Epoxy and varnish indicated slightly higher workability compared to sodium hydroxide. The fibre content of around 1% (by cement mass) in CFRC gave the best compressive strength, flexural strength and split tensile strength. At a fibre content of 1%, the compressive strength and flexural strength increased by 5.59% and 12.96%, respectively. For split tensile strength, the results vary from 2.99 to 3.25 MPa.

The previous studies show two tests essential for normal concrete strength: compressive and flexural strength tests. Also, two kinds of fibre treatment were selected, treatment with tap water and treatment with NaOCl. One percent of fibre [17] was chosen as additional material to the original concrete mix.

Materials and Methodology

This study used two treatments: treatment using tap water and treatment using NaOCl solution. First, the coconut fibres were oven-dried for two hours at 30 °C. Then, the dried fibres were soaked in tap water for 30 minutes and washed. These steps were repeated three times to remove dust in the coconut fibres that may cause degradation. Once completed, these soaked coconut fibres were sun-dried to remove any moisture and cut into 50 mm [18] in length. These coconut fibres are tap water-treated coconut fibre (TWF).

For bleach treatment, a solution consisting of 4 litres of bleach (4-6% of NaOCl) and 4 litres of tap water was used. TWF was immersed in the sodium hypochlorite solution for 24 hours at room temperature. After being immersed, the TWF was exposed to the sun again for drying. These coconut fibres are known as NaOCl-treated coconut fibres (NaF). Figure 1 shows the coconut fibre in several conditions. Figure 1a shows the coconut fibre's condition before being treated, while Figure 1b shows the condition of the coconut fibre after being treated with tap water. Figure 1c illustrates the coconut fibres being soaked in NaOCl, and Figure 1d portrays the coconut fibres after being treated with tap water.

All concrete batches were designed as plain concrete (without fibre) with a 28th day compressive strength of 30 MPa. The concrete mix design followed Othman [19] with the mix design ratio by unit weight per meter cube (kg/m^3) of 1:0.53:1.74:2.13 for cement: water: sand: gravel, respectively. The maximum size of aggregate used is 10 mm. The concrete was mixed in a

concrete mixing machine. All the materials were carefully added to the drum while mixing. Mixing was stopped once all the materials had been thoroughly mixed. The number of specimens for each concrete batch is shown in Table 1. The cube size is 100 x 100 x 100 mm, while the prism size is 100 x 100 x 500 mm. Due to a lack of power and material, only one prism was moulded for each flexural strength test. Before pouring the concrete into the cube mould, the density and the workability of the concrete were tested. Figure 2 shows the slump test being conducted, while Figure 3 shows the container used to measure density.

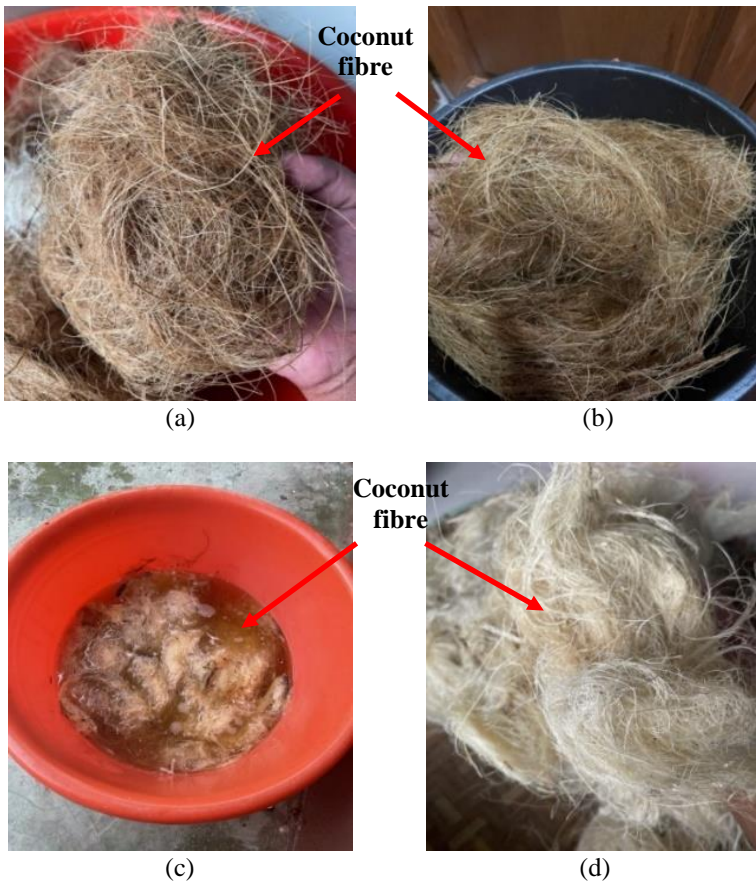


Figure 1: (a) Coconut fibre before treatment, (b) coconut fibre after being treated with tap water, (c) coconut fibre being soaked in NaOCL, and (d) coconut fibre after being treated with NaOCL

Table 1: Number of specimens for each concrete batch

	Coconut fibre (%)	Sample names	Compressive strength			Flexural strength
			7 days	14 days	28 days	28 days
Plain concrete	0.0	PC	3	3	3	1
Concrete with TWF	1.0	1.0TWF	3	3	3	1
Concrete with NaF	1.0	1.0NaF	3	3	3	1

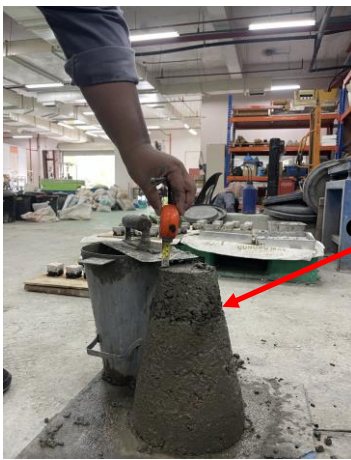


Figure 2: Slump test being conducted



Figure 3: Container for density measurement

Results and Discussion

Table 2 shows that plain concrete exhibits the most considerable density. Meanwhile, adding concrete with 1% fibre treated with either tap water or sodium hypochlorite solution reduced the density of the concrete by 3.58 and 4.67%, respectively. Similar findings were obtained by Hwang et al. [20] and Ahmad et al. [21]. This reduction in density can be attributed to the relatively low density of the coconut fibres, which is from 145 to 1200 kg/m³ [10].

Table 2: Density of the concrete

Concrete	PC	1.0TWF	1.0NaF
Density (kg/m ³)	2494.04	2404.67	2378.87
Increase (%)	0.00	-3.58	-4.67

Table 3 shows the slump test result of the fresh concrete. The plain concrete shows a slump value of 37 mm, considered low workability [15]. Adding 1% coconut fibre even reduced the workability of the fresh concrete. Similar findings were observed by Hettiarachchi and Thamarajah [17], Bamigboye et al. [15], and Hwang et al. [20]. Adding 1% of non-treated coir fibre reduced the slump from 114 mm to 82 mm but increased to 88 mm for coir fibre treated with sodium hydroxide [17]. The finding from the current study is also supported by Ali [6], which concluded that coir as a fibre reinforcement is harmful to the workability of normal strength concretes. The increase in fibre content beyond 0.5% decreased the workability [15] due to the hydrophilic character of coir, where moisture absorption is very high, leading to poor interfacial adhesion with the hydrophobic cement matrix [17]. Water absorption of specimens made with 1% volume fractions of coconut fibre was 7.1% [20]. Hence, Ali [6] recommended the application of superplasticizers in coir-reinforced mixes to avoid workability issues. The optimum range suggested is 1.0% by weight of cement. Coconut fibre treated with sodium hypochlorite solution has the lowest slump value.

Table 3: Workability of the concrete

Concrete	PC	1.0TWF	1.0NaF
Slump (mm)	37	20	11
Increase (%)	0.00	-45.95	-70.27

The compressive strength result is displayed in Table 4. After seven days of curing, plain concrete has the highest compressive strength (34.19 MPa) compared to concrete added with 1% concrete fibre and the same after 14 days of curing. However, concrete fibre with water-treated coconut fibre shows the highest 28th-day compressive strength with 44.30 MPa, followed by plain concrete with 42.55 MPa. The lowest 35.59 MPa is demonstrated by concrete with coconut fibre treated with sodium hypochlorite. These results indicate that adding 1% of coconut fibre treated with sodium hypochlorite solution without any superplasticizer decrease the compressive strength of the concrete. Concrete with coconut fibre treated with tap water also reduced the compressive strength at 7 and 14 days. This finding agrees very well with Hwang [20]. However, the strength of CFRC using coir treated with tap water increased when tested at the age of 28 days. This increase shows a good sign of significant improvement from 14 to 28 days. Although Ali [6] suggested

that coir fibre is helpful for normal-strength concrete, this study indicates that this suggestion is valid for concrete mixed with coir treated with tap water at 28 days.

Table 4: Average compressive strength (CS) of the concrete

Type of concrete	PC		1.0TWF		1.0NaF	
Concrete age (day)	CS (MPa)	CS (MPa)	Increase (%)	CS (MPa)	Increase (%)	
7	34.19	32.70	-4.36	28.67	-16.14	
14	39.19	38.25	-2.40	32.13	-18.01	
28	42.55	44.30	4.11	35.59	-16.36	

Flexural strength tests were conducted after 28 days of curing. Results are shown in Table 5. Concrete with 1% coconut fibre treated with tap water showed higher strength than the other two. This result is parallel with the results obtained from the compressive strength test.

Table 5: Flexural strength (FS) on 28th days

Type of concrete	PC		1.0TWF		1.0NaF	
Concrete age (day)	FS (MPa)	FS (MPa)	Increase (%)	FS (MPa)	Increase (%)	
28	24.77	26.73	3.19	22	-17.70	

According to Ahmad et al. [21], the most crucial factor for better concrete performance is the coconut fibre dosage, as a higher dose causes more voids in hardened concrete due to a lack of workability, which lowers the concrete's mechanical and durability performance. Ahmad et al. [21] further explained that different concrete doses are appropriate depending on the fibre length, diameter, and aspect ratio. Therefore, Figure 4 illustrates the relationship of slump value on the compressive strength and flexural strength of the CFRC at 28 days. It is observed from the graph that the development of compressive strength agrees very well with the progress of flexural strength. This finding demonstrates that the highest compressive and flexural strength on the 28th day is obtained from CFRC with a slump value of 20 mm, which comes from concrete added with coir fibre treated with tap water.

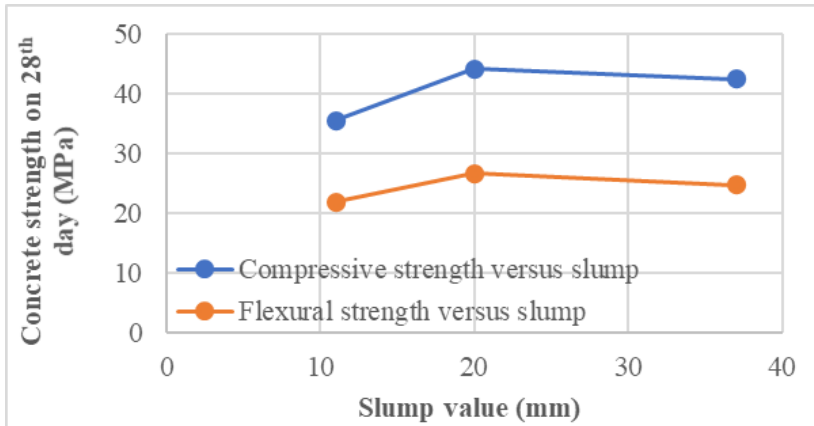


Figure 4: Concrete strength on 28th day versus slump value

Conclusion

The study discovered that adding coconut fibre treated with tap water into the concrete mix increased the compressive and flexural strength of the concrete after 28 days of curing. This strength increase shows that coconut fibres treated with water gave higher concrete strength due to reduced hydrophobic surface impurities such as hemicellulose, pectin and waxes, which makes the fibre more hydrophilic [22], hence increasing the bond between the fibre and cement matrix [23]. However, when coconut fibre treated with sodium hypochlorite was added to concrete, it resulted in lower compressive strength than tap water treated fibre and plain concrete. This is because, treatment with sodium hypochlorite removes the hemicelluloses and surface lignin of the coconut fibre. Removal of hemicellulose increases moisture adsorption, and lignin removal increases the water retention ability. Hence the concrete becomes weaker. In addition, water penetrating the fibre breaks the bond between the fibre and cement matrix, resulting in more void and increased water permeability [24].

Contributions of Authors

The authors confirm the equal contribution in each part of this work. All authors reviewed and approved the final version of this work.

Funding

This work received no specific grant from any funding agency.

Conflict of Interests

All authors declare that they have no conflicts of interest

Acknowledgment

The authors would like to thank all the laboratory staff in the concrete laboratory in the School of Civil Engineering, College of Engineering, Universiti Teknologi MARA, Shah Alam, for their expertise and assistance throughout all aspects of the laboratory work.

References

- [1] M. Gu, W. Ahmad, T.M. Alaboud, A. Zia, U. Akmal, Y.A. Awad, and H. Alabduljabbar, "Scientometric analysis and research mapping knowledge of coconut fibers in concrete", *Journal of Materials*, vol. 15, no. 5639, pp. 1-19, 2022. <https://doi.org/10.3390/ma15165639>
- [2] T. Raja, P. Anand, M. Karthik and M. Sundaraj, "Evaluation of mechanical properties of natural fibre reinforced composites: A review", *International Journal of Mechanical Engineering and Technology*, vol. 8, no.7, pp.915-924, 2017. <https://www.researchgate.net/publication/319041556>
- [3] M. Ali, A. Liu, H. Sou and N. Chouw, "Mechanical and dynamic properties of coconut fibre reinforced concrete". *Construction and Building Materials*, vol. 30, pp. 814-825, 2012. <https://doi.org/10.1016/j.conbuildmat.2011.12.068>
- [4] M. Avubothu, S. Ponaganti, R. Sunkari, M. Ganta, "Effect of high temperature on coconut fiber reinforced concrete", *Proceedings of Materials Today*, vol. 52, Part 3, pp. 1197-1200, 2022. <https://doi.org/10.1016/j.matpr.2021.11.036>
- [5] M. Bhowmick, S. Mukhopadhyay and R. Alagirusamy, "Mechanical properties of natural fibre-reinforced composites", *Textile Progress*, vol. 44, no. 2, pp. 85-140, 2012. <https://doi.org/10.1080/00405167.2012.676800>
- [6] B. Ali, A. Hawreen, N. B. Kahla, M. T. Amir, M. Azab, A. Raza, "A critical review on the utilization of coir (coconut fiber) in cementitious

- materials”, *Construction and Building Materials*, vol. 351, pp. 1-18, 2022. <https://doi.org/10.1016/j.conbuildmat.2022.128957>
- [7] A. I. S. Brígida, V. M. A. Calado, L. R. B. Gonçalves and M. A. Z. Coelho, “Effect of chemical treatments on properties of green coconut fiber”, *Carbohydrate Polymers*, vol. 79, no. 4, pp. 832-838, 2010. <https://doi.org/10.1016/j.carbpol.2009.10.005>
- [8] P. N. E. Naveen, and T. D. Maju, “Evaluation of mechanical properties of coconut coir fiber reinforced polymer matrix composites”. *Journal of Nano Research*, vol. 24 pp. 34-35, 2013. Available online: 2013-09-18. <https://doi.org/10.4028/www.scientific.net/JNanoR.24.34>
- [9] M. Ali and N. Chouw, “Experimental investigations on coconut-fibre rope tensile strength and pullout from coconut fibre reinforced concrete”, *Construction and Building Materials*, vol. 41, pp. 681-690, 2013. <https://doi.org/10.1016/j.conbuildmat.2012.12.052>
- [10] M. Ali, “Coconut fibre: A versatile material and its applications in engineering”, *Journal of Civil Engineering and Construction Technology*, vol. 2, no. 9, pp. 189-197, 2011. Available online at <http://www.academicjournals.org/jcect>
- [11] F.O . Slate, “Coconut fibers in concrete”. *Engineering Journal of Singapore*, vol. 3, no. 1, pp. 51-54, 1976.
- [12] Z. Li, L. Wang and X. Wang, “Flexural characteristics of coir fiber reinforced cementitious composites”, *Fibers and Polymers*, vol. 7, no. 3, pp. 286-294, 2006. <https://doi.org/10.1007/BF02875686>
- [13] P. Baruah, S. A. Talukdar, “A comparative study of compressive, flexural, tensile and shear strength of concrete with fibres of different origins, *Indian Concrete Journal*, vol. 81, no. 7 pp. 17-24, 2007. [Online]. Available:https://www.researchgate.net/publication/290567582_A_comparative_study_of_compressive_flexural_tensile_and_shear_strength_of_concrete_with_fibres_of_different_origins
- [14] K. Nadgouda, “Coconut fibre reinforced concrete”, In *Thirteenth IRF International Conference*, Chennai, India, pp. 5-7, 2014. ISBN: 978-93-84209-51-3. [Online]. Available: https://www.digitalxplore.org/up_proc/pdf/102-14109319585-7.pdf
- [15] G. Bamigboye, B. Ngene, O. Aladesuru, O. Mark, D. Adegoke and K. Jolayemi, “Compressive behaviour of coconut fibre (cocos nucifera) reinforced concrete at elevated temperatures”, *Fibers*, vol. 8, no. 5, pp. 1-12, 2020. <https://doi.org/10.3390/fib8010005>
- [16] H. Syed, R. Nerella, S. R. C. Madduru, “Role of coconut coir fiber in concrete”, *Materials Today : Proceedings*, vol. 27, Part 2, pp. 1104-1110, 2020. <https://doi.org/10.1016/j.matpr.2020.01.477>
- [17] C. Hettiarachchi and G. Thamarajah, “Effect of surface modification and fibre content on the mechanical properties of coconut fibre reinforced concrete, *In Advanced Materials Research*, vol. 1159, pp. 78-99, 2020. doi:10.4028/www.scientific.net/AMR.1159.78

- [18] M. D. Bijo, U. Sujatha, "Mechanical strength and impact resistance of hybrid fiber reinforced concrete with coconut and polypropylene fibers", *Materials Today : Proceedings*, vol. 65, Part 2, pp. 1873-1880, 2022. <https://doi.org/10.1016/j.matpr.2022.05.048>
- [19] N. H. Othman, "Design of normal concrete mixes Bre," *Academia.edu*, 08-Aug-2017. [Online]. Available: https://www.academia.edu/34172199/Design_of_normal_concrete_mixes_BRE.
- [20] C. L. Hwang, V. A. Tran, J. W. Hong and Y. C. Hsieh, "Effects of short coconut fiber on the mechanical properties, plastic cracking behavior, and impact resistance of cementitious composites", *Construction and Building Materials*, vol. 127, pp. 984-992, 2016. <https://doi.org/10.1016/j.conbuildmat.2016.09.118>
- [21] J. Ahmad, A. Majdi, A. Al-Fakih, A. F. Deifalla, F. Althoey, M. H. El Ouni and M. A. El-Shorbagy, "Mechanical and durability performance of coconut fiber reinforced concrete: A state-of-the-art review", *Materials*, vol. 15, no. 3601, pp. 1-24, 2022. doi: 10.3390/ma15103601
- [22] L. Mishra and G. Basu, "Coconut fibre: Its structure, properties and applications," In *Handbook of Natural Fibres, Woodhead Publishing Series in Textiles*, pp. 231-255, 2020. <https://doi.org/10.1016/B978-0-12-818398-4.00010-4>
- [23] J. G. Alotaibi, A. E. Alajmi, B. F. Yousif and N. D. Salih, "Effect of Fibre Content on Compressive and Flexural Properties of Coconut Fibre Reinforced Epoxy Composites", *American Journal of Applied Sciences*, vol.17, no.1, pp.141-155, 2020. <https://doi.org/10.3844/ajassp.2020.141.155>
- [24] O. I. Akpokodje, H. Uguru, D. Esegbuyota. "Study of flexural strength and flexural modulus of reinforced concrete beams with raffia palm fibers", *World Journal of Civil Engineering Construction Technology*, vol. 3 no. 1, pp. 057- 064, 2019.

Corrosion Resistance Enhancement for Low Carbon Steel by Gas Phase Coating

Sameer K. Fayyadh*

Department of Engineering Machine and Agriculture Equipment,
College of Agricultural Engineering Sciences, University of Baghdad, IRAQ
*samir.faiad@coagri.uobaghdad.edu.iq

Faras Q. Mohammed

Department of Production Engineering and Metallurgy,
University of Technology, Baghdad, IRAQ

ABSTRACT

Corrosion Resistance Enhancement for low carbon steel is very important to extend its life service, the coating process is one of the methods which can using to achieve this, and it's the most important in surface treatments to improve the properties of metals and alloys surfaces such as corrosion resistance. In this work, low carbon steel was nitrided and coated with nano zinc using gas phase coating technical, to enhance the resistance of corrosion. The process included adding two layers. The first, a nitride layer, was added by precipitating nitrogen (N) gas, and the second, a zinc (Zn) layer, was added by precipitating Zn. The process of precipitating was carried out at different periods (5, 10, and 15 minutes). Scan electron microstructure (SEM), X-ray diffraction (XRD) and corrosion tests were carried out. The SEM and XRD results showed a new microstructure with the emergence of new phases (C_3N_4 , $Zn(N_3)_2$, and γN). Also, the results of the corrosion test showed a significant improvement in corrosion resistance through a reduction in the corrosion rate (CR) and corrosion current density (i_{corr}) which reached $(1.598 \times 10^{-3} \text{ mmpy})$ and $(1.422 \times 10^{-7} \text{ Amp/cm}^2)$ respectively, for coated samples, compared with 1.803×10^{-1} and 1.604×10^{-5} , respectively, for the base metal. also found an appreciable increase in corrosion protection efficiency (CPE), which reached 99.11%.

Keywords: Carbon Steel; Coating; Corrosion; Gas Phase, Surface Treatment

Introduction

Low carbon steel (0.25% C max.) is usually applied in numerous industries, including automotive, bridges, ships, storage tanks, large pipes, etc., for its low price and excellent mechanical properties, machinability, weldability, and formability [1]-[2]. However, carbon steel has low resistance to corrosion, which is considered a major economic problem worldwide. Because low carbon steel equipment and machine parts are highly corrosive in chloride or seawater environments, which have varying corrosive levels depending on ion concentration, evaluating corrosion problems in carbon steel is critical [3]-[5]. However, corrosion can be controlled in several ways, including the use of a protective coating, which is the recommended solution for developing materials for resistance to corrosion [6]-[7]. It plays a significant part in forming a barrier between metal surfaces and corrosive media, in addition to improving wear and hardness by modifying the surface's characteristics and forming a new transition region between the deposited layer and the base metal. Metal protection can be achieved by forming thin layers on their surface with thicknesses ranging from a few microns to many atomic layers [8]-[10].

The coating offers protection for the metal by acting either as a sacrificial coating or as a physical barrier. It is essential to have strong adhesion between the protected metals and the coating [11]-[12]. The effectiveness and durability of anti-corrosion coatings depend on the properties of both the substrate and the coating material [10], [13]-[16]. Numerous studies have been done in this field; Ibrahim et al. [17] found that the corrosion resistance of stainless steel 316L was improved after coating it with epoxy-zinc oxide nanocomposite. Also, Dorofeeva et al. [8] reported that stainless steel coated with multi-layers exhibits significantly (tenfold) greater corrosion resistance than the substrate. The coating is made using either the chemical vapour deposition (CVD) or physical vapour deposition (PVD) processes, and sometimes both together, to increase their lifespan. These methods can produce different types of nanostructure coatings. In PVD, the coating material is first evaporated and subsequently condensed onto the substrate. The CVD process, on the other hand, is a chemical reaction that involves the deposition of solid material from a gas or vapour phase onto a heated metal surface [18]-[21]. The deposition of nanostructure coatings on the substrate is usually performed by gas phase deposition procedures. Gas phase deposition has numerous advantages, including high density, chemical stability, good substrate adhesion even on complex shapes, deposition on any desired substrate, and high purity [22]-[24]. Choosing the appropriate coating type for a specific material plays a fundamental role in directly improving or consolidating the surface performance during service. In general, a protective coating made of Zn and Zn alloys is used for a wide variety of applications, including carbon steel to prevent corrosion. Zn

coatings have excellent resistance to corrosion and the possibility for economic competitiveness [25]-[29]. On the other hand, adding nitrogen gas to steel through the nitriding process leads to improving the surface properties, such as increasing the corrosion resistance by the formation of nitriding layers [30]-[31]. This work is aimed at protecting low carbon steel from corrosive ingredients present in the working environment and enhancing the corrosion resistance through the deposition of the layers of coating of N and Zn using the gas-phase method.

Materials and Methods

Materials

The low-carbon steel AISI 1020 was used as a substrate material in all of the practical experiments. The chemical analysis of low carbon steel is shown in Table 1 and compared with American Standard [32]. N, Ammonia (NH₃) gas, and Zn solid target with a purity of 99.9% were supplied from a local market.

Table 1: Chemical composition of AISI 1020

Elements	C	Mn	P	S	Fe
Actual value %	0.20	0.55	0.01	0.04	Bal.
Standard value %	0.18-0.23	0.3-0.6	0.04 max.	0.05 max	Bal.

Methods

Samples prepared

Specimens that were used for microstructure tests were cut with dimensions of 10x10x3 mm, while specimens used for the corrosion test were cut with dimensions of 15x15x3 mm. All specimens were conventionally prepared before being ready for the nitriding and Zn coating processes.

Coating processes

The nitriding process was performed by the CVD technique. For this process, a GSL-1600-60X high-temperature vacuum tube furnace was utilized. It consists of a tube with a length of 1000 mm, a 60 mm diameter, and an inner diameter of 54 mm. Using a high-precision SCR (Silicon controlled Rectifier-digital controller) power controller (± 1 °C) accuracy, the temperature of the GSL 1600-60X tube furnace is controlled. A two-stage rotary vacuum pump with a 120 SLPM (Standard Litter Per Minute) capacity was equipped for the furnace. In the nitriding process, NH₃ (gas) was utilized to supply the gas reactant with atoms of nitrogen, while N₂ gas was employed as a carrier gas to carry out the process. To reduce residual stresses, all nitriding samples were heated to 550 °C. To deposit a thin film of the Zn

nano-structure coating, the VTC-16-D device was used, which, a desktop Plasma Sputtering Coater involving a height-adjustable sample holder and a 3-target head, especially suitable for coating conductive metal film samples. The parameters of the sputtering process were vacuum pressure of 10-1 Torr, current of 18 mA, and 2 cm³/min of the flow rate of argon gas. The coating processes were performed with different deposition times of 5, 10, and 15 minutes.

Characterizations

Microstructure and X-ray diffraction

XRD analysis was carried out using an x-ray diffractometer, type XRD-6000 Shimadzu, with Cu-K α radiation and a 0.154 nm angle of incident. Also, a microstructure examination was carried out using a Tescan VEGA 3SB SEM with an accelerating voltage range of 200 v to 30 kv and a power magnification range of 6x to 100000x.

Electrochemical performance

The Tafel polarization test was used to evaluate the coating's ability to protect and prevent low-carbon steel from corrosion. The experiment was conducted using CHI 604E POTENTIOSTAT. The conventional three-electrode electrochemical cell was used to measure the test output. The electrochemical cell includes, (Pt) as a counter electrode, saturated Ag/AgCl as a reference electrode, and a sample holder as the working electrode. The cell parameters were the scanning of electrode potential between -1.6 and +0.6 V at a scan rate of 0.01 V.s⁻¹ and 1.0 cm² was the area of exposed work to the aqueous solution. All specimens were examined at room temperature and using an aqueous solution of 3.5% NaCl. It's a simulated marine environment which is the most corrosive medium for the steel substrate.

Results and Discussion

XRD analysis

The XRD analysis and identifying the presence phases were done using the International Center for Diffraction Data (ICDD) cards and Match! 3 software. Figure 1 shows the XRD pattern that was conducted for the nitriding and Zn-coated low carbon steel samples. Both samples confirm the existence of α -Fe as the original alloy substance at 2θ angles of 64.41 and 44.63 with an index of (200) and (101), respectively (from ICDD card no. 00-006-0696). Regardless of the Fe phase, the two analyzed samples can show considerable differences in the microstructure and phases existing in the figure. The nitride sample's XRD analysis revealed the presence of the C₃N₄ phase at 2 angles of, 62.47, 37.026, and 30.06 with (112), (110), and (100) indices, respectively (from ICDD card no. 00-053-0671). This proves that the

intermixing was done between the nitriding layer and substrate through the process of nitriding under the process condition. Additionally, the γN phase was observed in this pattern at 2θ angles of 54.02, 43.051, and 35.485, with (200), (111), and (101) indices. The XRD patterns for the Zn-N coatings deposited under different conditions are also shown in Figure 1. These phases were formed as a result of the interactions between the substrate and the coating materials under the conditions of the deposition processes. The nitriding and coating of low carbon steel by zinc confirmed the presence of several compounds in addition to the C_3N_4 and γN phases that were formed as a result of the nitriding processes. The XRD analysis of the other sample revealed the presence of a new phase in this pattern in comparing to other nitriding samples, with three distinct peaks for $\text{Zn}(\text{N}_3)_2$ identified at 47.319, 33.44, and 22.44 with indices of (123), (210), and (200) that may be identified [from ICDD card no. 00-023-0740]. The XRD analysis can be used to find many information regarding material crystallography and the microstructure examination. In this regard, the diffraction peak intensities corresponding to some of the presented phases was found to be gradually decrease and a peak-broadening were reduced for these samples as it was shown in Figure 1. Also, the shifting in the diffraction peaks angles for these samples (at 10 minutes toward higher diffraction angles was observed as the deposition time was increased to 20 minutes. indicating a decrease in the coating lattice parameter which indicates that a polycrystalline structure was developed for this sample in Figure 1.

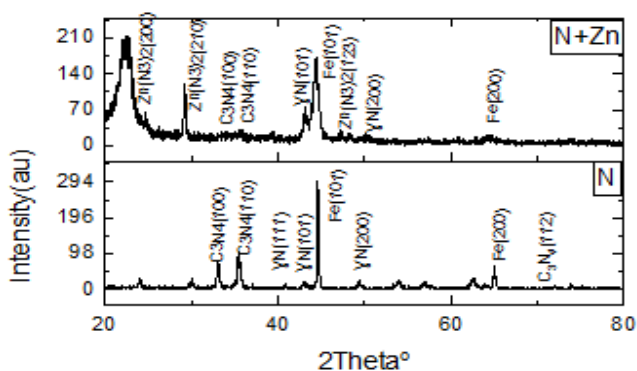


Figure 1: XRD analysis for surface treated samples

SEM

Figures 2, 3, and 4 show the morphology of the low carbon steel surface, which was nitrided and coated with a film of Zn at different deposition times. In Figure 2, the surface morphology after nitriding treatments at 500 °C shows a dense structure for the layer of nitrogen expanded austenite (γN),

accompanied by a uniform nitriding layer with a very smooth finish of the surface, and no visible cracks were observed. It was due to the intensive nitride precipitation that occurred that expanded austenite was also detected, as was evidenced in XRD test results. The surface morphology for the Zn coating on the nitriding low carbon steel surface is shown in Figures 3 and 4 with different deposition times. Deposition of Zn at a low deposition time will result in a surface that is characterized by an amorphous matrix that contains a fine nanocrystal fiber structure that is visible in SEM images of this sample. Also, a longitudinal micro void can be detected in this image that formed in the coating's surface because of the short deposition period, which caused a decrease in the amount of deposited coating. A so-called thin film of the coating was produced with an $8.3 \mu\text{m}$ thickness for the zinc coating layer, which was determined by the longitudinal gap shown in Figure 2. As the deposition time for Zn coatings increased to 20 minutes, a higher deposition rate occurred, which resulted in a change in the morphology towards a denser microstructure, more uniform coating, a much coarser surface finish than the former surface layer, and no visible microvoids. Also, a nano-crystalline fiber structure can be detected. A higher deposition time offers more deposition, which can increase the average coating thickness. It was revealed that the Zn coating's thickness was obtained from coating for 20 minutes (Figure 5). and was approximately $23 \mu\text{m}$. This thickness, regarded as relatively large, was obtained as a result of higher deposition time for the zinc coating layer.

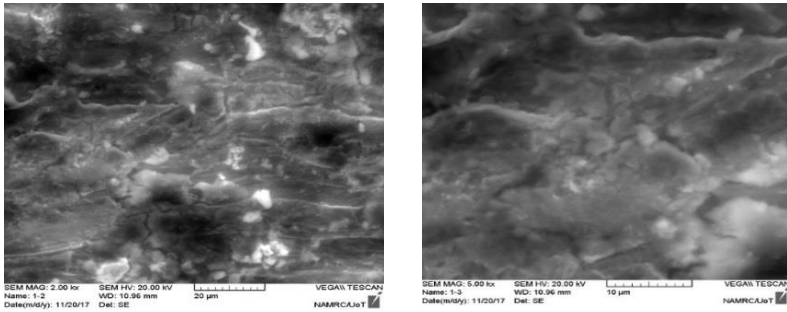


Figure 2: SEM micrograph for nitriding low carbon steel surface with different magnifications

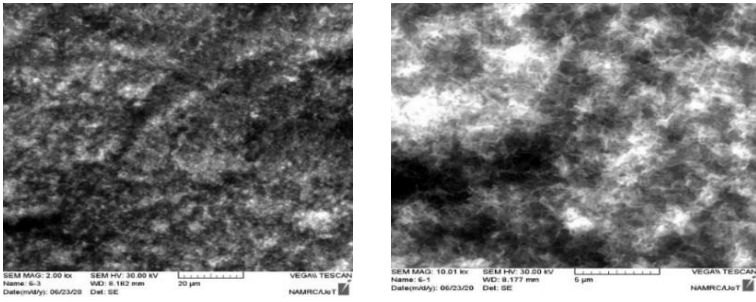


Figure 3: SEM micrograph for nitriding and Zn coated low carbon steel surface at 10 minutes with different magnifications

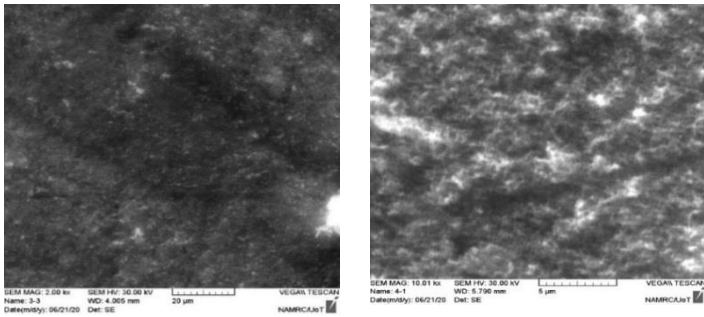


Figure 4: SEM micrograph for nitriding and Zn coated low carbon steel surface at 20 minutes with different magnifications

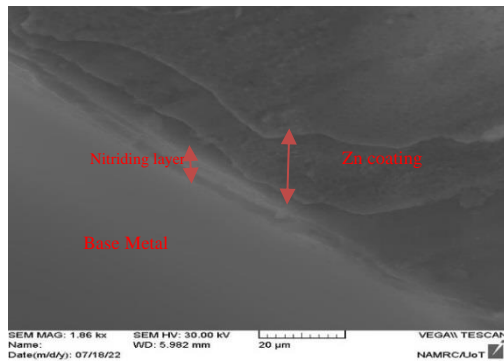


Figure 5: Cross section SEM image for nitriding and Zn coated low carbon steel surface at 20 minutes

Corrosion behaviour

Figure 6 shows the Tafel polarization curves for coated and uncoated low carbon steel. It provides several significant parameters, such as corrosion current density (i_{corr}), corrosion potential (E_{corr}), and corrosion rate (CR), which was calculated by using the following equation [33].

$$CR = \frac{K1(i_{corr}) EW}{\rho} \quad (1)$$

where CR: corrosion rate (mm/y), $K1 = 3.27 \times 10^{-3}$ mm g/ μ A cm y, EW: Equivalent weight (the atomic weight of the element in gram/ valence of the element), ρ : density in g/cm³, and to evaluate the protective effect of coatings on low carbon steel, the criterion of corrosion protection efficiency (CPE) was also used and determined using the following equation [16], [34].

$$CPE(\%) = \frac{(I^{o_{corr}} - I^c_{corr})}{I^{o_{corr}}} 100\% \quad (2)$$

where $I^{o_{corr}}$ represents the corrosion current density (Amp/cm²) for the uncoated sample, while I^c_{corr} represents the corrosion current density (Amp/cm²) of the coated specimens. According to Figure 6, the (i_{corr}) for coated samples shifts to a lower value compared with (i_{corr}) for uncoated ones, which means that the corrosion resistance was increased after the coating processes, and it was observed that this increased depending on the parameters of the coating processes. From Table 2, it can be seen that the (i_{corr}) (1.604×10^{-5} Amp/cm²) of the uncoated sample was significantly higher compared with the (i_{corr}) (3.657×10^{-6}) for the sample that was only nitrided and (1.422×10^{-7} Amp/cm²) for samples that were coated with Zn after the nitriding process, which demonstrated the protective effect of the coating processes. In another word, the (CR) significantly decreased from (1.80×10^{-1} mmpy) for uncoated samples to (4.111×10^{-2} mmpy) for the sample that was only nitrided and (1.598×10^{-3} mmpy) for samples that were coated with Zn after the nitriding process, as shown in Table 2. Also, it was observed that incorporation of N and N + Zn nano-crystalline fiber structure into the substrate surface led to the addition of a significant decrease in (CR) and (i_{corr}), which led to a significant increase in CPE, reaching 77.20% for N coating and 99.11% for N + Zn coating. This result was in agreement with the findings of Zhang et al. [16]. The high CPE and low CR indicate that the coating by N+Zn causes the formation of a barrier that has a superior ability to prevent the penetration of corrosive species and, therefore, provides excellent resistance to corrosion due to the barrier properties offered by this coating. Compared between coated and uncoated samples, the coated one showed lower CR and higher CPE. This demonstrates the effectiveness of utilizing zinc as an insulating coating layer to prevent the transition of

corrosive media to the substrate, thereby enhancing the resistance to corrosion. Additionally, the zinc coating acts as a sacrificial or cathodic protection to prevent iron corrosion because zinc is more electronegative (more reactive) than steel in the galvanic series, which means the zinc coating acts as an anode. Also, it was observed that zinc coating after nitride achieved better results than only the nitride process, where the (i_{corr}) (1.422×10^{-7}) and CR (1.598×10^{-3}) lower compared to the (i_{corr}) (3.657×10^{-6}) and CR (4.111×10^{-2}) for only nitride. Also, the zinc coating after nitride achieved a higher corrosion protection efficiency (99.11%) compared to (77.20%) for only the nitriding process. On the other hand, it was observed that both (i_{corr}) and CR were significantly reduced while CPE highly increased as deposition time increased, to clarify this: as it was noted in the previous section, the thickness of the coating increases as time deposition increases; therefore, if a zinc coating is exposed to severe damage, the steel won't corrode until the surrounding zinc has been consumed. So, the amount of protection provided by a zinc coating is roughly proportional to the coating's thickness. finally, the results showed that the coating using N+Zn nanocrystalline fiber structure could be an active barrier and anti-corrosion performance enhancer that enhances the corrosion resistance of the low carbon steel, these results are in agreement with what was obtained by Dorofeeva et al. [8] and Ibrahim et al. [17].

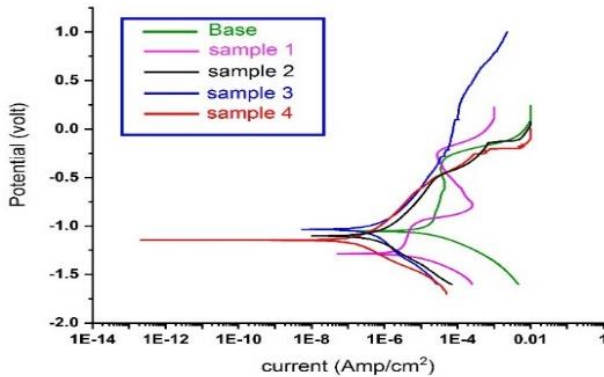


Figure 6: Tafel plots of base metal and coated samples at different deposition times measured in 3.5 % NaCl aqueous solutions at room temperature

Table 2: Tafel plots parameters

Sample no.	Process	Time	Ecorr. (volt)	icorr. (Amp/cm ²)	Corr rate (mmpy)
Base metal	uncoated	/	-1.055	1.604×10^{-5}	1.803×10^{-1}
1	N	5	-1.288	3.657×10^{-6}	4.111×10^{-2}
2	N+Zn	5	-1.102	4.777×10^{-7}	5.370×10^{-3}
3	N+Zn	10	-1.035	3.809×10^{-7}	4.282×10^{-3}
4	N+Zn	15	-1.144	1.422×10^{-7}	1.598×10^{-3}

Conclusions

From the previous results, it can be concluded, that the protection of low carbon steel from corrosion can be achieved by nitriding and the Zn coating process, where the coating led to a significant reduction in corrosion rates and a clear increase in the corrosion protection efficiency as follows:

1. Decrease the corrosion rate from 1.803×10^{-1} (mmpy) for uncoated samples to 4.111×10^{-2} (mmpy) for samples treated with nitridation only.
2. Reduce the corrosion rate from 1.803×10^{-1} (mmpy) for uncoated samples to 1.598×10^{-3} (mmpy) for zinc-coated samples after nitridation.
3. Compared with uncoated samples, the corrosion protection efficiency for samples treated with only nitride reached 77.20%, while it increased even more in samples that were coated with zinc after the nitridation process, reaching 99%.
4. A greater reduction was achieved in corrosion rate (5.370×10^{-3}) and a greater increase in corrosion protection efficiency (86.93%) for samples that were zinc-coated after nitriding, compared to corrosion rate (4.111×10^{-2}) (mmpy) and corrosion protective efficiency (77.2%) for samples that were only nitrided at the same period of deposition.
5. Corrosion rates decreased as Zn deposition time increased, with corrosion rates of 5.370×10^{-3} , 4.282×10^{-3} , and 1.598×10^{-3} for deposition times of 5, 10, and 15 minutes, respectively, and protection efficiency increased for the same periods.

Contributions of Authors

The authors confirm the equal contribution in each part of this work. All authors reviewed and approved the final version of this work.

Funding

This work received no specific grant from any funding agency.

Conflict of Interests

All authors declare that they have no conflicts of interest.

Acknowledgment

The authors would like to thank the microscopy and X-ray laboratories at the Nano Technology and Advanced Materials Research Center, University of Technology, as well as the corrosion laboratory in the Materials Research Department of the Science and Technology Authority.

References

- [1] A. E. S. Fouda, S. M. A. Motaal, A. S. Ahmed, and H. B. Sallam, "Corrosion Protection of Carbon Steel in 2M HCl Using Aizoon canariense Extract," *Biointerface Research in Applied Chemistry*, vol. 12, no. 1, pp. 230–243, 2021, doi: 10.33263/briac121.230243.
- [2] A. N. Mohsin, H. M. Yousif, and S. S. Ahmed, "Investigation of the Diffusion Depth of Ni-Cu Thermal Spray Coating for the Low Carbon Steel," *Engineering and Technology Journal*, vol. 39, no.11, pp. 1734–1739, 2021.
- [3] Esmaeil Jafari, "Improving the Corrosion Resistance of Carbon Steel by Ni-P Nano-Structured Coating," *Russian Journal of Electrochemistry*, vol. 57, no. 6, pp. 663–670, 2021, doi: 10.1134/S1023193520120083.
- [4] J. T. Stephen, A. Adebayo, and B. S. Oluwadare, "Corrosion Inhibition of Alkaline Solution on Low Carbon Steel In Local Water (Oku River)," *International Journal of Scientific and Technical Research in Engineering*, vol. 14, no .4, pp. 1-7, 2019.
- [5] N. Ali, T. E. Putra, Husaini, V. Z. Iskandar, and S. Thalib, "Corrosion Rate of Low Carbon Steel for Construction Materials in Various NaCl Concentrations," In *IOP Conference Series: Materials Science and Engineering*, vol. 536, no. 1, pp. 012015, 2019, doi: 10.1088/1757-899X/536/1/012015.
- [6] O. A. Abdulrazzaq, S.M. Saeed, Z.H. Ali, S.A. Tuma, O.A. Ahmed, A.A. Faridoon, and S.K .Abdulridha, "Enhancement of low carbon steel corrosion resistance in acidic and saline media using superhydrophobic

- nanocomposite”, *Experimental and Theoretical Nanotechnology*, vol. 5, no. 1, pp. 77-78, 2021, doi.org/10.56053/5.1.77.
- [7] Y. Tian, Z. Bi, and G. Cui, “Study on the corrosion resistance of graphene oxide-based epoxy zinc-rich coatings,” *Polymers*, vol. 13, no. 10, pp. 1–20, 2021, doi: 10.3390/polym13101657.
- [8] T. Dorofeeva, T. Gubaidulina, V. Sergeev, and M. Fedorischeva, “Si-Al-N-O Multi-Layer Coatings with Increased Corrosion Resistance Deposited on Stainless Steel by Magnetron Sputtering,” *Metals*, vol. 12, no. 2, pp. 254, 2022, doi.org/10.3390/met12020254
- [9] A. A. H. Kadhum and M. Ahmed, “Corrosion Inhibition of Low Carbon Steel in HCl Medium Using Thiadiazole derivative: Weight loss, DFT Studies and Antibacterial Studies,” *International Journal of Corrosion and Scale Inhibition*, vol. 10, no. 4, pp. 1812–1828, 2021, doi: 10.17675/2305-6894-2021-10-4-27.
- [10] G. Lazorenko, A. Kasprzhitskii, and T. Nazdracheva, “Anti-corrosion coatings for protection of steel railway structures exposed to atmospheric environments: A review,” *Construction and Building Materials*, vol. 288, pp. 123115, 2021, doi: 10.1016/j.conbuildmat.2021.123115.
- [11] K. K. Maniam and S. Paul, “Corrosion Performance of Electrodeposited Zinc and Zinc-Alloy Coatings in Marine Environment,” *Corrosion and Materials Degradation*, vol. 2, no. 2, pp. 163–189, 2021, doi: 10.3390/cmd2020010.
- [12] S. Fryska and J. Baranowska, “Corrosion properties of S-phase/Cr₂N composite coatings deposited on austenitic stainless steel,” *Materials*, vol. 15, no. 1, pp. 266, 2022, doi: 10.3390/ma15010266.
- [13] A. A. Uгла, M. I. Hasan, Z. A. Ibrahim, D. J. Kamil, and H. J. Khudair, “Effects of nano coating on the mechanical properties of turbine blades: A review,” *Journal of Mechanical Engineering Research and Developments*, vol. 44, no. 4, pp. 134–144, 2021.
- [14] Y. I. Kuznetsov and G. V. Redkina, “Thin Protective Coatings on Metals Formed by Organic Corrosion Inhibitors in Neutral Media,” *Coatings*, vol. 12, no.2, pp. 149, 2022, doi.org/10.3390/coatings12020149.
- [15] J. N. Panda, B. C. Wong, E. Medvedovski, and P. Egberts, “Enhancement of tribo-corrosion performance of carbon steel through boronizing and BN-based coatings,” *Tribology International*, vol. 153, pp. 106666, 2021, doi: 10.1016/j.triboint.2020.106666.
- [16] M. Zhang, H. Wang, T. Nie, J. Bai, F. Zhao, and S. Ma, “Enhancement of barrier and anti-corrosive performance of zinc-rich epoxy coatings using nano-silica/graphene oxide hybrid,” *Corrosion Reviews*, vol. 38, no. 6, pp. 497–513, 2020, doi: 10.1515/correv-2020-0034.
- [17] N. F. Ibrahim, W. R. W. Abdullah, M. S. Rooshde, M. S. M. Ghazali, and W. M. N. W. Nik, “Corrosion inhibition properties of epoxy-zinc oxide nanocomposite coating on stainless steel 316l,” In *Solid State Phenomena*, vol. 307, pp. 285–290, 2020, doi: 10.4028/www.scientific.

- net/SSP.307.285.
- [18] D. Lu, Y. Huang, J. Duan, and B. Hou, "A zinc-rich coating fabricated on a magnesium alloy by oxide reduction," *Coatings*, vol. 9, no. 4, pp. 278, 2019, doi: 10.3390/coatings9040278.
- [19] A. D. Thamir, "Corrosion Resistance Enhancement in Acidic solution for Austenitic Stainless Steel by Gas- Phase Hybrid Deposition Process," *Engineering and Technology Journal*, vol. 35, no. 8, pp. 788-794, 2017, doi.org/10.30684/etj.35.8A.1
- [20] A. Baptista, F. Silva, J. Porteiro, J. Míguez, and G. Pinto, "Sputtering physical vapour deposition (PVD) coatings: A critical review on process improvement and market trend demands," *Coatings*, vol. 8, no. 11, pp. 402, 2018, doi: 10.3390/COATINGS8110402.
- [21] A. D. Thamir, A. J. Haider, F. Q. Mohammed, and K. M. Chahrour, "Hybrid gas phase Ti-B-C-N coatings doped with Al," *Journal of Alloys and Compounds*, vol. 723, pp. 368–375, 2017, doi: 10.1016/j.jallcom.2017.06.281.
- [22] G. V. Pachurin, N. A. Kuz'min, A. A. Filippov, and T. V. Nuzhdina, "Mechanical Characteristics of Steels with a Gas-Phase Nickel Coating," *Russian Metallurgy*, vol. 2019, no. 13, pp. 1407–1409, 2019, doi: 10.1134/S0036029519130251.
- [23] V. N. Popok and O. Kylián, "Gas-Phase Synthesis of Functional Nanomaterials," *Applied. Nano*, vol. 1, no. 1, pp. 25–58, 2020, doi: 10.3390/applnano1010004.
- [24] Y. Huttel, L. Martínez, A. Mayoral, and I. Fernández, "Gas-phase synthesis of nanoparticles: Present status and perspectives," *MRS Communications*, vol. 8, no. 3, pp. 947–954, 2018, doi: 10.1557/mrc.2018.169.
- [25] J. Votava, V. Kumbár, A. Polcar, and M. Fajman, "Change of Mechanical Properties of Zinc Coatings after Heat Treatment," *Acta Technologica Agriculturae*, vol. 23, no. 1, pp. 7–11, 2020, doi: 10.2478/ata-2020-0002.
- [26] S. C. Shi, P. W. Huang, and J. H. C. Yang, "Low-temperature large-area zinc oxide coating prepared by atmospheric microplasma-assisted ultrasonic spray pyrolysis," *Coatings*, vol. 11, no. 8, pp. 1001, 2021, doi: 10.3390/coatings11081001.
- [27] M. Khiari, M. Gilliot, M. Lejeune, F. Lazar, and A. Hadjadj, "Preparation of Very Thin Zinc Oxide Films by Liquid Deposition Process: Review of Key Processing Parameters," *Coatings*, vol. 12, no. 1, pp. 1–24, 2022, doi: 10.3390/coatings12010065.
- [28] C. M. P. Kumar, M. P. G. Chandrashekarappa, R. M. Kulkarni, D. Y. Pimenov, and K. Giasin, "The effect of zn and zn–wo₃ composites nano-coatings deposition on hardness and corrosion resistance in steel substrate," *Materials*, vol. 14, no. 9, pp. 2253, 2021, doi: 10.3390/ma14092253.

- [29] N. Boshkova, K. Kamburova, T. Radeva, and N. Boshkov, "Hybrid zinc-based multilayer systems with improved protective ability against localized corrosion incorporating polymer-modified zno or cuo particles," *Coatings*, vol. 11, no. 10, pp. 1223, 2021, doi: 10.3390/coatings11101223.
- [30] V. Timm Bonow, D. Stefani Maciel, A. Zimmer, and C. G. Zimmer, "Nitriding in low carbon steels using non-toxic salt baths," *Revista Liberato*, vol. 1, pp. 177–186, 2019, doi: 10.31514/rliberato.2019v20n34.p177.
- [31] P. Landgraf, T. Bergelt, L. Rymer, C. Kipp, T. Grund, G. Bräuer and T. Lampke, "Evolution of Microstructure and Hardness of the Nitrided Zone during Plasma Nitriding of High-Alloy Tool Steel," *Metals*, vol. 12, no. 5, pp. 866, 2022, doi: 10.3390/met12050866.
- [32] A. Afnor, "Handbook of Comparative World Steel Standards, 5th Edition," *Handbook of Comparative World Steel Standards, 5th Ed.*, 2016, doi: 10.1520/ds67d-eb.
- [33] G. ASTM, "Standard practice for calculation of corrosion rates and related information from electrochemical measurements," *G102-89*, Reapproved 2004, pp. 1–7, 2015, doi: 10.1520/G0102-89R15E01.2.
- [34] I. Chung, V. Hemapriya, K. Ponnusamy, N. Arunadevi, Subramanian Chitra, Chi Hee-Youn, Seung-Hyun Kim, and M. Prabakaran, "Assessment of low carbon steel corrosion inhibition by eco-friendly green chaenomeles sinensis extract in acid medium," *Journal Electrochemical Science and Technology*, vol. 9, no. 3, pp. 238–249, 2018, doi: 10.5229/JECST.2018.9.3.238.

Effects of Pre-Treated Crumb Rubber as Sand Partial Replacement on Compressive Strength of Engineered Cementitious Composites (ECC)

Atiqah Abdul Aziz*, Mohd Ikmal Fazlan Rozli@Rosli,
Kay Dora Abd Ghani, Nor Asyiqin Jafri, Noorliyana Zakaria
Centre for Civil Engineering Studies, Universiti Teknologi MARA (UiTM),
Cawangan Pulau Pinang, 13500 Permatang Pauh, Pulau Pinang,
MALAYSIA

*atiqahaziz96.aa@gmail.com

ABSTRACT

This study was conducted to determine the surface morphology of crumb rubber (CR) treated with 10% Sodium Hydroxide (NaOH) solution at different periods and the compressive strength of the treated rubberised engineered cementitious composites (R-ECC). R-ECC is a type of engineered cementitious Composite (ECC) with CR as partial sand replacement. In contrast to the quasi-brittle nature of conventional concrete, engineered cementitious Composite (ECC) is distinguished for its tensile strain-hardening behaviour and tensile ductility. However, adding crumb rubber (CR) in ECC as partial sand replacement reduces the composites' compressive strength owing to its smooth surface. The Scanning Electron Microscopy (SEM) test was conducted on the CR samples, which had been treated with 10% NaOH for 1, 2 and 3 days. Meanwhile, the compressive strength test was conducted on 45 cubes consisting of standard ECC, untreated R-ECC and treated R-ECC. The results discovered that 2 and 3 days of 10% NaOH treatment on CR enhanced its surface roughness, and 2 days NaOH treated R-ECC is the optimum duration for the highest compressive strength reduction. Therefore, the enhanced surface roughness of the CR used as partial sand replacement in the ECC can lessen the compressive strength reduction owing to better bonding between CR and cement matrix in the composites.

Keywords: *Rubberized ECC (R-ECC); Compressive Strength; Engineered Cementitious Composites (ECC); Crumb Rubber; Sodium Hydroxide (NaOH)*

Introduction

There are a few problems with normal concrete, including its high brittleness, weakness under tension, and susceptibility to tension cracks [1]-[2]. The use of conventional concrete as the main material for high-rise buildings exposed the structure to crack failure under dynamic loading due to its brittleness. The micro-crack formation on the structure may propagate to crack failure. In an effort to overcome these drawbacks, the engineered cementitious Composite (ECC) was created [3] on the basis of the micromechanical and fracture propositions [4]. ECC is a specific class of high-performance concrete with excellent mechanical qualities and permanence that has received a lot of interest from researchers and engineers [5]. The main ingredients in ECC production are supplementary cementitious materials, sand, polyvinyl alcohol (PVA) fibre, and admixture. Research and development for novel ECC mix using wastes are ongoing to meet the industrial demands for producing green and sustainable ECCs [6].

Meanwhile, rubberised engineered cementitious composites (R-ECC) are a type of ECC in which sand is partially or entirely replaced by crumb rubber (CR). By integrating CR into ECC, concerns caused by the rising waste tyre demolition process, such as unsustainable landfill dumping and an increase in carbon footprint as a result of combustion, may be lessened [7]. CR can be an excellent construction material due to its capability to serve as a vibration damper and enhance the ductility of the composite [8]. However, the addition of CR in the composite can lead to the reduction of the compressive strength of the ECC. As a consequence, a substantial amount of earlier studies explored alternative methods to minimise the strength reduction of ECC brought on by rubber particles. Nonetheless, the research on the ECC incorporating treated CR is still not well explored.

Literature Review

ECC displays many subparallel fine crack growth and tensile strain-hardening, the latter of which cause deformation [3]. Besides that, the ECC can self-consolidate, which derives from the fibre bridge activated during Serviceability Limit State (SLS) [4]. The purpose of ECC is to overcome conventional concrete's high brittleness and crack tendency due to the high compressive strength by enhancing the ductility, tensile strength and repairability as stated by [9]. Furthermore, ECC's ability to absorb energy and

seismic load is better than conventional concrete; hence the durability of the structure can be enhanced and prolonged its service life as stated by [10].

[11] verified that the incorporation of CR in the ECC had reduced the compressive strength and stiffness of the specimen; however, the result still fulfils the structural standard and requirement. The CR's smooth surface resulted in less bonding with the cement paste [12], and low-strength CR replaced the high-strength aggregate and reduced composite strength [13]. As a result, adding high-stiffness fibres like steel fibre can increase compressive strength [14], while adding polyvinyl alcohol (PVA) fibre, which has the potential to bridge over composites' crack volumes, can increase the mechanical strength of the R-ECC [11]. According to [15], the ECC is usually reinforced with short PVA, which has a length between 6 to 12 mm and an inconsistent diameter of 10 to 100 μm micro-fibres.

Moreover, previous studies have stated that the bonding between the CR particles and the cement paste can be enhanced by pre-treating the CR before adding it to the concrete. Hence, the reduction of the composite's mechanical strength can be lessened [16]. According to [17], among the surface treatments done to make the rubber surface more hydrophilic, the usage of sodium hydroxide (NaOH) solution produced the best results. Once treated CR is added to the composite, the cement hydration around rubber particles can be improved as NaOH solution pre-treatment can provide weak alkaline conditions surrounding rubber particles. Additionally, by treating CR with NaOH solution, the hydrophilicity of rubber particles can be enhanced, which lowers the porosity of the interface transition zone (ITZ) between rubber particles and cement matrix. As a result, rubber particles and cement paste may adhere together and become better over time [18]. [26] had investigated the effect of the pre-treatment of CR on rubberised concrete using NaOH solution at 10% concentration under different periods (20 minutes, 2, 24, 48 hours and 7 days). The results showed that the rubberised concrete with 1-day treatment of 10% NaOH pre-treated CR achieved the highest compressive strength with a 20% increment compared to untreated CR [16].

In this study, CR was used as sand partial replacement in the ECC and 10% sodium hydroxide (NaOH) solution was used as a pre-treatment on CR for a different duration (1 day, 2 days and 3 days). Hence, the effect of the CR treatment using 10% NaOH on the CR's surface roughness and compressive strength of R-ECC was investigated. The optimal time for pre-treating CR with 10% NaOH to minimise the compressive strength in R-ECC from deteriorating was established.

Materials and Methods

Materials

The binder used in this study is Composite Portland Cement (CPC), while silica sand and CR are employed as aggregates in the ECC. The average size of silica sand is 1.19 mm to 0.25 mm, whereas the average size of CR is 1 mm to 3 mm. CR was treated with 10% NaOH solution with different durations before blending into the mixture. The ECC is reinforced with the PVA fibre of 6 mm in length, and superplasticiser (SP) was added to the mixture. Figures 1a and 1b show the picture of the CR and PVA used in the ECC, respectively.

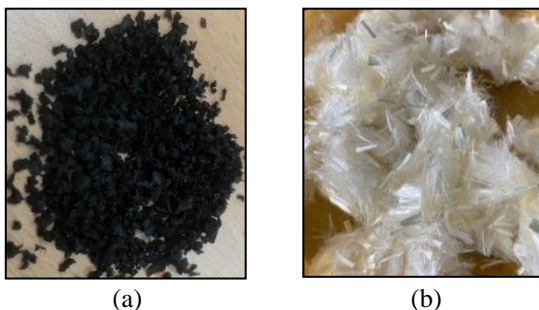


Figure 1: Picture of; (a) CR, and (b) PVA fibres

Crumb rubber treatment

Before the casting process, the 10% NaOH solution must be prepared for CR treatment. 400 g NaOH granules were heated with 1 L distilled water and stirred until the solution became clear. Then, the heat was turned off, and continued to stir the solution for 2 to 3 hours to allow it to cool. After pouring the 10% NaOH solution into the CR container and made it completely soaked, leave it for 1 day, 2 days, and 3 days. Finally, the CR was cleaned with tap water until it reached a pH of 7 ± 0.5 , then dried at room temperature. The treatment process was done by modifying the procedure conducted by [19].

Mixture design and sample preparation

Five different ECC mixtures were prepared with the inclusion of 10% CR as a partial silica sand replacement by volume. Normal ECC is employed as the Control, whereas R-ECC is made up of CR that has been untreated (UT) and treated with 10% NaOH solution for 1 day (T1), 2 days (T2), and 3 days (T3). Table 1 shows the modified proportion of materials from Wang et al. (2020) for the ECC. The water-cement ratio, volume of PVA fibre, and superplasticiser (SP) were fixed at 0.35, 1.5% by volume of the mixture, and 0.89% of cement weight, respectively. The control sample is a normal ECC with no CR as partial sand replacement.

When making the R-ECC, the dry ingredients consisting of sand, cement and CR were combined to achieve a uniform and thorough dispersion of constituent materials. The mixture was then filled with half as much water and let to continue rotating. After that, SP and the leftover water were added to the mixture while stirring for another 2 to 3 minutes. Finally, PVA fibres were added to the mixture as the mixing continued until they were blended together. After the mixing process was completed, the wet mixture was immediately cast into cube moulds with 50 mm sides and demoulded after 24 hours. Next, the samples were cured in an airtight bag at room temperature before being tested.

Table 1: Material proportion of ECC

Mix	Cement (kg/m ³)	Sand (kg/m ³)	CR (kg/m ³)	Water (kg/m ³)	PVA (%)	SP (%)
Control	1193	990	0	417	1.5	0.89
UT, T1, T2, T3	1193	891	27	417	1.5	0.89

Methods

The physical properties of untreated and treated CR were determined using Scanning Electron Microscopy (SEM) to get the surface roughness of the material. SEM was carried out using the TM3030Plus Tabletop Microscope, as presented in Figure 2a. The test was conducted on the CR, consisting of untreated, 1 day, 2 days, and 3 days 10% NaOH-treated CR. A small amount of CR was placed on the base using a carbon tape, as shown in Figure 2b. Next, the base with CR was placed inside the chamber to vacuum and centralised the CR under the lens using the manual adjuster. Later, the chamber was closed and the machine was run to obtain the surface roughness of the CR.

The fresh properties of the ECC with and without CR were determined using the flow table test in accordance with ASTM C230/C230M. The flow table test was carried out using the automatic flow table test machine as shown in Figure 3. The mixture was filled inside the mould in two layers and tamped 20 times for each layer using the steel rod. Then, the mould was removed vertically from the mixture, and the plate dropped 25 times. Lastly, the longest diameter of the wet ECC and R-ECC was measured and recorded.

As indicated in Figure 4a, the specimens were put through a compressive strength test utilising NL Scientific apparatus model, NL 4000 X/018U at the intervals of 7, 14, and 28 days. In this investigation, the test was performed on cube specimens with the diameter of 50 mm on each side, as shown in Figure 4b. Before testing, the samples were taken out of the sealed bag and allowed to cure in the open air. The compressive strength test was executed following BS EN 196-1. The cube specimens were positioned in the middle of the lower platen and perpendicular to the load direction. Based on

the size of the samples and the equipment's manual, the compressive strength test was carried out at a rate of 0.9 kN/s.

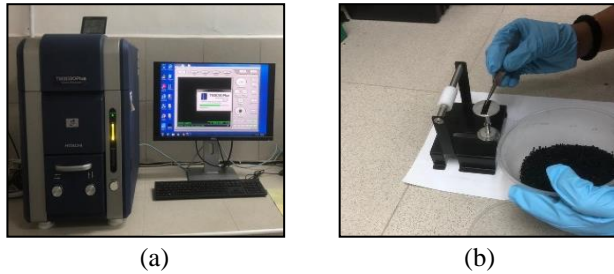


Figure 2: (a) Scanning Electron Microscopy (SEM) equipment, and (b) base of the sample



Figure 3: Automatic flow table test machine



Figure 4: Image of (a) compression test machine, and (b) cube specimen

Results and Discussion

Scanning Electron Microscopy (SEM)

Figure 5 shows Scanning Electron Microscopy (SEM) images of untreated CR, and 10% NaOH-treated rubber particles. The surface roughness of the CR particles treated with 10% NaOH solution is better than untreated CR caused by the corrosion of CR's surfaces by the solution. According to [26], the zinc stearate layer on CR, which is in charge of giving it its hydrophobic characteristics, reacts with NaOH to produce soluble sodium stearate, which may be eliminated by washing CR in tap water [16]. Consequently, the bonding between 10% NaOH-treated CR and the cement matrix can be enhanced. Besides that, [26] affirmed that the NaOH solution treatment on CR discarded the forbid material such as oil and other pollutants or chemicals that may attach to its surface and reduce the bonding as well as weaken the strength of the composites, supported by [16]. Moreover, the NaOH solution can produce the best results among the surface treatments evaluated to improve the hydrophilicity of the rubber surface, mentioned by [17].

Flowability

Figure 6 presents the flowability of the ECC with and without CR. The Control has the lowest flow value, followed by untreated R-ECC mixtures (UT). The inclusion of CR in ECC has an increment in diameter and flowability compared to the normal ECC. The increase in R-ECC flowability may be affected by the low water absorption of CR compared to sand, as stated by [20]. Moreover, the hydrophobic nature of CR, which repelled water, led to an increment of water content in the mixture. However, 10% NaOH-treated R-ECC achieved a higher flowability than untreated R-ECC. The untreated CR particles may have impurities coating on the external surfaces that cause a higher water demand compared to the treated CR particle which had been cleaned [16]. At a two-day duration of CR treatment with 10% NaOH (T2), the R-ECC achieved the highest flow value and flowability of 147 mm and 46.67%, respectively. However, the T3 had a slight reduction of flowability which is 45%. This might be created by the enhancement of CR's surface roughness, which resulted in an increment of flow resistance [21]. The enhancement of surface roughness reduced air trapped on CR surfaces and promoted the adhesion between the cement matrix and CR particles [20].

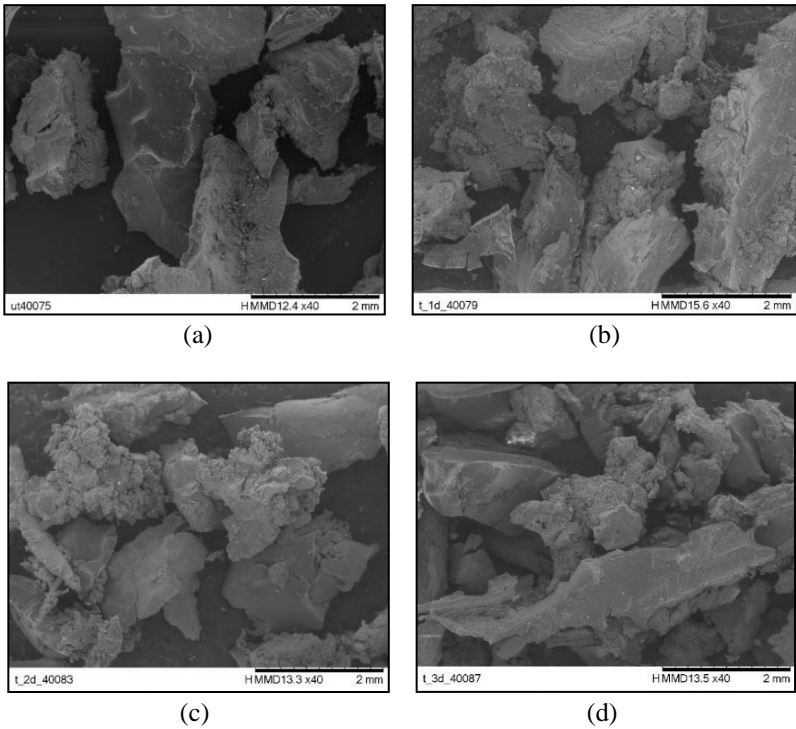


Figure 5: SEM image (a) untreated (b) 1 day (c) 2 days, and (d) 3 days 10% NaOH treated CR

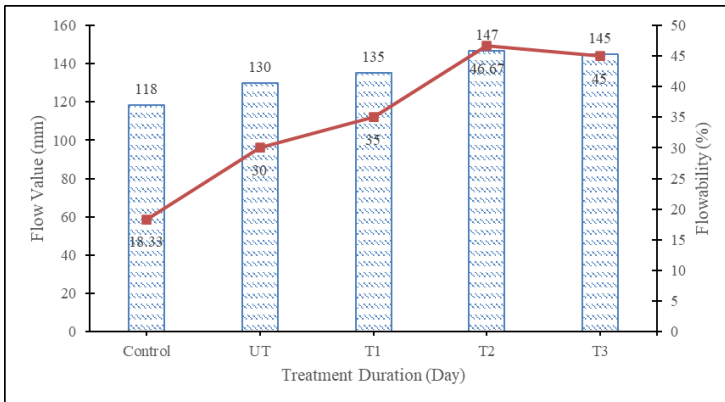


Figure 6: Flowability of ECC/R-ECC

Compressive strength

Figure 7 presents the results of the compressive strength of R-ECC at the age of 7, 14, and 28 days against the duration of 10% NaOH pre-treatment on CR incorporated as a sand partial replacement. Based on the compressive strength of untreated CR (UT) and 10% NaOH-treated CR for 1 day (T1), 2 days (T2), and 3 days (T3), the employment of CR as partial sand replacement in the ECC contributed to the reduction of compressive strength. Since CR was not added to the normal ECC or Control specimens, it obtained the highest compressive strength at 7, 14, and 28 days. The strength reduction of R-ECC may be caused by the smooth surface of CR, which weakened the cement paste's adhesion [12]. Besides that, incorporating CR in ECC reduced strength because there was less bonding with cement paste and lesser stiffness of CR than sand [22]. Nonetheless, the compressive strength achieved by T1, T2, and T3 was greater than UT. Meanwhile, T2 experienced the highest strength at all ages for R-ECC specimens. UT had the least compressive strength, owing to the hydrophobic nature of rubber particles. Therefore, treatment with 10% NaOH on CR for 2 days is optimal to enhance the compressive strength of the R-ECC. [23] reported that NaOH-treated CR improved the adhesion between its particles and the cement matrix, resulting in less compressive strength reduction, as supported by [24].

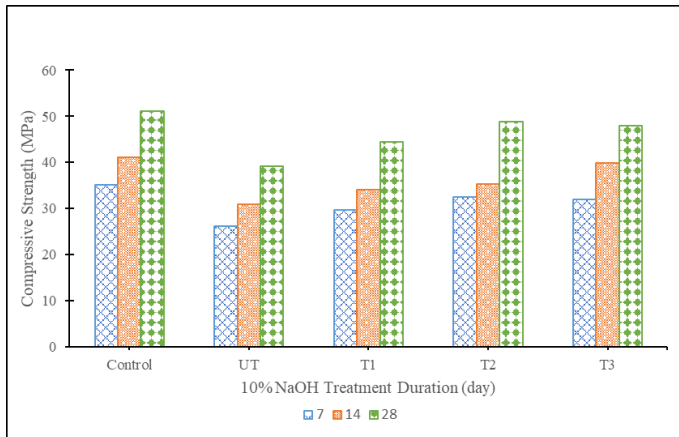


Figure 7: The effect of treatment duration of CR on compressive strength

Figure 8 shows the relative strength determined based on Equation 1 against the age of the rubberised ECC. The line graph displays the relative strength of the Control and R-ECC (UT, T1, T2, and T3). The relative strength of untreated R-ECC (R-UT) achieved the bottommost relative strength of 74.49%, 75.15%, and 76.61% of control at the age of 7, 14, and 28 days respectively, compared to the relative strength of T1 (R-T1), T2 (R-T2), and

T3 (R-T3). The weaker adhesion of CR particles to the blended materials in the ECC might be the reason for the less strength achieved by R-UT due to its smooth surface. According to [20], the probable weak interfacial zone between cement paste and CR may be the source of the reduced ECC's compressive strength. Besides that, the development of voids in the cement matrix may increase due to the incorporation of CR. Therefore, compressive strength reduction occurs due to the nature of those voids. [27] mentioned that the elasticity of CR is anticipated to reduce the bonding strength with the cement matrix, which results in a decrease in compressive strength, as supported by [25]. Additionally, the relative strength of R-T1, R-T2, and R-T3 is better than R-UT, which may have been influenced by the enhancement of surface roughness of the CR, as mentioned by [25]. R-T3 had a slightly lower percentage than R-T2, which may derive from the 10% NaOH solution that permeated the CR particles and reduced its rigidity rather than corroded its outlying surface [25]. Hence, the 10% NaOH solution pre-treatment on CR may be a credible method to minimise the reduction in the compressive strength of the R-ECC.

$$\frac{\text{Strength of R-ECC (MPa)}}{\text{Strength of control (MPa)}} \times 100 = \text{relative strength (\%)} \quad (1)$$

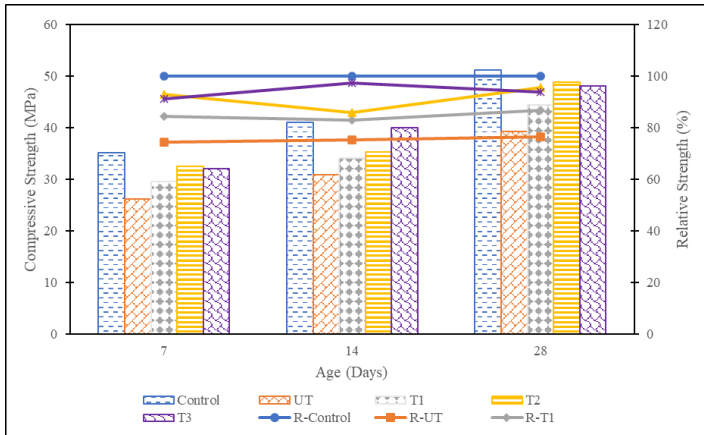


Figure 8: The relative strength of R-ECC

Conclusions

This research presents the effect of utilising untreated CR and 10% NaOH pre-treated CR at different durations to partially replace the sand on the strength of the R-ECC. 10% volume of sand in the mixture was replaced with CR to

evaluate compressive strength performance at 7, 14, and 28 days. Based on the results from the experimental study, it can be concluded that 10% NaOH-treated R-ECC obtained a greater compressive strength than the untreated R-ECC due to the reaction between NaOH and zinc stearate layer on the rubber surface, making it hydrophilic and enhancing its surface roughness. Hence, a lesser strength reduction for R-ECC can be obtained owing to the enhancement of the adhesion between the treated R-ECC materials. T2 achieved the highest compressive strength among the R-ECC; therefore, 2 days of CR treatment with 10% NaOH solution is the ideal duration.

Moreover, R-ECC achieved a higher flowability than normal ECC, owing to the low water absorption of the CR particles compared to the sand. 10% NaOH pre-treatment cleaned the impurities on the CR particles' surface, which can hinder the bonding between CR and cement paste. Lastly, CR pre-treated with 10% NaOH-treated for 2 and 3 days had a better surface roughness than untreated CR and 1-day treated CR, leading to a lower compressive strength reduction. Be that as it may, the NaOH may permeate into the CR when a longer duration of CR pre-treatment with 10% NaOH solution takes place. Hence, the strength of R-ECC might be lowered, incurring a decrease in the rigidity of the CR rather than enhancing its surface roughness.

A few recommendations can be proposed, such as to investigate other mechanical properties of the composites like tensile and flexural strength. In addition, the study on the structural behaviour of 10% NaOH-treated R-ECC can be identified by applying the Composite as a structure and testing it under static and dynamic loads. Last but not least, conduct an experiment to study the different concentrations of NaOH solution to treat CR.

Contributions of Authors

The authors confirm the equal contribution in each part of this work. All authors reviewed and approved the final version of this work.

Funding

This work received no specific grant from any funding agency.

Conflict of Interests

All authors declare that they have no conflicts of interest

Acknowledgement

The authors would like to acknowledge Universiti Teknologi MARA (UiTM) Cawangan Pulau Pinang, Malaysia, for supporting this research. The authors declare that they have no conflict of interest.

References

- [1] Q. Wang, M. H. Lai, J. Zhang, Z. Wang, and J. C. M. Ho, “Greener engineered cementitious composite (ECC) – The use of pozzolanic fillers and uncoiled PVA fibers,” *Construction Building Materials*, vol. 247, 2020, [https://doi: 10.1016/j.conbuildmat.2020.118211](https://doi.org/10.1016/j.conbuildmat.2020.118211)
- [2] L. S. Wee, O. C. Lian, and M. R. M. Zain, “Mechanical properties of engineered cementitious composites using local ingredients,” *Journal of Mechanical Engineering*, vol. 16, no. 2, pp. 145–157, 2019, [https://doi: 10.24191/jmeche.v16i2.15332](https://doi.org/10.24191/jmeche.v16i2.15332)
- [3] V. C. Li, “Engineered cementitious composite (ecc): Material, structural, and durability performance,” in *Concrete Construction Engineering Handbook, Second Edition*, no. June, pp. 1001–1048, 2008.
- [4] A. C. Mircea, H. Szilagyi, A. Hegyi, and C. Baera, “Study of self-healing engineered cementitious composites for durable and sustainable infrastructure,” *Procedia Manufacturing*, vol. 46, pp. 871–878, 2020, [https://doi: 10.1016/j.promfg.2020.05.002](https://doi.org/10.1016/j.promfg.2020.05.002)
- [5] B. H. AbdelAleem and A. A. Hassan, “Use of rubberized engineered cementitious composite in strengthening flexural concrete beams,” *Engineering Structures*, vol. 262, no. January, pp. 114304, 2022, [https://doi: 10.1016/j.engstruct.2022.114304](https://doi.org/10.1016/j.engstruct.2022.114304)
- [6] C. L. Oh, S. W. Lee, N. A. Yahya, G. Pandulu, and M. R. M. Zain, “Tensile Behaviour of Slag-based Engineered Cementitious Composite,” *Pertanika Journal of Science and Technology*, vol. 30, no. 1, pp. 303–317, 2022, [https://doi: 10.47836/pjst.30.1.17](https://doi.org/10.47836/pjst.30.1.17).
- [7] B. Zhang and C. S. Poon, “Sound insulation properties of rubberized lightweight aggregate concrete,” *Journal of Cleaner Production*, vol. 172, pp. 3176–3185, 2018, [https://doi: 10.1016/j.jclepro.2017.11.044](https://doi.org/10.1016/j.jclepro.2017.11.044)
- [8] A. Hamdi, G. Abdelaziz, and K. Z. Farhan, “Scope of reusing waste shredded tires in concrete and cementitious composite materials: A review,” *Journal of Building Engineering*, vol. 35, no. November 2020, pp. 102014, 2021, [https://doi: 10.1016/j.job.2020.102014](https://doi.org/10.1016/j.job.2020.102014)
- [9] M. A. Kewalramani, O. A. Mohamed, and Z. I. Syed, “Engineered Cementitious Composites for Modern Civil Engineering Structures in Hot Arid Coastal Climatic Conditions,” *Procedia Engineering.*, vol. 180, pp. 767–774, 2017, [https://doi: 10.1016/j.proeng.2017.04.237](https://doi.org/10.1016/j.proeng.2017.04.237)

- [10] S. Wang, H. Du, J. Lv, J. Guo, G. Yue, and J. Ma, "Test research on mechanical properties of engineered cementitious composites," *IOP Conference Series: Earth and Environmental Science*, vol. 647, no. 1, pp. 1-8, 2021, [https://doi: 10.1088/1755-1315/647/1/012071](https://doi.org/10.1088/1755-1315/647/1/012071)
- [11] Isyaka Abdulkadir, Bashar S. Mohammed, M.S. Liew, M.M.A. Wahab, "Mechanical and deformation properties of rubberized engineered cementitious composite (ECC)," *Case Studies Constructions Materials*, vol. 13, pp. 1-20, 2020, [https://doi: 10.1016/j.cscm.2020.e00385](https://doi.org/10.1016/j.cscm.2020.e00385)
- [12] K. Bisht and P. V. Ramana, "Evaluation of mechanical and durability properties of crumb rubber concrete," *Construction and Building Materials*, vol. 155, pp. 811–817, 2017, [https://doi: 10.1016/j.conbuildmat.2017.08.131](https://doi.org/10.1016/j.conbuildmat.2017.08.131)
- [13] J. Xue and M. Shinozuka, "Rubberized concrete: A green structural material with enhanced energy-dissipation capability," *Construction and Building Materials*, vol. 42, pp. 196–204, 2013, [https://doi: 10.1016/j.conbuildmat.2013.01.005](https://doi.org/10.1016/j.conbuildmat.2013.01.005)
- [14] M. K. Ismail, B. H. Abdelaleem, and A. A. A. Hassan, "Effect of fiber type on the behavior of cementitious composite beam-column joints under reversed cyclic loading," *Construction and Building Materials*, vol. 186, pp. 969–977, 2018, [https://doi: 10.1016/j.conbuildmat.2018.08.024](https://doi.org/10.1016/j.conbuildmat.2018.08.024)
- [15] E. H. Yang, S. Wang, Y. Yang, and V. C. Li, "Fiber-bridging constitutive law of engineered cementitious composites," *Journal of Advanced Concrete Technology*, vol. 6, no. 1, pp. 181–193, 2008, [https://doi: 10.3151/jact.6.181](https://doi.org/10.3151/jact.6.181)
- [16] R. Alwi, M. Rizwan, S. U. Al-dulaijan, and M. Maslehuddin, "Properties of concrete with untreated and treated crumb rubber e A review," *Journal of Materials Research and Technology*, vol. 11, pp. 1753–1798, 2021, [https://doi: 10.1016/j.jmrt.2021.02.019](https://doi.org/10.1016/j.jmrt.2021.02.019)
- [17] E. Ganjian, M. Khorami, and A. A. Maghsoudi, "Scrap-tyre-rubber replacement for aggregate and filler in concrete," *Construction and Building Materials*, vol. 23, no. 5, pp. 1828–1836, 2009. [https://doi: 10.1016/j.conbuildmat.2008.09.020](https://doi.org/10.1016/j.conbuildmat.2008.09.020)
- [18] R. Si, S. Guo, and Q. Dai, "Durability performance of rubberized mortar and concrete with NaOH-Solution treated rubber particles," *Construction and Building Materials*, vol. 153, pp. 496–505, 2017, [https://doi: 10.1016/j.conbuildmat.2017.07.085](https://doi.org/10.1016/j.conbuildmat.2017.07.085)
- [19] O. Youssf, J. E. Mills, and R. Hassanli, "Assessment of the mechanical performance of crumb rubber concrete," *Construction and Building Materials*, vol. 125, pp. 175–183, 2016, [https://doi: 10.1016/j.conbuildmat.2016.08.040](https://doi.org/10.1016/j.conbuildmat.2016.08.040)
- [20] A. Adesina and S. Das, "Performance of engineered cementitious composites incorporating crumb rubber as aggregate," *Construction and Building Materials*, vol. 274, pp. 122033, 2021, [https://doi: 10.1016/j.conbuildmat.2020.122033](https://doi.org/10.1016/j.conbuildmat.2020.122033)

- [21] Z. Chen, L. Li, and Z. Xiong, "Investigation on the interfacial behaviour between the rubber-cement matrix of the rubberized concrete," *Journal of Cleaner Production*, vol. 209, pp. 1354–1364, 2019, [https://doi: 10.1016/j.jclepro.2018.10.305](https://doi.org/10.1016/j.jclepro.2018.10.305)
- [22] S. Guo, Q. Dai, R. Si, X. Sun, and C. Lu, "Evaluation of properties and performance of rubber-modified concrete for recycling of waste scrap tire," *Journal of Cleaner Production*, vol. 148, pp. 681–689, 2017, [https://doi: 10.1016/j.jclepro.2017.02.046](https://doi.org/10.1016/j.jclepro.2017.02.046)
- [23] N. Segre and I. Joekes, "Use of tire rubber particles as addition to cement paste," *Journal of Materials Research and Technology*, vol. 30, pp. 1421–1425, 2000, [https://doi.org/10.1016/S0008-8846\(00\)00373-2](https://doi.org/10.1016/S0008-8846(00)00373-2)
- [24] T. C. Ling, K. H. Mo, L. Qu, J. Yang, and L. Guo, "Mechanical strength and durability performance of autoclaved lime-saline soil brick," *Construction and Building Materials*, vol. 146, pp. 403–409, 2017, [https://doi: 10.1016/j.conbuildmat.2017.04.106](https://doi.org/10.1016/j.conbuildmat.2017.04.106)
- [25] Y. Li, X. Yang, P. Lou, R. Wang, Y. Li, and Z. Si, "Sulfate attack resistance of recycled aggregate concrete with NaOH-solution-treated crumb rubber," *Construction and Building Materials*, vol. 287, pp. 123044, 2021, [https://doi: 10.1016/j.conbuildmat.2021.123044](https://doi.org/10.1016/j.conbuildmat.2021.123044)
- [26] I. Mohammadi, H. Khabbaz, K. Vessalas, "Enhancing mechanical performance of rubberised concrete pavements with sodium hydroxide treatment," *Materials and Structures*, vol. 49 pp. 813-827, 2016, <https://doi.org/10.1617/s11527-015-0540-7>
- [27] Q. Dong, B. Huang, X. Shu "Rubber Modified Concrete Improved by Chemically Active Coating and Silane Coupling Agent." *Construction and Building Materials*, vol. 48, pp. 116–123, 2013, <https://doi.org/10.1016/j.conbuildmat.2013.06.072>

The Analysis of Dual Axis Solar Tracking System Controllers Based on Adaptive Neural Fuzzy Inference System (ANFIS)

M.S.I Zulkornain

*School of Electrical Engineering, College of Engineering,
Universiti Teknologi MARA, 40450 Shah Alam, Selangor, MALAYSIA*

*S.Z. Mohammad Noor**

*Solar Research Institute, Universiti Teknologi MARA, 40450 Shah Alam,
Selangor, MALAYSIA
sitizaliha@uitm.edu.my

N.H. Abdul Rahman

*Faculty of Electrical Engineering, Universiti Teknologi MARA,
81750 Masai, Johor, MALAYSIA*

Suleiman Musa

Kaduna Polytechnic, Kaduna, NIGERIA

ABSTRACT

Artificial intelligence is commonly used in Photovoltaic (PV) control systems. Adaptive Neural Fuzzy Inference System (ANFIS) is one of the intelligent strategies that can be employed in the system controller. ANFIS technique shows high accuracy as it involved several processes which are the Fuzzy layer, Fuzzy Rule layer, Normalization layer, and Output Membership layer. The main objective of the proposed work is to model the dual-axis solar tracker using MATLAB software by utilizing the ANFIS technique, hence improving the performance of the solar system. The data used for training and testing are elevation angle and azimuth angle. 80% of the data is used for training and another 20% for testing in order to predict the solar radiation toward PV panels. A different set of input membership functions (MFs) is used in the system, which are Five MFs, Ten MFs, and Fifteen MFs. These MF are simulated to produce the best prediction of solar radiation. The results show

average error gained for both training and testing data and minimum error indicates the accuracy of the predicted angle of dual axis solar tracker. In the finding, overall results show a good correlation between the actual and prediction value with 15 input MFs as it produced the lowest error value.

Keywords: *Dual Axis Solar Tracker; Adaptive Neural Fuzzy Inference System (ANFIS); Artificial Neural Networks (ANN); Membership Function (MF); Photovoltaic (PV); Artificial Intelligence (AI)*

Introduction

In recent years, global economic expansion and population growth have necessitated more energy, which is critical for both developing and developed countries' socioeconomic development [1]. Therefore, energy usage is extremely important. Renewable energy is obtained from natural resources where these resources, including sunshine, wind, biomass, thermal energy and others are stored in the earth's crust and have the benefit of being present in almost every part of the world in some form. They are almost infinite, and they have no effect on the climate or the environment. Fossil fuels, on the other hand, such as oil, coal, and natural gas, are limited in supply. Based on [2], the depletion of fossil fuels and their negative environmental effects, increase the use of clean and renewable energy sources. Therefore, generating electricity from renewables, and improving energy efficiency are becoming more important. Other than that, if we keep extracting them, they will ultimately run out. They do not refill as quickly as we humans consume them, despite the fact that they are formed naturally.

The rate of solar energy consumption is increasing in this new era today. Solar energy has been considered as a potential alternative energy source in recent years due to its unique traits of being free, eco-friendly, and widely available in most parts of the world [3]. Solar cells composed of silicon or other materials that convert sunlight directly into electricity are known as Photovoltaic (PV) cells [4]. Solar energy provides a clean alternative to fossil-fuel-generated electricity, with no pollution of the air or water, no global warming pollution, no risk of electricity price spikes, and no health risks. This is particularly relevant due to the growing concern about climate change [5]. The tiny PV solar cells can directly convert sunlight into solar energy, giving solar energy a significant advantage over other traditional power sources [6].

The solar panels can be mounted as a fixed type or tracker type. The power created from a PV system with tracker type (Dual Axis Solar Tracker) was compared by [7]. The system generated an average output power of 9838.35 W, whereas the fixed-type PV system only provided 8326.18 W of electricity. In addition, the earth constantly rotates around the sun, meaning that the sun's position will always move every minute along with the earth's

rotation [8], and this required the implementation of solar tracker. The energy generated by utilizing a solar tracking system is larger compared to fixed type system as investigated by [9].

Solar tracking systems are separated into two categories based on the number of axes include in following the sun's trajectory, which are single and dual axis solar tracker. A single axis tracker can only rotate either vertically or horizontally at single time [10], however, a dual axis tracker can rotate vertically and horizontally at each time. As compared to this two-axis type, studies have been conducted to identify the rate of sun tracking between these two types of axes, and the results revealed that dual axis solar trackers have the maximum power efficiency than single axis solar trackers [10]. In [11], two degrees of freedom serve as rotation axes in dual axis trackers. With a dual axis solar tracker, panels will always be positioned at the best angle for maximum efficiency [12]. Other than that, to optimize the functionality of the panels, the selection of control methods is very important. The algorithm, microprocessor, motor, electronic circuits, artificial intelligence (AI), and technical approaches are some of the strategies that may be used as a controller to regulate the PV panel [13]. AI techniques are one of the recent and popular methods in control systems, based on their adaptability in doing predictions.

Furthermore, installing solar panels in the optimal position will extract the maximum amount of solar radiation. Various studies on this subject have been published due to the importance of tracking the sun's rays for effective performance. Several solar tracking strategies to optimise sun radiation toward PV panels, including fuzzy logic [14], ANFIS [13], [15], LDR sensor [10], [12], and algorithm techniques [16]. Regarding the investigation of the rate of absorption of sunlight against solar panels by using all these various methods, there are some conclusions that have been identified. ANFIS, for example, is an intelligent principle that combines layers of neural networks and fuzzy logic. This technique has the capability to track the sunray precisely because it has adaptation capability and rapid learning capacity.

On the other hand, fuzzy logic is one of the intelligent techniques which on its basis allows the translation from logic statement to nonlinear mapping. However, the construction of its model is much more complicated, and it also needs rules to conduct a process because it cannot recognize machine learning or neural networks. Furthermore, the algorithm technique is complex because each angle must be analysed individually in order to determine the proper position of the solar panel. Finally, the LDR method has a low response speed and is greatly affected by temperature, despite its building technique being simpler than other techniques. Overall, in terms of solar tracking system performance, the ANFIS method can be categorised as the best technique to be implemented in the system because of high prediction accuracy with minimum error.

This proposed research focuses on the Adaptive Neural Fuzzy Inference System (ANFIS) technique by integrating fuzzy logic and neural network

layers in designing and controlling solar tracking system [17]. The goal of the ANFIS system is to represent a fuzzy system as a network structure by fuzzifying a neural network using a learning mechanism derived from artificial neural networks (ANN). The proposed system analyse and predicted the best angles that followed the sun's position throughout the sky. Furthermore, it also improves the accuracy of determining the sun's best position. Therefore, it lowers the error (MSE) and improves the prediction rate of output solar radiation.

Methodology

This section explained the ANFIS implementation in the solar system. ANFIS adjusts the membership function and related parameters to approach the required data sets using the neural network training process [18]. The adaptive neural fuzzy inference system is a useful neural network method for solving problems with function approximation. A mapping relationship between the input and output data is provided by an ANFIS, where the optimal distribution of membership functions is determined using a hybrid learning method [19]. The learning methods used in the ANFIS are a backpropagation algorithm and a hybrid algorithm [20]. This inference system is generally built using five layers in total as shown in Figure 1. The node function describes each ANFIS layer, which is made up of many nodes. The nodes in the previous layer provide the inputs for the current layers [21].

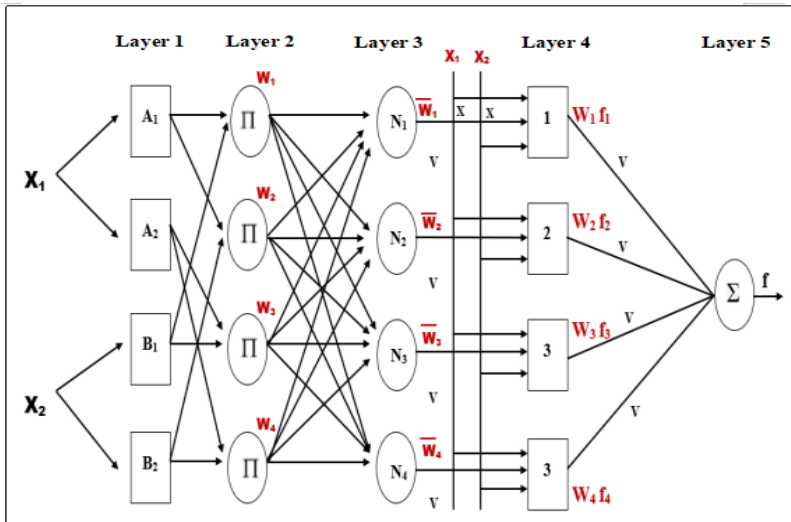


Figure 1: Block diagram of ANFIS modeling

Layer 1 is the fuzzy layer, where the main operation in the fuzzy logic principle is the fuzzification process. Each node in the fuzzy layer represents the degree of membership function from the input. The fuzzification method scales and fuzzy values become input variables by converting crisps input to linguistics variables using membership functions [22]. In other words, this layer will take the input value and determine the membership function. The adaptive node i of this layer has the following node function, which refers to the Grade of Membership on fuzzy set formula by Equations 1 and 2.

$$O_1, i = \mu_{Ai}(x) \text{ for } i=1,2,3 \text{ or} \quad (1)$$

$$O_1, i = \mu_{Bi-3}(y) \text{ for } i=4,5,6 \quad (2)$$

where either 'x' or 'y' is the node I input, and 'Ai' or 'Bi' can be a possible linguistic name for this node. In other words, the membership grade of a fuzzy set 'A1', 'A2', and 'A3' or (B1, B2, and B3) is output O_1 from this layer, and it describes the degree to which the provided input 'x' or 'y' meets the quantifier 'A' (or B).

Next is Layer 2, known as the Fuzzy Rule Layer. The fuzzy logic operators are used at this layer. Each node output in this layer represents the rule process's firing strength. The AND operator is used to multiply the incoming signals from layer 1 to obtain the output of firing strengths in this layer. Each node is a fixed node where the output from this layer is equal to the product of all incoming signals, as indicated in Equation 3.

$$O_2, i = w_i = \mu_{Ai}(x) \mu_{Bi}(y) \text{ } i=1,2,3 \quad (3)$$

For the normalising layer, which is Layer 3, every node in this tier is a fixed node with the label "N." The node determines the ratio of the firing strength of the rule to the sum of the firing strengths of all rules. Every node i in this layer has an adaptive node, and the node functions according to Equation 4.

$$O_3, i = w_i f_i = w_i r_i \text{ } i=1,2,3 \quad (4)$$

This node's parameter set is represented by r_i , and the following parameters are the parameters in this section.

Every node has a node function and is adaptable in Layer 4, which is known as the Output Membership Layer. The output membership layer can be defined using Equation 5.

$$O_4, i = w_i f_i = w_i (p_i x + q_i y + r_i) \quad (5)$$

where w_i is the normalised firing strength from layer 3 (p_i, q_i, r_i) and the parameter set of subsequent parameters. In other words, each node layer gets its output based on the previous layer. The defuzzification values are returned by this layer, which computes a parameter function from layer 3 and its parameter known as the consequent parameter. The last Layer 5 is the Defuzzification Layer, where it is generally a single node that aggregates the entire output as the sum of all incoming signals and is used to provide a single output for the ANFIS model.

This study technique using ANFIS simulation for a dual axis solar tracker is based on the flowchart illustrated in Figure 2. The process for the prediction of ANFIS starts with defining input and output data where input data were elevation and azimuth angle while output data is solar radiation. In this process, all the data will be categorized into Training and Testing and it's stored in a separate folder on MATLAB workspace, and this process is conducted before the simulation of ANFIS.

Next is to load Training and Testing data into Neuro-Fuzzy Designer in the MATLAB simulation model. Then, the process continued with generating FIS where in this section, several options and parameters need to be selected such as Options for FIS generation, number of Input MFs, and types for membership function use. There are four selection options available in this ANFIS simulation, and the Grid Partition system has been chosen for this study with the integration of fuzzy logic controller on its system.

Next, for the input MF, three sets of input are used which are Five, Ten and Fifteen MF while for the MF's type, the Gaussian membership function is selected. The various number of inputs MFs selected is to identify the effect of this parameter on prediction's accuracy. Other than that, process flow continued with setting up the value of error tolerance and epoch (iteration) before train (prediction) is simulated. Error tolerance refers to the rate of error need to achieve by ANFIS when the simulation for data prediction is conducted. From this research, error tolerance is set to zero while epoch or iteration is hundred. The precision achieves when the error value gained from the simulation is near or the same as the error tolerance set up. If the predicted value does not match the actual output, a new set of input MFs will be created, and the process will be repeated until the value of output data before and after ANFIS implementation is almost the same. When the prediction is exact, the final step is to record the ANFIS simulation's output performance.

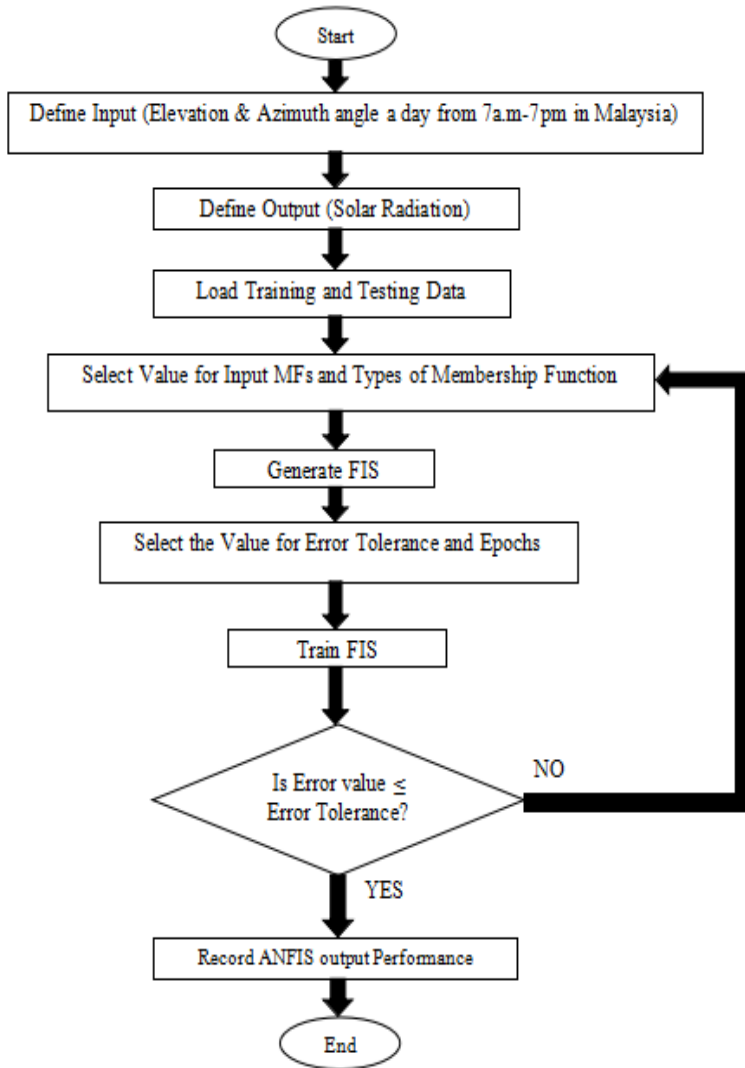


Figure 2: Flowchart for ANFIS dual axis solar tracker

Result and Discussion

The results and discussion for the proposed Dual Axis Solar Tracking System with ANFIS controller are presented in this part. The data for ANFIS is applied using MATLAB to assess the output value of solar radiation on solar panels.

This simulation is based on two types of input value, elevation and azimuth angle in the targeted area which is Shah Alam, Selangor, Malaysia. The prediction conducted which are training and testing data are used to investigate the effect of the ANFIS technique on the solar tracking system. The training and testing procedures are repeated using three different sets of input membership functions: 5MFs, 10MFs, and 15MFs. The MFs are chosen to quantify the impact on the low, medium and large value of MFs. Next, the total data used is 49 data, where 80% (39 data) was used for training and another 20% (10 data) was used for testing.

ANFIS training process

The result shown in Figures 3, 4 and 5 is the training data for 5MF, 10MF and 15MF, respectively. Based on the obtained graph, the 'blue circle' represent the actual data while the 'Red Dot' are the prediction data for the training process after the ANFIS method is applied. The graphs show that the different numbers of MF affected the accuracy of prediction data. The 15MFs show a good result compared to the lowest value of MF which is 5MFs. It can be observed that the large number of MFs able to rise the ANFIS intelligence level, hence increasing the prediction for the output data.

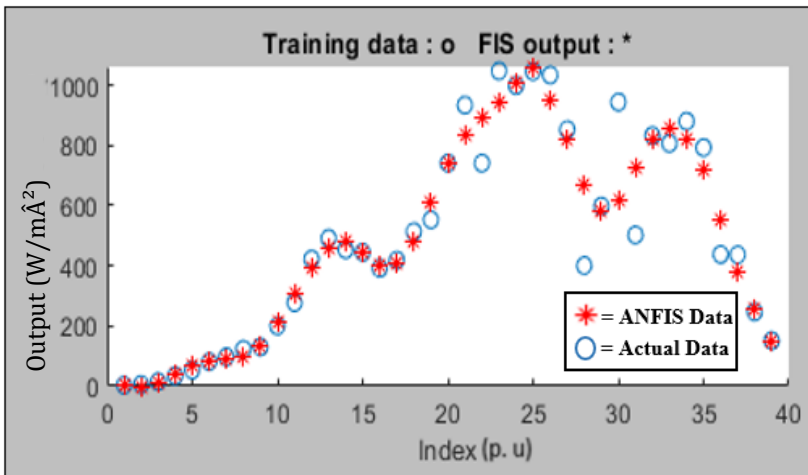


Figure 3: 5MFs

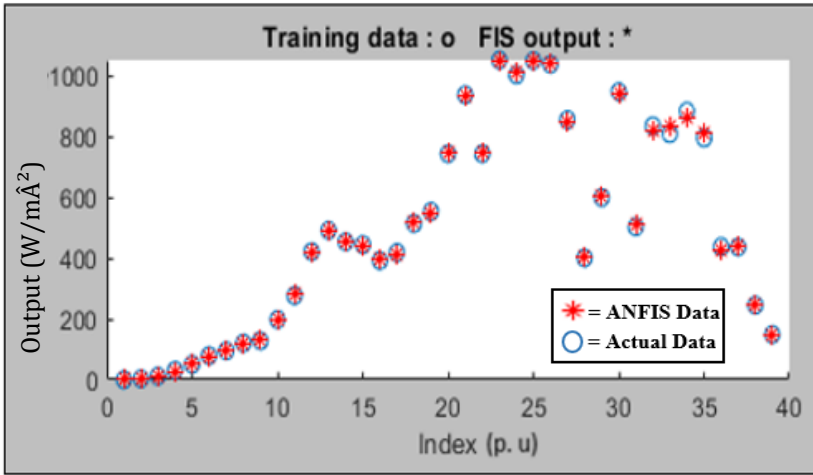


Figure 4: 10MFs

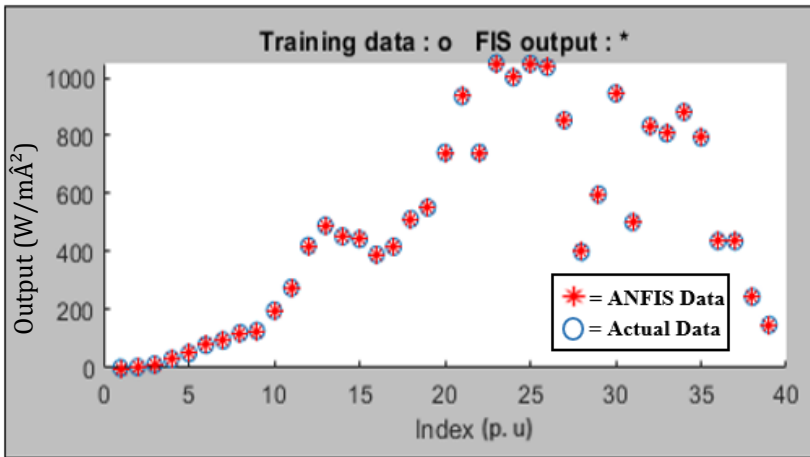


Figure 5: 15MFs

ANFIS testing process

The graph illustrated in Figures 6, 7, and 8 indicate the simulation results of testing data for 5MF, 10MF and 15MF, respectively.

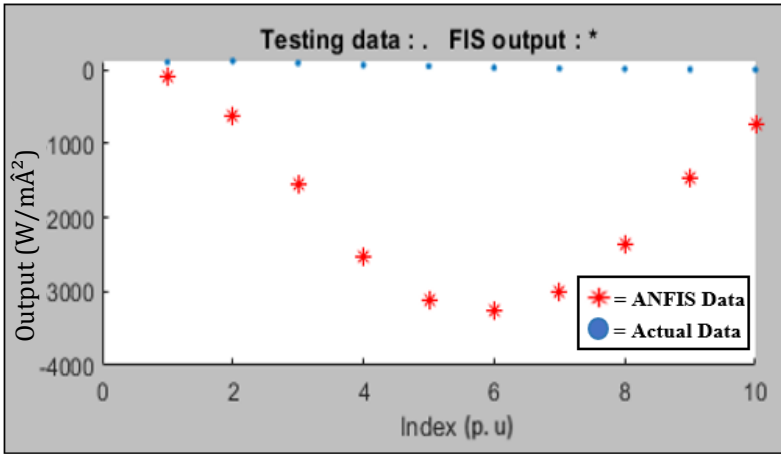


Figure 6: 5MFs

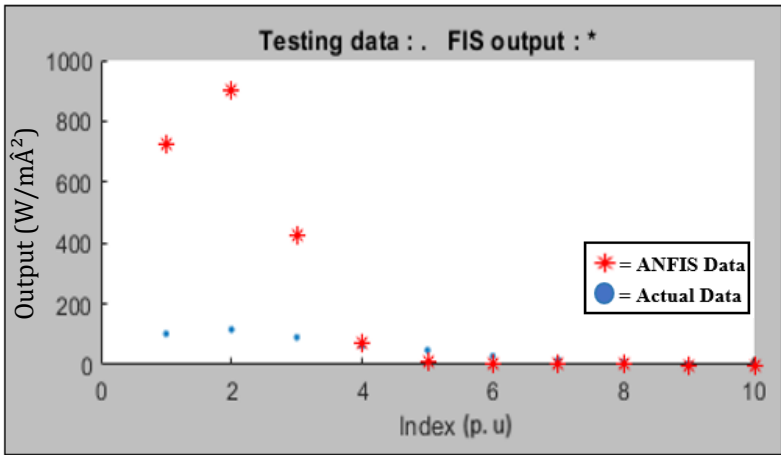


Figure 7: 10MFs

Figures 6, 7 and 8 show generated output for ANFIS testing process in MATLAB. ‘blue dot’ represents the actual data while ‘red dot’ are the testing data after ANFIS is implemented into the system. Compared to the training phase, the results reveal that when a different set of membership functions is utilised, the accuracy of prediction for data before and after ANFIS varies. From the results, 15MFs show the most accurate data while 5 MFs generate the lowest accuracy of prediction. The same goes to training process, by increasing the number of inputs, the model's accuracy and capability improved,

and it was able to anticipate the process in membrane technology. Next, the comparison between actual and ANFIS (prediction) will be discussed.

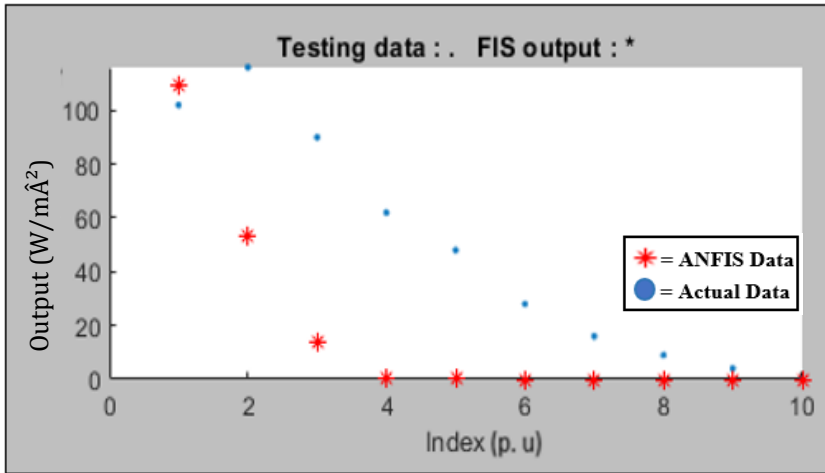


Figure 8: 15MFs

Comparison graph between actual and ANFIS output

The plotted graph for the solar radiation based on actual and ANFIS output is shown in Figures 9, 10 and 11. Based on the graphs, the 'X-Axis' is the number of samples used in the system and 'Y-Axis' represent the value of solar radiation. The 'blue line' shows the actual data while the 'orange line' represents ANFIS data. The curve generated from both outputs is in the form of bell-shaped because the membership function selected for this system is Gaussian type.

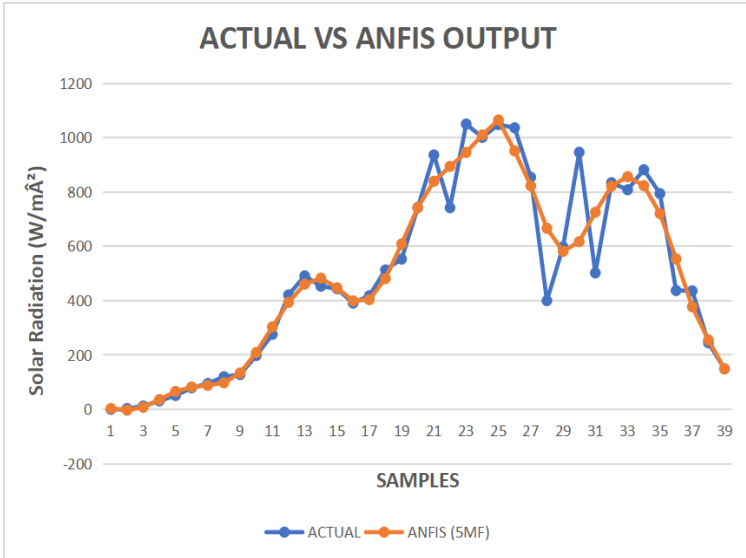


Figure 9: Comparison between actual vs ANFIS output for 5 membership function

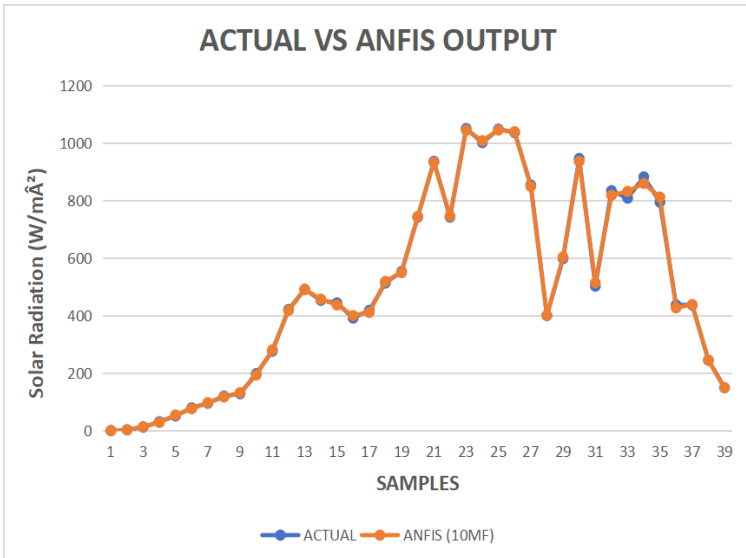


Figure 10: Comparison between actual vs ANFIS output for 10 membership function

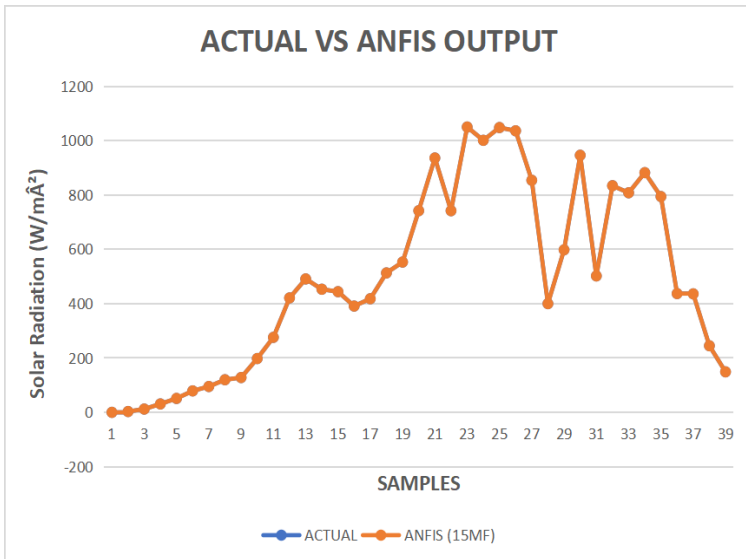


Figure 11: Comparison between actual vs ANFIS output for 15 membership function

Average data obtain for different input MFs

The data in Table 1 summarized the different MF used for 100 iterations on Gaussian MF's type using 49 data.

Table 1: Error value for a different set of membership functions (MF)

Number of input MF	Average training error	Average testing error
5MF	90.3618	2197.1362
10 MF	8.0445	334.5203
15MF	0.0637	41.3420

To achieve the prediction value in ANFIS simulation, there are several steps to be followed. First is to select the data for the training and testing process to be loaded into the system. In this study, the amount of data utilized for training purposes exceeds the number of data used for testing purposes. The objective for this selection is due to the size of the data, which is the larger the data used for training, the better the model learns. Next is to select the type of membership function, which has several models which are Triangle, Trapezoidal, Gaussian, and Sigmoid membership functions, where each type of model will generate a different curve. Then, the selection number for the

input membership function, where this parameter will be affected by the output prediction by ANFIS, either the result is close to the actual value (minimum error) or vice versa. After the selection of input and types of membership functions were made up, next is to train the FIS. In this section, the value of error tolerance and the Epoch (iteration) need to be set up. The output data prediction can be assumed as accurate when it achieved the minimum value of error while for the epoch, the more the epoch value, the more precise prediction output will be generated. The last step are testing the FIS, which is the actual and ANFIS data will be automatically plotted to evaluate the result.

From the overall results shown in Figure 3 to Figure 11, the data represent that the ANFIS technique was able to make an accurate prediction output. All the parameters such as types and number of MF to be used, how much the iteration is to be repeated and the selection for train or test data is very important to optimize the effectiveness of ANFIS prediction toward the whole system. Regarding this analysis, different types of MF have a significant impact on the overall performance of fuzzy representation. The MF are the basic building blocks of fuzzy set theory, the fuzziness of a fuzzy set is dictated by its MF. As a result, the forms of MF are critical for a certain case since they affect a fuzzy inference system. The Gaussian membership function was chosen in this simulation because it is a popular technique for specifying fuzzy sets due to its smoothness and concise notation. As illustrated by [24], this function has the advantage of always being smooth and nonzero.

The objective of using various input numbers of MF is to identify which type will generate the precision of output data for both training and testing when the ANFIS simulate. In line with [13], the output value will be more accurate when the input membership function increase and produce a small error value at the end of the ANFIS process. By referring to the result generated in Figures 9, 10 and 11, the closeness of data between actual and ANFIS implementation is increased when the value of MF is added up which shows the accuracy of the system. Based on error data stated in Table 1, when the number of inputs MF is 5MF, the value of average training and testing error is high which are 90.3618 and 2197.1362, respectively. However, at 10MF, the error reduces to 8.0445 for training and 334.5203 for testing, showing the high accuracy of the model as well as its high capability in the prediction of the membrane process [25]. Furthermore, the input is increased to 15MF, and the error is 0.0637 in training, which shows that the data are almost identical to the actual value of solar radiation while for Testing the error reduces to 41.3420. Hence, this error shows that the number of MF has a bigger impact because it decides how long it takes to compute [26]. Thus, the best model for achieving the highest system performance can be found by adjusting the number/type of MFs.

Conclusion

ANFIS has been successfully utilised to operate solar tracking systems by accurately anticipating the optimum elevation and azimuth angles. The simulations revealed a high rate of prediction and a small Mean Square Error (MSE), where the prediction result by using ANFIS could achieve a similar value to actual data. Other than that, this study has proven that the prediction will be more accurate when the value of the input membership function is large. This can be found when by using 15MF, the optimum efficiency is obtained. In comparison to other concepts, the evaluation findings demonstrate that ANFIS could be more effective at driving solar tracking systems to follow the sun's path across the sky. In conclusion, the objective of the research is achieved, where the modelling of dual axis solar tracker by using MATLAB software was successfully implemented and the analysis shows the performance of the tracking system is improved by using the ANFIS method.

Funding

This work was supported by College of Engineering, Universiti Teknologi MARA (UiTM), Shah Alam, Selangor, Malaysia

Conflict of Interests

All Authors declare that they have no conflict of interest.

Acknowledgement

I would like to express my deepest gratitude to Solar Research Institute (SRI) and College of Engineering, Universiti Teknologi MARA (UiTM), Shah Alam, Selangor, Malaysia for knowledge, facilities and financial support.

References

- [1] F. Dinc, "The analysis on photovoltaic electricity generation status, potential and policies of the leading countries in solar energy," *Renewable and Sustainable Energy Reviews*, vol. 15, pp. 713–720, 2011, doi: 10.1016/j.rser.2010.09.026.
- [2] M. S. Guney, "Solar power and application methods," *Renewable and Sustainable Energy Review*, vol. 57, pp. 776–785, 2016, doi:

- 10.1016/j.rser.2015.12.055.
- [3] S. Karthikeyan, G. Ravikumar Solomon, V. Kumaresan, and R. Velraj, "Parametric studies on packed bed storage unit filled with PCM encapsulated spherical containers for low temperature solar air heating applications," *Energy Conversion and Management*, vol. 78, pp. 74–80, 2014, doi: 10.1016/j.enconman.2013.10.042.
 - [4] 2018 L. S. June 15, "Renewable energy: The clean facts," NRDC, 25-Aug-2021. [Online]. Available: <https://www.nrdc.org/stories/renewable-energy-clean-facts>. [Accessed: 25-Jan-2022].
 - [5] "The importance of Solar Energy," Venture Solar, 16-Feb-2017. [Online]. Available: <https://venturesolar.com/blog/the-importance-of-solar-energy/>. [Accessed: 27-Jan-2022].
 - [6] M. R. S. Shaikh, "A Review Paper on Electricity Generation from Solar Energy," *International Journal Research Applied Science Engineering Technology*, vol. V, no. IX, pp. 1884–1889, 2017, doi: 10.22214/ijraset.2017.9272.
 - [7] M. A. Ponce-Jara, C. Velásquez-Figueroa, M. Reyes-Mero, and C. Rus-Casas, "Performance Comparison between Fixed and Dual-Axis Sun-Tracking Photovoltaic Panels with an IoT Monitoring System in the Coastal Region of Ecuador," *Sustainability*, vol. 14, no. 3, 2022, doi: 10.3390/su14031696.
 - [8] M. Rosyadah, R. Kusumanto, and T. Dewi, "Smart optimization of PV panel output using Fuzzy Logic Controller based solar tracker," *Sinergi*, vol. 26, no. 1, pp. 73, 2022, doi: 10.22441/sinergi.2022.1.010.
 - [9] P. Pangaribuan, D. Darlis, and R. Prabudi, "Implementation of the Sun Tracker System with fuzzy logic on solar panels," *VOLT Jurnal Ilmiah Pendidikan Teknik Elektro*, vol. 3, no. 2, pp. 78–84, 2018, doi: 10.30870/volt.v3i2.3578.
 - [10] D. S. Ponni A, and Ranjitha R, "Comparison of Efficiencies of Single-Axis Tracking System and Dual-Axis Tracking System with Fixed Mount," *Certified International Journal Engineering Science Innovation Technology*, vol. 9001, no. 2, pp. 2319–5967, 2008, [Online]. Available: http://www.ijesit.com/Volume 2/Issue 2/IJESIT201302_66.pdf.
 - [11] M. Prakash and K. Govindarajulu, "Analysis and Testing of Dual Axis Solar Tracker for Standalone PV Systems using Worm Gear," vol. 8, no. 01, pp. 1–8, 2022, [Online]. Available: https://www.researchgate.net/profile/EditorIjmtst/publication/357622354_Analysis_and_Testing_of_Dual_Axis_Solar_Tracker_for_Standalone_PV_Systems_using_Worm_Gear/links/61d6c812da5d105e55209346/Analysis-and-Testing-of-Dual-Axis-Solar-Tracker-for-Standalon.
 - [12] A. Sawant, D. Bondre, A. Joshi, P. Tambavekar, and A. Deshmukh, "Design and analysis of automated dual axis solar tracker based on light sensors," *Proceedings of the International Conference on I-SMAC (IoT in Social, Mobile, Analytics and Cloud)*, I-SMAC 2018, pp. 454–459, 2018,

- doi: 10.1109/I-SMAC.2018.8653779.
- [13] N. AL-Rousan, N. A. Mat Isa, and M. K. Mat Desa, "Efficient single and dual axis solar tracking system controllers based on adaptive neural fuzzy inference system," *Journal King Saud University - Engineering Science*, vol. 32, no. 7, pp. 459-469, 2020, doi: 10.1016/j.jksues.2020.04.004.
- [14] H. Hijawi and L. Arafeh, "Design of Dual Axis Solar Tracker System Based on Fuzzy Inference Systems," *International Journal Soft Computing Artificial Intelligence Applications*, vol. 5, no. 2/3, pp. 23-36, 2016, doi: 10.5121/ijsc.ai.2016.5302.
- [15] A. Mellit, S. Kalogirou, and S. A. Kalogirou, "An ANFIS-based Modeling for a Photovoltaic Power Supply (PVPS) System," 2006. [Online]. Available: <https://www.researchgate.net/publication/30500345>.
- [16] A. K. Suria and R. M. Idris, "Dual-axis solar tracker based on predictive control algorithms," *2015 IEEE Conference Energy Conversion, CENCON 2015*, pp. 238-243, 2015, doi: 10.1109/CENCON.2015.7409546.
- [17] A. Kusagur, S. F. Kodad, and B. V. S. Ram, "Modeling, Design and Simulation of an Adaptive Neuro-Fuzzy Inference System (ANFIS) for Speed Control of Induction Motor," *International Journal Computing Applications*, vol. 6, no. 12, pp. 29-44, 2010, doi: 10.5120/1123-1472.
- [18] J. Da Wu, C. C. Hsu, and H. C. Chen, "An expert system of price forecasting for used cars using adaptive neuro-fuzzy inference," *Expert System Application*, vol. 36, no. 4, pp. 7809-7817, 2009, doi: 10.1016/j.eswa.2008.11.019.
- [19] L. C. Ying and M. C. Pan, "Using adaptive network based fuzzy inference system to forecast regional electricity loads," *Energy Conversion Management*, vol. 49, no. 2, pp. 205-211, 2008, doi: 10.1016/j.enconman.2007.06.015.
- [20] T. W. Septiariini and S. Musikasuwan, "Investigating the performance of ANFIS model to predict the hourly temperature in Pattani, Thailand," *Journal of Physics: Conference Series*, vol. 1097, no. 1, pp. 0-10, 2018, doi: 10.1088/1742-6596/1097/1/012085.
- [21] U. Çaydaş, A. Hasçalik, and S. Ekici, "An adaptive neuro-fuzzy inference system (ANFIS) model for wire-EDM," *Expert Systems Applications*, vol. 36, no. 3 Part 2, pp. 6135-6139, 2009, doi: 10.1016/j.eswa.2008.07.019.
- [22] F. Lai and T. Lee, "Fuzzy Competitive Learning," *Elsevier Neural Network*, 1994.
- [23] "Solar elevation angle (for a day) Calculator," High accuracy calculation for life or science. [Online]. Available: <https://keisan.casio.com/exec/system/1224682277>. [Accessed: 27-Jan-2022].
- [24] N. Talpur, M. N. M. Salleh, and K. Hussain, "An investigation of membership functions on performance of ANFIS for solving classification problems," *IOP Conference Series Materials Science*

Engineering, vol. 226, no. 1, 2017, doi: 10.1088/1757-899X/226/1/012103.

- [25] M. Babanezhad, A. Masoumian, A. T. Nakhjiri, A. Marjani, and S. Shirazian, "Influence of number of membership functions on prediction of membrane systems using adaptive network based fuzzy inference system (ANFIS)," *Scientific Reports*, vol. 10, no. 1, pp. 1–20, 2020, doi: 10.1038/s41598-020-73175-0.
- [26] A. Sadollah, "Introductory Chapter: Which Membership Function is Appropriate in Fuzzy System?," *Fuzzy Logic Based Optimization Methods Control Systems and its Applications*, pp. 3–6, 2018, doi: 10.5772/intechopen.79552.

Optimization of Uniaxial Tensile Stress-Strain Response of 3D Angle Interlock Woven Fabric Composite using Weft Density and Draw-In Plan Variables

Muhammad Nasrun Faris Mohd Zulkifli, Mohamad Faizul Yahya*,
Suzaini Abdul Ghani
Textile Research Group, Faculty of Applied Sciences,
Universiti Teknologi Mara (UiTM), Shah Alam, MALAYSIA
*mfy@uitm.edu.my

Bilal Zahid
Department of Textile Engineering,
Faculty of Mechanical and Manufacturing Engineering,
NED University of Engineering and Technology, Karachi, PAKISTAN

ABSTRACT

Currently, 2D woven composites are extensively incorporated into a variety of technical automotive body parts and protective body armor owing to their excellent fabric strength performance. However, there is still a lack of attempts to utilize 3D woven fabrics for the same technical application. Hence, it is vital to examine the fundamental tensile strength of woven fabric composite materials when determining their suitability for end-use applications. This study aimed to investigate the novel effects of two parameters on the uniaxial tensile strength of a high-tenacity polyester three-layer 3D angle interlock (3DAI) woven fabric composite, namely, weave drafting draw-in insertion and weft density. Four different drafting patterns were considered: pointed (DRW 1), broken (DRW 2), broken mirror (DRW 3), and straight (DRW 4), for weft density at 14 and 25 pick.cm⁻¹. Samples of the 3DAI woven fabric reinforced with epoxy composite at different drafting patterns and weft density combinations were produced and tested. Consequently, the maximum tensile stress and strain were recorded in the woven fabric composite sample with DRW 4 and 25 pick.cm⁻¹ at 113 MPa and 11%, respectively. The study shows

that different weft densities and draw-in plan settings play a significant role in the tensile strength performance of the 3DAI woven composite.

Keywords: *3D Angle Interlock; Woven Composite; Uniaxial Tensile; Draw-In Plan; Weave Density*

Introduction

Previously, conventional 2D woven fabrics were extensively utilized as the main material for textile composites in technical applications. In addition, 2D woven composites have been used to replace metal and ceramic materials in automotive parts, especially because of their light weight, durability, and low manufacturing costs. Nevertheless, further studies have shown that 2D woven fabrics have weak delaminating resistance. This causes the ply fabrics inside the composite to split during matrix cracking upon force application, leading to out-of-plane properties in textile composites [1]-[4]. To resolve the interlaminar failure caused by 2D woven composites, scientists have developed a solution by introducing a three-dimensional (3D) woven fabric. The preference for 3D woven fabric in the composite is due to its better delamination resistance, good impact and ballistic resistance, and high in-plane properties. These mechanical properties are important for optimizing the technical applications of 3D woven fabrics. In general, knowledge of 3D woven fabric parameters and their impact on strength performance will promote the adoption of woven fabric composites in various technical applications. The existing literature shows a potential research gap regarding the drafting draw-in and weft density effects on 3DAI woven fabric performance. Thus, this paper aimed to investigate the uniaxial tensile stress-strain variation of a 3DAI woven fabric composite with different draw-in patterns and weft density combinations.

Literature Review

Recently, application of the 3D woven fabric to manufacture automotive body part has been receiving many interests from researchers. For an instance, study on 3D orthogonal fabric for the possibility of leaf spring application suggested that 3D fabric able to provide better tensile and flexural strength than 2D fabric [5]. Finite element simulation work on 3D woven composite on shock tower and fender applications able to achieve 25% and 30% lighter weight property respectively while successfully optimize the strength factor of the model [6], [7]. Analysis of different 3D weave structure for intend interior automobile application indicated that through thickness weave able to provide higher tensile strength performance than layer to layer weave [8]. Those studies

shows that determination and optimization the tensile breaking strength of the woven composite structure before its use is vital to ensure that the durability to withstand high amount of stress-strain load and elastic modulus can be meet.

Investigation of the tensile strength of 3D woven fabrics is vital, as it will help researchers to evaluate the fundamental hardness and ductility properties of woven composites before they can be recommended for suitable end-use applications. The tensile strength performance could be optimized by determining the woven fabric characteristics. Few studies have shown that the tensile strength of woven textile fabric depends on the fabric weft density and weave structure [8]-[11]. The weft density is the number of weft yarn insertions per fabric length; a high weft density indicates tightly packed weft yarns. Previous studies on the effects of weft density on single weave structures, such as 3D angle interlock [11], 2D plain [12] and 2D twill [13], found that a higher weft density produces a higher tensile strength owing to the increased yarn friction force at the weft horizon of the woven fabric. On the other hand, a study on a 2D plain weave by [9] reported an increase in weft density from 138 to 141 pick.10 cm⁻¹ had no effect on the tensile strength, as the increase in the weft density gap did not significantly elevate the yarn friction build-up. In addition to the weft density, different weave interlacement architectures affect the tensile strength of the woven fabric. The drafting approach played an important role in the resulting weave structure. During the weaving process, different drafting approaches involve varying the number of heald shafts used in drawing warp yarns [14]. Manipulation of the yarn-yarn interlacement sequence within the weave structure resulted in different woven fabric patterns. A comparative study on different types of weave structures showed that the 2D plain structure has the highest tensile strength compared to the twill and satin structures owing to a tighter interlacement pattern [15]. A compact weave structure contains tightly packed yarns, leading to friction force build-up and a higher tensile strength [16]-[17]. In contrast, a weave structure with a loose interlacement pattern allows for longer yarn elongation, leading to a lower tensile strength [18].

Research Method

Material preparation

The draw-in plan or drafting plan is a technique in which a certain number of heald frames are used during weaving manufacturing to produce the weave design, and the sequence order of the warp yarns (yarns from the vertical direction) is lifted or lowered by the heald frames. Four different draw-in plans were considered for the samples, which are pointed (DRW 1), broken (DRW 2), broken mirror (DRW 3), and straight (DRW 4) as depicted in Figure 1. For each draw-in plan, weft densities of 14 and 25 pick.cm⁻¹ were manufactured. The amount of weft density represents the total amount of weft yarns (yarns

inserted in the horizontal direction) per centimetre. All samples of the three-layer 3D angle interlock woven fabric were manufactured using the Sulzer rapier loom at 50 revolutions per minute (rpm), located at the Textile Weaving Workshop, UiTM Shah Alam, Malaysia. Throughout the weaving process, the weft density was automatically controlled by the system according to the warp density rate, which was set constant at 16 end.cm^{-1} . For all samples, the warp (90° , vertical) and weft (0° , horizontal) directions were constructed using spun and ply multifilament polyester yarns, respectively. Once completed, using the hand lay-up technique, a 3.7:1.7 mixture ratio of epoxy resin (BJC-39) and hardener was poured and spread evenly onto each sample in a mold plate, resulting in a polymer composite reinforced with 3D angle interlock woven fabric. The samples were left for 24 hours to ensure proper curing.

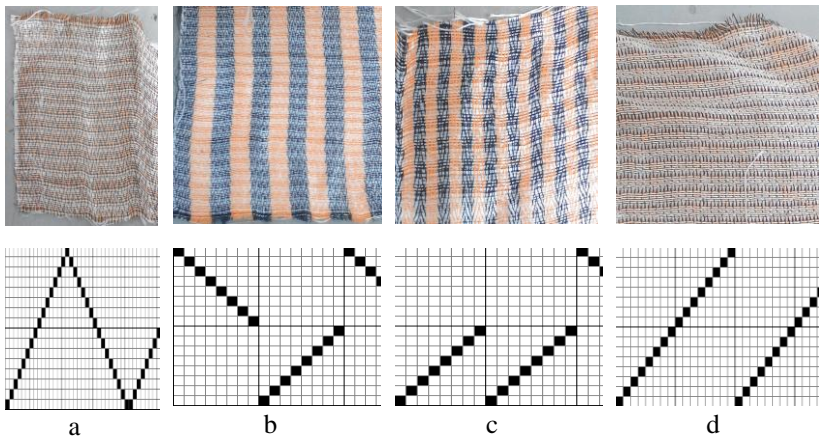


Figure 1: 3D angle interlock woven fabric samples based on the four draw-in plans; a) pointed (DRW 1), b) broken (DRW 2), (c) broken mirror (DRW 3), and d) straight (DRW 4)

Additionally, Figure 2 illustrates the 3D cross-sectional model of three-layer 3DAI woven fabric developed by using TexGen software. The model represents the actual yarn-yarn interlacing sequence order of the 3DAI used in this study.

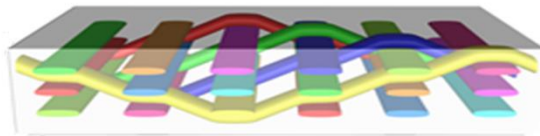


Figure 2: 3D illustration of three-layer 3DAI woven fabric

Yarn strength analysis

Yarn samples were prepared with 250 mm sample length. Yarn strength analysis was experimented on Tenso Lab 5000 strength tester machine. All yarn specimens were subjected to tenacity test based on the ASTM D2256, using a 5 kN load cell with the speed constant at 500 mm/min and the yarn pretension was set at 0.1 N. Yarn tenacity were calculated as the maximum amount of force at break of the yarn divided with the yarn linear density in Tex. Five readings were recorded to calculate the average result of yarn tenacity performance.

Crimp analysis

The fabric crimp samples were prepared with 200 mm length accordingly to the warp and weft directions based on ASTM D3883. A single yarn was carefully pulled out from the woven fabric specimen and ten readings were recorded to ensure consistency. In Equation 1, the crimp presence, C , can be measured by identifying the length of yarn within the woven fabric, L_f and the length of yarn pulled out and straighten from the woven fabric, L_y . The analysis was repeated five times to calculate the average result.

$$C = \frac{L_y - L_f}{L_f} \times 100\% \quad (1)$$

Woven composite tensile strength

The prepared samples were cut into specimens with 200 mm length, 25 mm width, and 1 mm thickness. The uniaxial tensile strength evaluation was conducted on Tenso Lab 5000 strength tester machine. All samples were subjected to tensile tests based on the ASTM D3039 standard, using a 50 kN load cell with a crosshead speed set constant at 100 mm/min. For each combination of draw-in plan and weft density, five samples were prepared and tested to measure the average breaking strengths in the weft and warp directions, respectively.

Result and Discussion

Yarn properties

Table 1 presents the details of spun and plied filament polyester yarns used in this research work. Identification of physical property shows that plied filament yarn provided with high value of yarn linear density compared to both spun yarns. In addition, plied filament yarn outperformed yarn tenacity strength performance by 1036.9 cN/Tex higher than both black and orange spun yarns at 105.9 and 331.4 cN/Tex. Configuration of ply technique between two sets of filament yarn shows a good outcome to improve the yarn strength.

Table 1: Yarn properties used to manufacture 3D angle interlock woven composite

Type of yarn structure	Mass of yarn (g)	Yarn linear density (Tex)	Yarn tenacity (cN/Tex)
Spun polyester black	8	26	105.9
Spun polyester orange	9	30	331.4
Plied filament polyester	1.5	100	1036.9

Crimp properties

Table 2 shows the readings of yarn crimp presence on warp and weft direction of the woven fabric respectively based on the variations of draw-in plan (DRW). It can be seen from the Table 2 that 14 pick.cm⁻¹ and 25 pick.cm⁻¹ on DRW 1 and 4 resulted highest crimp presence in warp direction with 7.8%, and 9.5%, respectively. Meanwhile, 14 pick.cm⁻¹ and 25 pick.cm⁻¹ on DRW 2 and 3 at weft direction consistently presented the lowest crimp with 3.1 and 4.3%, respectively.

Table 2: Crimp presence (%) in warp and weft directions of 3DAI woven fabric sample

Direct. Sample	Crimp in warp direction (%)				Crimp in weft direction (%)			
	DRW1	DRW2	DRW3	DRW4	DRW1	DRW2	DRW3	DRW 4
14	7.7	7.1	7.1	7.8	3.6	3.1	3.1	3.7
25	9.5	9.1	9.1	9.5	4.7	4.3	4.3	4.8

This finding were consistent with several studies [19]-[20] reported on crimp. The observation on this 3DAI woven fabric shows that warp direction fabric produced high crimp percentage as it exhibited more yarn interlacement sequence than weft counterpart. Meanwhile, changes of different draw-in plan factor indicate an interesting pattern where DRW 1 and 4 produced higher percentage of crimp than DRW 2 and 3.

Uniaxial tensile response on weft density of 14 pick.cm⁻¹

Figure 3 shows the tensile stress-strain of 3DAI woven composite based on 14 pick.cm⁻¹. According to the curve line behaviour, the composite stress-strain curve line was reacted as elastic behavior which majorly affected by the woven fabric. Hence the graph was divided into 3 phases to represents the behavior of composite [18]-[19]. In the first phase, the stress-strain curve pattern of DRW 1 and 2 is shown to be above on top of DRW 3 and 4 by % strain at the first tensile load. Within phase 1, however, the stress-strain value of the DRW 1 curve line had abruptly altered from 0.4% to 0.6% strain. In the second phase,

all of the work's draw-in plans demonstrated a close curve pattern in strain ranges of 0.6% to 1.2%. The curve of all draw-in plans demonstrated significant stress-strain fluctuation between 1.2% and 1.6% strains in the third phase. It's worth noting that the DRW 4 curve behaviour has the highest stress and strain results, with 31.77 MPa and 1.6%, respectively. DRW 2, on the other hand, had the lowest stress value of 21.00 MPa and the smallest strain of 1.4%.

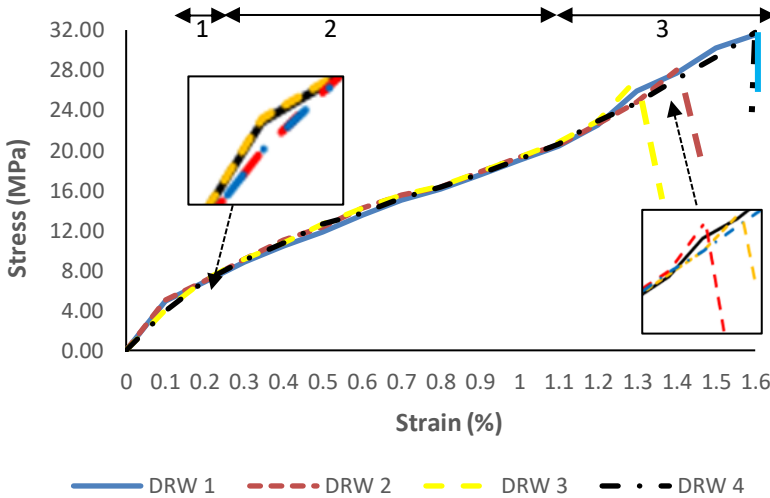


Figure 3: Stress-strain curves in the warp direction, for all draw-in plans with 14 pick.cm⁻¹ density

The stress-strain curve behaviour of 14 pick.cm⁻¹ of 3D woven composite in the weft direction is shown in Figure 4. The curve line was divided into two distinct phases in general. Phase 1, DRW 1 and 4, produced the highest stress-strain curve line in the 0 to 2.5 % strain region. Within the 2.5% strain range, however, DRW 2 and 3 had the lowest stress-strain curve. All draw-in plans in the second phase revealed a stress-strain fluctuation curve line in 4% to 5% strain ranges. At 6 % strain, the DRW 1 and 4 curve lines appeared on top of the DRW 2 and 3 curve lines. In general, DRW 4 has the greatest stress value of 64 MPa and accordingly % strain.

Uniaxial tensile response on weft density of 25 pick.cm⁻¹

Figures 5 and 6 show the stress-strain variations in the warp and weft directions, respectively, for the four draw-in plans with 25 pick.cm⁻¹. Compared to the 14 pick.cm⁻¹ cases, the stress-strain curves in the warp direction for the 25 pick.cm⁻¹ indicated three distinct phases. In the first phase, all curves followed a linear trend with similar values. The second phase was in between 0.6% to 2.7% strain. In the initial part of the second phase, between

0.6% and 1.7%, DRW 3 had the lowest stress value, while DRW 1 and DRW 4 had the highest values. At the start of the third phase, DRW 1 had the lowest value. However, the trend was reversed with DRW 1 recording the highest stress after 3.7% strain. Marked deviations between the curves were then observed between 3.7% and 4.5% strain. Eventually, the curves for DRW 1 and DRW 4 ended at a strain of 4.6%, whereas DRW 2 and DRW 3 ended at 4.5%. The highest and lowest maximum stresses were 48 MPa and 46 MPa, for DRW 1 and DRW 3, respectively.

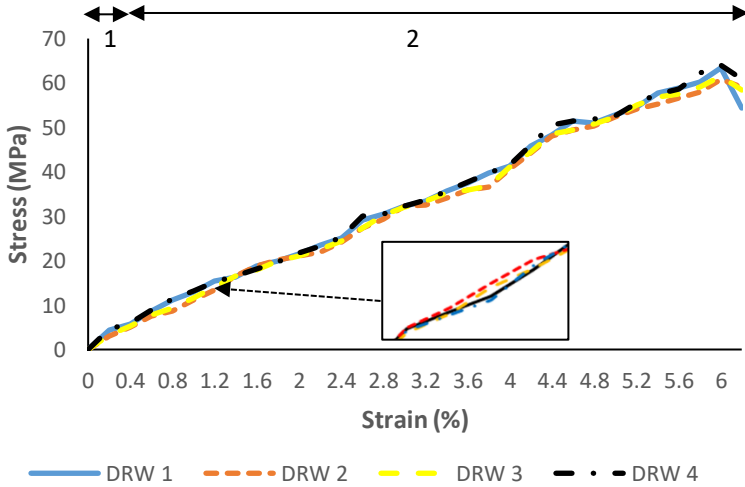


Figure 4: Stress-strain curves in the weft direction, for all draw-in plans with 14 pick.cm^{-1} density

The three distinct phases of the stress-strain curves were also present in the weft direction, as shown in Figure 6. Similarly, close trends of all curves in the first stage were observed until 0.7% strain. Similar profiles were seen for DRW 1 and DRW 4, indicating markedly higher stress values than DRW 2 and DRW 3 in the second phase. At 5.5%, there was a noticeable rise in DRW 2 to yield the highest stress value at this point, and this trend continued until DRW 2 reached the failure point at around 9% strain. Eventually, DRW 4 reached its failure point at a strain of 11%, with the highest maximum stress of 113 MPa. The lowest maximum stress was for DRW 2, at 108 MPa and 9% strain.

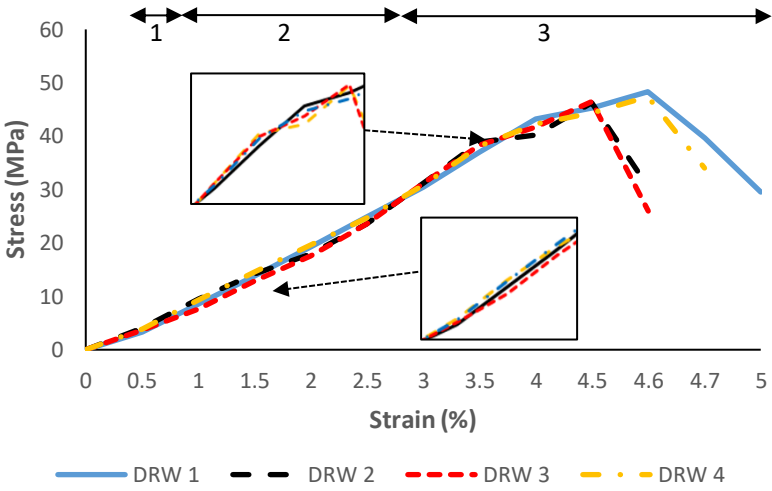


Figure 5: Stress-strain curves in the warp direction, for all draw-in plans with 25 pick.cm⁻¹ density

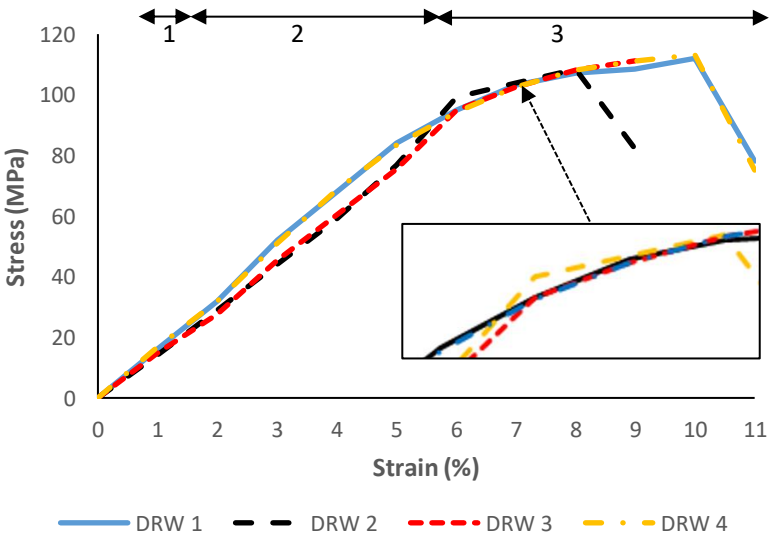


Figure 6: Stress-strain curves in the weft direction, for all draw-in plans with 25 pick.cm⁻¹ density

Uniaxial tensile stress-strain response discussion

In general, it can be seen that weft densities of 14 and 25 pick.cm⁻¹ in the warp direction samples in Figures 3 and 4 produced a nearly straight or linear line look alike pattern compared to the other counterparts in the weft direction, as shown in Figures 4 and 6. This condition shows that the uniaxial tensile stress-strain behaviour of was still significantly affected by the epoxy resin. Meanwhile, the woven composite sample in the weft direction tends to generate a nonlinear pattern. The presence of more weft yarn directly impacts yarn-yarn interlacement, thus resulting in a high requirement build-up [21]-[24]. Hence, the uniaxial tensile stress-strain of high weft density in the weft direction begins to react according to the nature of the nonlinear woven fabric tensile stress-strain performance. The close trends of the stress-strain curves for all draw-in plans in the 14 pick.cm⁻¹ samples indicate that the stress resistance build-ups were almost uniform, particularly for the first and second phases. In the first phase, when the tensile loads were low, all draw-in plans exhibited similar behavior. The fluctuation of the curved lines within the third phase of 14 pick.cm⁻¹ of the warp sample suggested an uneven stress performance of the loaded warp yarn. It can be seen that, DRW 1 and 4 gave the highest maximum stress before break value. This is because both DRW 1 and 4 recorded the least stress value reduction on the loaded yarn during composite elongation compared to the other counterparts, DRW 2 and DRW 3. The elongation rate of deformation is dependent on the stress performance of the loaded warp yarn. A greater length of warp yarn floating on woven fabric will produce a high amount of loaded warp yarn stress strength. The increasing tensile strengthening induced slightly higher resistance build-ups in the warp direction for all the plans in the second phase. The discrepancies in the resistance build-ups were significant in the third phase, with DRW 1 and DRW 4 indicating the least strength loss after tensile straightening.

On the other hand, 14 and 25 pick.cm⁻¹ in the weft direction in Figures 4 and 6 have a tendency to generate a nonlinear or straight curve line. The inconsistency of uniaxial tensile stress-strain behavior between low and high amounts of weft density is highly due to the woven fabric interlacement-resistant break capability within the composite matrix [22], [25]. The presence of more yarn-yarn interlacement sequences owing to the high weft density will create a more interlacement sequence. As a result, a large amount of load-breaking resistance is produced. Evidently, in the latter, there were higher stress build-ups in the weft direction for DRW 1 and DRW 4, as shown by the larger discrepancies between DRW 2 and DRW 3. This finding agrees with those of the studies reported in [14], [19]. For all draw-in plans, the tensile straightening in the weft direction induced inconsistent stress, which resulted in fluctuations in the maximum stress, leading to the failure point. This inconsistent behavior can be attributed to the different yarn interlacement amounts in each draw-in plan. Thus, the lowest interlacement and crimp

percentages in DRW 1 and DRW 4 resulted in the highest maximum stresses at failure.

Conclusion

In this study, the novel effects of weave draw-in plans and weft density on the tensile strength performance of 3DAI woven composites were investigated. Samples comprising various combinations of the four draw-in plans and four weft densities were tested. It can be noticed that the DRW 4 draw-in plan with 25 pick.cm⁻¹ weft density resulted in the highest maximum stress and strain at 113 MPa and 11%, respectively. Interestingly, the DRW 1 plan was found to exhibit a similar stress-strain profile similar to that of the other plans at lower loads. As the load increased, higher stress values were recorded for DRW 1. It is concluded that the stress-strain performance of the 3DAI woven composite varies with the draw-in plan and weft density. A high weft density positively influences the tensile strength. Meanwhile, each DRW plan showed that different settings produced a distinctive tensile performance.

Contributions of Authors

The authors confirm the equal contribution in each part of this work. All authors reviewed and approved the final version of this work.

Funding

This work was supported by through research grant 600-IRMI 5/3/LESTARI (044/2019).

Conflict of Interests

All authors declare that they have no conflicts of interest.

Acknowledgment

The authors would like to thank Faculty of Applied Sciences, Universiti Teknologi MARA (UiTM) Shah Alam for the facilities support, Universiti Teknologi MARA (UiTM) for the internal funding.

References

- [1] B. Kumar and J. Hu, "Woven fabric structures and properties," *Engineering of High-Performance Textiles, The Textile Institute Book Series*, pp. 133–151, 2017, doi: 10.1016/B978-0-08-101273-4.00004-4.
- [2] Mohamed Nasr Saleh, Ying Wang, Arief Yudhanto, Adam Joesbury, Prasad Potluri, Gilles Lubineau and Constantinos Soutis, "Investigating the Potential of Using Off-Axis 3D Woven Composites in Composite Joints' Applications," *Applied Composite Materials*, vol. 24, no. 2, pp. 377–396, 2017, doi: 10.1007/s10443-016-9529-9.
- [3] B. Kazemianfar, M. Esmaceli, and M. R. Nami, "Response of 3D woven composites under low velocity impact with different impactor geometries," *Aerospace Science and Technology*, vol. 102, pp. 105849, 2020, doi: 10.1016/j.ast.2020.105849.
- [4] T. Gereke and C. Cherif, "A review of numerical models for 3D woven composite reinforcements," *Composite Structures*, vol. 209, no. October, pp. 60–66, 2019, doi: 10.1016/j.compstruct.2018.10.085.
- [5] V. Khatkar, B. K. Behera, and R. N. Manjunath, "Textile structural composites for automotive leaf spring application," *Composites Part B: Engineering*, vol. 182, no. November 2019, pp. 107662, 2020, doi: 10.1016/j.compositesb.2019.107662.
- [6] W. Tao, P. Zhu, Z. Liu, and W. Chen, "Lightweight design of three-dimensional woven composite automobile shock tower," *Proceeding. Conference: ASME 2018 International Design Engineering Technical Conferences*, vol. 3, pp. 1–10, 2018, doi: 10.1115/DETC2018-85519.
- [7] W. Tao, Z. Liu, P. Zhu, C. Zhu, and W. Chen, "Multi-scale design of three dimensional woven composite automobile fender using modified particle swarm optimization algorithm," *Composite Structures*, vol. 181, pp. 73–83, 2017, doi: 10.1016/j.compstruct.2017.08.065.
- [8] M. Kashif, S. T. A. Hamdani, Y. Nawab, M. A. Asghar, M. Umair, and K. Shaker, "Optimization of 3D woven preform for improved mechanical performance," *Journal of Industrial Textiles*, vol. 48, no. 7, pp. 1206–1227, 2019, doi: 10.1177/1528083718760802.
- [9] J. S. Lim, B. H. Lee, C. B. Lee, and I.-S. Han, "Effect of the Weaving Density of Aramid Fabrics on Their Resistance to Ballistic Impacts," *Engineering*, vol. 04, no. 12, pp. 944–949, 2012, doi: 10.4236/eng.2012.412a119.
- [10] M. Dahale et al., "Effect of weave parameters on the mechanical properties of 3D woven glass composites," *Composite Structures*, vol. 223, no. March, pp. 110947, 2019, doi: 10.1016/j.compstruct.2019.110947.
- [11] F. M. Z. Nasrun, M. F. Yahya, S. A. Ghani, and M. R. Ahmad, "Effect of weft density and yarn crimps towards tensile strength of 3D angle interlock woven fabric," *AIP Conference Proceedings*, vol. 1774, pp. 1-7,

- 2016, doi: 10.1063/1.4965051.
- [12] H. Özdemir and E. Mert, “The effects of fabric structural parameters on the breaking, bursting and impact strengths of diced woven fabrics,” *Tekst. ve Konfeksiyon*, vol. 23, no. 2, pp. 113–123, 2013.
- [13] O. G. Ertaş, B. Zervent Ünal, and N. Çelik, “Analyzing the effect of the elastane-containing dual-core weft yarn density on the denim fabric performance properties,” *The Journal of The Textile Institute*, vol. 107, no. 1, pp. 116–126, 2016, doi: 10.1080/00405000.2015.1016319.
- [14] M. Ashir, D. M. P. Vo, A. Nocke, and C. Cherif, “Adaptive fiber-reinforced plastics based on open reed weaving functionalization,” *IOP Conference Series: Materials Science and Engineering*, vol. 406, no. 1, pp. 1–9, 2018, doi: 10.1088/1757-899X/406/1/012063.
- [15] G. A. Nassif, “Effect of weave structure and weft density on the physical and mechanical properties of micro polyester woven fabrics,” *Journal of American Science*, vol. 9, no. 3, pp. 1326–1331, 2012.
- [16] S. Dai, P. R. Cunningham, S. Marshall, and C. Silva, “Influence of fibre architecture on the tensile, compressive and flexural behaviour of 3D woven composites,” *Composites Part A: Applied Science and Manufacturing*, vol. 69, pp. 195–207, 2015, doi: 10.1016/j.compositesa.2014.11.012.
- [17] J. S. Jones, R. R. Rowles, K. N. Segal, and D. L. Polis, “Comparative study of 3-dimensional woven joint architectures for composite spacecraft structures,” *International SAMPE Technical Conference*, pp. 1–18, 2011.
- [18] J. Hu, *Structure and Mechanics of Woven Fabric*. Woodhead Publishing, 2004.
- [19] C. Huang, L. Cui, H. Xia, and Y. Qiu, “Influence of Crimp and Inter-Yarn Friction on the Mechanical Properties of Woven Fabric under Uniaxial / Biaxial Tensile Loading,” *Fibres and Textiles In Eastern Europe*, vol. 6, no. 144, pp. 43–52, 2020, doi: 10.5604/01.3001.0014.3797.
- [20] S. Ö. Hacıoğulları and O. Babaarslan, “An investigation on the properties of polyester textured yarns produced with different fiber cross-sectional shapes,” *Industria Textila*, vol. 69, no. 4, pp. 270–276, 2018, doi: 10.35530/it.069.04.1281.
- [21] H. Zhou, X. Xiao, K. Qian, and Q. Ma, “Numerical simulation and experimental study of the bursting performance of triaxial woven fabric and its reinforced rubber composites,” *Textile Research Journal*, vol. 90, no. 5–6, pp. 561–571, 2020, doi: 10.1177/0040517519871943.
- [22] H. Özdemir and B. M. İçten, “The mechanical performance of plain and plain derivative woven fabrics reinforced composites: tensile and impact properties,” *The Journal of The Textile Institute*, vol. 109, no. 1, pp. 133–145, 2018, doi: 10.1080/00405000.2017.1333719.
- [23] H.A. Aisyah, M.T. Paridah, A. Khalina, S.M. Sapuan, M.S. Wahab, O.B. Berkalp, C.H. Lee and S.H. Lee, “Effects of fabric counts and weave designs on the properties of Laminated Woven Kenaf/Carbon fibre

- reinforced epoxy hybrid composites,” *Polymers*, vol. 10, no. 12, pp. 1-19, 2018, doi: 10.3390/polym10121320.
- [24] M. N. F. M. Zulkifli and M. F. Yahya, “3D angle interlock woven fabric mechanical tensile strength based on various fabric weft densities,” *Journal of Mechanical Engineering*, vol. 5, no. Specialissue 1, pp. 92–103, 2018.
- [25] M. Li, P. Wang, F. Boussu, and D. Soulat, “Investigation of the Strength Loss of HMWPE Yarns During Manufacturing Process of 3D Warp Interlock Fabrics,” *Applied Composite Materials*, vol. 29, no. 0123456789, pp. 1-15, 2021, doi: 10.1007/s10443-021-09951-6.

Evaluating and Predicting Overall Equipment Effectiveness for Deep Water Disposal Pump using ANN-GA Analysis Approach

Soud Al-Toubi*, Babakalli Alkali, David Harrison
Glasgow Caledonian University, Department of Mechanical Engineering,
Glasgow, UK
*soud.saleh.toubi@gmail.com

Sudhir C.V.
National University of Science and Technology,
Department of Mechanical & Industrial Engineering,
Muscat, SULTANATE OF OMAN

ABSTRACT

This study proposes the Artificial Neural Network with a Genetic Algorithm analysis approach to investigate the Overall Equipment Effectiveness of the deep-water disposal pump system. The ANN-GA model was developed based on six big losses over eighteen successive months of the operating period to evaluate the current and future performance of the DWD system. 70% of the data was used for training and 15% for each data validation and testing. The DWD system faces frequent failure issues, significantly impacting its performance, so it is important to reveal the main causes of these failures to manage them properly. ANN-GA is applied to make a linear trend prediction and assesses the confidence and accuracy of the results obtained. Analysis of ANOVA (variance) was adopted as an additional decision tool for detecting the variation of process parameters. ANN-GA results showed that the current OEE value ranges between 29% to 54%, whereas the predicted future system performance average is approximately 49%, which reflects the poor performance of the DWD pump system in the future compared to the world-class target (85%). ANN-GA analysis results indicated were very close and matched with the actual values. The model framework and analysis presented are used to develop a decision support tool for managers for early intervention to minimize system deterioration, reduce maintenance costs and increase productivity. Furthermore, it allows early identifying the potential area of

improvement to support continuous improvement (CI) objectives by identifying and eliminating unnecessary maintenance activities. The proposed model framework uses the ANN approach to identify the current state and predict the future of the system performance to ensure confidence in the results. The contribution of the paper will be helpful for experts like managers, reliability engineers, and maintenance engineers to identify the state of the system's performance in advance.

Keywords: Overall Equipment Effectiveness; Genetic algorithm; Artificial Neural Network; Performance; Six Big Losses

Introduction

Deep Water Disposal (DWD) pumps are widely used in the Oil and Gas industries. Their primary function is to dispose of contaminated water associated with oil and gas production. The DWD is vital to the smooth operation, representing a significant segment of the entire operation. High reliability of these pumps is envisaged to reduce the maintenance cost (failure cost), and thus reduce the process disruption and ensure continuous plant productivity, which reflects positively on the revenue generated. The current state of the pump system performance is decreasing based on the number of failures during the specified operating period. Identification and prognosis of the cause of the main failures will help to set a clear maintenance strategy to reduce these deficiencies and maintain system performance and effectiveness. The rated capacity of each DWD pump was approximately 20,000 m³/day. The pump is supplied by Sulzer (HPCP 200-330, 5 stages) and connected to the electric motor by coupling through a gearbox. The electric motor from ABB 11 KV/4.50 MW brush type is used in all the pumps. Moreover, 11 KV motor switching fed through the circuit breaker make Alstom GEC rated from the step-down transformer 33/11 KV, rated current 1250 Amps with closing and opening voltage of 50 V DC. The gearbox (fluid coupling) is situated between the motor and driven machine (pump), and it's made by Voith type R 17K2, which provides variable speed (discharge pressure) depending on the well's reservoir condition.

The concept of lean manufacturing is widely adopted by engineering organizations to maintain their position in the competitive business arena. This has prompted organizations to evaluate their challenges continuously and use appropriate techniques to improve their efficiency" [1]. Overall Equipment Effectiveness (OEE) is a critical measurement that has evolved over the years and its relevance was discussed extensively by Seiichi Nakajima in 1988 [2]. The OEE measurement is becoming increasingly popular, and the TPM concept is used as a standalone powerful benchmark key performance indicator (KPI) tool for productivity improvement [3]. Nakajima defined OEE

as a metric to evaluate the equipment's effectiveness [4]. OEE quantifies how well a machine performs relative to its designed capacity during the scheduled periods. It is a well-known notion in maintenance and is a way of measuring the machine effectiveness and assess how effectively an equipment is utilized to its full potential. Initially, the OEE metrics consisted of six big losses: breakdowns, setup and adjustment, idling and minor stoppage, reduced speed, defects in the process, start-up losses, and reduced yield. On the other hand, it identifies and measures losses of essential aspects of equipment, focusing on three analyzing tools based on availability, performance, and quality rate directly related to six big equipment losses [5]. OEE provides a systematic process to readily identify and eliminate the six big loss sources and support continuous improvement to achieve zero breakdowns and defects related to equipment [6]. OEE is a global best practice measure to monitor and improve the effectiveness of manufacturing processes.

Over recent years, management has focused on the wastes generated due to failure or breakdown of machines that incurred a significant organization investment through loss in production and time. One of the significant challenges faced in the industrial environment is the appropriate and efficient use of the available resources for operation and workforce to sustain productivity. According to Dal et al. [7], the OEE role could go beyond just monitoring and controlling of process improvement initiatives, it provides a systematic method to achieve the production target and combines practical management techniques and tools to realize operational excellence and optimize the whole process individually. The optimal utilization of the machine during its productive life with minimum investment is the crucial goal of any organization. Therefore, the OEE philosophy acts as one of the tools used for continuous improvement. The Overall Equipment Effectiveness model is shown in Figure 1 [8].

The Artificial Neural Network (ANN) is inspired from the human brain neuron network. It has a motivating design that effectively models highly complicated problems and nonlinear systems [9]-[11]. Evolutionary feed forward single layer configuration using Levenberg Marquardt backpropagation algorithm has been employed in this study. The architecture of ANN consists of two input layers, ten hidden layers and one output layer, and each layer has some nodes representing artificial neurons. These neurons are usually assembled in layers [12]. Each layer has some nodes or neurons that interact through weighted connections [13]. Training of the network is carried out by refinement of the weight of the neurons, so the error condition is minimized and achieves the desired result, and this method is called backpropagation. Training patterns are formed of a set of matching input and output vectors, and a learning algorithm (LM) uses these vectors to train the network. It measures the difference between the desired output vector and actual output and modifies the weight's connection to decrease the propagated error. This process will continue until the error reaches the desired level [9].

ANN and GA are two of the most promising natural computation techniques and have applications in several studies for parameter optimization. These two techniques are considered adequate in process optimization, and their use has recently increased [14]. Thereby, integration of ANN with GA is implemented in this paper to model and optimize the OEE data analysis of the DWD pump system.

This research paper aims to assess the current overall effectiveness of the deep-water disposal pump system and categorize the major losses that lead to poor performance according to their weight, which allows managers to evaluate the equipment's effectiveness. Therefore, investigate inputs to the production process and eliminate the relative losses. Also, it will form a decision support tool for managers to prevent loss and then act and react to maximize and improve production effectiveness. Eighteen-month values were collected of the six big losses: total operating time, downtime, actual production, design capacity, proposed amount, and defect amount. Thereby find out the availability, performance efficiency, and quality rate, then take an average of the given period to estimate the OEE.

The remainder of this paper is organized as follows: literature review is discussed in Section 2. While Section 3 presents the research methodology in detail. Section 4 introduce the results and discussion of the research. Finally, the conclusion is offered in Section 5.

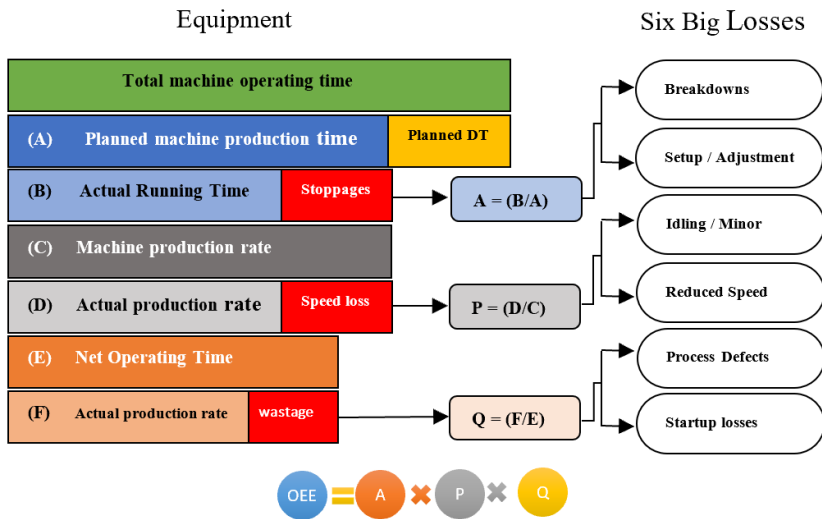


Figure 1: Overall equipment effectiveness model [2]

Literature Review

Overall equipment effectiveness is frequently used as a key metric in Total Productive Maintenance (TPM) and lean manufacturing programs to deliver operational excellence. It gives the industrials a consistent way to measure the effectiveness of the TPM and other initiatives (5S and world-class manufacturing) by providing an overall framework for measuring production efficiency. It considers three factors quality, speed, and downtime. It is merely the ratio of fully productive time to planned production time. In other words, it represents the percentage of production time spent making a reasonable production rate (no quality loss), as fast as possible (no speed loss), without interruption (no downtime loss). The Implementation of TPM has shown considerable results in Japanese enterprises. It has been unusual to increase the level of overall utilization from 60% to 90% according to [15], and Schaffer et al. [16] have observed that most companies implementing continuous improvement (CI) failed to achieve results. Its mission is to focus on results rather than on activities. If the magnitude and reasons for losses are unknown, the activities will be unallocated toward optimally solving the major losses. If the measurable results are not provided within a short period, the management and operator can lose reliance on TPM. If the success tastes unexperienced soon enough, the driving force of change will eventually vanish. Ahuja et al. [17] said that “TPM is a production-driven improvement methodology designed to optimize equipment reliability and efficiently manage plant assets through employee involvement linking manufacturing, maintenance, and engineering”.

Ng Corrales et al. [18] worked in their research on reviewing and analyzing OEE, presenting modifications made over the original model, and identifying future development areas. They are establishing procedures and criteria to present a structured and transparent methodical literature review. They obtained 862 articles, and after implementing duplicates and applying certain inclusion and exclusion criteria, 186 articles were used in this review. The research outcomes are summarized in three principles: (1) the academic interests increased in the last five years and the keywords being developed from maintenance and production to lean manufacturing and optimization; (2) creating a list of authors who have developed models based on OEE; (3) OEE is an emerging topic in areas like services and logistics. The research serves as a basis for future relevant studies. Williamson [19] defined OEE as a measure of total equipment performance which is the degree to which the equipment is doing what it is supposed to do. OEE broke down into three availability, performance, and quality analysis tools. These metrics help to gauge the machine's effectiveness and categories the big six productivity losses to improve asset performance and reliability. According to Jonsson and Lesshammar [20], the losses occur due to process interruptions that are either chronic or sporadic. Chronic disturbances are small and hidden and result from

several concurrent causes. In contrast, sporadic disturbances are more apparent since they happen faster and significantly exceed the normal state. Nakajima [21] stated that it is a bottom-up approach where an integrated workforce strives to achieve overall equipment effectiveness by eliminating six significant losses. Blanchard [22] has reported that the OEE world-class figures are widely argued to be around 85%. Parida et al. [23] argue that the most massive problem that exists in the industry today is low OEE being 15%-25% below the target level. Several studies showed that 30% of energy consumption in industry is wasted on machines in repair, idle, and standby states, which negatively impacts ecological sustainability [24].

The essence of lean is removing waste and identifying anything that does not add value. Domingo and Aguado [25] stated that OEE is associated with lean and green manufacturing, considered OEE for environmental issues, and gave the term Overall Environmental Equipment Effectiveness (OEEE). They carry out OEE calculations for various manufacturing industry lines, and the effect of factors associated with OEE is examined. Castro and Araujo [26] identified how to reduce waste and assure compliance production process as a key variable in the beverage industry. They applied OEE in the plant production line, filling beverages in bottles. Gibbons et al. [5] introduced enhancement to OEE, which is very useful for the OEE measurement framework by providing a benchmark. Enhanced OEE framework as an indicator of lean six sigma capability is introduced.

Artificial neural networks are the most popular in machine learning (ML) algorithms. The first invention of these neural networks was in 1943 and then developed by Frank Rosenblatt in 1958, based on McCulloch and Pitts model. It gained massive popularity over the years due to its computation power [27]. Artificial neural networks are sophisticated nonlinear computational tools capable of modelling extremely complex functions. ANN operates the nonlinear statistical mapping between an input set and a corresponding output set (target) to discover a new pattern [28]. Marini et al. [29] implemented deep learning in their study to measure production performance on fresh product packing. The goal is to predict future values of the key performance of machines' overall equipment effectiveness (OEE) and Machine Mechanical Efficiency (MME). Thus, avoiding sudden machine breakdowns by leveraging historical data. Sari et al. [30] conducted a study to evaluate metrics of production of OEE and overall line effectiveness (OLE) using intelligence techniques aiming to improve the calculative methods. Mamdani fuzzy interface system (FIS) and Sugeno were used to evaluate OEE, whereas FIS and Artificial neural networks (ANNs) were employed for OLE metrics evaluation. This study will allow the operator to share his knowledge and intervene in these measurements. Moreover, this method was tested in different scenarios. Bekar et al. [31] conducted a study to predict the overall equipment effectiveness (OEE) using simulation software aiming to identify the optimal level of the OEE to increase the time between failures and reduce

the mean repair time. OEE process optimization used various methods like Artificial Neural Network (ANN), Adaptive Neuro-Fuzzy Interface System (ANFIS), and Response Surface Methodology (RSM). It used Sequential Quadratic Programming (SQP) algorithm to determine the input values. The study outcomes influence avoiding frequent failures in the production process.

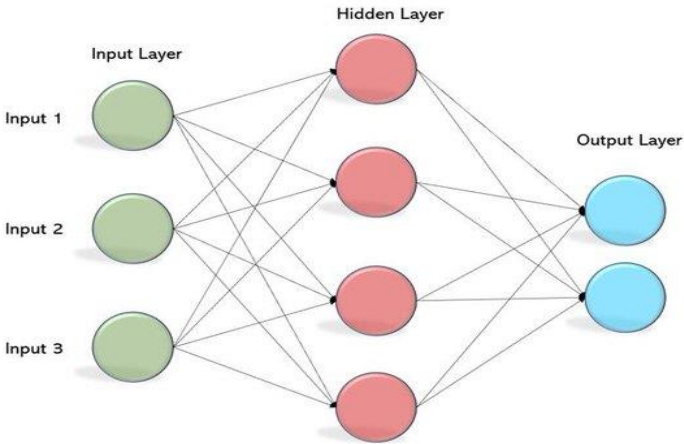


Figure 2: Artificial neural network structure [32]

A genetic algorithm (GA) is a search algorithm inspired by Charles Darwin's theory of natural evolution is based on survival of fitness; that is, some parents with stronger fitness ability to the environment will be chosen. The genes of these parents will be exchanged with each other to produce offspring. In this way, some offspring are expected to have higher fitness than their parents since the good genes would be preserved, and the chromosome could become even better after the crossover operation. With the processes of crossover, reproduction, and selection, the best chromosome with the strongest fitness ability to the environment will eventually evolve [33]. These algorithms maintain and manipulate a population of solutions and perform their search for the best solutions. This algorithm can treat linear and non-linear problems by selecting the fittest individuals from a population through crossover, selection, and mutation operations. Genetic algorithm uses involve determining six essential problems: genetic operator making up the reproduction function, selection function, chromosome representation, the creation of the initial population, termination criteria, and the evaluation [9], [34]. The methodology of combining ANN with GA is illustrates in Figure 3.

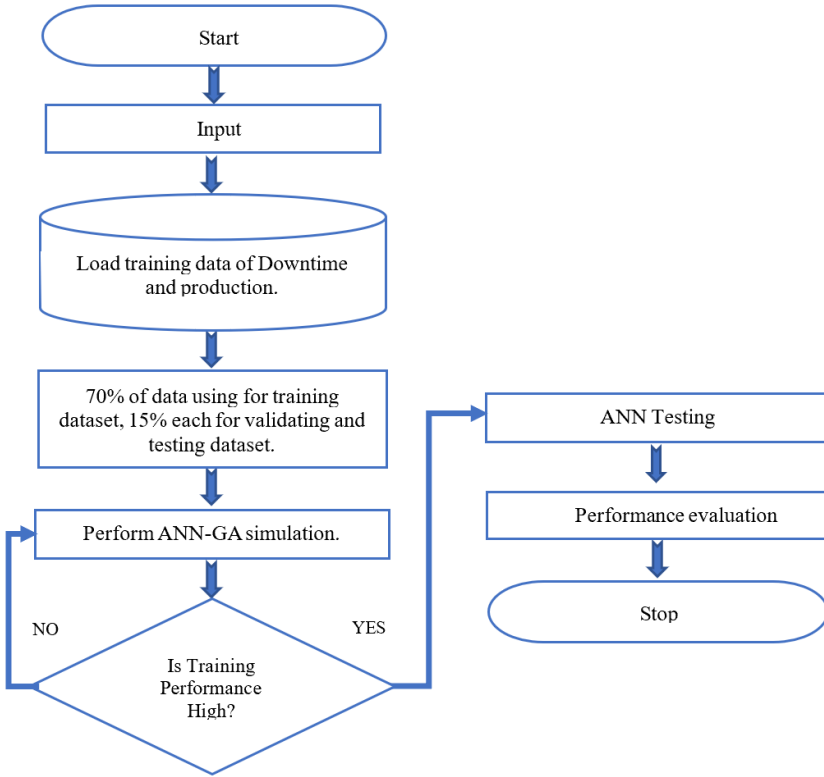


Figure 3: Flow diagram of ANN with GA

Methodology

The deep-water disposal (DWD) pump system data for eighteen successive months period is presented in this paper based on six big losses. The data information is used for computing OEE metrics (availability, performance, and quality) and therefore estimating the OEE value. The collected data were classified as total operating time, total downtime, actual produce amount, design capacity amount, proposed amount, and defect amount (Figure 1 shows the six big losses and OEE metrics).

$$OEE = Availability \times Performance \times Quality \quad (1)$$

Equation 1 is used to calculate the OEE metrics as follows:

- **Availability:** represents the percentage of scheduled time that the equipment is available to operate. 100% availability means the process has been running without any stops machine. The availability formula can be expressed as [35]:

$$Availability = \frac{(Total\ time - Total\ down\ time)}{Total\ time} \times 100 \quad (2)$$

Availability considers “Downtime losses” from
Pumps failures (pump is breakdown >15 min)
Setup and adjustments (pump breakdown >15 min)

- **Performance:** represents the percentage of the total actual amount of water produced on the pump machine to the machine’s production rate (actual vs designed capacity). 100% performance means the process has been consistently running at its theoretical maximum speed. The formula to calculate the performance rate can be expressed as [35]:

$$Performance\ rate = \frac{(Actual\ amount\ of\ \frac{produced}{Total}\ operating\ time)}{Design\ capacity\ of\ produced} \times 100 \quad (3)$$

Performance considers “Speed Losses” from
Idling and minor stoppages (pump is stop < 15 min)
Reduced speed operation (actual vs. design cycle time)

- **Quality:** represents the percentage of good amounts produced out of the proposed amounts produced on the pumping machine. 100% quality means there has been no defect amount. The quality rate can be expressed in a formula as follows [35]:

$$Quality\ rate = \frac{(Proposed\ amount - Defect\ amount)}{Proposed\ amount} \times 100 \quad (4)$$

where, defect amount = proposed amount – actual amount of contaminated water supply.

Quality considers “Defect Losses” from
Start-up losses (pump required warm-up time)
Production losses (no production according to specification)

The Artificial Neural Network (ANN) models developed for Downtime (DT) and Actual Produced amount (AP) data where employed optimization procedures using Genetic Algorithm (GA) using MATLAB (version-2019b) software. These two data sets are variables and will be employed as input for the ANN-GA model, whereas the rest are independent (identical values for all months) and will ignore in the model. Consequently, these two parameter

values' changes will reflect on the OEE value and consider different losses weight. Integrated ANN with GA as an effective tool to study the current performance status of the DWD system and identify the main losses influencing the system performance and use its full design capacity.

After that, estimated future Downtime (DT) and actual production (AP) values based on eighteen months gained data to predict the DWD system performance in the coming thirty-six months. To provide a status report about DWD system behavior patterns and their effectiveness to give management adequate time and allow them for an early intervention to minimize system deterioration, reduce maintenance costs, and increase productivity.

Analysis of variance (ANOVA) was adopted as an additional decision tool for detecting the variation of process parameters. It is a statistical method to determine the optimal level of factors that impact independent variables have on the dependent variable in a regression study [36]. In this study, ANOVA of the 36-month data will be carried out the variable 1 (downtime) and variable 2 (actual produced amount) directly related to OEE. Linear regression analysis using two variables provides a basis for estimating the OEE. The predicted OEE of the developed model through ANOVA techniques is more realistic and reliable. The ANOVA equation has been presented below (Equation 5) [37].

$$F = \frac{MST}{MSE} \quad (5)$$

where F is the ANOVA coefficient, MST is the mean sum of squares due to treatment, and MSE is the mean sum of squares due to error.

$$r = \frac{\sum(x_i - \bar{x})(y_i - \bar{y})}{\sqrt{\sum(x_i - \bar{x})^2 \sum(y_i - \bar{y})^2}} \quad (6)$$

where r is the correlation coefficient x_i are values of X-variable, \bar{x} is the mean of the values of the x-variable, y_i is values of y-variable, and \bar{y} is the mean of the values of the y-variable.

$$y = \beta_0 + \beta_1 X_1 + \dots + \beta_n X_n + \epsilon \quad (7)$$

where y is the predicted value of the dependent variable (OEE value in our study), β_0 is the y-intercept (y value when all parameters are set to 0), $\beta_1 X_1$ is the regression coefficient (β_1) of the first independent variable (X_1), $\beta_n X_n$ is the regression coefficient of the last independent variable, and e is the model error (known as residuals).

Data Analysis and Results

ANN-GA analysis modelling of OEE evaluation

The Deep-Water Disposal (DWD) pump system is vital to smooth operation, and they represent a significant segment of the entire operation. The high reliability of these pumps is envisaged to reduce the maintenance cost (failure cost), thus reducing the process disruption, and ensuring continuous plant productivity, which reflects positively on the revenue generated. These pumps have to operate 24 hours a day / seven days a week. The current state of the pump system performance observed is decreasing based on the number of failures during the specified operating period. Obtained data for eighteen operated months was trained using ANN-GA analysis modelling to evaluate the present DWD pump system OEE performance. Figure 4 shows the mean square error (MSE) versus the iteration plot of ANN for training, validation, and test performance of the Overall Equipment Effectiveness (OEE) evaluation. The sample data used can be referred to the appendix A. The most popular algorithm is backpropagation because it is a capable and efficient simulation. Also, used Levenberg–Marquardt algorithm (LM) because it has more successive performance predictions for complicated relationships between input variables. The LM algorithm, a trust-region model, contains three primary steps: data enters the input and crosses the network layers, then the mean square error ((MSE) (Equation 8) of the output computed by the net is propagated and lessened to the training target; finally, the connection weights are adjusted and updated [38].

$$MSE = \frac{1}{n} \sum_{i=1}^n (t_i - y_i)^2 \quad (8)$$

where y_i denoted the network's output, t_i denoted the desired goal and n is the number of inputs.

During training, errors are propagated back through the neurons, thereby adjusting the neurons' weights. Each cycle of error propagation during the network training is an epoch, and the number of epochs indicates how long the ANN simulation lasts. This performance plot shows unnoticeable problems, and the validation and test curves do not indicate overfitting. This training process undergoes till it gets saturated. Thereby, once the network's performance reaches the best fit, it will undergo training for the other six epochs, stop the training process, and avoid overfitting the network. The green ring circle indicates the best-fit point of the performance parameter neural network achieved with Mean Square Error (MSE) is 0.0003388 at epoch 9, which is very small and close to zero. In other words, the MSE mean (average) the magnitude of the error square estimates that the distance between the test value and the actual test value is close to each other. Moreover, the training and validation datasets gap is minimal and referred to as the "generalization

gap". At epoch 15, the generalization stops improving, and the training is halted.

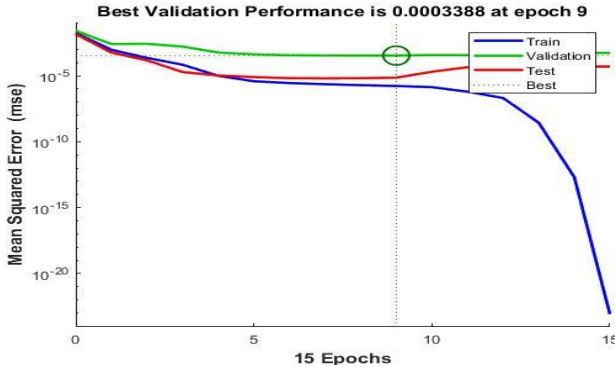


Figure 4: Plot of validation performance of the network

The correlation coefficient R regression plot is a valuable measurement of how well the ANN-GA network fits the data. The correlation coefficient is used to measure the strength of the relationship between two variables (Equation 6). The regression plot illustrates the correlation between the actual network output and the respective targets of the present OEE evaluation experiment. A correlation coefficient R-value of 1 means the output precisely matches the targets. In training, 70% of the provided data sets are used for training, 15% are used to validate the network, and 15% are used to test the network. In the case of a small number of learning data, like in our case, the training data should be subtracted sparingly; therefore, we have chosen 70 % for training data. There are no hard rules for data division. It depends on the complexity of the problem and the amount and nature of the learning data (much or less noise). However, there not a clear connection between the data division and the network performance. But 70% for training, 15% for validation, and 15% for testing data are recommended in certain literature [39]-[42].

Multiple linear regression (Equation 7) predicts the outcome variable based on two or more variables, also called multiple regression. This technique enables the determination of the model variation and the relative contribution of each independent variable in the total variance. Generally, the regression plot has four curves showing output for training, validation, test, and combination, as shown in Figure 5. It observes a higher value of regression R and indicates greater than 99% for both training and validation sets. For all data sets, the fit value is exceptional. The regression plot for this experimental network illustrates that all data sets are appropriately fitted to the line and indicate that the neural network structure is accurate and coherent.

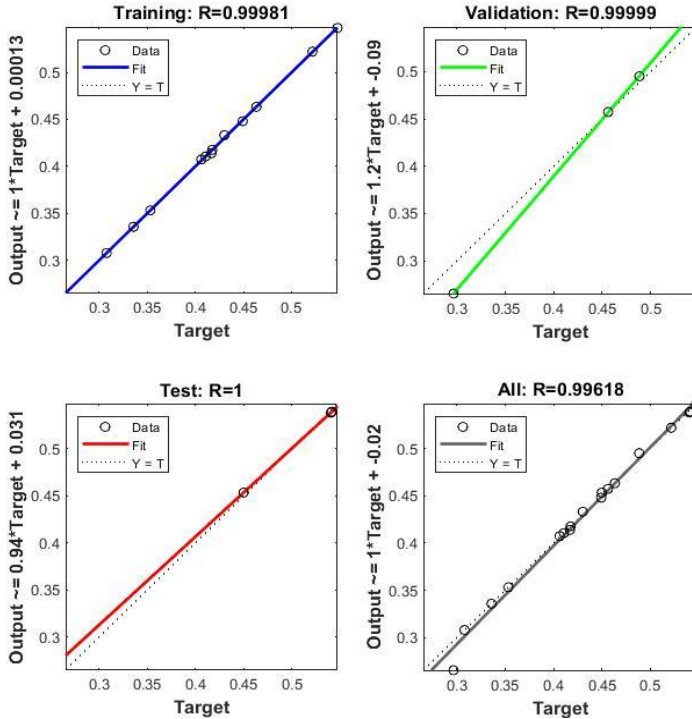


Figure 5: Regression Plot results for the current DWD system performance

Figure 6 shows the topology of the ANN model with two input neurons and output neurons (OEE) along with the optimum number of ten hidden layer neurons. The learning rate was adjusted to 0.01, the maximum number of epochs set to 1000, and the performance set to 0.0. During analyzing datasets, 70% were used to train the network and 15% each for the validation and the test. The network used in this study is a single-layer perceptron feed forward learning algorithm (Levenberg Marquardt backpropagation). This study will frame the input variables as machine downtime and actual production in the network, and the output/ target variables are considered to evaluate and maximize overall equipment effectiveness, improve efficiency, and recognize the main losses of the Deep-Water Disposal (DWD) pump system. The input/output variables data sets are loaded in the neural network structure to train the network using the Trainlm function. This function type updates the weight and bias values according to the Levenberg Marquardt optimization method. Gradient descent with momentum weight and bias learning function (LearnGdm) is used for adoption. Input neurons use the Logsig function to generate the output signal, and the transfer function used for the hidden layer is the Tansig function.

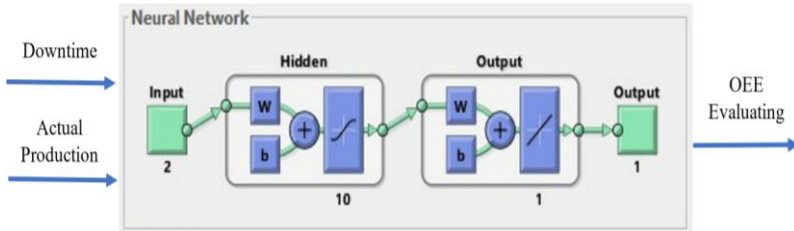


Figure 6: Neural network structure of OEE evaluation

In Figure 6, ‘w’ denotes the weight, whereas ‘b’ denote the bias, and the network randomly assigned their values. The associated transfer function Tansig showed a curve in the hidden layer and the output layer associated transfer function is Purelin and shown as a straight line. The number of hidden neurons was adjusted to 10 found optimum to increase the training performance and decrease the mean square error (MSE). The Levenberg-Marquardt training algorithm requires the least number of epochs for training the network. The MSE represents the average square difference between the output and the target. In other words, the lower values of the MSE are the better. The artificial neuron gets several input data as a vector $x = (x_1, x_2, \dots, x_n)$ where n is the number of the input. It weights each input x_i with a pre-determined weight w_i and sums up all the weighted input. A bias b is added to the sum and the result is provided to an activation found λ which is nonlinear. The output of the artificial neurons can be written as follows [42]. The Levenberg-Marquardt algorithm needs more memory but less time.

$$\text{Output from neurons} = \lambda(\sum_{i=1}^n w_i x_i + b) \tag{9}$$

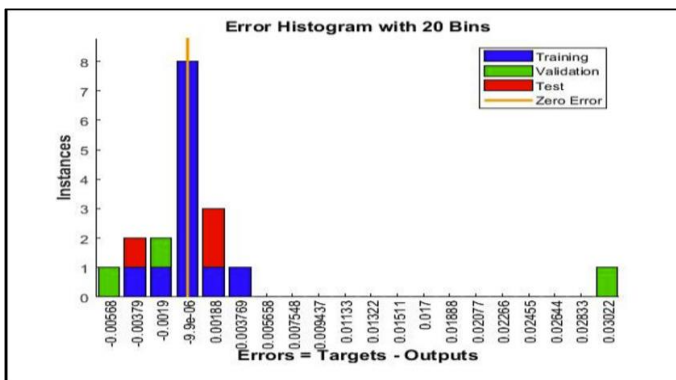


Figure 7: Error histogram network with 20 bins of the ANN-GA

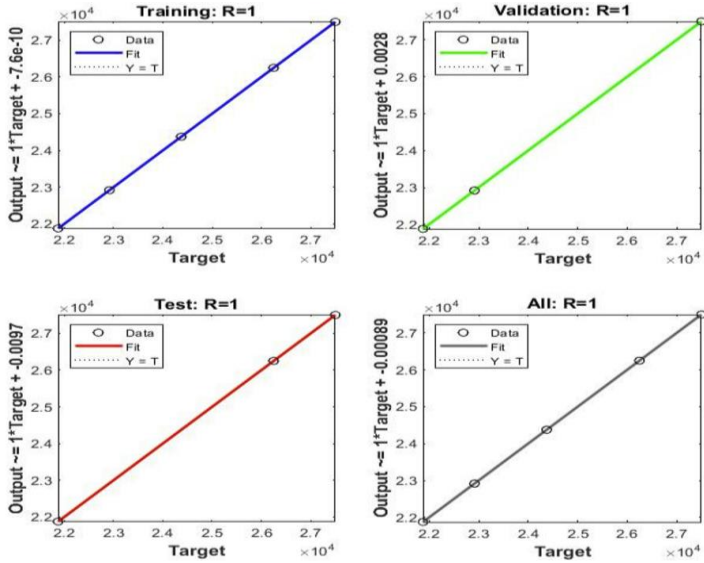


Figure 8: Regression plot results for the predicted DWD system performance

Error histogram values were calculated as demonstrated in Figure 7 through mean square error (MSE) by measuring the distance of the observed y values from the predicted y values at each value of x, then squaring each distance, followed by taking the mean of each square distance. It shows that the residual coverage between targets and the network output = [-0.00568 _ 0.03022]. Moreover, this histogram illustrates the target and predicts values errors with 20 bins after training the feedforward neural network for training, validation, and testing. Y-axes represent the number of dataset samples. A bin corresponds to the error shown at mid-plot, and the height of the bin for the training dataset lies around eight instances. Zero error point falls under the bin with the center -9.9e-06. The data from eighteen months was collected for two variables, downtime, and actual production amount, for forecasting the effectiveness of the deep-water disposal pump system in the coming thirty-six months. 70% of provided data sets are used for training, 15% of data sets are used for testing the prediction, and the rest 15% of data sets are used for validating the network. Figure 8 shows the performance regression plot result of the prediction of the two parameters. It is observed that the correlation coefficient (R) value of 1 for training, test, validation, and all datasets implies a perfect fit of outputs precisely equal to the target. Error histogram can help assess the quality of the trained network because it demonstrates the residuals between targets and network output and indicates outliers.

Figure 9 illustrates the error histogram and shows that most errors lie at -0.05, which is within the acceptable limit. Hence, the quality of learning data is exceptionally close to a value of 1 and without any outliers.

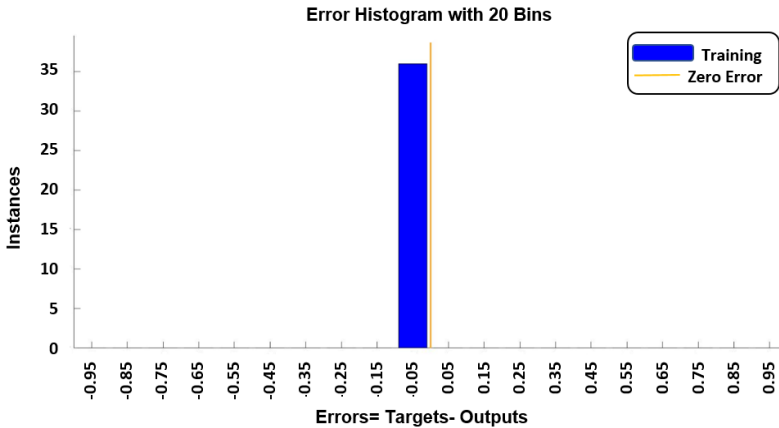


Figure 9: Error histogram network with 20 bins of the ANN-GA predicted dataset

The error has been calculated as shown in Equation 10 [42].

$$Errors = Targets - ANN\ outputs \tag{10}$$

The error histogram figure shows that the fitting data errors are distributed within a reasonably good range around zero, denoted as the orange vertical line for the training (blue) validation (green) and test (red) data. The number of bins of 20 represents the vertical bars observed in the error histogram ranging from -0.95 (leftmost bin) to 0.95 (rightmost bin). This error range is then divided into 20 smaller bins, so each bin has a width of 0.095, by c

o The vertical bar represents the number of samples from the datasets which lie in a particular bin and their corresponding error. As can be seen, the higher the number of datasets plugged in ANN, the lower the error associated. As the number of instances (dataset combinations) decreases, the associated error increases (positive and negative errors), directly affecting the ANN prediction performance.

ANOVA

ANOVA or variance analysis is a statistical procedure that separates variance data into different components for additional tests and measures the dependent variable from an independent variable. Moreover, it is used to model the

relationship strength between two variables where a dependent variable is predicted based on one or more independent variables. This study used thirty-six months of data on downtime (hrs) and actual produced amount (m³/hrs) to perform the ANOVA.

Table 1: The test evaluation of the multiple regression statistics

Regression statistics	
Multiple R	0.99862195
R square	0.9972458
Adjusted R square	0.99707888
Standard error	0.00481302
Observations	36

Table 1 shows that the value of the multiple R is 0.998; close to 1 means having a positive and robust linear relationship. Whereas the R square value indicates the points that fall in the regression line is 0.997, which is very good. 97%, close to 1, and the regression line fits the data. The standard error of 0.0048 illustrates that regression analysis is precise and that the average distance of the data point falls from the regression line is very small.

Table 2: The ANOVA analysis statistics

ANOVA					
	df	SS	MS	F	Significance F
Regression	2	0.276793992	0.1384	5974.36	5.7533E-43
Residual	33	0.000764451	2.3E-05		
Total	35	0.277558443			

	Coefficients	Standard error	t Stat	P-value	Lower 95%	Upper 95%
Intercept	-0.4483	0.0104	-43.058	1.4E-30	-0.4695	-0.4272
*DT	-0.0006	2.3582E-05	-27.556	2.4E-24	-0.0007	-0.0006
*AP	3.9241E-05	4.0551E-07	96.770	4.4E-42	3.8416E-05	4.0066E-05

* AP: Actual produced amount (M³/hrs.)

* DT: Downtime

In the ANOVA analysis (Table 2), F statistics (ratio of mean squares) is equal to $0.138396996 / 2.31652 \times 10^{-5} = 5974.355$. The distribution is F (2, 33), and the probability of observing significance F (P-value) is very low, 5.75334×10^{-43} ; this means 5.75×10^{-43} . The convention is that the relationship is highly statistical significance because the P-value is very small ($P < 0.001$).

Also, strong evidence that the slope of the regression line is not equal to zero. The squared multiple correlations (regression SS) $R^2 = SSM / SST = 0.276794 / 0.277558 = 0.997$, indicating that 99.7% of the variability in the “ratings” variables is explained by downtime and actual production amount variables. The lower and upper 95% confidence interval for downtime is -0.0007 and -0.0006, whereas 0.000038 and 0.00004 for the actual produced amount and the boundaries prove that does not contain zero and 95% confidence the significant linear relationship between downtime scores and actual production amount and the chance of acceptance. Where DF denoted the degree of freedom, SS denoted the sum of squares, and MS denoted the mean square.

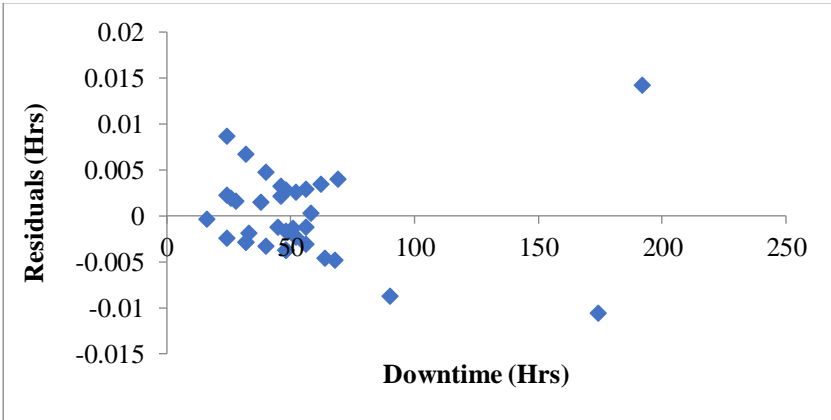
A residual plot is a graph that shows residual values on the vertical axis and the independent variable on the horizontal axis. The vertical distance is called residual, which means when the data point is above the line, the residual is positive, and the residual is negative for the data point below the line. The closer the data point residual is to 0, the better the fit. The residual output shows that the difference between the actual value and the predicted value of the regression model is minimal and very close to each other refer to appendix B. Both residual downtime and actual produced amount plots in Figure 10 show a reasonably random pattern and indicate that a linear model fits the data well. There is a strong correlation between model prediction and the actual result for both residual plots. It is observed that both plots have a high density of points close to the origin and low-density points away from the origin.

The regression analysis can be used to predict the OEE for any future combination of variables 1 (downtime in hours) and variable 2 (actual production m^3/hr). This means the data obtained in ANN prediction modelling of variables 1 and 2 meet the actual data (refer to Appendix B). Analysis showed a linear relationship with the OEE, and selected variables and Equation 11 can be used to predict the OEE with 99.7% accuracy.

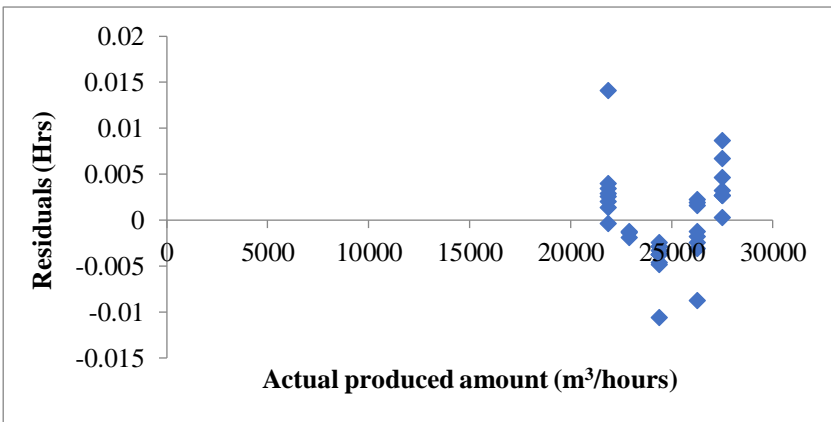
$$\text{Predicted OEE} = -0.000649834 \times \text{Down time (hours)} + 3.9241E - 05 \times \text{Actual produced amount} \left(\frac{m^3}{hrs} \right) + (-0.448339865) \quad (11)$$

Figure 11 shows the plot of actual residual OEE and predicted OEE for 36 observations used for the study. The regression model developed shows very low residuals indicating that the predicted model closely matches the actual one. Thus, this OEE prediction model is satisfactory and can be used to set a target for improving the OEE value of DWD pumps. To achieve the desirable higher OEE level at the DWD pump system, Equation 11 can be used in two ways. For the desired OEE, field operators can target actual production for a month in m^3/hr for a maximum allowable monthly downtime (hours) to meet the desired OEE. Conversely, for the desired OEE, maintenance departments can work towards the maximum allowable downtime per month (hours) for targeted actual production m^3/hr to meet the desired OEE. For

instance, if desired OEE of 70%, the maintenance team has to maintain frequent failures (downtime) not exceeding 30 hours per month; and ask the production team to produce an output within 30000 m³/hr.



(a)



(b)

Figure 10: (a) Downtime; and (b) actual produced amount of residual prediction plots

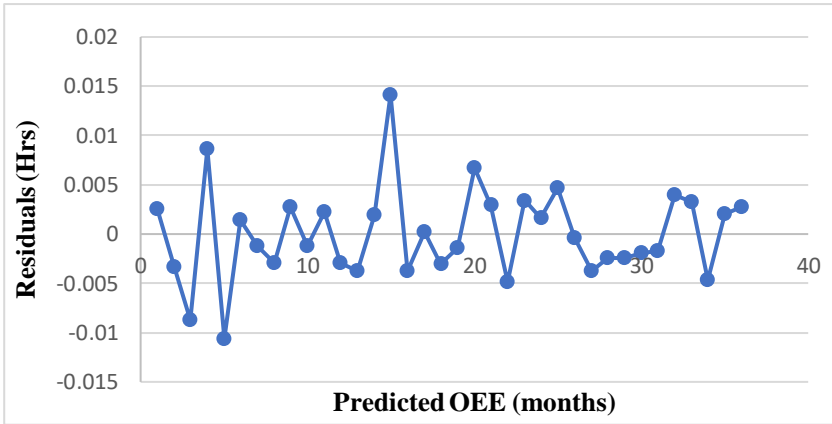


Figure 11: The residual plot of actual OEE and predicted OEE for 36 observations

Conclusion

This paper presents the overall equipment effectiveness (OEE) current performance evaluation of the deep-water disposal (DWD) pump system using an ANN-GA modelling analysis approach by MATLAB software based on eighteen months of historical data collected. The results show that the system OEE currently performed between 29% and 54%, with an average of around 43.5%, far from the world-class target (85%). Also noticed is that the availability factor has a stronger impact on the OEE formula than the performance and quality factors, which means it has a higher weight. Accordingly, concentrating on and improving the DWD system availability will make a difference in the system's effectiveness without sacrificing performance and quality factors. To achieve that, minimize the frequent failures (breakdown) of the DWD system and align all system setup and adjustments activities according to the operator's weekly schedule plan. Integration of ANN-GA analysis was used to predict the DWD pump system's overall equipment effectiveness future for the coming thirty-six months and was developed and validated. The results showed that the predicted future system performance average is approximately 49%, which reflects the poor performance of the DWD pump system in the future compared to the world-class target. In addition, the prediction data observed matched the actual data, proving that the data quality used in the analysis was reasonable. Also, the ANN-GA analysis result confidence was very close and matched the actual values. In an analysis of variance (ANOVA) of the 36-month data, it is observed that variable 1 (DT) and variable 2 (AP) are directly related to OEE.

Linear regression analysis using two variables provides a basis for estimating the OEE with 99.7% confidence with a standard error of 0.0048. This demonstrates that regression analysis is precise and that the average distance of the data point falls from the regression line very small. The lower and upper, 95% confidence, is the significant linear relationship between downtime scores, actual production amount, and the chance of acceptance. The linear regression equation developed in this study helps determine the combined impact of variables 1 and 2 on OEE. The residuals of predicted OEE were significantly lower; it is observed that both plots have a high density of points close to the origin and low-density points away from the origin, and thus the model developed through ANOVA techniques is more realistic and reliable. This study analysis can help maximize the OEE target level from a poor level to an acceptable level and support management with a clear vision report of DWD system performance behaviour in the current and future. Furthermore, it provides a base for identifying the potential area of early improvement and supports continuous improvement (CI) objectives by identifying and eliminating associated maintenance waste.

Contributions of Authors

Soud Al-Toubi conducted all research sections and wrote the original draft manuscript as part of his Ph.D. project. Babakalli Alkali, David Harrison, and Sudhir C.V.: supervision, reviewing, and guidance. All authors reviewed and approved the final version of this work.

Funding

This work received no specific grant from any funding agency.

Conflict of Interests

All authors declare that they have no conflicts of interest

Acknowledgement

The authors would like to express appreciation to the National University of Science and Technology Oman- mechanical and industrial department team for contributing to data analysis support and valuable guidance.

References

- [1] S. Al-Toubi, P. B. Alkali, P. D. Harrison, and P. S. C.V., “Application of 5s Methodology: A Case Study Towards Enhancing Spare Parts Processing Efficiency”, *International Journal of Engineering and Advanced Technology*, vol. 11, no. 5, pp. 1–15, 2022.
- [2] S. Nakajima, “Introduction to total productive maintenance (TPM),” *Productivity Press Cambridge, MA*, 1988.
- [3] T. Ylipää, A. Skoogh, J. Bokrantz, and M. Gopalakrishnan, “Identification of maintenance improvement potential using OEE assessment”, *International Journal of Productivity and Performance Management*, vol. 66, no. 1, pp. 126–143, 2017.
- [4] D. Yuniawan, T. Ito, and M. E. Bin, “Calculation of overall equipment effectiveness weight by Taguchi method with simulation”, *Concurrent Engineering*, vol. 21, no. 4, pp. 296-306, 2013.
- [5] P. M. Gibbons and S. C. Burgess, “Introducing OEE as a measure of lean Six Sigma capability”, *International Journal of Lean Six Sigma*, vol. 1, no. 2, pp. 134–156, 2010.
- [6] A. S. Badiger and R. Gandhinathan, “A proposal: evaluation of OEE and impact of six big losses on equipment earning capacity”, *International Journal of Process Management and Benchmarking*, vol. 2, no. 3, pp. 234–248, 2008.
- [7] B. Dal, P. Tugwell, and R. Greatbanks, “Overall equipment effectiveness as a measure of operational improvement—a practical analysis”, *International Journal of Operations & Production Management*, vol. 20, no. 12, pp. 1488-1502, 2000.
- [8] M. Singh and M. Narwal, “Measurement of Overall Equipment Effectiveness (OEE) of a manufacturing industry: An effective lean tool”, *International Journal of Recent Trends in Engineering and Research*, vol. 3, no. 5, pp. 268-275, 2017.
- [9] K. V. Kumar, L. Paradeshi, M. Srinivas, and S. Jayaraj, “Parametric studies of a simple direct expansion solar assisted heat pump using ANN and GA”, *Elsevier, Energy Procedia*. vol. 90, pp. 625-634, 2016.
- [10] B. Wang, G. Zhang, H. Wang, J. Xuan, and K. Jiao, “Multi-physics-resolved digital twin of proton exchange membrane fuel cells with a data-driven surrogate model”, *Energy and AI Journal*, vol. 1, pp. 100004, 2020.
- [11] Y. Wang, B. Seo, B. Wang, N. Zamel, K. Jiao, and X. C. Adroher, “Fundamentals, materials, and machine learning of polymer electrolyte membrane fuel cell technology”, *Energy and AI Journal*, vol. 1, pp. 100014, 2020.
- [12] S. G. Barad, P. V. Ramaiah, R. K. Giridhar, and G. Krishnaiah, “Neural network approach for a combined performance and mechanical health

- monitoring of a gas turbine engine”, *Journal of Mechanical Systems and Signal Processing*, vol. 27, pp. 729-742, 2012.
- [13] Y. Peng, M. Dong, and M. J. Zuo, “Current status of machine prognostics in condition-based maintenance: a review”, *The International Journal of Advanced Manufacturing Technology*, vol. 50, no.1, pp. 297-313, 2010.
- [14] C. Shen, L. Wang, and Q. Li, “Optimization of injection molding process parameters using combination of artificial neural network and genetic algorithm method”, *Journal of Materials Processing Technology*, vol. 183, no 2-3, pp. 412-418, 2007.
- [15] S. Nakajima, “TPM development program: implementing total productive maintenance”, *Productivity press*, 1989.
- [16] R. H. Schaffer and H. A. Thomson, “Successful change programs begin with results”, *Harvard Business Review*, vol. 70, no. 1, pp. 80-89, 1992.
- [17] I. P. S. Ahuja and J. S. Khamba, “Assessment of contributions of successful TPM initiatives towards competitive manufacturing”, *Journal of Quality in Maintenance Engineering*, vol. 14, no. 4, pp. 356-374, 2008.
- [18] L. del C. Ng Corrales, M. P. Lambán, M. E. Hernandez Komer, and J. Royo, “Overall equipment effectiveness: systematic literature review and overview of different approaches”, *Applied Sciences*, MDPI AG, vol. 10, no. 18, pp. 6469, 2020.
- [19] R. M. Williamson, “Using overall equipment effectiveness: the metric and the measures”. *Strategic Work System, Inc.*, pp. 1-6, 2006. Available online at: <https://swspitcrew.com/wp-content/uploads/2018/01/OEE.pdf>. (Accessed 15 May 2022).
- [20] P. Jonsson and M. Lesshammar, “Evaluation and improvement of manufacturing performance measurement systems-the role of OEE”, *International Journal of Operations & Production Management*, vol. 19, no. 1, pp. 55-78, 1999.
- [21] S. Nakajima, “Introduction to TPM: total productive maintenance”, (Translation), *Productivity Press, Inc.*, pp.129, 1988.
- [22] B. S. Blanchard, “An enhanced approach for implementing total productive maintenance in the manufacturing environment”, *Journal of Quality in Maintenance Engineering*, vol. 3, no. 2, pp. 69-80, 1997.
- [23] A. Parida, U. Kumar, D. Galar, and C. Stenström, “Performance measurement and management for maintenance: a literature review”, *Journal of Quality in Maintenance Engineering*, vol. 21, no. 1, pp. 2-33, 2015.
- [24] A. Skoogh, B. Johansson, and L. Hansson, “Data requirements and representation for simulation of energy consumption in production systems”, *Anonymous Proceedings of the 44th CIRP Conference on Manufacturing Systems*, pp. 1-3, 2011.

- [25] R. Domingo and S. Aguado, "Overall environmental equipment effectiveness as a metric of a lean and green manufacturing system", *Sustainability*, MDPI AG, vol. 7, no. 7, pp. 9031–9047, 2015.
- [26] F. P. Castro and F. O. Araujo, "Proposal for OEE (Overall Equipment Effectiveness) indicator deployment in a beverage plant", *Brazilian Journal of Operations & Production Management*, vol. 9, no. 1, pp. 71–84, 2012.
- [27] F. Marini, R. Bucci, A. L. Magrì, and A. D. Magrì, "Artificial neural networks in chemometrics: History, examples, and perspectives". *Micro chemical Journal*, vol. 88, no. 2, pp. 178–185, 2008.
- [28] G. Dreyfus, "Neural networks: an overview", *Neural Networks*, pp. 1–83, 2005.
- [29] L. Brunelli, C. Masiero, D. Tosato, A. Beghi, and G. A. Susto, "Deep learning-based production forecasting in manufacturing: a packaging equipment case study", *Procedia Manufacturing*, vol. 38, pp. 248–255, 2019.
- [30] M. F. Sari and S. A. Darestani, "Fuzzy overall equipment effectiveness and line performance measurement using artificial neural network", *Journal of Quality in Maintenance Engineering*, vol. 25, no. 2, pp. 340–354, 2019.
- [31] E. T. Bekar, M. Cakmakci, and C. Kahraman, "Using Adaptive Neuro-Fuzzy Inference System, Artificial Neural Network and Response Surface Method to Optimize Overall Equipment Effectiveness for An Automotive Supplier Company", *Journal of Multiple-Valued Logic & Soft Computing*, vol. 28, no. 4–5, pp. 375–407, 2017.
- [32] M. Belaissaoui and Y. Maleh, "Machine Learning techniques optimized by Practical Swarm optimization for Intrusions Detection in IoT", *Journal of Information Assurance & Security*, vol. 16, no. 3, pp. 105–116, 2021.
- [33] K.-Y. Chang, "The optimal design for PEMFC modeling based on Taguchi method and genetic algorithm neural networks", *International Journal of Hydrogen Energy*, vol. 36, no. 21, pp. 13683–13694, 2011.
- [34] P. Tian, X. Liu, K. Luo, H. Li, and Y. Wang, "Deep learning from three-dimensional Multiphysics simulation in operational optimization and control of polymer electrolyte membrane fuel cell for maximum power", *Applied Energy*, vol. 288, pp. 116632, 2021.
- [35] D. D. S. Verma and R. Dawar, "Measurement of Overall Equipment Effectiveness for Water Discharge System: A Case Study". *International Journal of Engineering Research & Technology (IJERT)*, vol. 3, no. 4, pp. 737–743, 2014.
- [36] A. B. Naik and A. C. Reddy, "Optimization of tensile strength in TIG welding using the Taguchi method and analysis of variance (ANOVA)", *Thermal Science and Engineering Progress*, vol. 8, pp. 327–339, 2018.

- [37] B. Thakur, G. Gupta, and N. Kumar, "Hybrid genetic model with ANOVA for predicting breast neoplasm using METABRIC gene data". *Materials Today: Proceedings*, vol. 56, pp. 1847-1852, 2022.
- [38] D. Podstawczyk, A. Witek-Krowiak, A. Dawiec, and A. Bhatnagar, "Biosorption of copper (II) ions by flax meal: empirical modeling and process optimization by response surface methodology (RSM) and artificial neural network (ANN) simulation", *Ecological Engineering Journal*, vol. 83, pp. 364-379, 2015.
- [39] M. J. Moradi, K. Daneshvar, D. Ghazi-Nader, and H. Hajiloo, "The prediction of fire performance of concrete-filled steel tubes (CFST) using artificial neural network", *Thin-Walled Structures*, vol. 161, pp. 107499, 2021.
- [40] A. Patra, S. Abdullah, and R. C. Pradhan, "Application of artificial neural network-genetic algorithm and response surface methodology for optimization of ultrasound-assisted extraction of phenolic compounds from cashew apple bagasse", *Journal of Food Process Engineering*, vol. 44, no. 10, pp. e13828, 2021.
- [41] K. Purohit, S. Srivastava, V. Nookala, V. Joshi, P. Shah, R. Sekhar, S. Panchal, M. Fowler, R. Fraser and M. Tran, "Soft sensors for state of charge, state of energy, and power loss in formula student electric vehicle", *Applied System Innovation*, vol. 4, no. 4, pp. 78, 2021.
- [42] S. Salih and R. Olawoyin, "Intelligent Performance Analysis of Automated Steering Systems for Autonomous Vehicles" *In: Anonymous 2020 IEEE International Conference on Electro Information Technology (EIT), IEEE*, pp. 200-205, 2020.
- [43] M. H. F. Al Hazza, M. Y. Ali, and N. Razif, "Performance improvement using analytical hierarchy process and Overall Equipment Effectiveness (OEE): Case study". *Journal of Engineering Science and Technology*, vol. 16, no. 3, pp. 2227-2244, 2021.
- [44] O. C. Chikwendu, A. S. Chima, and M. C. Edith, "The optimization of overall equipment effectiveness factors in a pharmaceutical company", *Heliyon*, vol. 6, no. 4, pp. 03796, 2020.
- [45] B. V. De Souza, S. R. B. Dos Santos, A. M. De Oliveira, and S. N. Givigi, "Analyzing and Predicting Overall Equipment Effectiveness in Manufacturing Industries using Machine Learning", *IEEE International Systems Conference (SysCon), IEEE*, pp. 1-8, 2022.
- [46] S. Nallusamy, V. Kumar, V. Yadav, U. K. Prasad, and S. K. Suman, "Implementation of total productive maintenance to enhance the overall equipment effectiveness in medium scale industries", *International Journal of Mechanical and Production Engineering Research and Development*, vol. 8, no. 1, pp. 1027-1038, 2018.

Appendix A

The table below shows the current OEE values results in actual and ANN-GA analysis output where both values match each other.

Months	Jan	Feb	Mar	Apr	May	Jun	July	Aug	Sept	*Oct	Nov	Dec	Jan	Feb	Mar	Apr	May	June
T/ Time	720	720	720	720	720	720	720	720	720	600	720	720	720	720	720	720	720	720
DT	97	138	82	203	116	211	254	218	243	114	109	175	117	109	128	143	177	197
(A)	86.53%	80.83%	88.61%	71.81%	83.89%	70.69%	64.72%	69.72%	66.25%	81.00%	84.86%	75.69%	83.75%	84.86%	82.22%	80.1%	75.4%	72.64%
Actual	21875	27500	24375	27500	27500	27500	27500	27500	24375	20313	27500	27500	27500	24375	24375	24375	21875	21875
Design Cap	37500	37500	37500	37500	37500	37500	37500	37500	37500	31250	37500	37500	37500	37500	37500	37500	37500	37500
(P)	58.33%	73.33%	65.00%	73.33%	73.33%	73.33%	73.33%	73.33%	65.00%	65.00%	73.33%	73.33%	73.33%	65.00%	65.00%	65.0%	58.3%	58.33%
Proposed	31250	31250	31250	31250	31250	31250	31250	31250	31250	26042	31250	31250	31250	31250	31250	31250	31250	31250
Defect	9375	3750	6875	3750	3750	3750	3750	3750	6875	5729	3750	3750	3750	6875	6875	6875	9375	9375
(Q)	70%	88%	78%	88%	88%	88%	88%	88%	78%	78%	88%	88%	88%	78%	78%	78%	70%	70%
Actual OEE	35.33%	52.16%	44.93%	46.34%	54.14%	45.62%	41.77%	44.99%	33.59%	41.07%	54.76%	48.85%	54.05%	43.02%	41.69%	40.63%	30.80%	29.66%
ANN-GA	0.3533	0.522	0.4481	0.4633	0.5393	0.4573	0.4177	0.4534	0.3359	0.4106	0.5472	0.4951	0.5382	0.4332	0.414	0.4074	0.308	0.2654

DT: Downtime

A: Availability

P: Performance

Q: Quality

***All** production amounts are measured in cubic meters per day

Cap: Capacity

T/Time: Total Time in hours

Defect: The loosed amount of production.

Proposed: The amount target set by the operation team.

Appendix B

The below table shows the predicted future OEE values results for the 36 months. It observed that the OEE actual values were matched with ANN-GA analysis output.

S/N	T/ Time Hrs	DT	A %	APA M ³ /hrs.	DPA m ³ /hrs.	P %	PPA M ³ /hrs.	DA m ³ /hrs.	Q %	OEE %	ANN-GA %
1	720	52	92.78	21875	37500	58.33	31250	9375	70	37.88	38
2	720	40	94.44	24375	37500	65.00	31250	6875	78	47.88	48
3	720	90	87.50	26250	37500	70.00	31250	5000	84	51.45	52
4	720	24	96.67	27500	37500	73.33	31250	3750	88	62.38	62
5	720	174	75.83	24375	37500	65.00	31250	6875	78	38.45	40
6	720	38	94.72	21875	37500	58.33	31250	9375	70	38.68	39
7	720	45	93.75	26250	37500	70.00	31250	5000	84	55.13	55
8	720	32	95.56	24375	37500	65.00	31250	6875	78	48.45	49
9	720	48	93.33	27500	37500	73.33	31250	3750	88	60.23	60
10	720	56	92.22	22917	37500	61.11	31250	8333	73	41.33	41
11	720	24	96.67	26250	37500	70.00	31250	5000	84	56.84	57
12	720	32	95.56	24375	37500	65.00	31250	6875	78	48.45	49
13	720	48	93.33	24375	37500	65.00	31250	6875	78	47.32	48
14	720	26	96.39	26250	37500	70.00	31250	5000	84	56.68	56
15	720	192	73.33	21875	37500	58.33	31250	9375	70	29.94	29
16	720	48	93.33	24375	37500	65.00	31250	6875	78	47.32	48
17	720	58	91.94	27500	37500	73.33	31250	3750	88	59.33	59
18	720	56	92.22	26250	37500	70.00	31250	5000	84	54.23	55
19	720	51	92.92	22917	37500	61.11	31250	8333	73	41.64	42
20	720	32	95.56	27500	37500	73.33	31250	3750	88	61.67	61
21	720	56	92.22	21875	37500	58.33	31250	9375	70	37.66	37
22	720	68	90.56	24375	37500	65.00	31250	6875	78	45.91	46
23	720	62	91.39	21875	37500	58.33	31250	9375	70	37.32	37
24	720	28	96.11	26250	37500	70.00	31250	5000	84	56.51	56
25	720	40	94.44	27500	37500	73.33	31250	3750	88	60.95	60
26	720	16	97.78	21875	37500	58.33	31250	9375	70	39.93	40
27	720	48	93.33	24375	37500	65.00	31250	6875	78	47.32	48
28	720	52	92.78	26250	37500	70.00	31250	5000	84	54.55	55
29	720	24	96.67	24375	37500	65.00	31250	6875	78	49.01	49
30	720	33	95.42	22917	37500	61.11	31250	8333	73	42.76	43
31	720	48	93.33	26250	37500	70.00	31250	5000	84	54.88	55
32	720	69	90.42	21875	37500	58.33	31250	9375	70	36.92	37
33	720	46	93.61	27500	37500	73.33	31250	3750	88	60.41	60
34	720	64	91.11	24375	37500	65.00	31250	6875	78	46.19	47
35	720	46	93.61	21875	37500	58.33	31250	9375	70	38.22	38
36	720	48	93.33	27500	37500	73.33	31250	3750	88	60.23	60

DT: Downtime **A:** Availability

DPA: Defect Produced amount.

PPA: Proposed Produced Amount

P: Performance

APA: Actual Produced Amount.

T/Time: Total Time.

Q: Quality